



UNIVERSITÀ
DEGLI STUDI
FIRENZE

**DOTTORATO DI RICERCA IN
FISICA E ASTRONOMIA**

CICLO XXXIV

COORDINATORE: Prof. Raffaello D'Alessandro

*Study of quasi-projectile breakup in semiperipheral
collisions of $^{64,58}\text{Ni} + ^{64,58}\text{Ni}$ at 32 A MeV and 52 A MeV
with the INDRA-FAZIA apparatus*

Settore Scientifico Disciplinare: FIS/04 Fisica Nucleare e Subnucleare

Dottoranda

Dott. Caterina Ciampi

Caterina Ciampi.....

Tutore

Prof. Gabriele Pasquali

Gabriele Pasquali.....

Coordinatore

Prof. Raffaello D'Alessandro

Raffaello D'Alessandro.....

Anni 2018-2021

Contents

Introduction	1
1 Physics case	5
1.1 Heavy Ion Collisions	5
1.1.1 The intermediate energy regime	7
1.1.2 Isospin observables in peripheral collisions at Fermi energies	10
1.2 Nuclear Equation of State (NEoS)	12
1.2.1 Isospin transport phenomena	18
1.3 QP breakup or dynamical fission	19
2 The INDRA-FAZIA experimental apparatus	23
2.1 The FAZIA apparatus	23
2.1.1 The detectors	25
2.1.2 The read-out electronics	28
2.1.3 Data flow and digital treatment of the signals	32
2.2 The INDRA apparatus	33
2.3 Coupling INDRA and FAZIA	34
2.4 Identification techniques	37
2.4.1 ΔE -E method	37
2.4.2 Pulse Shape Analysis in silicon	39
2.4.3 Pulse Shape Analysis in CsI(Tl)	42
3 The E789 experiment	45
3.1 Scientific goal and experimental setup	45
3.2 Particle identification procedure	48
3.2.1 Choice of the identification method	55
3.3 Energy calibration	57
3.3.1 Calibration of FAZIA detectors	57
3.3.2 Calibration of INDRA detectors	63
3.3.3 Energy assignment	64
3.4 Event selection	66
3.4.1 Charge and velocity distributions	68
4 Theoretical models and simulations	71
4.1 Dynamical model: the AMD code	72
4.1.1 Characteristics of the primary fragments	74
4.2 Statistical model: the GEMINI code	83

4.2.1	The Evaporation Attractor Line (EAL)	85
4.3	Software filter	86
4.4	First comparisons with experimental data	88
5	Selection of the reaction channels	91
5.1	QP evaporation channel selection	91
5.2	QP breakup channel selection	98
5.3	Centrality estimation	107
5.4	Comparison between QPr and QPb channels	117
6	Isospin analysis	119
6.1	General isospin characteristics	119
6.1.1	Comparison with AMD+GEMINI model predictions	121
6.2	Isospin characteristics of the QP fragment	123
6.2.1	Isospin equilibration in the QPr channel	123
6.2.2	Isospin equilibration in the QPb channel	127
6.2.3	Comparison between QPr and QPb channels	129
6.2.4	AMD+GEMINI model predictions	132
6.3	Isospin characteristics of LCPs and IMFs	134
6.3.1	Ejectiles of the QP: isospin diffusion	134
6.3.2	Isotopic composition and emission pattern of LCPs and IMFs: isospin drift	137
6.4	Isospin characteristics of QP breakup fragments	139
	Summary and conclusions	143
	Bibliography	149

Introduction

The properties of nuclear matter far from equilibrium are a widely studied topic in nuclear physics, where the *nuclear matter* is defined as an ideal system composed of an infinite number of nucleons interacting only via nuclear forces. In fact, there is a great interest in describing the behaviour of nuclear matter as a function of thermodynamic variables like temperature, pressure, density. In particular, the behaviour of the energy as a function of these thermodynamic variables and of the neutron/proton content is expressed by the Nuclear Equation of State (NEoS). More specifically, many efforts are being made in order to constrain the values of the parameters defining the dependence of the NEoS on the nuclear density and on the isospin asymmetry¹ [1, 2]. This is needed in order to predict the behaviour of asymmetric nuclear matter at both low and high density, far from the saturation value $\rho_0 = 0.16 \text{ fm}^{-3}$. The interest in this topic is manifold [3]. In nuclear physics, the NEoS is strongly related to the characteristics of nucleon-nucleon interaction and to nuclear properties such as the density profile [4]. In astrophysics, the interest stems, as an example, from the implications of the NEoS in the study of neutron stars [5, 6].

Heavy ion collisions in the intermediate energy regime (20 – 100 A MeV) are a widely employed tool to study the properties of nuclei far from equilibrium, in the hope of extrapolating the information to infinite nuclear matter [7–10]. A collision is generally schematised as composed of two phases. The first one is the *dynamical phase*, when the primary interaction between projectile and target takes place. The second one is the *statistical phase*, in which the hot primary fragments produced in the dynamical phase undergo statistical de-excitation. Different outcomes of the dynamical phase, reflecting in the characteristics of the fragments produced at the end of the process, are expected depending on the reaction centrality [11]. In particular, the present work is focused on semiperipheral and peripheral collisions, for which a binary output channel is the most probable result: two heavy fragments, called quasi-projectile (QP) and quasi-target (QT), are generally produced, together with some lighter ejectiles. During their interaction, an elongated low-density *neck region* can be formed between projectile and target. This region is unstable and tends to break up quite early, originating the so called *midvelocity emissions*, whose characteristics are strongly related to the dynamics of the reaction [12]. Many phenomena taking place during a heavy ion collision can be interpreted in

¹With the term *isospin* we generally refer to the neutron and proton content of a system. The *isospin asymmetry* of nuclear matter refers to the imbalance between its neutron and proton content, that can be expressed by means of a difference between the neutron and proton densities of the system. In the literature related to the study of the isospin content of the reaction products, with the term *isospin* we generally refer to the neutron to proton ratio N/Z of the ejectiles.

the framework of the NEOs. An example can be found in the isospin transport phenomena [13], i.e. the effects related to the nucleon exchange between projectile and target during the dynamical phase of the reaction. The *isospin diffusion* takes place whenever an isospin gradient is present; therefore, it induces the isospin equilibration between two asymmetric reaction partners (i.e. with different N/Z). The *isospin drift* is instead a nucleon transport process driven by a density gradient, and it can be considered responsible for the observed neutron enrichment of the midvelocity emission. Since the strength of these two dynamical processes depends on the NEOs, we can gather information on its parametrisation by studying the isospin content of the ejectiles, assuming that the statistical de-excitation does not wash out the information about the dynamical phase.

The NEOs is usually included in a theoretical model, whose predictions must be compared to detailed experimental observations in order to extract information on the NEOs parametrisation. The simulation of the reaction is generally performed in two steps, that mimic its dynamical and statistical phases. In this work, the AMD (Antisymmetrized Molecular Dynamics) dynamical code [14] has been employed for the former, coupled to GEMINI++ [15] used as *afterburner* (i.e. statistical code).

The investigation of isospin dynamics requires experimental apparatuses capable of detecting and identifying the ejectiles of the reaction over the largest possible range in Z and energy, determining both their atomic (Z) and mass (A) numbers. The INDRA-FAZIA setup [16], employed in this work, is an example of such an apparatus. In this thesis we present the data analysis of the E789 experiment, which is the first campaign after the coupling of the INDRA and FAZIA setups. FAZIA [17], covering the forward polar angles, provides an optimal identification of the fragments belonging to the QP phase space. INDRA [18] provides a large angular coverage, useful for building reaction centrality estimators. In the E789 experiment, the four reactions $^{64,58}\text{Ni}+^{64,58}\text{Ni}$ at two beam energies (32 AMeV and 52 AMeV) have been investigated. The availability of data for all the four projectile-target combinations allows to study the isospin equilibration by comparing the products of the two asymmetric reactions with those of both the neutron rich and neutron deficient symmetric reactions, e.g. by exploiting the *isospin transport ratio* technique [19]. The use of different beam energies slightly modifies the timescale of the interaction process and the inspected nuclear density range. Two main reaction channels will be selected and examined: the QP evaporation channel and the QP breakup channel [20–22]. The isospin characteristics of the QP remnant in the evaporation channel and the QP reconstructed from the two fragments in the breakup channel will be compared, in order to highlight differences and similarities in the equilibration mechanisms between the two event classes.

This work is organised as follows. In Chapter 1 the main physics goal of this study is addressed. Starting from a description of the reaction mechanisms that intervene in heavy ion collisions, we then present the isospin transport phenomena and their interpretation in the framework of the NEOs. Chapter 2 is devoted to a description of the INDRA-FAZIA experimental apparatus. The employed identification techniques will also be introduced. The details of the E789 experiment will be

given in Chapter 3, that also includes a description of all the preliminary operations on the raw data that are mandatory for the event reconstruction, namely the particle identification and energy calibration procedures. In Chapter 4 the employed theoretical models will be presented. The selection criteria for the two reaction channels that are studied in this work will be shown in Chapter 5, together with an overview of the events thus selected. Finally, Chapter 6 is dedicated to the analysis of the isospin dynamics. Unless otherwise specified, the work presented in Chapters 3, 4, 5, and 6 has been carried out by the author of this thesis.

Physics case

Nuclear matter is defined as an ideal uniform system of an infinite number of nucleons interacting only via nuclear forces¹. Heavy ion collisions are a widespread tool for obtaining information on nuclear matter properties [1, 7–9]. In fact, they allow to inspect the behaviour of real nuclei far from equilibrium conditions of temperature and density ($T = 0$ MeV, $\rho_0 = 0.16 \text{ fm}^{-3}$), from which a description of the properties of infinite nuclear matter can be extrapolated. Heavy ion collisions can be studied in various energy regimes, thus allowing to explore various regions of the phase diagram of nuclear matter (see Fig. 1.5 in Sec. 1.2) and to highlight different aspects of nuclear interactions.

In this chapter the main features of the reaction mechanisms in heavy ion collisions at different energies will be examined, with a particular focus on the so called Fermi energies. The main experimental observations in this field will be described, together with their possible interpretation in terms of Nuclear Equation of State (NEoS), which describes the properties of nuclear matter as a function of thermodynamic variables such as temperature, pressure, density. Moreover, it governs various phenomena that take place during the interaction, like isospin transport phenomena. The last section is devoted to a brief introduction on the quasiprojectile breakup reaction channel, one of the main subjects of the analysis presented in this work.

1.1 Heavy Ion Collisions

Two complementary pictures are generally used to describe the interactions between the nucleons of the projectile and of the target nuclei involved in a heavy ion collision: the mean field approach (collective interactions) and the two body (nucleon-nucleon) interactions. Which picture is most appropriate for describing the interaction mechanism depends on the energy at which the reaction takes place [23]. Heavy ion collisions are usually classified basing on the energy regime and the centrality of the reaction, as schematised in Fig. 1.1.

At **low energies**, with a bombarding energy per nucleon (considering fixed tar-

¹In this picture, the electromagnetic interaction among protons is not considered.

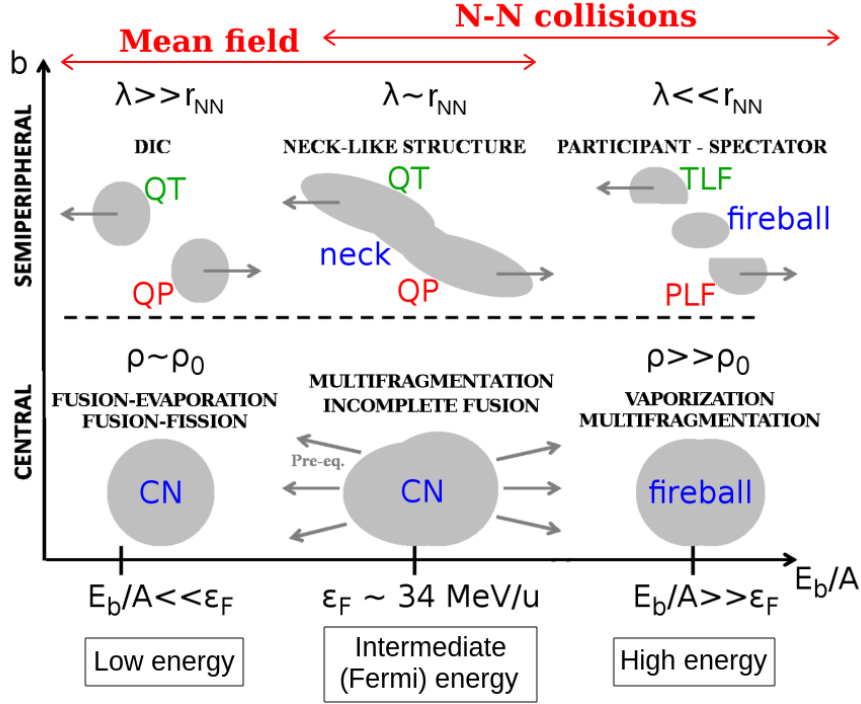


Figure 1.1: A schematic of the possible heavy ion reaction outcomes, as a function of the bombarding energy per nucleon (on the x -axis) and the reaction centrality (or impact parameter b , on the y -axis).

get experiments) below ~ 20 A MeV, the de Broglie wavelength² $\lambda = \frac{\hbar}{m_n v_r}$ associated with the nucleons is much greater than the average distance between the nucleons inside a nucleus ($r_{NN} \approx 1.2$ fm). In fact, due to the low energy, the target is “seen” by the projectile as a single entity (and vice versa). The kinetic energy that can be transferred to the interacting nucleons is limited, and there is a low probability for them to reach a single particle free state. The importance of nucleon-nucleon collisions is therefore reduced due to the effectiveness of the Pauli exclusion principle, and the interaction can be described in terms of mean field approach: in this picture, each nucleon interacts with an average potential generated by the surrounding nucleons.

As anticipated, the reaction mechanism strongly depends also on the centrality, i.e. on the impact parameter b , defined as the distance between the center of the target and the undeflected original trajectory of the projectile. The impact parameter is related to how much projectile and target “overlap” during the interaction phase: since it is not an experimentally accessible observable, it can only be estimated from other correlated measured observables. The minimum impact parameter for which Rutherford scattering prevails over nuclear interactions is called *grazing* impact parameter b_{gr} : above this value, only elastic scattering is possible. For $b < b_{gr}$ the

²In the expression, m_n is the mass of the nucleon and v_r the relative velocity between projectile and target, which is equivalent to the beam velocity in a fixed target experiment.

two nuclei start to experience the strong nuclear interaction. We can distinguish between:

- peripheral and semiperipheral collisions ($b \lesssim b_{gr}$): in the most peripheral collisions ($b \sim b_{gr}$), only a small fraction of the available energy is transferred to the internal degrees of freedom, resulting in the so called *quasi-elastic scattering*. Towards lower impact parameters, the cross section is almost saturated by the *Deep Inelastic Collisions (DIC)*, where the energy dissipation is larger. However, in both cases the exit channel is mainly binary: the two heavy reaction products keep partial memory of their initial characteristics, and therefore they are called quasi-projectile (QP) and quasi-target (QT). After the interaction phase the two excited products decay towards their ground state.
- central collisions ($b \ll b_{gr}$): in the most central collisions, the relatively long interaction time at low energy ($\sim 10^{-21}$ s) favours the fusion of the two nuclei in a thermally and chemically equilibrated central source, known as *Compound Nucleus (CN)*. First theorised by Bohr in 1936 [24], the highly excited CN is supposed to lose memory of the entrance channel, and its de-excitation is only governed by the statistical weights of all the open decay channels available in the phase space, e.g. particle evaporation, statistical fission, γ -decay. The light particle evaporation from a CN is usually described with the Statistical Model approach, e.g. by means of the original theory developed by Bohr, Bethe and Weisskopf [25] or the more accurate Hauser-Feshbach model [26].

On the other hand, at **high energies**, for beam energies higher than ~ 100 AMeV, we find that $\lambda \ll r_{NN}$: the collective properties become negligible, and projectile and target “see” each other almost as colliding bunches of nucleons. In fact, the kinetic energy transferred to the interacting nucleons is now high enough to let them reach a single particle free state, the Pauli exclusion principle is no more effective, and therefore nucleon-nucleon interactions become predominant. For $b \lesssim b_{gr}$ the collision is usually described in terms of the so called *participant-spectator* model [27]: in this scenario, only the nucleons of the overlapping region of the two nuclei participate, forming a hot and dense region, the *fireball* [28]. The highly excited fireball undergoes vaporisation or multifragmentation, emitting highly energetic nucleons. The spectator remnants³ are much less excited, and eventually decay mostly by statistical particle evaporation. For $b \sim 0$, if the colliding nuclei have similar size, all nucleons participate in forming the fireball, which travels at the center of mass (CM) velocity of the colliding system.

1.1.1 The intermediate energy regime

The **intermediate energies** are a transition region between the low and high energies described above, with a beam energy approximately between 20 AMeV and

³In the high energy domain the remnants coming from the projectile and the target are usually referred to as projectile-like-fragment (PLF) and target-like-fragment (TLF) respectively, instead of QP and QT.

100 A MeV. This domain has also the alternative name of **Fermi energy regime**, since it refers to the reactions performed with a beam energy close to the Fermi energy of the nucleons inside the nucleus ε_F ($\sim 30 - 38$ MeV, depending on the nuclear species). Here, the wavelength λ associated with the nucleons is comparable to the relative distance between them. In this case, both mean field and nucleon-nucleon collisions play a role in the interaction mechanism [29], the latter being more and more relevant as the beam energy increases. Moreover, in this energy domain the time scale of the interaction is approximately one order of magnitude shorter than at low energy ($\sim 10^{-22}$ s), too short to allow the system to reach the full equilibration of its internal degrees of freedom. Therefore, the CN formalism cannot be properly applied to describe the features of the occurring phenomena. Some de-excitation (e.g. through light particle emission) can already occur for the highly deformed object formed before the separation phase between QP and QT.

The reaction centrality, also in this case, plays a fundamental role in determining the outcome of the reaction. An evidence of this is presented in Fig. 1.2, showing invariant CM velocity plots for protons and α particles for different centrality bins. The abscissa (ordinate) corresponds to the parallel (perpendicular) component of the particle velocity in the CM reference frame with respect to the beam axis. For the most peripheral collisions (on the left) the binary character of the exit channel can be inferred from the two well-defined circular emission patterns, known as *Coulomb rings*, that arise in the plot due to the particle evaporation from the QP and QT sources. Moving towards the most central collisions (on the right), this binary feature is less and less evident, until only one central emission source can be found. We can therefore identify two large categories:

- peripheral and semiperipheral collisions: in analogy to what occurs at low energy, the cross section of peripheral reactions is largely dominated by deep inelastic collisions. Therefore, in the exit channel a QP and a QT are generally produced, together with some Light Charged Particles (LCP) and Intermediate Mass Fragments (IMF). Most of the LCPs are emitted in the de-excitation of the QP and the QT, which are produced in an excited state. The position of the QP and QT sources on the velocity axis is shown in Fig. 1.2. Also the contribution of pre-equilibrium emissions to the production of LCPs must be taken into account: these emissions occur during the dynamical phase of the collision, when projectile and target are forming a rapidly evolving deformed single object. However, the importance of pre-equilibrium emissions decreases with increasing impact parameter, and is more relevant for central collisions [30, 31].

Many other light products are emitted in the *midvelocity region*, i.e. at a velocity between those of the QP and the QT. According to the most common interpretation⁴, in this class of reactions, in a late stage of the dynamical phase, a strongly deformed di-nuclear object arises: between the QP and the QT, an elongated low density zone usually called *neck region* is formed, which

⁴This interpretation is based on a dynamical origin of the emission. Also an alternative interpretation, based on statistical arguments, has been proposed [33].

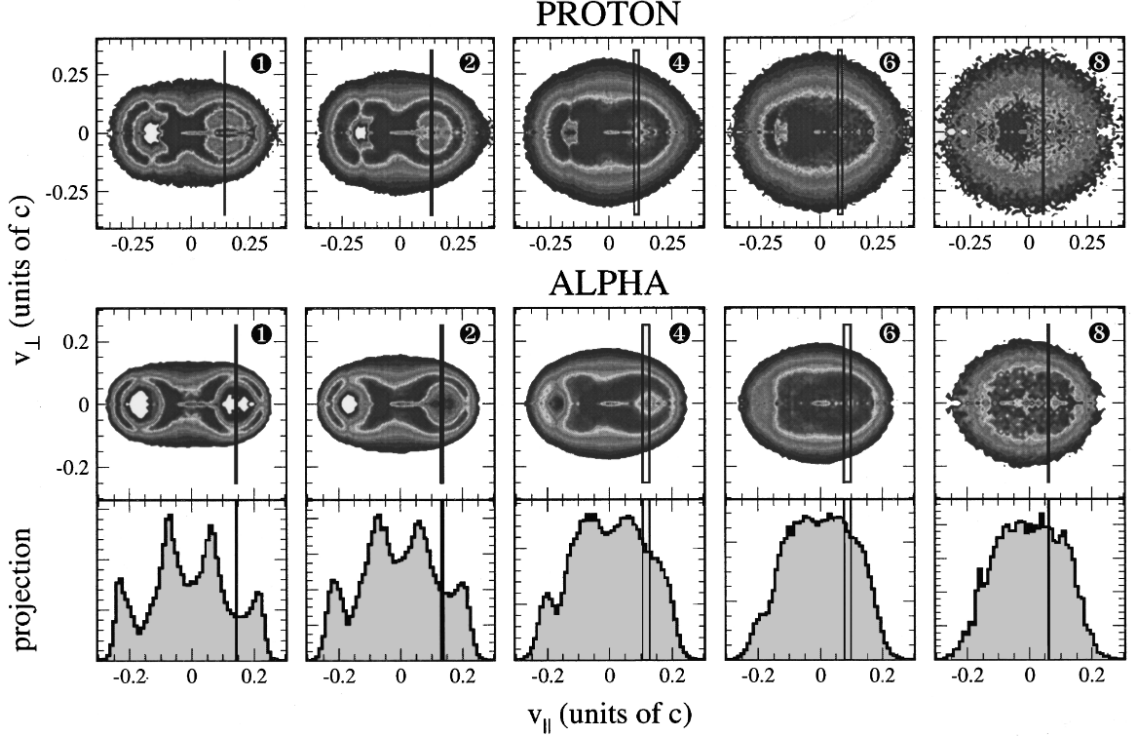


Figure 1.2: Invariant CM velocity plots for protons and α particles produced in Xe+Sn at 50 A MeV for specific centrality bins, from peripheral (left) to central (right) collisions, obtained with the INDRA apparatus (see Sec. 2.2). The rectangles superimposed on the velocity plots correspond to the source velocities. From Ref. [11].

tends to break up quite early due to its thermo-mechanical instability. This results in the production of IMFs and LCPs that promptly move away from the origin area due to Coulomb repulsion, giving rise to the observed midvelocity emissions [1, 32]. As highlighted by many experimental observations, most of the IMFs are emitted at midvelocity; in fact, they are less likely to be produced in the de-excitation of the QP and the QT. Some other experimental observations on this class of events will be presented in the next section.

- central collisions: from the observation of the rightmost plots in Fig. 1.2 the formation of a single central source is evident. However, the outcome for the most central collisions in this domain evolves with the energy of the reaction. For the lowest energies included in the intermediate regime, the *incomplete fusion* is the most probable result of a central collision, with the formation of an excited product whose mass is lower than the sum of the masses of the two colliding nuclei [34]; this process can be interpreted as a fusion with an important contribution given by the pre-equilibrium emission, which takes away part of the mass of the total system. The incomplete fusion source subsequently de-excites by means of the statistical decay, mostly emitting LCPs. As the energy

deposited in the central source increases (above $\sim 3 - 5 \text{ A MeV}^5$), the probability of multifragmentation [36] increases. In this process, a central source that includes a large part of the total mass of the system promptly disassembles into many IMFs. If the excitation energy is higher, above $\sim 8 - 10 \text{ A MeV}$, the source can experience a complete dissolution breaking up into LCPs: this kind of event is called *vaporisation* [23, 37].

1.1.2 Isospin observables in peripheral collisions at Fermi energies

Since the technological improvements in particle detection allowed for a more precise isotopic fragment identification, special attention has been paid to the study of the isospin composition of the reaction products as a function of the characteristics of the entrance channel, e.g. the reaction energy or the isospin asymmetry between projectile and target. For this kind of studies, one needs to build isospin-related observables, like for example the ratio between the average neutron content and the charge $\langle N \rangle / Z$ or the quantity $\langle \Delta \rangle = \langle N - Z \rangle / Z$ for the fragments produced in the reaction, studied as a function of various different observables in order to highlight different aspects of the emissions; that is why a good isotopic identification capability of the experimental setup is mandatory.

Some experimental observations in this field have been widely shared by the scientific community. A prime example is the process of **isospin equilibration** between the QP and QT resulting from the interaction of a projectile and a target that are asymmetric, i.e. with different isospin contents. This phenomenon was first observed in the low energy regime [38–40], and it was soon confirmed also for higher beam energies within the Fermi domain [41–44]. The isospin content of the QP and the QT can be probed either by inspecting the characteristics of their de-excitation emissions or, in the case of the QP⁶, by the direct detection and identification in Z and A of its remnant. As an example, in Fig. 1.3, taken from Ref. [44], the average N/Z as a function of the charge of the fragments produced in the reactions $^{84}\text{Kr} + ^{112,124}\text{Sn}$ at 35 A MeV and identified with a FAZIA telescope (see Sec. 2.1) is reported. Both reactions involved the same projectile ($N/Z_{^{84}\text{Kr}} = 1.33$) at the same energy, but different targets ($N/Z_{^{112}\text{Sn}} = 1.24$ and $N/Z_{^{124}\text{Sn}} = 1.48$). Therefore, any difference found in the isospin content of the fragments belonging to the QP phase space must be ascribed to the different neutron richness of the two targets, hence to the different isospin asymmetry in the entrance channel of the two reactions. Indeed, a difference between the plots for the two systems can be clearly seen: the $\langle N \rangle / Z$ value of the QP fragments for the reaction with the neutron rich target is systematically higher than that for the system with the neutron poor target, showing

⁵The time scale of the fragment emission in multifragmentation depends on the excitation energy (see e.g. Fig.9 of Ref. [35]). The proper multifragmentation regime, in which the fragment emission is almost simultaneous to the source formation, is usually considered for $E^* \gtrsim 5 \text{ A MeV}$ [23].

⁶Due to kinematical reasons, the QT is often under the detection threshold of the experimental setup. In fact, in the CM reference frame, the QT is emitted backwards and its velocity in the laboratory reference frame is lower than that of the CM.

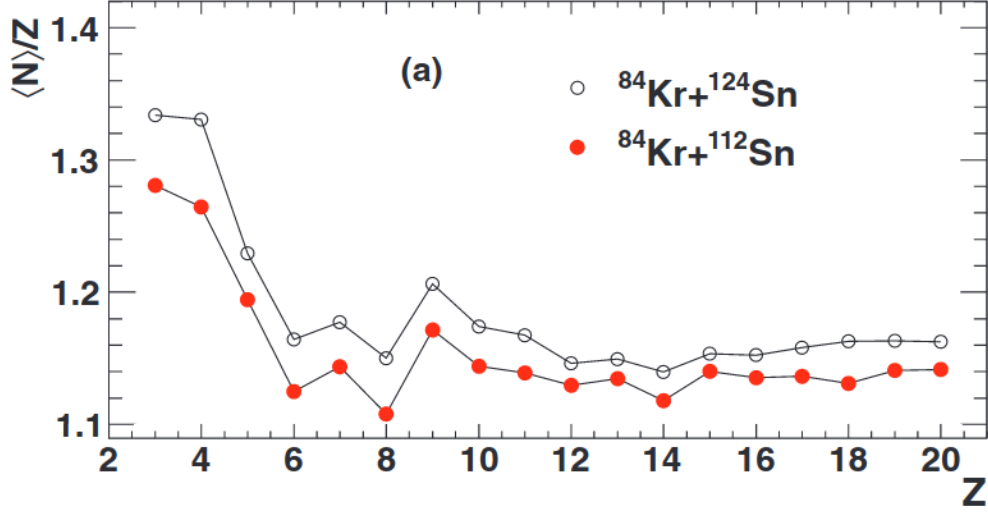


Figure 1.3: $\langle N \rangle / Z$ as a function of the charge Z for the fragments produced in the reactions $^{84}\text{Kr} + ^{112}\text{Sn}$ (full red dots) and $^{84}\text{Kr} + ^{124}\text{Sn}$ (open black dots) at 35 AMeV. These data were acquired during one of the first FAZIA tests performed with only one telescope, covering an angular range $4.8^\circ < \theta < 6.0^\circ$. Due to this positioning, mostly fragments belonging to the QP phase-space were collected. The isospin content of the fragments evidently depends on the neutron richness of the target. Adapted from Ref. [44].

that there is an *isospin transport* between target and projectile which depends on their original isospin content and tends to its equilibration.

Another well-known experimental observation in peripheral and semiperipheral collisions at intermediate energies is the **neutron enrichment of the midvelocity emissions** [12, 32, 45, 46]. In order to highlight this effect, the isospin content of the fragments is usually studied as a function of their emission pattern. For example, in Fig. 1.4, again from Ref. [44], the $\langle N \rangle / Z$ ratio of the fragments with $Z = 3, 4, 5$ produced in the aforementioned Kr+Sn reactions is plotted as a function of their laboratory velocity; here, the midvelocity region corresponds to the interval around the CM velocity in the laboratory reference frame, which is ~ 35 mm/ns. The midvelocity zone can be expected to be populated by a superposition of the QP (QT) backward (forward) emissions, i.e. towards the CM, and the fragments originating from the rupture of a necklike structure. Concerning the latter case, it has been shown that lighter fragments whose velocity is closer to the CM velocity are more likely to be originated from the most central part of the neck structure [47]. Besides the effect already noticed in Fig. 1.3 (the larger $\langle N \rangle / Z$ associated to the neutron rich target, which is an evidence of isospin equilibration), another feature is clearly visible in the figure: the $\langle N \rangle / Z$ of light fragments increases with decreasing velocities, towards the midvelocity region. This characteristic is more pronounced for $Z = 3, 4$ (IMF), and gradually disappears for heavier fragments (see Fig. 6 of Ref. [44]).

These experimental observations have found a possible interpretation within the

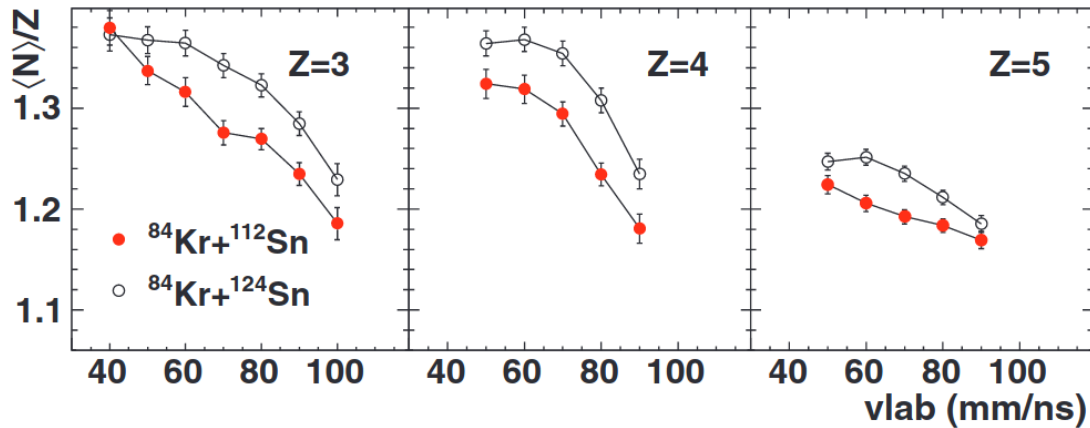


Figure 1.4: $\langle N \rangle / Z$ as a function of the velocity in the laboratory reference frame for the fragments produced in the reactions $^{84}\text{Kr} + ^{112}\text{Sn}$ (full red dots) and $^{84}\text{Kr} + ^{124}\text{Sn}$ (open black dots) at 35 A MeV. As a reference, the v_{lab} of the beam is 82.2 mm/ns, and the v_{lab} of the centers of mass of the two reactions are 35.2 mm/ns and 33.2 mm/ns, respectively. A higher $\langle N \rangle / Z$ is observed in the midvelocity region. Adapted from Ref. [44], where the same plots for other heavier QP fragments up to $Z = 20$ are also available.

study of the Nuclear Equation of State, which can be exploited to describe the isospin transport phenomena.

1.2 Nuclear Equation of State (NEoS)

Nuclear matter is defined as a system of an infinite number of nucleons (both neutrons and protons) interacting only via nuclear forces. The nuclear force can be described as a residual interaction of the strong interactions between the quarks composing each nucleon, similar, in some respects, to the Van-der-Waals forces acting between molecules. The *Nuclear Equation of State (NEoS)* aims at the description of the behaviour of nuclear matter in terms of observables like density, temperature, pressure, volume or isospin.

A nucleus in the ground state has a nuclear temperature⁷ $T = 0$ MeV and a density $\rho_0 = 0.16 \text{ fm}^{-3}$, known as *saturation density*, and shows liquid-like properties, as suggested by the success of the liquid drop model in describing the binding energies.

⁷The concept of nuclear temperature was introduced in the low energy regime by Bethe and Weisskopf, and later extended to the higher energy regimes. Its definition in the microcanonical approach for a system in full statistical equilibrium, according to statistical mechanics, can be written as:

$$\frac{1}{T} = \frac{\partial S(E, N)}{\partial E} = \frac{\partial \ln \rho(E, N)}{\partial E}$$

where N is the number of particles composing the system, ρ is the density of states at the energy E , and S is the entropy of the system [48].

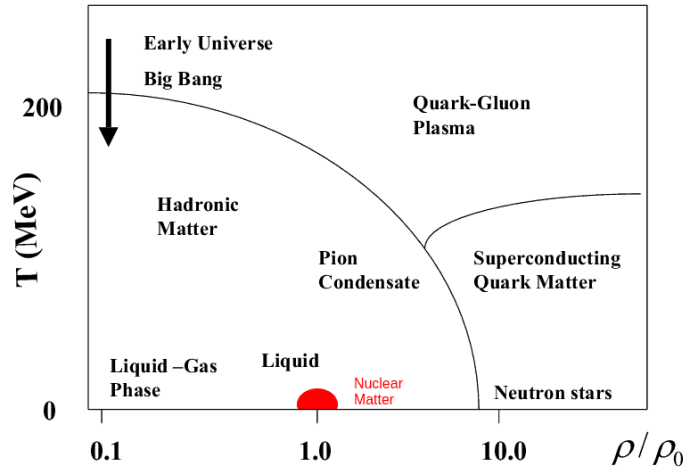


Figure 1.5: Phase diagram of nuclear matter, shown as a function of the temperature T and the nuclear density ρ normalised to the saturation density ρ_0 , i.e. the density of nuclear matter in equilibrium conditions. Heavy ion collisions at non-relativistic energies allow us to explore only the bottom left part of the plot, close to equilibrium conditions. Relativistic heavy ion collisions, like those available at LHC (CERN) or RHIC (Brookhaven), can lead to the formation of the quark-gluon plasma, that can be found on the top part of the diagram. Adapted from Ref. [9].

This condition corresponds to the red area indicated in the phase diagram of nuclear matter shown in Fig. 1.5. During the dynamical phase of a heavy ion collision, the nuclear system explores regions of the phase diagram far from the equilibrium condition. In fact, during the first contact phase, the density of the nuclear system can increase up to localised supra-saturation values ($\rho \gtrsim \rho_0$, the exact value depending on the energy involved in the reaction), while the separation phase is generally characterised by an expansion, and hence a decrease of the density down to sub-saturation values ($\rho < \rho_0$), particularly in correspondence of the neck region in case of peripheral collisions. It must be noted that in heavy ion collisions at Fermi energies only the region of the (ρ, T) phase diagram close to the equilibrium condition is explored. In order to move further away from this condition the energy of the collision must be increased. For example, the top part of the diagram in Fig. 1.5, corresponding to a condition of high temperature that can lead to the formation of the *quark-gluon plasma*, is accessible through heavy ion collisions at relativistic energies. The importance of the understanding of the nuclear phase diagram lies in its implications in studying the history of the early universe (in fact, in the first instants after the Big Bang the universe should have been in a phase state located at the top left region of the diagram), and on the properties of high-density objects like neutron stars.

Historically, the first effort to describe the nucleus in terms of thermodynamic observables can be identified in the *Bethe-Weizsäcker formula* [49], that expresses

the binding energy E_B of a nucleus composed of Z protons and N neutrons as:

$$E_B(Z, N) = a_V A - a_S A^{2/3} - a_C \frac{Z(Z-1)}{A^{1/3}} - a_A \frac{(N-Z)^2}{A} + \Delta \quad (1.1)$$

where $A = N + Z$ is the total number of nucleons (i.e. the mass number), a_V , a_S , a_C , a_A and Δ are parameters, with:

$$\Delta = \begin{cases} +\delta & \text{for even-even nuclei} \\ 0 & \text{for odd-mass nuclei} \\ -\delta & \text{for odd-odd nuclei} \end{cases}$$

The five terms of eq. (1.1) correspond to the contributions from the *volume energy*, the *surface energy*, the *Coulomb energy*, the *asymmetry energy* and the *pairing term*, respectively. It is to be noted that in the fourth term the isospin dependence of the nuclear force can be seen for the first time: this term evidently vanishes for symmetric nuclear matter, i.e. for $N = Z$. A commonly used set of values for the five parameters is:

$$a_V = 16 \text{ MeV}, \quad a_S = 17 \text{ MeV}, \quad a_C = 0.6 \text{ MeV}, \quad a_A = 30 \text{ MeV}, \quad \delta = \frac{25}{A} \text{ MeV}.$$

This equation, first formulated in 1935, is also known as *semi-empirical mass formula*, due to the fact that it is based partly on experimental observations and partly on the liquid drop model, developed some years before by George Gamow. According to Gamow's theory, the nucleus can be roughly treated as a drop of incompressible nuclear fluid made of nucleons interacting via the strong nuclear force. The five parameters of eq. (1.1) can be approximately estimated basing on this model. However, it works only for spherical nuclei in their ground state; it follows that the Bethe-Weizsäcker formula is suitable for the description of many stable nuclei in standard conditions of temperature and density, but cannot be used, e.g., to understand the properties of an excited nucleus.

For this reason, the *Nuclear Equation of State* needs to be introduced in order to describe the properties of nuclear matter far from equilibrium conditions. The NEOs is an expression of the energy per nucleon that includes the dependence on the nuclear density $\rho = \rho_p + \rho_n$, where ρ_p and ρ_n are the proton and neutron densities, respectively, and on the *isospin asymmetry parameter*⁸ I , defined as [8]:

$$I = \frac{\rho_n - \rho_p}{\rho_n + \rho_p} = \frac{\rho_n - \rho_p}{\rho} \quad (1.2)$$

We can separate the symmetric part of the energy per nucleon from its asymmetric part by expanding it in a Taylor series around $I = 0$ ($N = Z$, symmetric matter).

⁸This definition should not be confused with another one frequently present in the literature concerning the experimental studies on isospin in heavy ion collisions, where the quantity N/Z is often referred to as *isospin parameter*.

Since all the odd-order terms vanish due to the assumption of charge symmetry for nuclear force (neutron-proton exchange symmetry in nuclear matter), by expanding up to the second order in I we obtain:

$$\frac{E}{A}(\rho, I) = \frac{E}{A}(\rho, I = 0) + \frac{E_{sym}}{A}(\rho)I^2 + O(I^4) \quad (1.3)$$

where the first term, evaluated for $I = 0$, represents the energy per nucleon for symmetric nuclear matter, while $\frac{E_{sym}}{A}(\rho)$ is called *symmetry energy* and includes all the dependence on the isospin asymmetry I . The symmetry energy term, also known as *asymmetric term*, can be interpreted as the difference between the binding energy of pure neutron matter ($I = 1$) and that of symmetric nuclear matter ($I = 0$) [7]. Both terms in eq. (1.3) can be expanded in a Taylor series around the saturation density ρ_0 [2]:

$$\frac{E}{A}(\rho, I = 0) = \frac{E}{A}(\rho_0) + \frac{1}{2}K_0 \left(\frac{\rho - \rho_0}{3\rho_0} \right)^2 + O\left(\left(\frac{\rho - \rho_0}{3\rho_0} \right)^3 \right) \quad (1.4)$$

$$\frac{E_{sym}}{A}(\rho) = S(\rho_0) + L_{sym} \left(\frac{\rho - \rho_0}{3\rho_0} \right) + \frac{1}{2}K_{sym} \left(\frac{\rho - \rho_0}{3\rho_0} \right)^2 + O\left(\left(\frac{\rho - \rho_0}{3\rho_0} \right)^3 \right) \quad (1.5)$$

The two coefficients $\frac{E}{A}(\rho_0)$ and K_0 in the expansion of the **symmetric term** in eq. (1.4) are called *saturation energy* and *incompressibility modulus*, respectively. The value obtained for the saturation energy $\frac{E}{A}(\rho_0) \sim -16$ MeV is quite the same among many different analyses (see Tab. 1 of Ref. [2]), while the determination of the incompressibility modulus, mostly based on Giant Monopole Resonance (GMR) studies, is more model dependent, with $K_0 \sim 230$ MeV as the best estimate.

The **asymmetric term** (i.e. the symmetry energy) in eq. (1.5) includes three coefficients, i.e. the *symmetry energy* at the saturation density $S(\rho_0)$, the *slope* L_{sym} and the *curvature* K_{sym} (or *isovector incompressibility*) parameters. The symmetry energy at saturation $S(\rho_0)$ is similar to the coefficient a_A of the asymmetry energy term of the Bethe-Weizsäcker formula (1.1); its value is $S(\rho_0) \sim 32$ MeV, as derived from many different analyses [2], some of which are summarised in the top panel of in Fig. 1.6, taken from Ref. [3]. Results of both terrestrial (on the left) and astrophysical (on the right) observations are reported in the figure, showing a good agreement. Some measured values for the slope parameter L_{sym} are shown in the bottom panel of the same figure; the average value, affected by large uncertainties, is $L_{sym} \sim 60$ MeV. However, also some recent results in contrast with these values of the N.EoS parameters can be found in the literature [50]. On the other hand, the value of the curvature parameter K_{sym} is still unknown.

Many efforts have been made in order to narrow down the uncertainty on the estimation for these parameters, and many others are foreseen [2]. In fact, L_{sym} and K_{sym} determine the density dependence of the symmetry energy, and are therefore necessary to predict the behaviour of the asymmetric N.EoS at low and high density, far from saturation. This information is of great interest both in nuclear physics, for further investigating the nucleon-nucleon interaction and the properties of nuclear

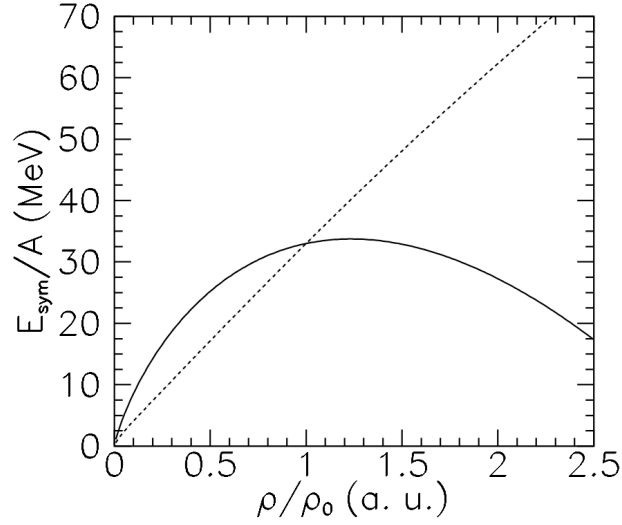


Figure 1.7: Density dependence of the symmetry energy for the two different parametrisations of the N_{EoS} asy-stiff (dashed line) and asy-soft (solid line). From Ref. [7].

matter, such as the nuclear density profile [4, 8], and in astrophysics, where it finds implications in the study of neutron stars [5, 6]. According to the currently available theoretical models, two different parametrisations of the N_{EoS} are possible, i.e. the **asy-stiff** and the **asy-soft** parametrisations⁹. Their behaviour as a function of the nuclear density is shown in Fig. 1.7: both parametrisations assume the empirically determined value for the symmetry energy at normal conditions for $\rho = \rho_0$, while they are in strong disagreement for $\rho \neq \rho_0$.

Heavy ion collisions allow to find constraints on the symmetry energy term by comparing the results of measurements with the predictions from theoretical models (see Chapter 4) that assume different parametrisations for E_{sym} . For such purposes, one must first define some observables which are sensitive to the symmetry energy.

⁹Another parametrisation of the symmetry energy can be found in the literature, in which the kinetic and potential contributions are separately expressed [7, 51]:

$$\frac{E_{sym}}{A}(\rho) = \frac{C_{kin}}{2} \left(\frac{\rho}{\rho_0} \right)^{2/3} + \frac{C_{pot}}{2} \left(\frac{\rho}{\rho_0} \right)^\gamma$$

where the first term can be expressed as the kinetic energy of a Fermi gas. In this picture, the potential contribution is the one that includes the “unknown” density dependence of the symmetry energy: the asy-stiff case corresponds to $\gamma \geq 1$ (potential term that linearly increases with ρ), while the asy-soft case to $\gamma < 1$ (potential term showing a maximum for $\rho > \rho_0$). The case with $\gamma > 1$ can be referred to as asy-superstiff [7]: in this case the potential term rapidly increases with ρ .

1.2.1 Isospin transport phenomena

In semiperipheral and peripheral heavy ion collisions the symmetry energy term governs the **isospin transport phenomena**. These effects are caused by the nucleon exchange between the projectile and target in the dynamical phase of the reaction.

The isospin transport can be expressed through the difference between the neutron and proton current densities \mathbf{j}_n and \mathbf{j}_p flowing between the colliding nuclei, as determined by their different chemical potentials [13]. The link between the symmetry energy of the NEoS and the isospin transport phenomena is clearly visible in the equation:

$$\mathbf{j}_n - \mathbf{j}_p \propto \frac{E_{sym}}{A}(\rho)\nabla I + I \frac{\partial \frac{E_{sym}}{A}(\rho)}{\partial \rho} \nabla \rho \quad (1.6)$$

In eq. (1.6) two contributions, related to two different neutron/proton transport mechanisms, can be distinguished¹⁰:

- **isospin diffusion**, driven by the presence of an isospin gradient ∇I in the system. This mechanism can be observed when projectile and target have a different isospin content, and leads to the *isospin equilibration* process between the resulting QP and QT, introduced in Sec. 1.1.2. The degree of equilibration depends on the duration of the contact phase (i.e. the contact time) between the two colliding nuclei, which in turn depends on the bombarding energy and the impact parameter of the collision. For a long enough interaction time we could expect a homogeneous distribution of the isospin content among the reaction products. An evaluation of the amount of equilibration between QP and QT provides information on the strength of the diffusion component of the isospin transport. This term is related to the value of the symmetry energy E_{sym}/A . In particular, the studies performed within the Fermi energy domain are more sensitive to the effects at sub-saturation densities, where the E_{sym}/A value for the asy-soft parametrisation is higher than for the asy-stiff one (see Fig. 1.7). Therefore, a higher degree of equilibration is commonly expected in theoretical predictions when an asy-soft parametrisation is assumed.
- **isospin drift** (or migration), which is associated to the presence of a density gradient $\nabla \rho$ in the di-nuclear object formed during the contact phase of the collision. It is independent of the isospin asymmetry between projectile and target; therefore, it can be studied separately from the isospin diffusion process by choosing a symmetric reaction, i.e. a projectile and a target with the same neutron to proton ratio. The isospin drift is present when regions with different density are formed, causing a net neutron flux towards the more diluted areas. It is therefore a possible explanation of the *neutron enrichment of the neck* observed through the isospin analysis of the midvelocity emissions, as previously introduced (Sec. 1.1.2). This term carries the information on the

¹⁰In addition to these contributions, also the effect of *isospin fractionation* is present [52, 53]: due to this mechanism, in a low-density isospin-asymmetric system, the gas phase is more neutron rich than the liquid phase.

first derivative of the symmetry energy with respect to the density, i.e. the slope of E_{sym}/A .

1.3 QP breakup or dynamical fission

This thesis work is focused on peripheral and semiperipheral collisions at intermediate energies, for which the binary exit channel is the dominant one. However, a ternary (or quaternary) outcome is also possible: in this case, one (or both) of the heavy products breaks up into two smaller fragments at some point of the reaction. The physical origin of this outcome may be different, depending on the phase of the reaction in which it takes place.

Historically, the first mechanism of this kind to be studied was the **statistical fission**, firstly explained by Meitner and Frisch [54] by exploiting the liquid drop model in order to interpret the empirical observations made by Hahn and Strassmann in 1938. After many years of research, statistical fission is nowadays a well known physical process. In heavy ion collisions it represents one of the possible statistical de-excitation mechanisms for a thermally equilibrated excited fragment produced in the dynamical phase of the reaction. The whole process can be described as a two-step mechanism, with a deep inelastic collision followed by the fission of one or both products, which for this reason is often referred to as *sequential fission* in the literature. According to the liquid drop model picture, when the excitation energy is greater than the fission barrier¹¹, the induced collective oscillations lead to a deformation that allows to overcome the so-called *scission point* (or *saddle point*), eventually breaking the nucleus into two smaller fragments. Since it is driven by collective phenomena, statistical fission is a rather slow process (with time scales ranging from 10^{-16} s to 10^{-19} s [23]) compared to other competing de-excitation mechanisms such as particle evaporation (whose time scale is typically around and even below 10^{-20} s, depending on the nuclear temperature, for the energy regime studied in this work [23]). The long time scale of this process has been confirmed also basing on the characteristic isotropic angular distribution of the two fission fragments on the reaction plane, related to the fact that the nucleus completes at least one full rotation before splitting into two fragments.

In heavy ion collisions another fission mechanism is also possible, i.e. the **dynamical fission** or **breakup** of the QP or QT, which has been the subject of many studies since it was distinguished from statistical fission [20–22]. As suggested by the name, this process has been linked to a dynamical origin, with a time scale of

¹¹The fission barrier is defined as the activation energy which is necessary for a nucleus to undergo fission: it is related to the deformation energy, i.e. the variation of potential energy resulting from a deformation of the nucleus (see Fig. 5.20 of Ref. [55]). In fact, a small deformation is associated to an increase of the potential energy, which tends to restore the initial condition of the nucleus. On the other hand, when the nucleus is deformed over the *scission point*, a further increase of the deformation reduces the potential energy, and therefore the nucleus tends to split into two fragments. The presence of an angular momentum reduces the activation energy, thus favouring the fission process.

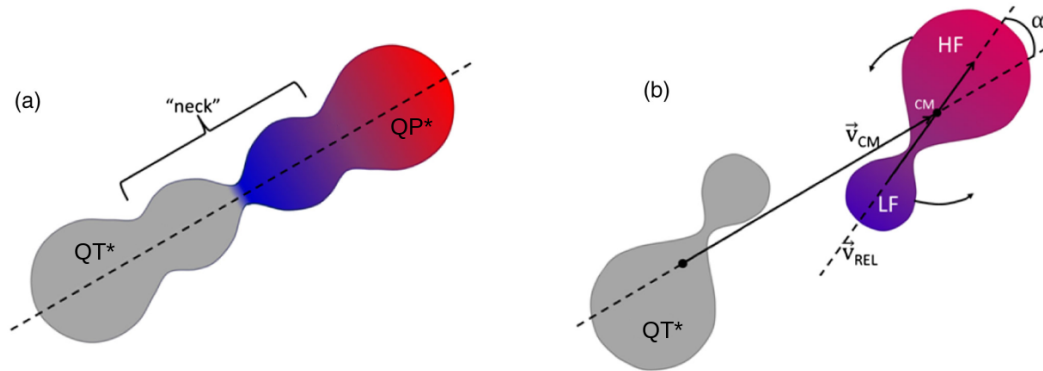


Figure 1.8: Representation of the dynamical deformation leading to a QP breakup. In the left panel the di-nuclear deformed object formed prior to the QP-QT split is shown, and the neutron rich neck region is indicated. The right panel illustrates the rotation of the strongly deformed QP (and QT) before its breakup. The colour is related to the isotopic composition of the nuclear matter, with the blue (red) corresponding to a neutron rich (deficient) area. The QT is drawn in grey to indicate that in most cases it is not detected. In the right panel the α angle, defined as the angle between the QP-QT separation axis and the QP fission axis, is also shown. Adapted from Ref. [58].

the order of ~ 200 fm/c: in fact, contrary to what happens for the sequential fission, the breakup products feature a strongly anisotropic emission pattern on the reaction plane, with the lighter fragment mostly backward emitted, towards the CM. Moreover, a larger mass asymmetry between the two breakup products has been associated with a more aligned configuration [21, 56, 57]. A widespread interpretation of these observations is as follows: during the contact phase between the colliding nuclei an elongated di-nuclear system is formed, as pictured in panel (a) of Fig. 1.8. This object ruptures in correspondence of the neutron rich neck region and splits into two products, the QP and the QT, which are strongly deformed along the separation axis. Due to their deformation and angular momentum, the QP and QT are likely to undergo a prompt breakup (see panel (b) of Fig. 1.8). Since this is a fast process, we can expect that the time elapsed between the QP-QT split and the breakup of one of them does not allow for a complete isospin equilibration between the two fission fragments: in fact, according to this picture, the light fragment (LF) originating from a region closer to the neck features its characteristic neutron enrichment, while on the other hand the heavy fragment (HF) is more neutron deficient. Therefore, the degree of isospin asymmetry between the LF and the HF carries information about the isospin equilibration process. Due to kinematics, the LF and the HF originating from a QP breakup are usually the only ones that can be detected and studied, and therefore in this work the QT breakup will not be considered.

In the literature regarding this topic, there are frequent references to the α angle¹², i.e. the angle between the QP-QT separation axis, defined by the direction of the QP velocity \mathbf{v}_{QP} , and the QP fission axis, defined by the direction of the relative velocity between the HF and the LF, $\mathbf{v}_{rel} = \mathbf{v}_{LF} - \mathbf{v}_{HF}$ (see Fig. 1.8):

$$\alpha = \arccos\left(\frac{\mathbf{v}_{QP} \cdot \mathbf{v}_{rel}}{|\mathbf{v}_{QP}| \cdot |\mathbf{v}_{rel}|}\right) \quad (1.7)$$

The configuration in which the LF is backward emitted, perfectly aligned with the QP and the QT, corresponds to $\alpha = 0^\circ$. According to a semi-classical interpretation, as the time between the QP-QT separation and the subsequent breakup of the QP increases, the deformed QP rotates on its axis and the α angle increases. In this scenario, α can be adopted as a “clock” for an estimation of the time scale of the breakup, provided that it is short enough compared to the period of the QP rotation. At the same time also the degree of isospin equilibration inside the original deformed QP increases, and this will be reflected in the neutron content of the resulting HF and LF. Following this assumption, in Ref. [58,59] a time scale of the isospin equilibration process has been obtained ($\sim 10^{-1}$ zs). However in Ref. [60] it has been verified that no correlation between the α angle and the time elapsed from the QP-QT split to the QP breakup can be found in the framework of the dynamical model AMD (see Chapter 4). The topics related to the QP breakup are clearly still an open field, and they deserve a deeper investigation.

¹²In some works the α angle is referred to as proximity angle θ_{PROX} (see e.g. Ref. [56]).

The INDRA-FAZIA experimental apparatus

INDRA is a 4π first-generation ΔE -E telescope array developed at GANIL (*Grand Accélérateur National d'Ions Lourds*) in Caen, France, during the 90s. FAZIA is a last-generation multi-telescope array with unprecedented Z and A identification capabilities. Both apparatuses were designed for the detection of nuclear fragments produced in heavy ion collisions at Fermi energies.

The members of the INDRA collaboration took part in the FAZIA collaboration since its very beginning.

To exploit both the large angular coverage of the INDRA multi-detector and the optimal (Z, A) identification provided by FAZIA, though with a limited solid angle coverage, a coupling of the two devices has been planned at a very early stage [16]. In particular, the forward part of INDRA has been removed and replaced by 12 FAZIA blocks (see Sec. 2.1).

In this chapter the two detector arrays will be described in detail, together with their coupling, that was completed in the first months of 2019 at GANIL. The last section is dedicated to the description of the identification techniques exploited in this work.

2.1 The FAZIA apparatus

FAZIA (*Forward-angle A and Z Identification Array*) is a multi-detector array optimized for the detection and identification both in Z and A of charged fragments produced in nuclear reactions at beam energies ranging from 10 to 100 A MeV approximately [17]. At present, it represents the state of the art of ion identification in the Fermi energy domain. This is the result of a long R&D activity aimed at both improving the detector performance and refining the digital treatment of the signals induced by the nuclear fragments in the detectors. The final purpose of these two parallel studies was to enhance the (Z, A) identification performance of the setup as obtained from two identification techniques, namely the ΔE -E and the Pulse Shape Analysis (PSA) methods (see Sec. 2.4). During the R&D phase, the ΔE -E charge identification capability has been successfully tested up to $Z \sim 54$ with a ^{129}Xe

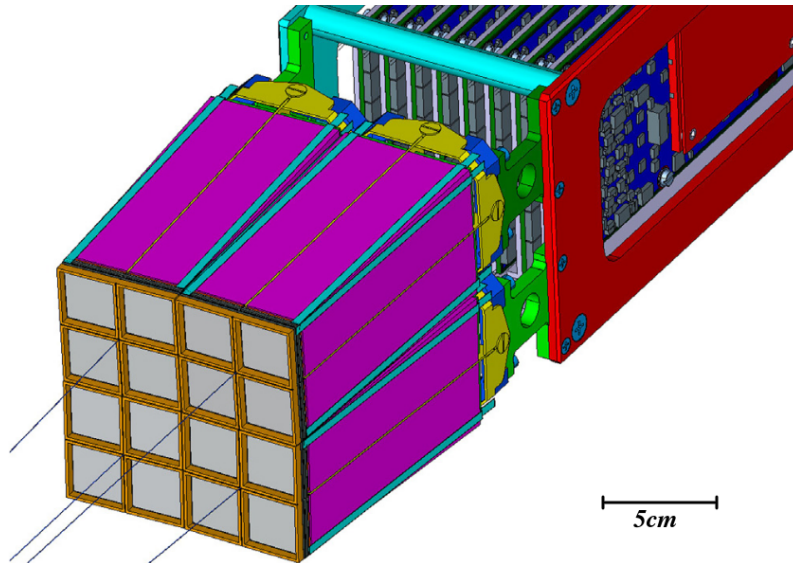


Figure 2.1: Rendering of the 16 detectors of a FAZIA block. The placement of the read out electronic cards is also visible. The dark blue lines indicate the center and the orientation axis of the four quartets. From Ref. [64].

beam [61]. Isotopic discrimination has been achieved up to $Z \sim 25$ with the ΔE - E technique [61] and up to $Z \sim 20$ with PSA in silicon [62]. A schematic of the energy thresholds for identification obtained for the techniques employed in FAZIA can be found in Ref. [63].

The basic module of the FAZIA setup is called *block* (BLK) and consists of 16 three stage ΔE - E *telescopes* arranged in four 2×2 telescope modules named *quartets*, arranged in turn in a 2×2 matrix, thus forming a 4×4 telescope matrix, as can be seen in the rendering in Fig. 2.1. The Front End Electronics (FEE) associated to each block is placed under vacuum, behind the block and quite close to it (there are about 20 cm from the detector output to the FEE input). In this way it is possible to reduce the signal distortion and to minimize the electronic noise. Thanks to this choice, also the number of connections between the inside and the outside of the vacuum chamber is quite small: in fact, each block needs only two connection cables, a 48 V power supply line and a 3 Gb/s optical link for data transfer, trigger management and synchronisation [64]. Altogether, this design favours the characteristics of modularity and portability of the setup, thus facilitating its transport and installation in various laboratories. The apparatus also offers the possibility to be coupled to different detectors.

The project has been launched in 2006 [65] as a scientific cooperation among many researchers and institutions from different countries, mainly Italy and France. After a thorough R&D activity (see Ref. [66] and references therein), a 4 block demonstrator of FAZIA started its experimental campaigns at the Laboratori Nazionali del Sud (INFN-LNS) in Catania. The experiments carried out in this first phase are, in chronological order [63]:

- ISO-FAZIA [60, 67], in June 2015 ($^{80}\text{Kr}+^{48,40}\text{Ca}$ at 35 AMeV) and FAZIA-SYM [68, 69], in December 2015 ($^{48,40}\text{Ca}+^{48,40}\text{Ca}$ at 35 AMeV) aimed at the investigation of isospin transport phenomena, exploiting the capability to isotopically discriminate the QP remnant and the QP breakup products.
- FAZIA-COR, in March 2017 (^{20}Ne , $^{32}\text{S}+^{12}\text{C}$ at 25 AMeV and 50 AMeV), to study the in-medium effects on the decay of light clusters by exploiting the particle correlation technique.
- FAZIA-PRE, in the first half of 2018, with an upgraded six block configuration, to study the reaction $^{48,40}\text{Ca}+^{12}\text{C}$ at two different energies (25 AMeV and 40 AMeV). Its goal is to examine the isospin transport phenomena at the two energies, in order to highlight whether the pre-equilibrium emission significantly affects the initial isospin difference between target and projectile.
- FAZIA-ZERO, in July 2018, in collaboration with the Beihang University, exploiting the well known reaction $^{12}\text{C}+^{12}\text{C}$ at 62 AMeV for a test of FAZIA blocks for cross section measurements at zero degrees with very low current beams.

After these experiments, the FAZIA setup, now including 12 blocks, has been moved to GANIL and coupled to INDRA: this is the originally designed configuration, including the maximum number of FAZIA blocks that can fit inside the INDRA scattering chamber. However, further experiments employing FAZIA blocks arranged in different configurations are being planned, e.g. at GANIL, INFN-LNS and RAON (Daejeon, South Korea [70]).

The present work concerns the E789 experiment, which is the first one of the INDRA-FAZIA scientific program: the experiment will be described more extensively in Chapter 3.

2.1.1 The detectors

Each FAZIA telescope includes three different detection stages. This configuration allows for the application of multiple and complementary techniques for the identification of the detected nuclear fragment, depending on the layer in which it is stopped. The composition of each telescope is as follows:

- The first layer is a $300\ \mu\text{m}$ thick silicon detector, referred to as **Si1** in the following. Its active area is $2\times 2\ \text{cm}^2$, which also defines the active area covered by a single telescope. The Si detectors are mounted on a purposely designed 2×2 holding frame made of an aluminum alloy [64], as shown in Fig. 2.2;
- The second layer is a $500\ \mu\text{m}$ thick Si detector¹, **Si2** from now on, with the same active area of Si1. A new configuration exploiting thicker Si2 detectors

¹Some telescopes feature a $300\ \mu\text{m}$ silicon detector also as second detection layer Si2. In the E789 experiment, these configurations are located only in BLK2. Those given in the text are nominal thicknesses. The actual Si detector thicknesses have been appropriately considered for calibration purposes (see Sec. 3.3).

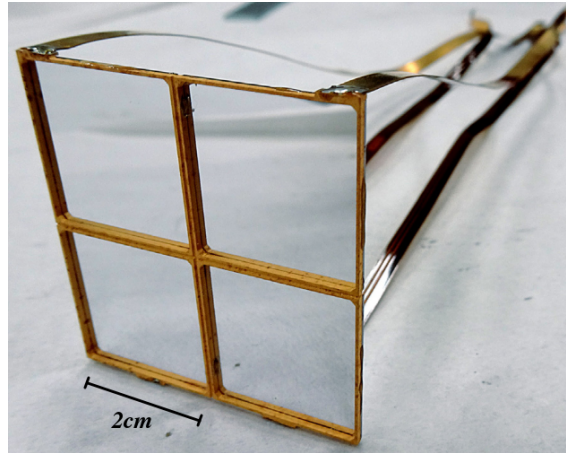


Figure 2.2: Four FAZIA silicon detectors mounted on a frame as a quartet. The kapton flexi cables needed to connect the single detectors to their own preamplifiers are also visible.

($\sim 750 \mu\text{m}$) is currently under test, but it has not been used in the present work. The second layer silicon detectors are mounted on a frame similar to that employed for the first layer;

- The third layer is a 10 cm thick CsI(Tl) scintillator, with a $\sim 5\%$ doping homogeneity, read out by a Si photodiode (either produced by FBK [71] or CIS [72]) placed at the back side. The crystal is shaped as a slightly tapered parallelepiped, adapted to the designed distance from the target (1 m): the front (rear) face has an area of $20.4 \times 20.4 \text{ mm}^2$ ($21.7 \times 21.7 \text{ mm}^2$). The scintillator is wrapped on the sides with a highly reflective (98%) polymer foil (ESR Vikuiti 3M), and the entrance face is covered with a thin reflective aluminised Mylar foil ($1.5 \mu\text{m}$ thick). This detector will be referred to as **CsI** in the following.

Each detector is connected to its own preamplifier by means of a 15 cm kapton strip cable, as shown in Fig. 2.2 for silicon detectors. In the case of Si detectors the ground contact of the kapton cable is soldered to the metal frame, which is also connected to the front face (n^+ contact) of the detector via conductive glue. The rear (p^+) contact of the detector is connected to the (negative) bias contact via ultrasonic microbonding. The silicon detector bulk is type-n and the detectors are mounted with the low field side (n^+ contact) facing the target, in order to optimise their identification capabilities (see below).

As previously mentioned, during the R&D phase, many efforts have been dedicated to the selection of the most suitable detectors to build FAZIA telescopes [66]. The main goal was to improve the energy resolution and the identification capability of the setup, both with ΔE -E and PSA techniques (see Sec. 2.4). As a result of this effort, the collaboration has formulated the so-called “FAZIA recipe”, summarising all the silicon detector characteristics needed for an optimal performance of the setup:

- High thickness uniformity: FAZIA Si detectors feature a thickness uniformity better than $\pm 1\%$. A good planarity and parallelism of front and rear sides is mandatory to reduce the dependence on the impact point of the ΔE released by a particle punching through the silicon pad [61], when the detector is used as ΔE stage for the ΔE -E technique² (i.e. Si1 for Si1-Si2 correlation or Si2 for Si2-CsI correlation, see Sec. 2.4.1).
- Minimised dead layers, to reduce undesired energy losses and the energy straggling that they would introduce.
- High doping uniformity (and therefore resistivity homogeneity, $\sim 3\%$), which is necessary to have a uniform electric field in the depletion volume of the detector. This feature is mandatory to achieve a good result with the PSA method, as explained in Sec. 2.4.2: in fact, a local variation of the electric field would result in a different time development of the charge collection, and therefore a different shape of the signal induced by an impinging ion with a given (Z, A) and energy. The signal shape would therefore depend on the impact position, thus compromising the performance of PSA identification. The FAZIA collaboration also developed a non-destructive method to determine the resistivity of the detector as a function of the position on its surface [73]. This technique, based on a detector scanning using collimated UV-light pulses, allows for the mapping of the resistivity values over the detector area and the evaluation of its doping uniformity. This information can be used to select the silicon detectors that fulfill the doping uniformity requirements before mounting them in a FAZIA telescope and using them in an actual experiment. The collaboration identified neutron Transmutation Doped (nTD) silicon pads as the best choice in terms of doping uniformity, and most of the sensors currently mounted in FAZIA are of this type. Lately, a new production of silicon detectors obtained from TOPSIL Ultra-homogeneous High Purity Silicon (UHPS) substrates [74] has been tested: according to the first results, their good resistivity uniformity is suitable for FAZIA applications.
- “Random cut” of the Si wafers, tilted with respect to the major axis of the lattice³, in order to reduce the channeling effect. The channeling effect is an orientation-dependent phenomenon observed for charged particles interacting with a crystalline detector [75]. If an impinging ion has a direction close to that of a principal crystal axis, it tends to travel through the “channels” formed in the lattice by neighboring atom layers. In this situation the stopping power of the particle is reduced: this introduces fluctuations in the range, in the ionisation profile and hence in the shape of the induced signal. In Ref. [76] it has been pointed out that this effect can spoil the identification capability of Si detectors, and must therefore be minimized. If the impact direction is

²As an example, a thickness uniformity better than $2\ \mu\text{m}$ is needed for Si1 in order to identify Ca isotopes exploiting the Si1-Si2 correlation.

³The Si wafers are cut at about 7° with respect to the $\langle 100 \rangle$ axis of the lattice.

“randomised”, the crystal is not viewed as an ordered structure by the particle, and channeling is reduced.

- Deposition of a $\sim 25 \mu\text{m}$ aluminum layer on both detector electrodes, in order to reduce the sheet resistance of the detector surface: this preserves the timing properties of the device [77]. Without the Al layer, the shape of the signal would depend on the impact position on the active area of the detector, thus jeopardising its identification capability through PSA. Since the aluminisation process introduces a dead layer, its thickness is the result of a compromise between the need to minimise the dead layer and its beneficial effect on the sheet resistance.
- Reverse mounting configuration: all silicon detectors are mounted with the low field side facing the target. In fact, as highlighted in Ref. [78] and explained also in Sec. 2.4.2, this configuration enhances the PSA identification performance of the setup, without affecting the ΔE -E method.
- Monitoring of the silicon reverse current during measurements and correction for the associated voltage drop over the bias resistor, in order to keep the detector bias voltage constant. This is done in order to obtain a constant electric field in the depletion region of the detector and therefore a constant shape of the signal induced by particles with the same (Z, A) and energy throughout the whole measurement.

2.1.2 The read-out electronics

The most updated review of the FAZIA electronics can be found in Ref. [64]; a brief description is given in the following.

The FAZIA FEE is placed inside the scattering chamber, in close proximity to the detectors of the telescopes. Since the electronic cards operate under vacuum, a cooling system is necessary to keep their temperature below 60°C . The cooling system of each block is based on a copper plate where all the electronic cards are fixed with screws and thermally coupled by means of a thermal grease. Inside this plate, some purposely designed channels distribute a heat-carrier liquid (water with 30% alcohol or glycol) throughout the copper volume, thus ensuring an efficient heat dissipation. The liquid that flows through all the blocks is refrigerated by a chiller (ACW LP60) placed outside the scattering chamber. Outside of the vacuum chamber, the optical fibers are connected to the so-called Regional Board (ReBo), which collects data from the different blocks and builds the complete “event” packages to be collected by the acquisition system.

A schematic diagram that represents the placement of the electronic cards, inside and outside the vacuum chamber, is shown in Fig. 2.3 [64]. Each block, represented by a pink area, exploits eight FEE cards, each of them serving two full telescopes, i.e. six detectors. The area of a FEE card can be virtually subdivided into three sections, as shown in Fig. 2.4. On the left side, the input stage, or *analogue stage*,

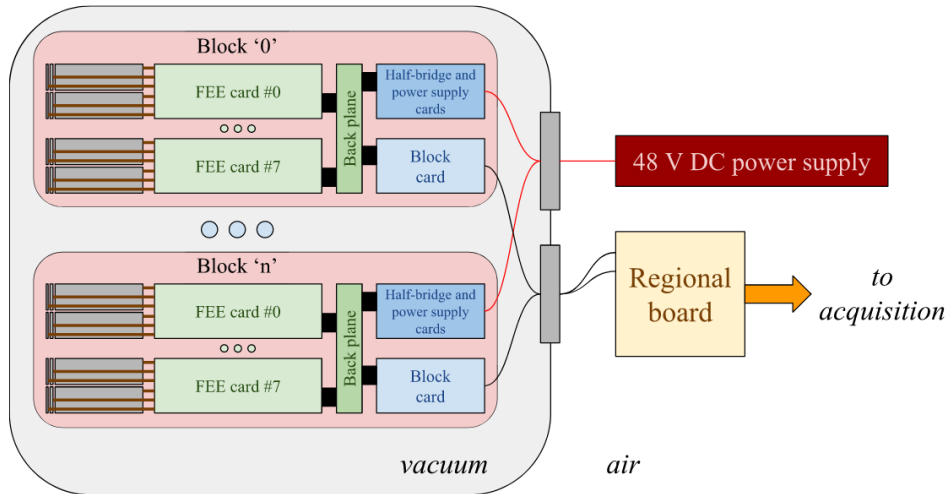


Figure 2.3: Schematic representation of FAZIA read-out electronics in vacuum and in air. From Ref. [64].

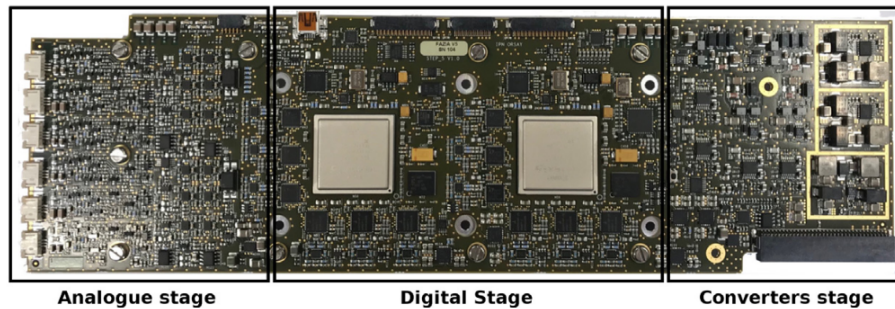


Figure 2.4: Picture of a FEE card. The three sections (analogue, digital and converters stage) of the board are indicated. The analogue stage also includes a built-in square pulse generator. From Ref. [64].

is visible. In this section, six charge sensitive preamplifiers are mounted, one for each detector of the two telescopes connected to the FEE card. A sketch of a single telescope read-out electronics is shown in Fig. 2.5: the analogue stage is on the left side of the picture. The offset voltage at the output of the preamplifiers can be tuned in order to exploit the whole dynamic range of the ADCs in the next stage. The preamplifier output signal is then treated differently, depending on the telescope layer. Each Si1 line is split into three channels: a high range charge signal (QH1), a low range charge signal (QL1) and a current signal (I1). For the Si2 line we have two paths, namely the high range charge signal (Q2) and the current signal (I2). For the CsI stage there is only one charge signal (Q3). The current signals I1 and I2 are obtained by means of analogue differentiation of the respective preamplifier outputs. The high range signals QH1, Q2 and Q3 are attenuated by a factor of 4, in order to match the full 8 V dynamic range of the preamplifiers with the 2 V input range of the ADCs. The low range signal, QL1, is amplified by a factor of about 3, in such a way that the energy range covered by its ADC is about 16 times

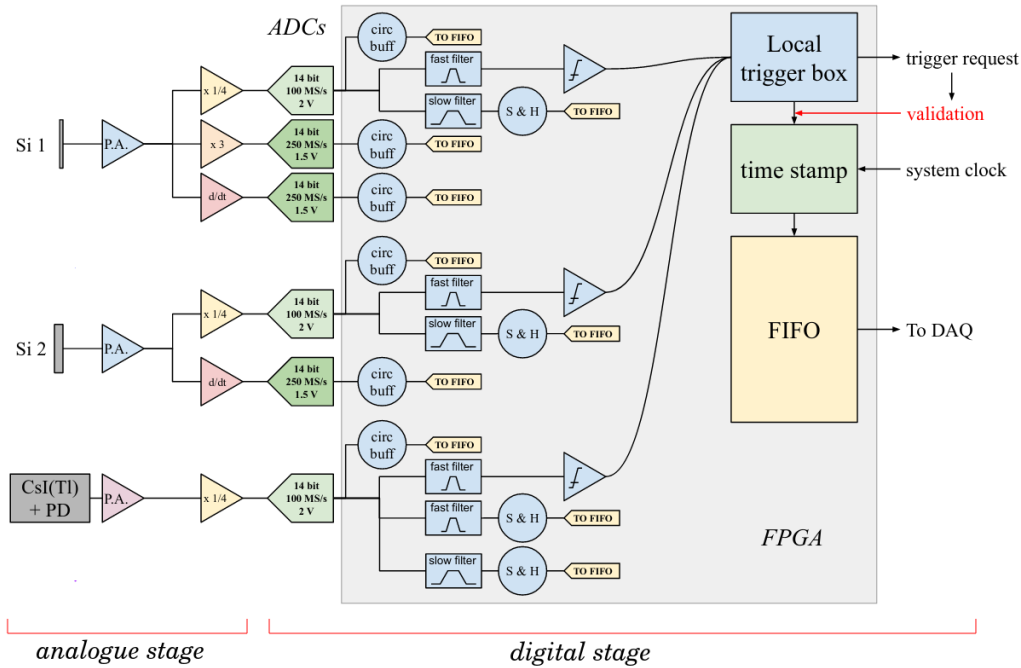


Figure 2.5: Scheme of a telescope read-out electronics. The grey area includes the signal processing and data flow that is carried out within the FPGA. Adapted from Ref. [79].

smaller than that covered by QH1 (the range of the ADC is 1.5 V instead of 2 V as for the QH1 signal). The current signal, I1, is also amplified, to compensate for the attenuation produced by the analogue differentiation stage. All the signals are filtered with an anti-aliasing filter before being sampled.

The central part of the FEE board hosts the *digital stage*. Here, the twelve analogue signals are sampled by twelve ADCs. In Fig. 2.5 the signal flow on the six channels related to one of the two telescopes connected to the same FEE card is schematised. The high range signals QH1, Q2 and Q3 are connected to 14-bit, 100 MSPS (11.4 ENOB, Effective Number Of Bits) ADCs, while the low range QL1 and the current signals I1 and I2 are served by three 14-bit, 250 MSPS (11.2 ENOB) ADCs. The higher sampling frequency of the QL1, I1 and I2 channels guarantees a better timing performance (QL1) and a better reproduction of the signal shape (I1 and I2). The digital samples continuously produced by the ADCs are processed on-board in real-time by two FPGAs, one for each telescope (we will refer to this as on-line processing). The operations performed by each FPGA are enclosed by the grey area in the sketch in Fig. 2.5. For each telescope stage, a fast trapezoidal shaper, followed by a leading edge discriminator, is used to produce a local trigger signal. Slow trapezoidal shapers (time constant $\sim \mu\text{s}$) are applied in order to estimate the deposited energy from the signal amplitude. In the following, the maximum amplitude of the trapezoidal shaper will be indicated with the same name as the corresponding signal (e.g. QH1 for the maximum amplitude of the trapezoidal shaper calculated on the QH1 signal). The digital stage of the FEE card also contains an 8-bit PIC

microcontroller which, among other functions, handles the voltage drop compensation on Si detectors. The *converters stage*, on the right side of the picture, produces the required bias voltages for the silicon detectors (up to 400 V), starting from the already mentioned 48 V supply.

All the FEE cards of the same block communicate through a common bus with three other electronic cards, namely the Block card, the Power Supply card and the Half Bridge card. The Half Bridge and Power Supply cards provide the low voltages that are required by the block electronics.

The Block card merges the data coming from the 8 FEE cards, building partial events. It also handles the I/O operations with the ReBo, through the aforementioned optical fiber. All the data coming from the Block cards are collected by the ReBo, that operates in air, outside of the vacuum chamber. Here, the complete event is built from the partial events transmitted by the Block cards. The ReBo also manages the slow control (e.g. bias voltage, DC offset, trigger thresholds, see Ref. [64]) requests from the PC, handles all the trigger informations coming from the blocks and sends back validation signals, as described below. It also features an *external trigger* input. A single ReBo can manage up to 36 blocks and can be connected to other regional boards to increase the maximum number of blocks that can be controlled. Moreover, it handles the coupling between FAZIA and other devices allowing for the synchronisation, event by event, of various acquisition systems: this feature has been exploited for the coupling of FAZIA with INDRA, as will be explained in Sec. 2.3.

Trigger system in FAZIA

The trigger generation process, managed by the ReBo, is a four step procedure:

1. Local triggers are generated by the FEE cards by exploiting on-line fast trapezoidal filters (rise time 200 ns and flat top 200 ns) applied to the QH1, Q2 and Q3 signals. The detector trigger is produced when the amplitude of the shaped signal crosses (with positive slope) the so-called "*fast*" *threshold*, which can be set by the user. The FEE card combines the logic signals from the detectors to form the *telescope local trigger*; the OR logic combination is usually chosen. The telescope triggers are then sent to the Block card.
2. Each Block card counts all the local triggers generated in the respective block. The local multiplicity values are sent every 40 ns to the ReBo.
3. A *global trigger* is generated inside the ReBo when the sum of all the local multiplicities over a fixed time window exceeds the global multiplicity threshold. A downscale factor K can also be imposed: in this case the global trigger is accepted only once every K occurrences.
4. When a global trigger is accepted a validation signal and an event number are generated and sent to all the Block cards. The Block cards distribute the validation and the event number to the FEE cards. However, if an alert

condition has been generated by a FEE, a VETO signal is generated instead of the validation. A full telescope is acquired when the amplitude of at least one of the slow trapezoidal shapers associated to the QH1, Q2 and Q3 signals is higher than a fixed threshold (*slow threshold*).

When coupled to other devices, FAZIA can also work in the so-called *slave mode*: in this case, when an external trigger is received and the VETO flag is false, a validation signal is generated.

2.1.3 Data flow and digital treatment of the signals

The beginning of the FAZIA R&D phase saw the development and study of off-line digital signal processing algorithms to extract energy and shape-related information from the digitised signals. After that, during the development of the FEE, the on-line analysis has been implemented on the FPGAs of the FEE cards; the results of the on-line signal processing algorithms have been compared to the off-line ones in order to be validated.

On the FPGAs, besides the fast trapezoidal filters used to generate the local triggers, slow trapezoidal shaping filters are applied to the detector signals to produce a real-time energy information by evaluating the maximum of the charge signal. In particular, one is applied to the QH1 signal and one to the Q2 signal. Two shapers with different time constants are applied to the Q3 signal (see Sec. 2.4.3) for identification purposes. The rise-time and the flat-top values of the slow trapezoidal filters can be set by the user. The typical rise time for the QH1 and Q2 shapers is $2\ \mu\text{s}$ while the typical flat top is $1\ \mu\text{s}$. For the Q3 signal, two shapers are applied in parallel, one with rise time $2\ \mu\text{s}$ and flat top $10\ \mu\text{s}$ ($Q3_{slow}$) and one with rise time $2\ \mu\text{s}$ and flat top $500\ \text{ns}$ ($Q3_{fast}$).

The current signals I1 and I2 are not processed on-line. Instead, a portion of the signal, containing the region of maximum amplitude, is sent to the acquisition, to be stored for the off-line analysis.

When a validation signal is sent from the ReBo to the FEE cards, the maximum amplitudes reached by the four slow trapezoidal shapers (QH1, Q2, $Q3_{slow}$, $Q3_{fast}$) and a portion of the digitised signals (QH1, QL1, I1, Q2, I2, Q3) are stored into FIFO memories. The acquisition (slow filter) thresholds are checked⁴. When a telescope is marked for acquisition, all its information is transferred to another FIFO memory, together with the event number provided by the ReBo, to build the local event. The local events from the FEE cards are collected by the respective Block cards, where the event number is also checked. The partial event thus built is written in the Block card FIFO buffer, ready to be read from the ReBo.

⁴Whenever a trigger is generated, this mechanism allows to acquire and use also the channels with an high noise level, whose fast threshold is set reasonably high in order to avoid spurious triggers. In fact, when a (good) trigger is received, all the channels are checked: if the slow filter, whose signal-to-noise ratio is better than that of the fast filter, is higher than the slow threshold, the channel (and the corresponding telescope) is acquired.

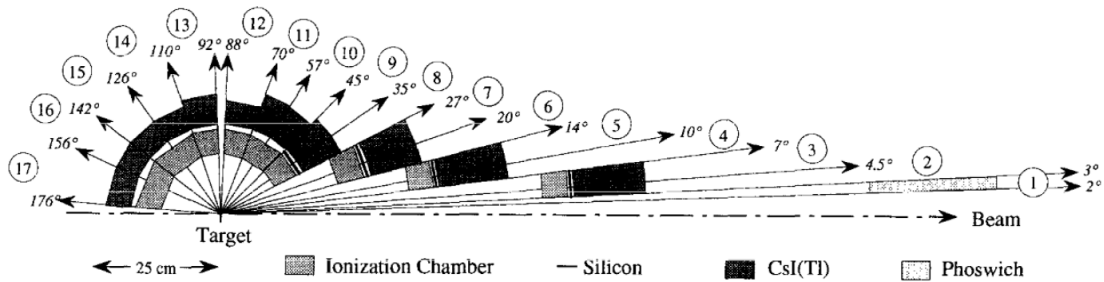


Figure 2.6: Sketch of the INDRA array original geometry. From Ref. [80].

The signal processing and data flow carried out in each FPGA is summarised in Fig. 2.5.

2.2 The INDRA apparatus

INDRA (*Identification de Noyaux et Detection avec Resolutions Accrues*) is a multi-detector array for light charged particles and fragments characterised by a large solid angle coverage (90% of the 4π solid angle, in its original configuration) and low detection thresholds. It is optimised for the study of heavy ion collisions at Fermi energies [18, 80, 81]. The apparatus has been in operation since 1993 at GANIL, where it is permanently installed in the experimental area D5. Its original configuration, shown in Fig. 2.6, consists of 336 independent modules arranged in 17 rings with cylindrical symmetry with respect to the beam axis. Such a high granularity allows for the detection of a maximum of about 50 fragments and light charged particles [80]. The target holder is placed in an opening between rings 12 and 13 ($88^\circ \leq \theta \leq 92^\circ$). There are two other openings on the front ($0^\circ \leq \theta \leq 2^\circ$) and the back ($176^\circ \leq \theta \leq 180^\circ$), along the beam trajectory. The total solid angle coverage loss due to these openings is about 2%; an additional 8% is lost due to the dead areas between the modules.

Each module is a multi-stage identification telescope, with a different configuration depending on the ring. The first ring was originally made of phoswich detectors, later replaced by 12 Si-CsI(Tl) telescopes. The rings from 2 to 9 are made of three stage telescopes (Ionisation Chamber-Si-CsI(Tl)), while the remaining rings (10 to 17) are made of two stage telescopes (Ionisation Chamber-CsI(Tl)). The ionisation chambers, not used in the E789 experiment, are 5 mm thick, usually filled with C_3F_8 , typically at a pressure of 50 mbar (rings 2 to 5) or 30 mbar (rings 6 to 17), enclosed by two $2.5 \mu\text{m}$ thick mylar foils. The silicon detectors (Si) are either $300 \mu\text{m}$ (rings 1 to 3, 8 and 9) or $150 \mu\text{m}$ thick (rings 4 to 7). The CsI(Tl) scintillators have thicknesses ranging from 5 cm to 14 cm (the complete list can be found in [80]), and are thus able to stop even the most energetic particles produced in the reactions at intermediate energies. The CsI(Tl) detectors are coupled to photomultipliers to collect the scintillation light. The nuclear fragment identification is achieved either by applying the ΔE -E method on the available detector layers, or the PSA in CsI(Tl)

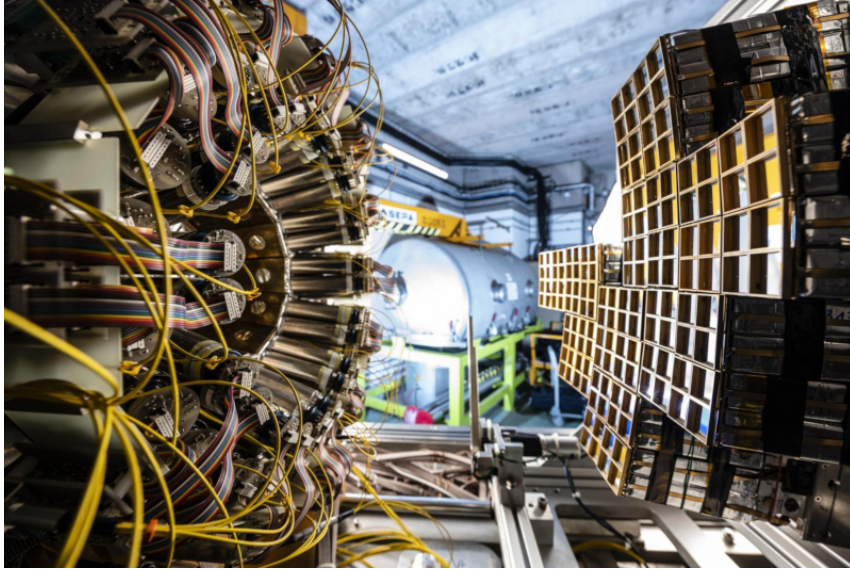


Figure 2.7: Picture of the INDRA-FAZIA apparatus during the mounting operations at GANIL (only 9 FAZIA blocks were mounted when the picture was taken). INDRA is the apparatus on the left side and FAZIA the one on the right side.

(see Sec. 2.4). Nuclear fragments up to $Z \sim 54$ can be identified in charge (the upper Z limit for identification depends on the identification method), and heavier products can be also identified with an uncertainty of a few charge units; isotopic identification can be achieved up to $Z = 4 - 5$.

2.3 Coupling INDRA and FAZIA

During the first months of 2019 the coupling between INDRA and FAZIA was completed: the E789 experiment (see Chapter 3), subject of the present work, is the first experimental campaign that exploits this setup. A picture of the INDRA-FAZIA setup during the mounting operations can be seen in Fig. 2.7.

Mechanical coupling In order to place FAZIA at forward (small) polar angles with respect to the beam direction, the first five rings of INDRA had to be removed. The most forward polar angles ($1.4^\circ < \theta < 12.6^\circ$) have been covered with 12 FAZIA blocks, arranged in a *wall* configuration⁵ placed at a distance of 1 m from the target, as can be seen in the rendering shown in Fig. 2.8: in this configuration, the active area of FAZIA covers $\sim 41\%$ of the forward polar angles ($\theta < 14^\circ$). This choice has been made in order to exploit the outstanding performances of the FAZIA apparatus

⁵In the *wall* configuration, the blocks are arranged around the beam axis, covering evenly the azimuthal angle φ . In some of the first FAZIA experiments, e.g. ISO-FAZIA, a *belt* configuration was adopted, with 4 blocks placed at the same height of the beam axis, covering only a limited φ interval.

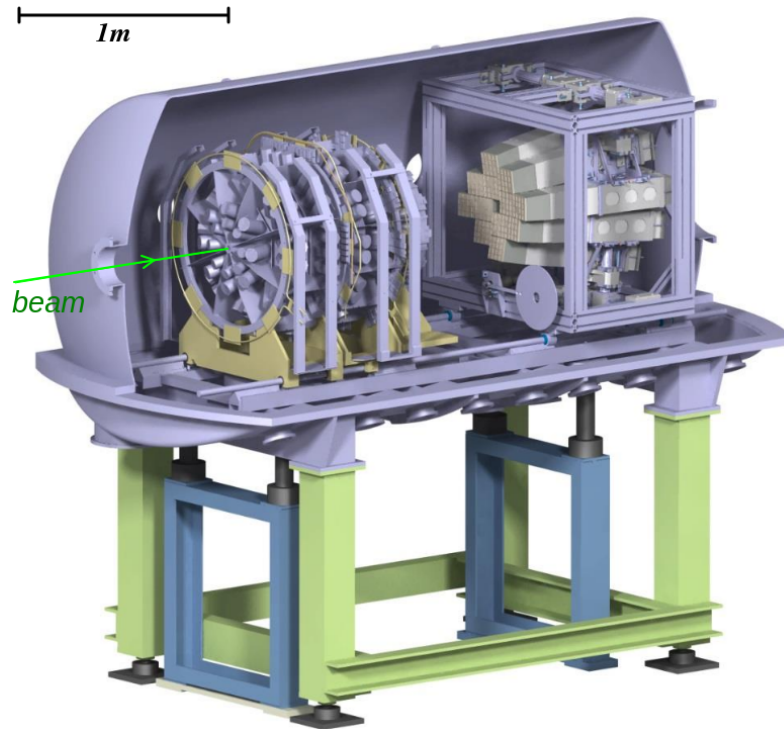


Figure 2.8: Rendering of the INDRA-FAZIA mechanical coupling, where INDRA is visible on the left side, FAZIA on the right side. The target holder is located inside the INDRA apparatus, and therefore it is not visible in the picture.

for the isotopic identification of the QP-like fragments, mostly forward emitted. The remaining part of INDRA (rings 6 to 17) covers the polar angles between 14° and 176° , i.e. $\sim 80\%$ of the 4π solid angle. The large angular coverage provided by INDRA allows in principle for the construction of global variables useful for the estimation of the reaction centrality, such as light charged particle multiplicity or transverse energy.

Acquisition coupling The coupling of the acquisition systems of the two apparatuses is implemented through the VXI CENTRUM (*Clock Event Number Transmitter Receiver Universal Module* [82]) technology, designed at GANIL at the beginning of the 2000s. This electronic module allows for the synchronisation of events detected by various acquisition systems connected to the same network, basing on the distribution of an event timestamp. In the case of FAZIA, the communication with the CENTRUM module is managed by the ReBo. The CENTRUM implementation in FAZIA ReBo works in *slave mode*. On the other hand, the CENTRUM module associated with INDRA acquisition works as the *master*: this module also has the role of incrementing the global event number, which will be shared with the slave CENTRUM module on request. We can pinpoint three different levels on which the acquisition coupling is based:

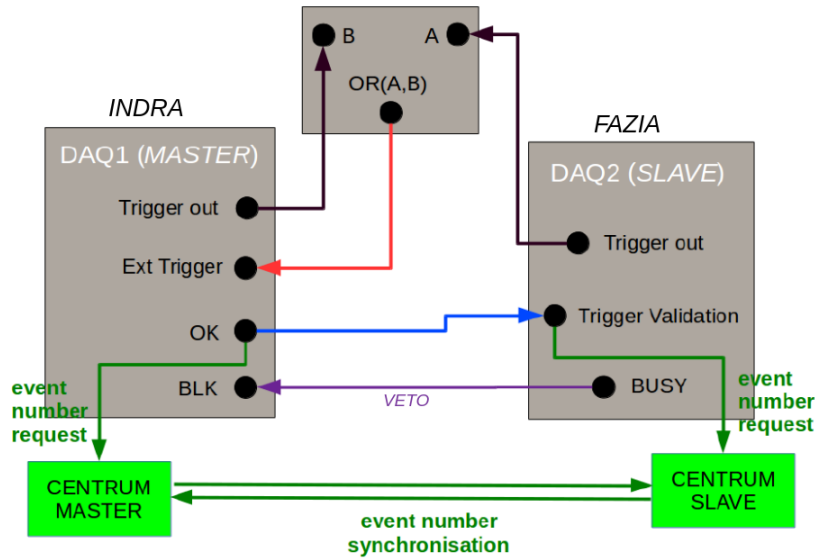


Figure 2.9: Schematic representation of INDRA-FAZIA trigger coupling in common dead-time mode. In this configuration events where either INDRA or FAZIA or both have triggered can be acquired. Adapted from Ref. [83].

- *Trigger generation:* INDRA-FAZIA works in a common dead-time mode, i.e. neither of the two apparatuses can generate a validation while the other is in a busy status. In order to do so, the trigger and VETO inputs and outputs are connected according to the scheme in Fig. 2.9. In this configuration, the pre-processed triggers from both apparatuses are exploited: the logical OR of these two triggers is sent as external trigger to the INDRA acquisition (DAQ1, master), which checks for the event validation conditions. The DAQ1 also receives a VETO (Busy) signal from the FAZIA acquisition (DAQ2, slave), in order to prevent desynchronisation. If the conditions (e.g. multiplicity) are properly met, a validation signal is produced by the INDRA acquisition, and propagated to the FAZIA acquisition.
- *Timestamp generation and distribution:* the second level is activated when a validation signal is produced. Both INDRA and FAZIA send a timestamp request to the CENTRUM module, which promptly dispatches the timestamp information together with an event number. This information is attached to the partial events produced by the two acquisition systems.
- *Event merging:* the partial events coming from FAZIA and INDRA are then collected by the NARVAL (*Nouvelle Acquisition temps-Reel Version 1.2 Avec Linux* [84]) acquisition system, developed by IPN Orsay, France. Here, an Event Merger builds the global event by merging the partial events with a timestamp difference lower than a user-defined coincidence window (usually around $1 \mu\text{s}$). The global event thus reconstructed is then stored on a hard disk.

Both CENTRUM and NARVAL support the connection with multiple apparatuses: thanks to this feature, other detectors will be able to be coupled with INDRA and FAZIA in the future.

2.4 Identification techniques

As discussed in Chapter 1, there are cases in which isospin related observables must be evaluated, and their dependence on the different entrance channel has to be studied. Therefore, a precise (Z, A) identification of the nuclear fragments produced in the reaction is mandatory. As it will be explained in Sec. 3.3, a correct identification both in mass and atomic number of the detected fragments is also useful for a precise detector calibration.

In this section the particle identification techniques that are possible with the INDRA-FAZIA apparatus will be described in detail, namely the ΔE -E method and the Pulse Shape Analysis (PSA) both in Si and in CsI(Tl) detectors. The collaboration is also investigating the use of time of flight identification techniques [85, 86]. However, this last method has not been used in the present work.

2.4.1 ΔE -E method

The ΔE -E technique is maybe the most widely used charged fragment identification method in the field of heavy ion collisions. This method relies on the mechanism of kinetic energy dissipation of charged particles in matter. The specific energy loss S (also referred to as linear stopping power), which is the energy loss per unit path length of an impinging fragment with charge Z , mass A and velocity v within an absorber, is well described by the Bethe-Bloch formula [87]:

$$S = -\frac{dE}{dx} = \frac{4\pi e^4 Z^2}{m_e v^2} NB \quad (2.1)$$

where

$$B = z \left[\ln \frac{2m_e v^2}{I} - \ln(1 - \beta^2) - \beta^2 \right] \quad (2.2)$$

N and z are the numerical density and atomic number of the absorber, m_e and e are the rest mass and charge of the electron, $\beta = v/c$ and I is the experimentally determined ionisation potential of the absorber.

In the non-relativistic limit ($v \ll c$), a simple analytical expression can be derived: only the first term of the factor B is significant, and its mild logarithmic dependence on the incident particle energy can be neglected. Thus we can simplify eq. (2.1) to:

$$S = -\left| \frac{dE}{dx} \right| \propto \frac{Z^2}{v^2} \propto \frac{Z^2 A}{E} \quad (2.3)$$

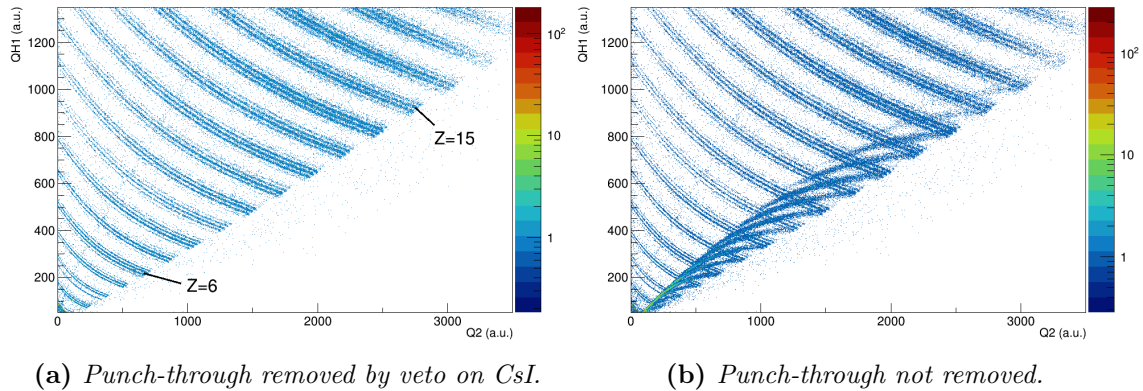


Figure 2.10: An example of Si1-Si2 ΔE -E correlation matrix of a FAZIA telescope. The matrix shown here is produced with the data of the E789 experiment. In the left panel the so called punch-through events are removed by means of a veto condition on the third stage (CsI(Tl) detector). The right panel shows the same matrix without the punch-through suppression condition.

where E is the initial kinetic energy of the impinging fragment, and the omitted proportionality constant only depends on the absorber⁶.

A ΔE -E telescope is a detector system including two stages, such as Si1-Si2 of FAZIA telescopes. Basing on eq. (2.3), we can deduce that the energy ΔE released in the first detector is such that $\Delta E \cdot E = kZ^2A$, where k depends only on the characteristics of the first stage detector. Therefore, in a ΔE -E matrix (i.e. a correlation plot between the ΔE released in the first detector and the residual energy $E_{res} = E - \Delta E$ deposited in the second detector) the different ion species will be distributed on distinct quasi-hyperbolic ridges depending on their Z and, more weakly, on their A , provided that the fragment is stopped in the second stage. Fig. 2.10a shows a typical Si1-Si2 ΔE -E correlation matrix obtained with a FAZIA telescope. Here, the different loci corresponding to different elements can be easily noted: each Z ridge also features a finer structure, related to the different isotopes of each element. The ΔE -E identification capability depends on the characteristics of the detectors that constitute the telescope, mainly their energy resolution, the absence of channeling effects and, for the ΔE stage, its thickness homogeneity. In fact, great efforts have been made by the FAZIA collaboration in order to select the best quality silicon detectors for the apparatus (see Sec. 2.1.1).

Only the fragments stopped within the second stage detector can be identified by means of the ΔE -E technique. The detected fragments with enough energy to punch through the second layer produce a typical “cusp” at the right end of the ΔE -E correlation ridges, as can be observed in Fig. 2.10b. The presence of these cusps hinders the identification of at least part of the events located at the rightmost

⁶Actually, strict proportionality of the fragment mass to the mass number A has been assumed. This is a good enough approximation for the present purpose.

part of each ridge. In a FAZIA telescope, the so called punch-through events can be eliminated from a Si1-Si2 ΔE -E matrix by excluding from the matrix the fragments which have deposited energy also in the third stage CsI detector (this has been done, e.g., in Fig. 2.10a). The CsI stage extends the dynamic range in energy of the telescope, stopping even the most energetic light charged particles. The ΔE -E method can then be applied using as ΔE the energy measured by the silicon detectors and as residual energy the energy measured by the CsI(Tl).

The ΔE -E method has also a low-energy threshold (see e.g. Fig. 3.12a). In fact, the fragments that do not have enough energy to reach the second layer cannot be identified. This lower threshold could be reduced by exploiting a thinner ΔE stage detector [88]. However, a thinner ΔE detector leads to an increased effect of the energy straggling on the ΔE -E correlation⁷. Moreover, the lower amplitude of the signals and the increased detector capacitance worsen the signal-to-noise ratio, thus deteriorating the identification capability of the telescope. A more effective way to overcome this limitation is to apply PSA techniques to those particles that are stopped within the first layer.

2.4.2 Pulse Shape Analysis in silicon

Pulse Shape Analysis (PSA) is a powerful tool for the identification of nuclear fragments. When applying PSA, the information coming from the detector actually stopping the fragment is enough for identification. Such a method turns out to be useful in those cases in which the fragment is stopped within the first layer of a telescope (as Si1 in FAZIA), because it allows to reduce the lower energy threshold for identification with respect to the one associated to the ΔE -E technique⁸. PSA in silicon detectors was first proposed by Ammerlaan in 1963 [90], but it underwent many developments in more recent times thanks to the technological advances in the production of fast sampling digitisers [91–94]. A great effort has been made to improve the PSA identification performance also during the FAZIA R&D phase, both in the design of the most suitable silicon detectors (see Sec. 2.1.1) and in the development of Digital Signal Processing algorithms aimed at the extraction of the required information from the digitised signals [95–98].

PSA methods are based on the dependence of the time evolution of the induced signal on the ionisation density along the track of the incident particle inside the detector. The ionisation profile, in turn, depends on the characteristics of the particle,

⁷Due to the statistical nature of the process of energy loss, the energy deposited in an absorber is affected by intrinsic fluctuations, known as *energy straggling*. In the Bohr regime, which is the case for the typical energies and detector thicknesses considered in this work, a beam of monoenergetic particles impinging in an absorber with thickness Δx emerges with a broader energy distribution that features a variance $\sigma_{Bohr}^2 = 4\pi e^4 N Z^2 z \Delta x$ (see [89]). From eq. (2.3) we can express the ΔE separation as $\delta(\Delta E)_{1,2} \propto \frac{1}{E} (Z_2^2 A_2 - Z_1^2 A_1) \cdot \Delta x$. Therefore, we find that the quality of the separation is such that $\delta(\Delta E)/\sigma_{Bohr} \propto \sqrt{\Delta x}$, i.e. it worsens when using thinner ΔE detectors.

⁸There is a minimum range in Si the fragment must penetrate in order to be identified with the PSA method. This is associated to the low-energy threshold for PSA identification (see Fig. 4 of Ref. [63]).

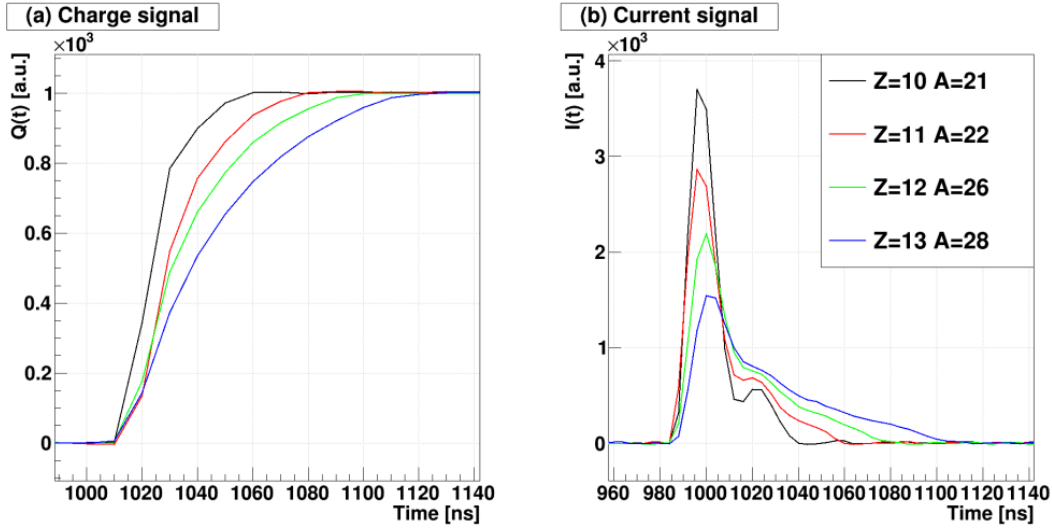


Figure 2.11: Experimental charge (panel (a)) and current (panel (b)) signals coming from the same Si1 detector for different incident fragments (^{21}Ne , ^{22}Na , ^{26}Mg and ^{28}Al) at the same energy (corresponding to 1000 a.u.). The difference between the four signals is evident. As expected, the signal associated to the lighter fragment is characterised by the fastest time development. From Ref. [98].

namely energy, atomic number and mass number. In fact, the density of the cloud of electron-hole pairs generated by the interaction of the impinging fragment with the detector is proportional to the *Bragg curve* [87]. Due to their higher stopping power, for a given energy, heavy ions produce relatively shorter tracks and with a higher ionisation density with respect to light ions. At large ionisation densities, the carrier cloud behaves as an electron-hole plasma. At first, the inner part of this plasma is not subject to the electric field which is present in the depletion region, since it is screened by the carriers in the outer layer. Only the outer carriers will drift immediately towards the electrodes, while the carriers in the inner part of the track will begin to migrate only when this field-screening effect becomes less effective. Therefore, some time will be required to erode the plasma cloud and to put all the carriers into motion, depending on the original ionisation density; this is the so-called *plasma time* [99–101], which adds up to the *charge transit time* to give the total collection time. The transit time, in turn, depends on the mass, charge and energy of the impinging particle via the length of the track. The shape of the signal induced in the detector reflects the details of the charge collection process, and it is therefore related to the characteristics of the incident fragment, as evident from Fig. 2.11. The picture shows a few charge (panel (a)) and current (panel (b)) signals for different fragments of the same energy stopped in a silicon detector. Their different time evolution (i.e. “shape”) is at the basis of the PSA methods. The PSA methods work by exploiting the correlation between a shape-related quantity and the deposited energy to identify the detected fragment. Two widely used shape

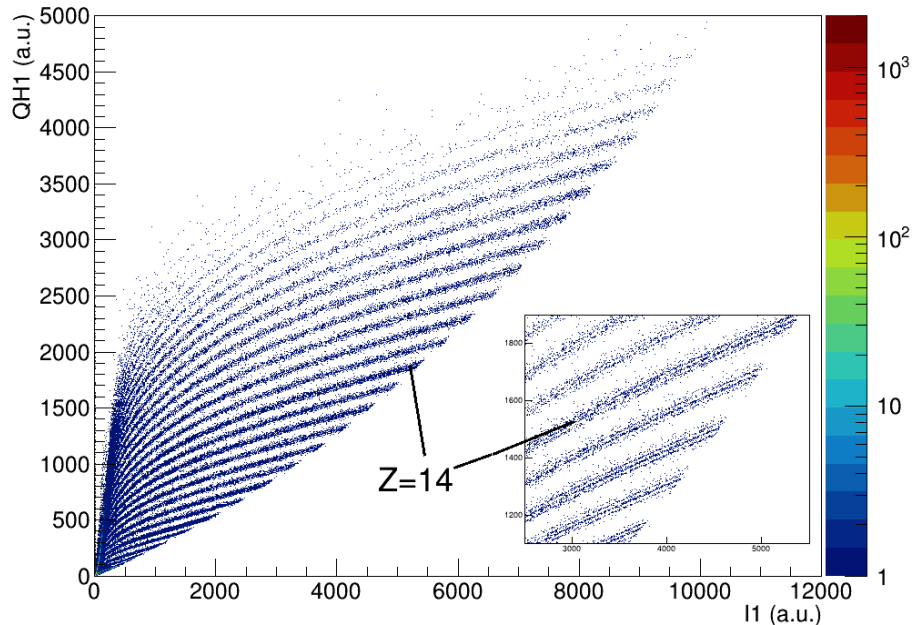


Figure 2.12: An example of Si1 “current PSA” matrix of a FAZIA telescope, i.e. a correlation plot between the energy deposited in Si1 and the maximum of the current signal I_{max} , both in arbitrary units. The inset shows an expanded view on the $Z \sim 14$ region, where isotopic discrimination is achieved. The correlation shown here is produced with the data of the E789 experiment.

parameters are the rise-time Q_{rise} of the charge signal and the maximum I_{max} of the current signal. Two correlation plots are usually built with these two shape parameters:

- Energy vs Q_{rise} , called “charge PSA”. A typical example can be found in Fig. 12 of Ref. [61];
- Energy vs I_{max} , called “current PSA”. An example of such correlation plot, obtained with the data of the E789 experiment, is shown in Fig. 2.12.

The FAZIA collaboration investigated both approaches [61], concluding that the second one leads to the better identification performance. As a result of this observation, the “current PSA” in Si1 is the adopted choice for the FAZIA apparatus. The off-line analysis on the digitised current waveforms is based on interpolation algorithms, that have been studied in detail by the FAZIA collaboration [62]. The adopted algorithm for the evaluation of the current maximum is based on a smoothing spline interpolation [102], which leads to the best identification results.

Special care is needed for PSA techniques to reach optimal results. For instance, since, for a given (Z, A) and energy of the fragment, the signal shape should *not* depend on the impact position (as it happens, e.g., when the electric field is not

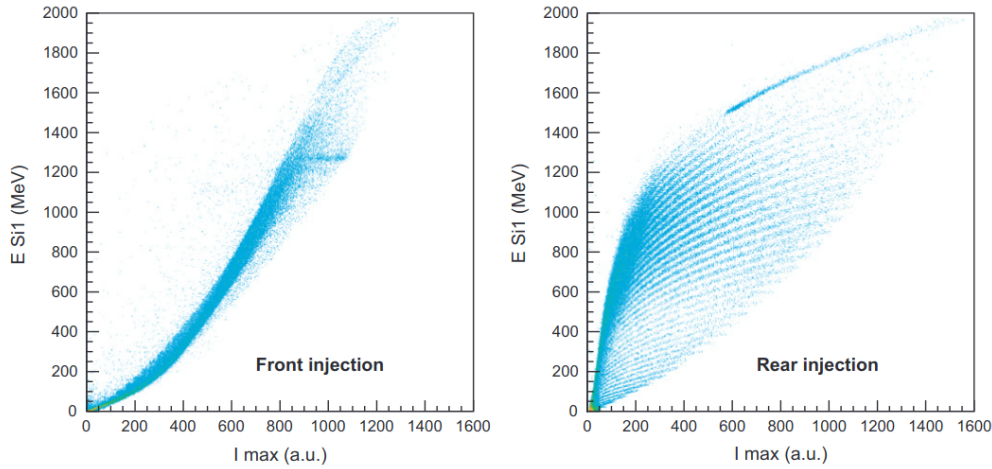


Figure 2.13: Comparison between Si1 “current PSA” correlation plots obtained in front mounting configuration (left panel) vs reverse mounting configuration (right panel). From Ref. [78]

uniform), a good doping uniformity is mandatory [73, 103–105]. Moreover, as anticipated in Sec. 2.1.1, in order to enhance the shape differences, and hence the PSA performance, the Si detectors of the FAZIA apparatus are reverse mounted [78]. In this configuration the fragment penetrates from the low field side (or ohmic side). For a fixed incident energy, a higher Z fragment produces a denser and shorter track, which is located in the low field region of the detector. On the other hand, a lower Z particle is more penetrating, producing most electron-hole pairs in correspondence of the Bragg peak, i.e. at the end of the track, in a region where the electric field is higher. Therefore, in the first case (higher Z) the longer plasma time expected due to the denser track is further enhanced by the low electric field experienced by the carriers, resulting in a much slower signal development than in the second case (lower Z). Fig. 2.13 (from [78]) shows the different PSA performances of a FAZIA Si1 obtained with the front injection and the rear injection: the better identification capability in the latter case is evident. In Ref. [78] it has also been demonstrated that the reverse mounting configuration of Si detectors does not affect the ΔE - E performance of FAZIA telescopes.

2.4.3 Pulse Shape Analysis in CsI(Tl)

In a FAZIA telescope, a particle with enough energy to punch through the second silicon stage Si2 can be identified exploiting the ΔE - E correlation between the ΔE released in Si2 and the residual energy E deposited in the CsI. However, the ΔE released in Si2 by high-energy light charged particles ($Z \sim 1, 2$) can be so small that the signal amplitude becomes comparable with the electronic noise, making it impossible to apply the ΔE - E method. In this case the PSA is a useful technique to isotopically identify the different light ions stopped in the CsI.

The intensity as a function of time of the scintillation light in a CsI(Tl) depends

on the (Z, A) and energy of the detected particle [106]. It can be described as the sum of two exponential contributions [107]:

$$I(t) = I_{fast} \cdot \frac{e^{-t/\tau_{fast}}}{\tau_{fast}} + I_{slow} \cdot \frac{e^{-t/\tau_{slow}}}{\tau_{slow}} \quad (2.4)$$

where the two time constants are estimated as $\tau_{fast} \sim 700$ ns and $\tau_{slow} \sim 5$ μ s respectively. It has been observed that the ratio between the intensity of the fast component I_{fast} and that of the slow component I_{slow} depends on (Z, A) and energy of the impinging fragment⁹. This is especially true for light particles [107] (up to $Z \sim 4$), while the ratio tends to become constant for heavier fragments. However, in the case of FAZIA, the CsI PSA method is applied where it can give the best results, namely for the identification of high-energy light particles, for which the Si2-CsI ΔE -E identification fails¹⁰.

A customary way of applying the PSA consists in processing the CsI charge signal with two different shapers in parallel. A shaper is set to a time constant close to the τ_{fast} value, and a shaper is set to a time constant of the same order as τ_{slow} . The amplitude of the former will mostly depend on the I_{fast} value, while the latter will be sensitive to the total emitted light. In the case of FAZIA, these shapers are $Q3_{fast}$ and $Q3_{slow}$ described in Sec. 2.1.3. It has to be noted that the slow component $Q3_{slow}$ also includes the fast one $Q3_{fast}$. This is why, in many previous works of the FAZIA collaboration, $Q3_{fast}$ is reported as a function of $Q3_{slow}$ minus a fraction of $Q3_{fast}$, as in the example in Fig. 2.14a, in order to disentangle the two contributions and to better separate the isotopes. However, a slightly different version has been recently proposed [108], namely the plot of the ratio $Q3_{fast}/Q3_{slow}$ as a function of the $Q3_{slow}$ component. An example of such a correlation plot is shown in Fig. 2.14b; it has been verified that this kind of correlation allows for a better visual separation of the isotopes, which helps the user in the particle identification procedure, that will be described in Sec. 3.2.

⁹Actually, even the fast time constant τ_{fast} depends on the same properties of the impinging fragment, increasing with decreasing ionisation density (i.e. for lighter fragments) for a given energy (see Fig. 6 of Ref. [107]). The typical values range from 0.5 μ s to 1 μ s. As pointed out in Ref. [107], both the variations of τ_{fast} and of the ratio between the intensities of the two components with the characteristics of the detected fragment play a role in the identification process.

¹⁰The PSA of CsI signals is also useful when the silicon detectors in front of the CsI are missing or not working. Unfortunately, only fragments up to $Z \sim 4$ can be identified with this technique.

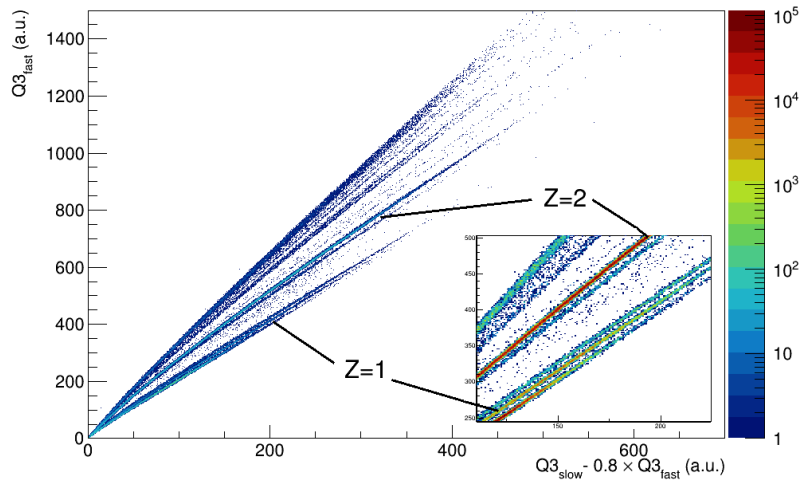
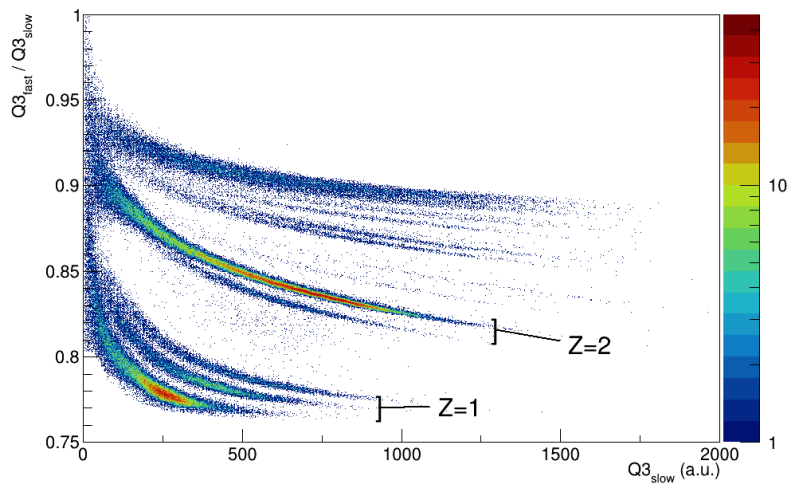
(a) *Fast vs. slow correlation.*(b) *Fast/slow vs. slow correlation.*

Figure 2.14: Two different approaches to PSA in FAZIA CsI. Both matrices are produced with the data of the E789 experiment. The events corresponding to neutrons or gamma detected by the CsI have been excluded by means of a graphical cut: an example of such cut can be seen in Fig. 3.8 in Chapter 3.

The E789 experiment

The E789 experiment, the first experimental campaign to exploit the coupled INDRA-FAZIA apparatus, was carried out at GANIL from April to May 2019 (see Tab. 3.1), after being approved by the GANIL Program Advisory Committee in 2018. The studied reactions are $^{58,64}\text{Ni}+^{58,64}\text{Ni}$ at 32 and 52 AMeV.

The scientific goal of the E789 campaign will be presented in the following section. This chapter includes a description of the particle identification and energy calibration procedures, i.e. all the preliminary operations performed on the raw data in order to reconstruct the events. The general features of the acquired data will also be described, together with a first selection of the events that will be considered in the present analysis.

3.1 Scientific goal and experimental setup

The excellent nuclear fragment identification capability and good angular coverage of the INDRA-FAZIA apparatus are optimal characteristics for the study of isospin transport phenomena. In fact, they allow for the construction of isospin related observables such as those presented in Sec. 1.1.2, so that the properties of nuclear matter and of its equation of state, like the density dependence of the symmetry energy (see eq. (1.5) and eq. (1.6)), can be studied.

In the E789 experiment, all of the four possible combinations of the two reaction partners ^{58}Ni and ^{64}Ni have been exploited. By doing so, we have the opportunity to compare the properties of the products of the two asymmetric reactions ($^{58}\text{Ni}+^{64}\text{Ni}$ and $^{64}\text{Ni}+^{58}\text{Ni}$), with those of both the neutron rich ($^{64}\text{Ni}+^{64}\text{Ni}$) and the neutron deficient ($^{58}\text{Ni}+^{58}\text{Ni}$) symmetric systems. This comparison enables to gather information on the two different contributions to the isospin transport between the reaction partners, i.e. the isospin drift and diffusion (see Sec. 1.2.1). Moreover, all the four reactions have been measured for two different incident energies, hence modifying the timescale of the interaction process and (slightly) the inspected nuclear density range. The nickel beams have been selected in order to fully exploit the isotopic identification capability of FAZIA (up to $Z \sim 25$ from ΔE -E, $Z \sim 20$ from PSA) [109]. In addition, the availability of INDRA data on the system $^{58}\text{Ni}+^{58}\text{Ni}$ at 52 AMeV from the 2nd experimental campaign [18, 42] has been helpful to estimate

Table 3.1: Data taking periods (April to May 2019) and collected statistics for all the reactions studied in the E789 experiment.

Reaction	Energy	Data taking period	Collected Statistics
$^{58}\text{Ni}+^{58}\text{Ni}$	52 AMeV	April, 19-21	32×10^6 events
$^{58}\text{Ni}+^{64}\text{Ni}$	52 AMeV	April, 21-22	30×10^6 events
$^{58}\text{Ni}+^{58}\text{Ni}$	32 AMeV	May, 8-9	27×10^6 events
$^{58}\text{Ni}+^{64}\text{Ni}$	32 AMeV	May, 9-10	31×10^6 events
$^{64}\text{Ni}+^{64}\text{Ni}$	52 AMeV	May, 21-22 and 24-25	28×10^6 events
$^{64}\text{Ni}+^{58}\text{Ni}$	52 AMeV	May, 22-24	27×10^6 events
$^{64}\text{Ni}+^{64}\text{Ni}$	32 AMeV	May, 26-28	32×10^6 events
$^{64}\text{Ni}+^{58}\text{Ni}$	32 AMeV	May, 28-30	33×10^6 events

Table 3.2: Characteristics of the reactions measured in the E789 experiment. For each system the grazing impact parameter b_{gr} and angle in the laboratory reference frame θ_{gr}^{lab} , the velocity of the CM $v_{\text{CM}}^{\text{lab}}$ and projectile $v_{\text{beam}}^{\text{lab}}$ in the laboratory reference frame, and the projectile velocity in the CM reference frame $v_{\text{beam}}^{\text{CM}}$ are listed. As reference, $v_{\text{beam}}^{\text{lab}}/c \sim 0.3$.

Energy	Projectile	Target	b_{gr} (fm)	θ_{gr}^{lab} (deg)	$v_{\text{CM}}^{\text{lab}}$ (mm/ns)	$v_{\text{beam}}^{\text{lab}}$ (mm/ns)	$v_{\text{beam}}^{\text{CM}}$ (mm/ns)
32 AMeV	^{58}Ni	^{58}Ni	10.6	3.3	39.3	78.6	39.3
		^{64}Ni	10.8	3.2	37.4	78.6	41.2
	^{64}Ni	^{58}Ni	10.8	2.9	41.2	78.6	37.4
		^{64}Ni	11.1	2.9	39.3	78.6	39.3
52 AMeV	^{58}Ni	^{58}Ni	10.9	2.0	50.1	100.2	50.1
		^{64}Ni	11.1	1.9	47.6	100.2	52.6
	^{64}Ni	^{58}Ni	11.1	1.8	52.6	100.2	47.6
		^{64}Ni	11.3	1.7	50.1	100.2	50.1

the expected performances of INDRA-FAZIA on the basis of real experimental data. A summary of the systems studied in the E789 experiment is reported in Tab. 3.2. A total of about $30 \cdot 10^6$ events has been acquired for each measured reaction: the collected statistics for each system is reported in Tab. 3.1.

The INDRA-FAZIA apparatus, already described in the previous chapter, has been mounted in a scattering chamber placed in the D5 experimental hall in GANIL. The vacuum inside the scattering chamber remained stable at $\sim 10^{-6}$ mbar during the whole experiment. Two different targets of ^{58}Ni and ^{64}Ni , $300 \mu\text{g}/\text{cm}^2$ and $400 \mu\text{g}/\text{cm}^2$ thick respectively, were mounted on a target holder inserted between rings 12 and 13 of INDRA. The trigger condition for FAZIA was multiplicity $M \geq 1$, as for INDRA. In order to generate a global trigger, INDRA needed FAZIA in coincidence, while FAZIA could be also acquired alone if INDRA was not in veto. The events with a total INDRA+FAZIA multiplicity equal to 1 were acquired with

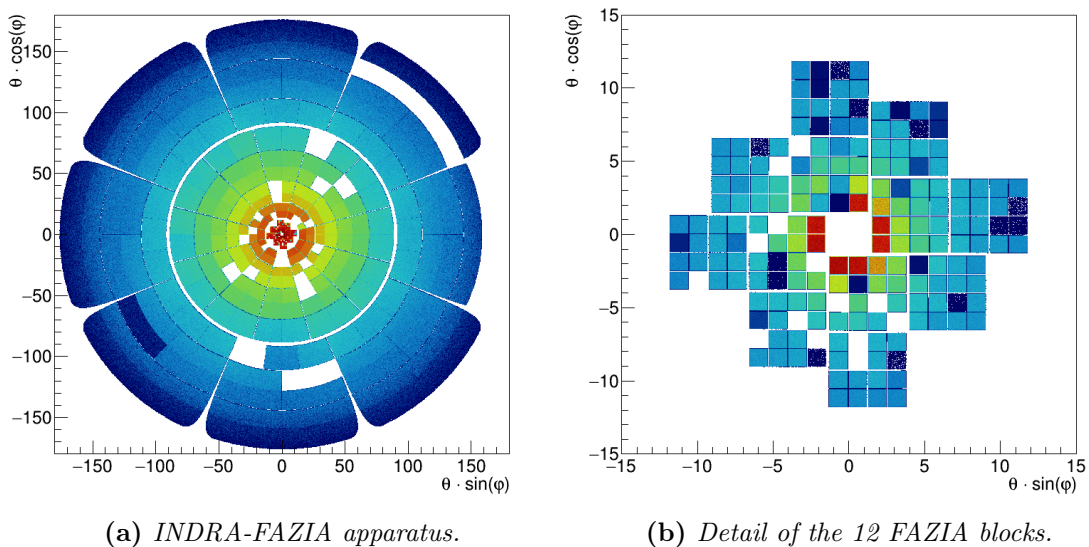


Figure 3.1: Polar plots representing the geometrical coverage of the experimental apparatus in the laboratory reference frame, obtained by reporting the polar coordinates $(\theta \sin \varphi, \theta \cos \varphi)$ of all the experimentally detected particles for the system $^{58}\text{Ni}+^{58}\text{Ni}$ at 52 AMeV. The plot in panel (b) is an enlarged section of the center of the plot in panel (a), showing only the 12 FAZIA blocks. The missing (white) modules were not functioning during the data taking.

a 100 downscale factor. All the data acquired during the E789 campaign have been stored at the IN2P3 Computing Centre in Lyon [111], where all the data reduction has been performed. The particle identification and energy calibration procedures have been carried out using an already available collection of C++ libraries based on the ROOT framework [112], the KaliVeda software [113]. KaliVeda has been originally developed at GANIL as a simulation and analysis toolkit for the INDRA apparatus, and later extended in order to implement some additional features to better handle the FAZIA setup. It allows to perform both data reduction and physics analysis on large datasets of multi-particle events. It includes other useful general tools like stopping power, range and energy loss calculations for ions with $E/A = 1 - 100$ MeV (exploiting the C++ implementation of the VedaLoss package [114], based on the energy loss tables compiled by Hubert et al. [115]). The package includes an interface to the GEMINI++ statistical decay code (see Sec. 4.2).

The geometrical coverage of the experimental apparatus is shown in the polar plot¹ in Fig. 3.1: panel (a) includes both INDRA and FAZIA, while panel (b) shows an enlarged central section of the plot corresponding to the 12 FAZIA blocks. The polar plots of Fig. 3.1 include all the detected particles for the reaction $^{58}\text{Ni}+^{58}\text{Ni}$

¹An emission angle (θ, φ) randomly distributed over the surface of the detecting module is assigned to each detected fragment.

at 52 AMeV. Since these are experimental data, some empty areas can be noticed, corresponding to not working modules. Even in case of a working module, its condition can change during the relatively long measuring time for the experiment, e.g. due to the radiation damage on the detectors, particularly those at low polar angles. A study of the radiation damage suffered by the silicon detectors of the FAZIA apparatus after the E789 campaign can be found in Ref. [110]. The working status of each detector, and therefore the operability of each module of the whole apparatus, is taken into account and updated for each measured reaction in order to implement the software filter described in Sec. 4.3. This filter is then applied to the simulated events (see Chapter 4) in order to directly compare them to the experimental data. Such a comparison is a key passage in order to extract information on the symmetry energy term.

3.2 Particle identification procedure

One of the steps of the data reduction is the identification of the detected particles in each event. In particular, the information on the mass of the fragments is mandatory in order to build isospin related observables. In the present work, both the ΔE - E method and the PSA in Si and in CsI(Tl) detectors, described in detail in Sec. 2.4, have been exploited for this purpose since their information is often complementary. Although the identification techniques are based on different physical processes and different correlations, a similar identification procedure, explained in the following, is applied to all of them. The procedure exploits some of the tools provided by the KaliVeda software.

As a general example, we present the application of the identification procedure on a FAZIA Si1 PSA correlation matrix (deposited energy vs I_{max}). In Fig. 3.2 the Energy vs I_{max} (i.e. $QH1$ vs $I1$, in arbitrary units) correlation plot obtained with the detector Si1-643² is shown. First of all, due to the relatively long measuring time, the stability of the detector response throughout the whole experiment must be verified. In fact, a variation on the detector behaviour causes a shift on the identification matrices relative to that module. If the variation is not a continuous drift, but two (or more) functioning regimes can be identified for the unstable detectors, then separate identification (and calibration) procedures can be applied in different run subsets. After the stability check, the first step of the procedure requires the manual drawing of the “identification grid”, consisting of several lines placed along the correlation ridges, plotted in black in Fig. 3.2. A graphical tool is used to “click” an adequate number of points on each ridge, in order to obtain

²In the following the telescope identification code will often be used. For the sake of clarity, we specify that for the FAZIA array this code is obtained as $100 \times n_{block} + 10 \times n_{quartet} + n_{telescope}$, so that Si1-643 means that we consider the Si1 of the 3rd telescope of the 4th quartet in the 6th block. In INDRA, the same code is defined as $100 \times n_{ring} + n_{module}$. The information on the detecting module is stored for each particle. There can be duplicate codes (i.e. the same code could refer either to a FAZIA or to an INDRA module). However, this does not cause ambiguities, since also the information on the detecting array is saved.

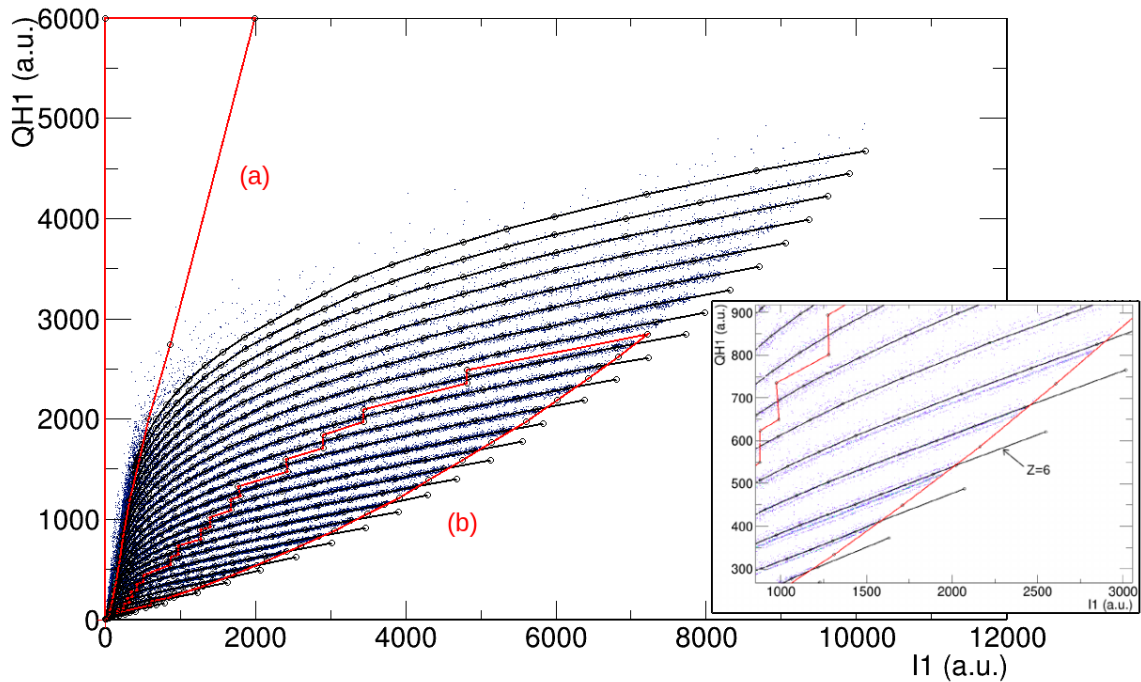


Figure 3.2: Deposited energy vs I_{max} correlation obtained with FAZIA Si1-643. The identification grid is plotted in black; a single line has been drawn for each element, generally following the ridge corresponding to the isotope at the center of each isotopic distribution, in order to achieve the best identification performance. The two red graphical cuts indicate the areas where (a) no element can be identified (b) the fragments can be identified both in Z and A . The inset shows a detail of the same correlation matrix in the region with $Z \sim 6, 7, 8$.

a segmented line that follows it as accurately as possible. Only one line has been drawn for each element, even when isotopic ridges can be recognised: to each line, a so-called *PID value* (from Particle IDentification) equal to the atomic number Z of the underlying experimental curve is assigned. The adopted choice significantly reduces the time needed to produce the identification grids for all the modules with respect to drawing a line for each isotopic ridge, still yielding good identification. In the inset of Fig. 3.2 an enlarged section of the same PSA correlation in the region around $Z \sim 6, 7, 8$ is shown, in order to evidence that each drawn line tracks the ridge corresponding to the isotope in the center of the isotopic distribution of each element, a choice which gives in fact the best performance. In Fig. 3.2 two graphical cuts are also visible (plotted in red). They delimit the areas where:

- (a) the resolution is not good enough to allow element identification, because their range in silicon is too small.
- (b) the fragments can be identified both in charge and mass number (Z and A).

Events falling in the region of type (a) must be excluded from the analysis, since

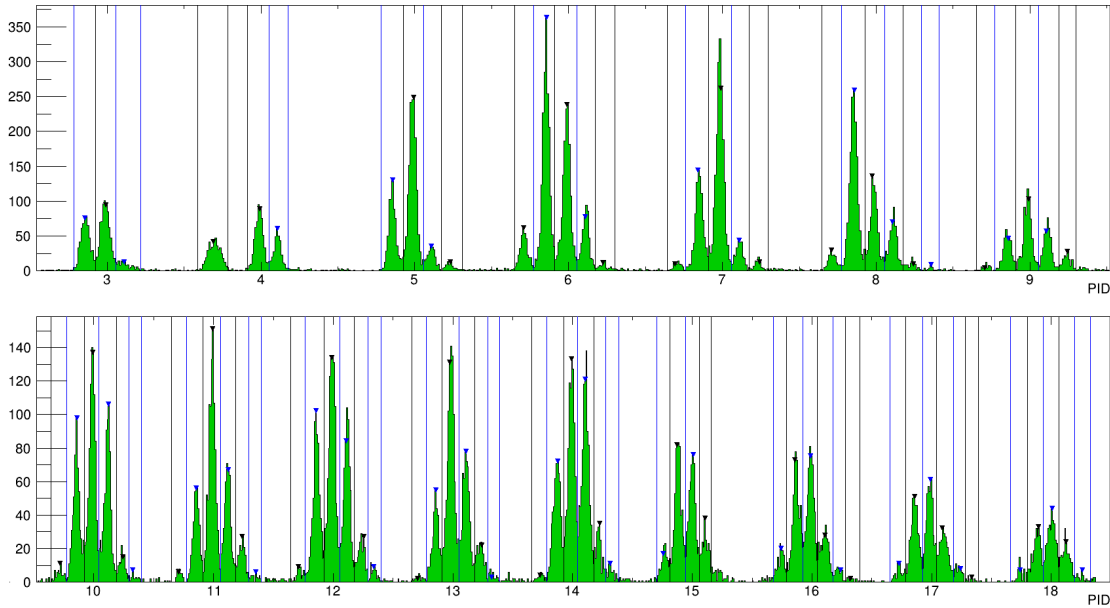


Figure 3.3: PID distribution obtained with FAZIA Si1-643 current PSA identification procedure. All the particles falling inside the graphical cut (b) of Fig. 3.2 have been included in this distribution. The mass intervals for each element are also indicated by means of vertical lines. In this example, a good isotopic discrimination has been achieved up to $Z = 18$.

they contribute to the background, thus spoiling the identification performance. A linearisation procedure is then applied to all the events unaffected by the exclusive cut (a). Basing on the position of the event on the correlation matrix, KaliVeda assigns a PID value to each fragment by interpolating between the PID values of the four closest Z -lines. As an example, in Fig. 3.3 the PID distribution including all the events inside the graphical cut (b) of Fig. 3.2 is shown. Several different groups of peaks can be readily recognised, corresponding to different elements. The single peaks within the groups correspond to different isotopes. At this point, the PID value of each fragment must be translated into a charge and mass number in order to complete the procedure. This is done by defining a PID interval for each peak, to which the “correct”³ (Z, A) is assigned: as an example, in Fig. 3.4 the PID histogram

³The assignment of the correct atomic number is a trivial task, and some characteristic isotopic distributions (e.g. for $Z = 4$, the missing peak corresponding to ${}^8\text{Be}$, whose short lifetime is not long enough to let it reach the detectors) help with it. The correct choice for the mass number is not as obvious, especially for the heavier elements, since the relative abundances of the various isotopes can change for different reactions. Therefore, at first, the user defines the sets of mass numbers basing on their experience and logic, maintaining the coherency among the modules placed at the same polar angle. Then, a check on the assigned masses is mandatory. This can be done both by populating the nuclide chart (see e.g. Fig. 3.5, where a shift on the N of the lighter fragments would be visible) and by checking the energy calibration, as will be explained in the next section. Moreover, in a late stage of the analysis, the behaviour of the isospin related observables is also verified.

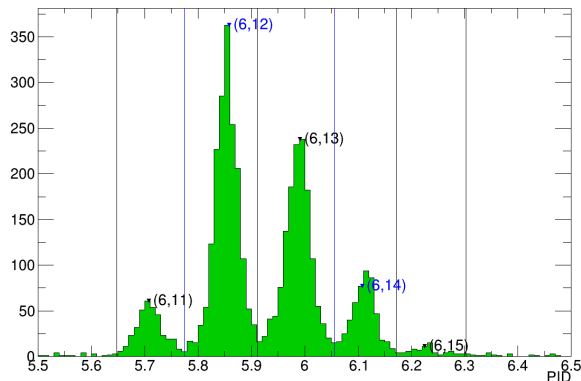


Figure 3.4: Detail of the PID distribution in the $Z = 6$ region, with the mass intervals corresponding to the detected carbon isotopes delimited by vertical lines. The (Z, A) values assigned to the defined intervals are also indicated.

around the carbon region $Z = 6$ is shown, together with the defined mass intervals (represented by the vertical lines) and the assigned mass numbers. The complete set of mass intervals defined for the Si1-643 current PSA identification is visible in Fig. 3.3. If the PID value assigned to a fragment falls inside a mass interval, the corresponding (Z, A) pair is attributed to it. Otherwise, the particle is identified with the charge and mass numbers of the mass interval closest to its PID value. A quality factor (IDQuality) is also assigned to the fragment, depending on whether its PID value fits into the mass interval. A list of the possible IDQuality factors is reported in Tab. 3.3. In this work, the result of the identification procedure is considered to be good when $\text{IDQuality} \leq 3$.

The result of the complete identification procedure can be viewed in Fig. 3.5, that shows the experimental (N, Z) nuclide chart including all the particles in the cut (b) of the Si1 current PSA matrix of Fig. 3.2: mass discrimination is achieved up to $Z = 18$, with an energy threshold ranging from around $3A\text{MeV}$ to $15A\text{MeV}$, depending on the Z of the fragment. The atomic number is identified for all the detected nuclear species (outside cut (a)), with an energy threshold lower than $5A\text{MeV}$. An evaluation of the energy thresholds for identification can be found in Sec. 3.3.1.

An identical procedure is applied to the ΔE - E identification in Si1-Si2 and Si2-CsI in FAZIA, and Si-CsI in INDRA. In Fig. 3.6 and Fig. 3.7, two examples of fragment identification obtained with FAZIA telescope 111 in the E789 experimental campaign can be seen. In Fig. 3.6a the low Z region of the Si1-Si2 ΔE - E correlation is shown, with the identification grid superimposed. The ridges associated to different isotopes are clearly resolved: in this case the mass discrimination is obtained over the whole correlation. The corresponding nuclide chart is reported in Fig. 3.6b: isotopes are correctly identified up to $Z = 25$. The Si1-Si2 ΔE - E identification gives in fact the best performance in terms of mass identification. Fig. 3.7a is the low Z region of the Si2-CsI ΔE - E matrix of the same telescope. A graphical cut (in red in Fig. 3.7a) has been drawn to remove the region close to the x axis, where there is a

Table 3.3: List of the possible IDQuality factors that can be assigned to a fragment. The fragments whose IDQuality codes are reported in red are rejected as “bad identified”. The IDQuality codes 1, 2, 3 are assigned when the upper limit of the mass interval of a given isotope and the lower limit of the mass interval of the adjacent heavier isotope do not coincide, and the PID value associated to the fragment falls within the gap between these two defined mass intervals.

IDQuality	Code meaning
0	PID inside a mass interval: perfect identification
1	PID between two mass intervals with same Z: lower A value assigned
2	PID between two mass intervals with same Z: higher A value assigned
3	PID between two mass intervals with same Z: A could be larger or smaller
4-5	Point between two lines with different Z
6	Point below the first line of the grid
7	Point above the last line of the grid
8	Point out of range

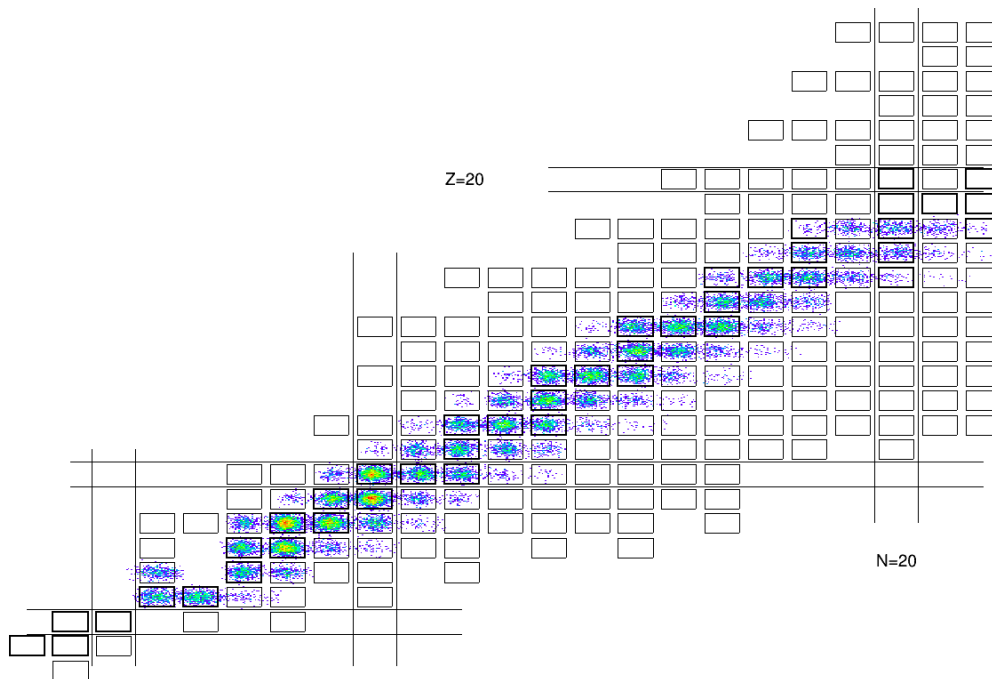


Figure 3.5: Experimental (N, Z) nuclide chart obtained with FAZIA Si1-643 current PSA identification procedure, including all the particles falling inside the graphical cut (b) of Fig. 3.2.

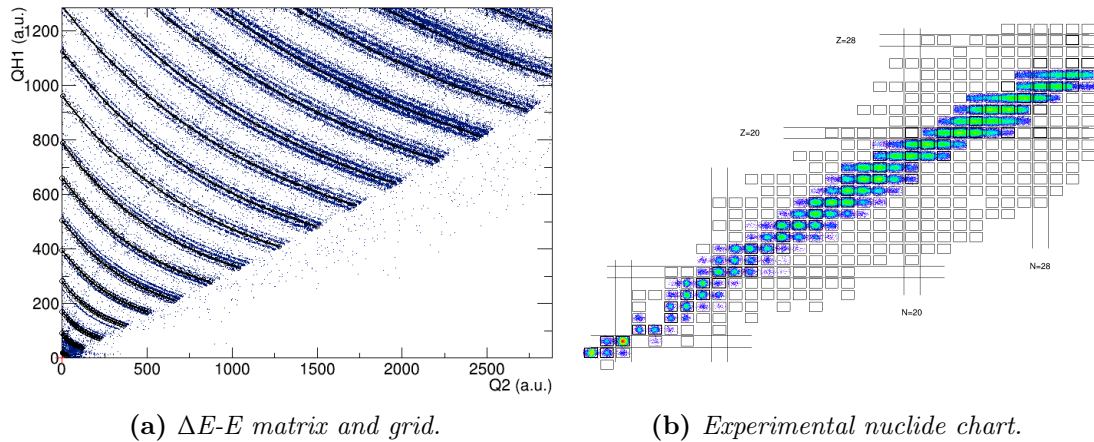


Figure 3.6: Si1-Si2 ΔE - E identification with FAZIA telescope 111. In this example isotopes up to $Z = 25$ can be recognised: the Si1-Si2 ΔE - E identification is in fact the one that gives the best results in terms of mass discrimination.

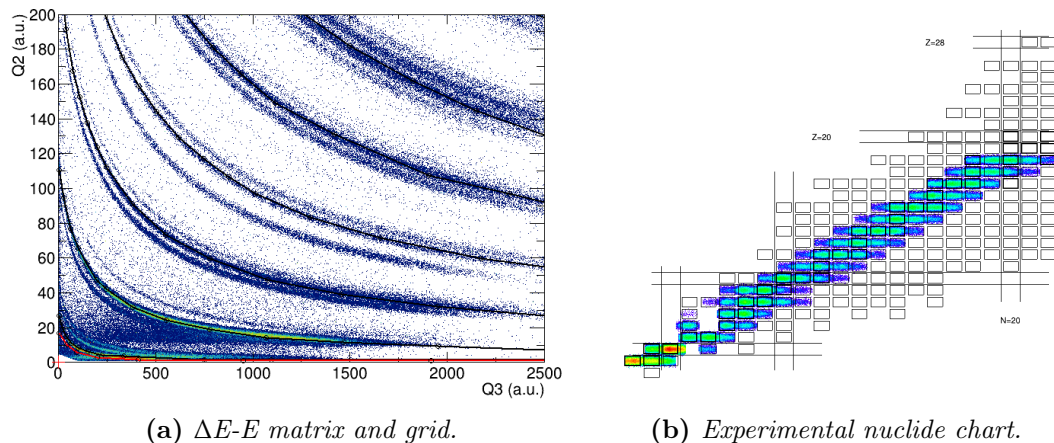


Figure 3.7: Si2-CsI ΔE - E identification with FAZIA telescope 111. In this example isotopes up to $Z = 18$ can be discriminated. All the events inside the red graphical cut have been removed from the analysis.

substantial amount of energy released in the CsI but the amplitude of the Si2 signal is compatible with the noise level; most of these events correspond to neutrons or gamma rays, whose probability to interact with the silicon detectors is quite small. The corresponding nuclear chart is presented in Fig. 3.7b: isotopes up to $Z = 18$ have been identified.

For the CsI PSA correlation matrices⁴, a different line for each isotope has been drawn, and a PI value with the information on both A and Z has been assigned.

⁴Two different approaches to CsI PSA identification have been used for FAZIA and INDRA CsI. In fact, for FAZIA the *fast/slow* vs *slow* correlation matrices have been used, while for INDRA the *fast* vs *slow* ones (see Sec. 2.4.3). The identification procedure is the same in both cases.

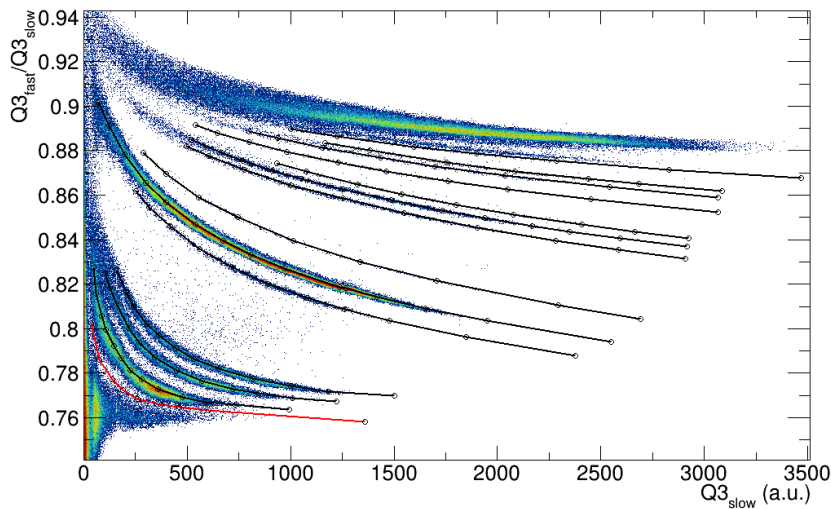


Figure 3.8: CsI PSA *fast/slow* vs *slow* correlation matrix obtained with FAZIA CsI-131. The identification grid is superimposed: in this case, a line has been drawn for each isotope. The events under the graphical cut (shown in red), corresponding to spurious signals, are excluded. Elements up to $Z = 4$ can be isotopically identified.

This approach has demonstrated to give the best results for the lighter ions, up to $Z = 4$. An example of such an identification grid can be seen in Fig. 3.8, where the correlation matrix for FAZIA CsI-131 is shown. A graphical cut is used to exclude all the events corresponding to particles that do not deposit their whole energy in the detector [108]. The particle identification procedure is then the same as previously described.

For a given identification method, since the various telescopes have slightly different responses, a different grid must be drawn for each of them. This work must be performed for each identification technique. Four different identification techniques have been exploited for each one of the 192 FAZIA telescopes (ΔE -E Si1-Si2 and Si2-CsI, Si1-PSA and CsI-PSA). Two methods (ΔE -E Si-CsI and CsI-PSA) have been used for the fragments stopped in the first four rings of INDRA (rings 6 to 9), including 96 modules, while on the remaining 8 INDRA rings, for a total of 144 modules, only the CsI-PSA technique has been applied. Therefore, more than one thousand identification grids had to be drawn. A few shifts in the correlations due to slight variations in detector response during the measurement have also been taken into account. Given the large number of identification grids that must be manually drawn, this time consuming task has been shared among a few members of the INDRA-FAZIA collaboration.

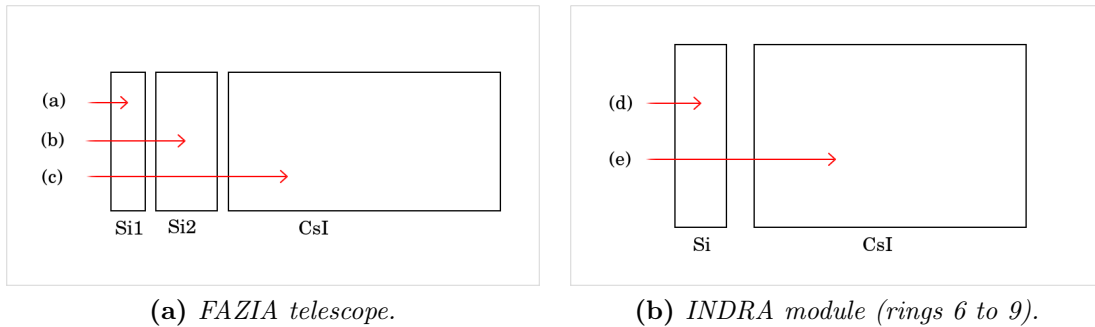


Figure 3.9: Possible stopping layer options in different detecting telescopes of the INDRA-FAZIA apparatus. For each option a different set of identification techniques is applied.

3.2.1 Choice of the identification method

The information collected by the telescopes of the INDRA-FAZIA apparatus offers the opportunity to exploit multiple ion identification techniques for the detected fragments. Depending on which detection layer the particle stops in, the most proper identification method is chosen.

In Fig. 3.9 the possible stopping layer options for the different kinds of telescope in the INDRA-FAZIA apparatus are shown. For a FAZIA telescope there are three possibilities, shown in Fig. 3.9a. The ion can be stopped:

- (a) in the first stage, Si1: only the identification via current PSA on Si1 can be applied. Isotopic discrimination is achieved up to $Z \sim 16 - 18$. See below (Fig. 3.12) for the energy threshold for identification.
- (b) in the second stage, Si2: when a particle punches through Si1 and stops in Si2, the Si1-Si2 ΔE -E method can be used. Thanks to the high resolution of the two silicon detectors of FAZIA, this technique gives the best results in terms of mass resolution, allowing for a good isotopic discrimination up to $Z \sim 25 - 27$.
- (c) in the third stage, CsI: in this case two identification techniques can be applied, namely the ΔE -E technique on Si2-CsI and the PSA applied to the CsI signal. For IMFs and heavier fragments (and also for low energy LCPs) the Si2-CsI technique allows for a good isotopic discrimination up to $Z \sim 20$. However, the most energetic LCPs leave only a small fraction of their energy in the Si2, so that the produced amplitudes are comparable with the noise level. In these cases the CsI-PSA technique comes in handy, since it works quite well for the isotopic identification up to $Z \sim 4$.

For the particles detected by the first four rings (6 to 9) of INDRA there are two options open, shown in Fig. 3.9b. The fragments can be stopped within:

- (d) the Si of the first stage: unlike FAZIA, the FEE of INDRA does not allow for the application of the PSA technique on silicon detectors. Therefore, the

particles stopped in the first detection layer cannot be identified⁵.

- (e) the CsI of the second stage: as for the particles stopped in the CsI in FAZIA, in this case two identification methods are available, the Si-CsI ΔE -E technique and the CsI-PSA. Isotopic identification via the ΔE -E technique in rings 6 and 7 is hindered by the small thickness of the Si detector (150 μm). In these rings, isotopic identification is obtained only for $Z \sim 4$, via PSA applied to CsI. Rings 8 and 9, on the other hand, exploit 300 μm thick Si detectors: in these rings isotopic identification is obtained up to $Z \sim 7$ via the ΔE -E technique, complemented with PSA applied to CsI.

When a particle is collected by an INDRA module belonging to a ring from 10 to 17, only one detection stage, a CsI(Tl), is available, and therefore only the CsI-PSA method, suitable for the identification of light ions up to $Z \sim 4$, can be exploited. However, since rings 10 to 17 detect mostly LCPs, this does not substantially affect the present work.

The identification procedure in KaliVeda starts by trying out all the identification techniques available considering the detectors that have been crossed by the particle, starting from the stopping detector. For example, for a particle stopped in a CsI of a FAZIA telescope, first the CsI-PSA and the Si2-CsI ΔE -E method are tried, then, in order, the Si1-Si2 ΔE -E and the Si1-PSA. The first successful method gives the identification, but for a particle stopped in a CsI, priority is given to the Si2-CsI method over the CsI-PSA. However, all the identification results of the different methods applied are stored for coherency checks. As an example, for the events in which a particle stopped in FAZIA Si2, but an unrelated signal is produced by the CsI of the same telescope⁶, a useful identification coherency check has been implemented. In fact, in this case, the particle is considered to be stopped in the CsI, and if the identification in Si2-CsI is wrongly marked as successful, wrong Z and energy are attributed to the reconstructed particle. However, if a particle really punched through the Si2 and stopped in the CsI, the identification via the Si1-Si2 method would give a smaller Z than the Si2-CsI method. Therefore, if the opposite situation is found, with the Z resulting from the Si1-Si2 higher than that resulting from the Si2-CsI, the CsI signal is discarded and the Si1-Si2 identification is kept.

At the end of the identification procedure, an IDCode related to which technique has been applied is assigned to each identified fragment and stored. The list of all the possible IDCodes for the particles collected in FAZIA and in INDRA is reported in Tab. 3.4.

⁵In its more common configuration, INDRA features ionisation chambers as first stage, so that the silicon layer would be the second one: in this case, the ΔE -E technique could be exploited for the identification of the ions stopped in the Si layer. However, the ionisation chambers have not been used in the E789 experiment.

⁶The unrelated CsI signal may be due to a casual coincidence with a gamma ray or neutron (which in this case cannot be eliminated with the graphical cut on the Si2-CsI ΔE -E correlation), or to noise.

Table 3.4: List of the possible IDCodes that can be assigned to a fragment depending on the identification method that has been exploited.

FAZIA IDCode	Identification method		INDRA IDCode	Identification method
11	Si1-PSA identification		0-1	gamma/neutrons
12	Si1-Si2 identification		2	CsI-PSA identification
23	Si2-CsI identification		3	Si-CsI identification
33	CsI-PSA identification		5-15	bad identification or incoherency

3.3 Energy calibration

In order to properly reconstruct the collision dynamics, an estimate of the energy of the detected particles is needed. The results of the identification procedure can be exploited in order to perform the energy calibration of the different detectors⁷. The energy calibration can in turn be used to check whether the mass numbers assigned to the identified isotopes are correct.

3.3.1 Calibration of FAZIA detectors

The calibration of each FAZIA telescope is a three step procedure starting from the calibration of the first detection layer (Si1) down to the last stage (CsI). The adopted method is different for silicon and CsI detectors, and the calibration of the latter depends on that of the Si2 layers.

Silicon detectors The calibration of Si detectors relies on the evaluation of the *punch-through energy* of multiple ions, i.e. the energy for which the range of the fragment in the detector is equal to its thickness. In principle, both the punch-through energies in Si1 and in Si2 can be exploited. These two cases correspond to, respectively:

- the maximum energy of a fragment stopped in Si1. These events are located at the right end of the ridges of a Si1-PSA correlation matrix⁸, as evidenced by the red dots in Fig. 3.10a. These punch-through points only allow for the calibration of the Si1 detector.
- the maximum energy of a fragment stopped in Si2. These fragments are identifiable in the $(E_{res}, \Delta E)$ points at the rightmost end of the correlation ridges

⁷The identification procedure is performed independently of the energy calibration, since it is based on correlation matrices whose variables are expressed in ADC units.

⁸The punch-through points in Si1 can be identified also at the left end of the correlation ridges in a Si1-Si2 ΔE -E matrix, in correspondence of the y -axis, i.e. $E_{res} \sim 0$. However, they are easier to spot in a Si1-PSA matrix, and this second solution has not been used.

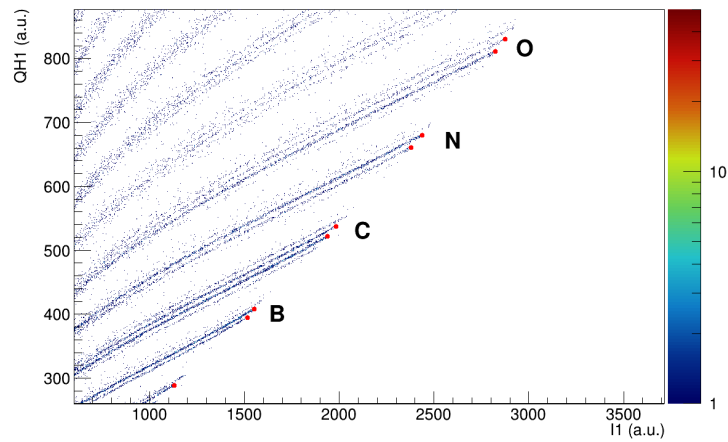
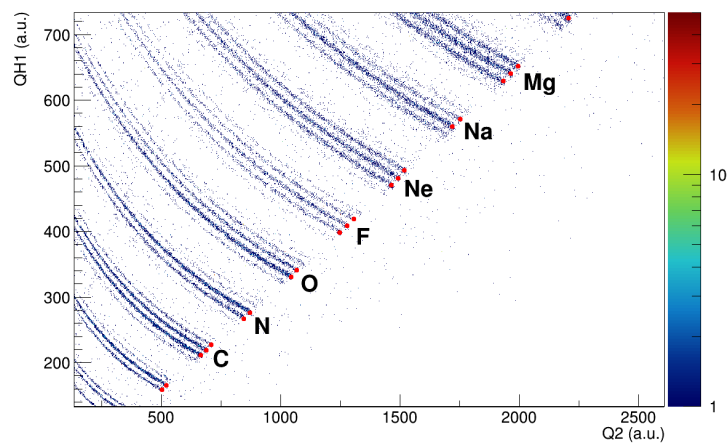
(a) *Punch-through points in Si1-PSA.*(b) *Punch-through points in Si1-Si2.*

Figure 3.10: Punch-through points (red dots) in Si1-PSA and Si1-Si2 ΔE -E correlation plots for a FAZIA telescope. A graphic tool has been used in order to “click” and store the coordinates of the punch-through points. After assigning the atomic and mass number to the different ridges, the punch-through points have been exploited for the energy calibrations and for evaluating the actual thickness of the two silicon detection layers.

in the Si1-Si2 ΔE -E matrix, as can be seen in Fig. 3.10b. If the detector thicknesses are known, these punch-through points allow for the calibration of both Si1 and Si2 detectors at the same time, because both the punch-through energy in Si2 and the associated ΔE loss in Si1 can be evaluated. Due to this fact, in many previous FAZIA experiments only the punch-through points in Si2 have been exploited for calibration purposes.

Since the (Z, A) of the fragments corresponding to each correlation ridge has been

already assigned, the punch-through energies can be calculated via software like the VedaLoss package [114] basing on energy loss tables, and then correlated to the punch-through points located on the correlation matrices. In this way, Energy vs ADC units correlations are obtained and used to fit a first order polynomial function⁹, whose parameters will be used to calibrate the detected fragments.

The actual thickness of the silicon detector is a key information in order to follow this procedure. In fact, 300 μm (Si1) and 500 μm (Si2) are just the nominal thickness of the first two stages; the actual thickness may differ by up to $\sim 10 \mu\text{m}$ from these values. Unfortunately, a precise mechanical measurement of the actual thickness is available only for a few of the 384 silicon detectors mounted in FAZIA. However, thanks to a few runs acquired with a triple alpha source before the E789 experiment, instead of just using the nominal thickness, the effective thickness has been evaluated, starting from that of the first detector, Si1. In fact, the Si1 can be calibrated by using either the runs acquired with the triple alpha source, or the punch-through points in Si1-PSA: this allows us to cross-check the two calibrations, also determining the Si1 thickness for which the calibration parameters obtained with the two methods are equal. If the obtained value falls in the acceptance interval (between 295 μm and 310 μm , basing on previous mechanical measurements and the average characteristics of the Si wafers declared by the manufacturer), it is assumed as the effective thickness of Si1, and the calibration parameters for Si1 are validated. In those few cases in which a previous measurement of the actual thickness was available, the evaluated and measured thicknesses generally agree within $\sim 1 \mu\text{m}$. If the obtained thickness value falls out of the acceptance interval (maybe due to some change in the detector response between the alpha runs and the beam runs) the detector is attributed the average thickness of the Si pads coming from the same wafer¹⁰.

An example of Energy vs ADC units calibration plot obtained with the Si1-PSA punch-through points (for an evaluated Si1 thickness of 308 μm) is shown in Fig. 3.11a. Since the resolution on the Si1-PSA matrix worsens for the heavier fragments, making it difficult to locate the punch-through points, only ions up to $Z \sim 16 - 18$ have been used for calibration in this work (up to $Z = 18$ in Fig. 3.11). As it can be seen in the bottom panel in Fig. 3.11a, the fit residues are all distributed around zero, the largest residue being $\sim 1 \text{ MeV}$ (while the points extend up to 700 MeV), showing no substantial systematic deviations. The residues are also useful to check the correctness of the mass numbers assigned to the isotopes in the identification phase. In Fig. 3.11b the same plots are shown for a different assumption on the mass number for two elements (a positive or negative shift by just one unit): the effects on the residues of the fit are dramatic, with the two shifted

⁹Silicon detectors are in fact expected to feature a linear response as a function of the energy deposited by the fragment. Moreover, the offset obtained through the fit is very close to zero, as expected due to the baseline subtraction performed by DSP before the trapezoidal shaping.

¹⁰If the information on the original Si wafer is not available, the average thickness of the Si1 mounted on the same block is assumed. In fact, most of the detectors assembled in the same block are part of the same production lot, and therefore they can be assumed to share many characteristics.

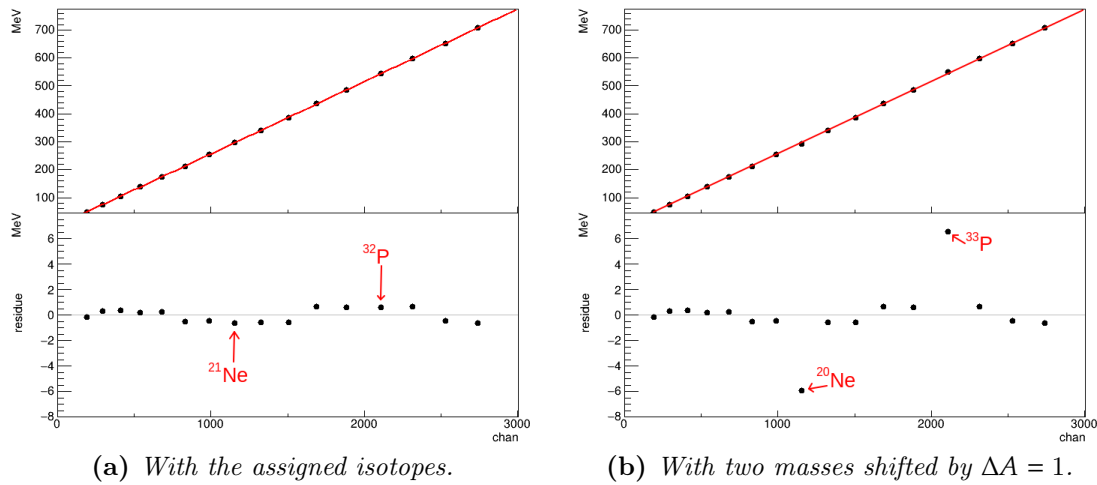


Figure 3.11: Energy vs ADC units calibration plots based on the Si1-PSA punch-through points for Si1-111. The linear fit result is superimposed and the fit residues are plotted in the bottom panel. The effect of a wrong mass assignment ($\Delta A = \pm 1$, in particular $^{21}\text{Ne} \rightarrow ^{20}\text{Ne}$ and $^{32}\text{P} \rightarrow ^{33}\text{P}$) is clearly visible on the residue plot on the right panel.

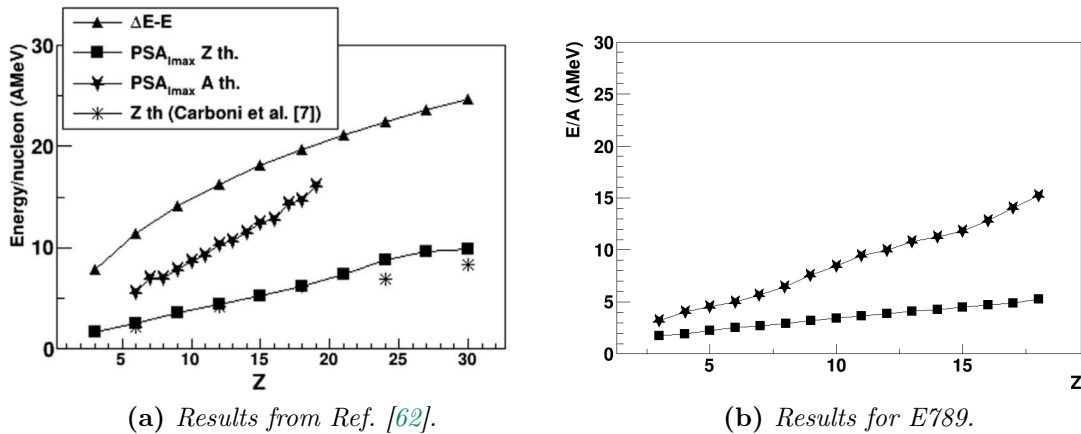


Figure 3.12: Energy thresholds for identification in Z e in (Z, A) via Si1-PSA with FAZIA. The performance obtained in the E789 experiment is compared to the results obtained during the FAZIA R&D phase [62]. The same legend is valid for both plots.

isotopes showing a strong deviation from zero.

The Si1-PSA is the identification technique featuring the lowest energy threshold among all the available methods for a FAZIA telescope. The energy thresholds for element and isotope identification obtained in the E789 experiment are plotted in Fig. 3.12b as a function of Z , while in Fig. 3.12a the same information as evaluated during the FAZIA R&D phase is shown; the results of the E789 experiment are comparable with those of Ref. [62], sometimes even better.

For the calibration of Si2 detectors, we use the punch-through points in the

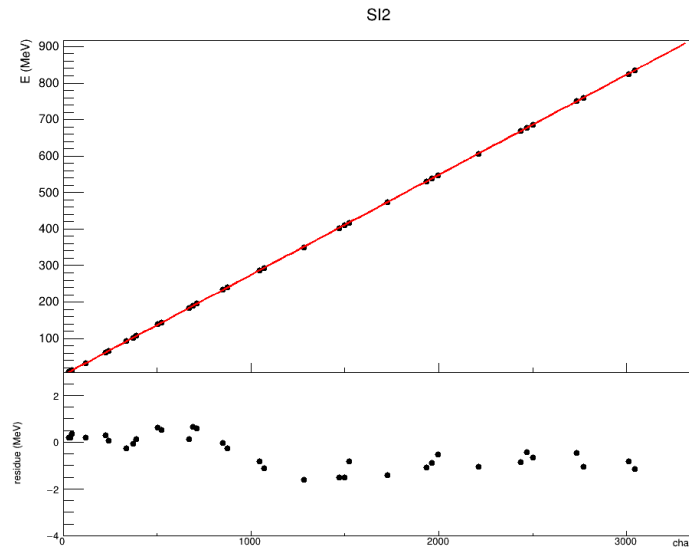


Figure 3.13: Energy vs ADC units calibration plots for Si2-111 obtained with Si1-Si2 punch-through points, with the fit result superimposed and the residues plotted in the bottom panel. This calibration plot has been obtained with the thicknesses extracted with the procedure described in the text (309 μm for Si1 and 510 μm for Si2).

Si1-Si2 ΔE -E correlations (see Fig. 3.10b): for each telescope a set of (E_{res} [a.u.], ΔE [a.u.]) values is extracted. For each impinging fragment with a given (Z, A), these values correspond to its punch-through energy in Si2 and the associated ΔE loss in Si1, respectively. Since for the Si2 thickness only a nominal value is available, the E_{res} [MeV] (hence the energy calibration) and thickness of the Si2 detector have been calculated as the residual energy and the range in silicon of a particle with a given (Z, A) which loses an energy ΔE [MeV] in Si1. Since the Si2 thickness thus obtained slightly depends on the (Z, A) of the considered fragment, we assume the value for which the Si2 calibration parameters obtained from the linear fit using the E_{res} [MeV] values calculated from the ΔE [MeV] in Si1 and those obtained exploiting the punch-through energies in Si2 are the same. An example of the calibration plot for Si2 obtained through the calculations of the punch-through energies in the extracted Si2 thickness, with the fit result superimposed, is shown in Fig. 3.13. The residues, plotted in the bottom panel of the figure, are close to zero, with a largest absolute value of ~ 2 MeV (over a range of almost 1 GeV). Therefore also the mass assignment for the ΔE -E identification is assumed to be correct.

The sensitivity of the energy calibration factors to a variation of the silicon detector thickness has also been evaluated: a variation of $\sim 1 - 2\%$ of the calibration parameters for Si1 and Si2 has been observed if the nominal thickness values instead of the calculated ones are assumed.

CsI detectors Once the energy calibrations of the two silicon stages are available and their thickness has been evaluated, the energy released in this last detection

layer (CsI) can be calculated from the ΔE in Si1 and Si2 basing on the energy loss tables. Therefore, for many ions, the energy calibration of the CsI is not required. However, for increasing energy of the impinging particle, the ΔE released in the silicon stages decreases, until the signal amplitude becomes comparable with the electronic noise, with a substantial worsening of the signal-to-noise ratio. This is especially true for high-energy light ions ($Z = 1, 2$) as can be seen in the Si2-CsI ΔE -E correlations (see, e.g., Fig. 3.7a). The uncertainty on the total energy evaluated from the ΔE and the energy loss tables correspondingly increases. Therefore, for light ions, an energy calibration of the CsI detector is mandatory in order to obtain a reliable reconstruction of the deposited energy.

For each FAZIA telescope, the ridges of the Si2-CsI ΔE -E correlations corresponding to the isotopes of H and He have been exploited to extract the CsI energy calibration points. Only the intervals in which the correlation ridges are narrow and well-defined have been considered: there, the estimate of the amount of energy deposited in the CsI calculated from the energy released in Si2 is still reliable. This value can be correlated to the scintillation light output of the CsI expressed in arbitrary units (LO), i.e. to the amplitude of the $Q3_{slow}$ signal. As an example, the energy calibration points obtained for FAZIA CsI-111 by exploiting hand-drawn lines on the Si2-CsI correlation ridges for $Z = 1, 2$ are shown in Fig. 3.14a for Hydrogen and in Fig. 3.14b for Helium isotopes.

The CsI light response is not linear with the deposited energy and depends on the (Z, A) of the detected ion [107, 116, 117]. Therefore, for their calibration, we used the following function relating the light output LO and the energy E_0 released in the CsI by a fragment (Z, A) :

$$LO = a_1 \left\{ E_0 \left[1 - a_2 \frac{AZ^2}{E_0} \ln \left(1 + \frac{E_0}{a_2 AZ^2} \right) \right] + a_4 a_2 AZ^2 \ln \left(\frac{E_0 + a_2 AZ^2}{Aa_3 + a_2 AZ^2} \right) \right\} \quad (3.1)$$

where the parameter a_1 depends on the electronic gain, while a_2 , a_3 , a_4 are characteristic of the CsI crystal. In particular, a_2 is the parameter used to take into account the *quenching* effect in the crystal [87], a_3 is the energy per nucleon threshold for δ -ray production, and a_4 is the fractional energy loss due to the δ -rays [117]. Equation (3.1) has been successfully used by the INDRA collaboration since many years and it is already implemented in KaliVeda [116, 117]. Only the calibration points corresponding to the isotopes for $Z = 1, 2$ have been taken into account in the fitting procedure, which fits simultaneously points for $Z = 1$ and points for $Z = 2$. In the two panels of Fig. 3.14 the results of the calibration fit are plotted in red for each (Z, A) .

The CsI energy calibration hereby described is used only for the evaluation of the energy deposited in the CsI by fragments with $Z = 1, 2$. For the heavier fragments, the reconstruction of the E_{res} in CsI from the ΔE in Si2 and energy loss tables is adopted.

Whenever a change in a ΔE -E correlation plot (both Si1-Si2 and Si2-CsI) has been observed, all the operations for the calibration of the detectors involved (except the evaluation of the Si thicknesses) have been performed independently in multiple

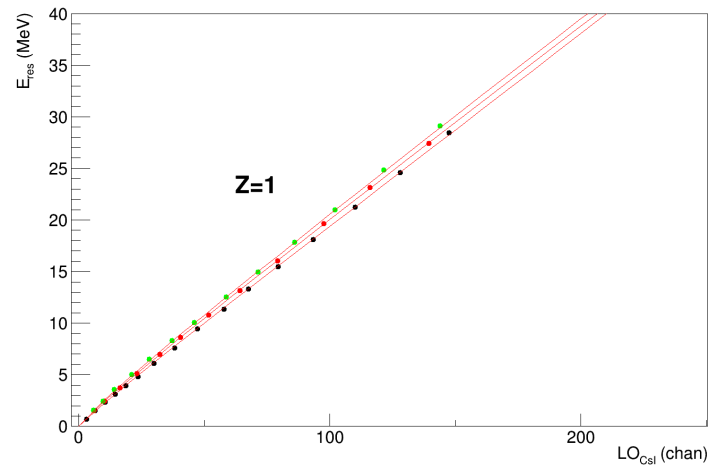
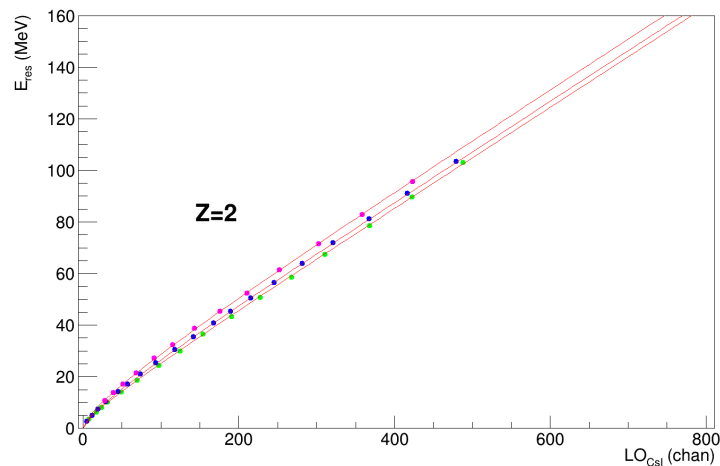
(a) *CsI-111 calibration for $Z = 1$.*(b) *CsI-111 calibration for $Z = 2$.*

Figure 3.14: Energy vs Light Output (LO) plots for FAZIA CsI-111, and result of the fit procedure for the calibration of $Z = 1$ and $Z = 2$. Different colours correspond to different isotopes of the considered elements.

run subsets within which the behaviour of the detectors can be considered to be stable.

3.3.2 Calibration of INDRA detectors

Concerning the INDRA modules, in previous experimental campaigns the calibration parameters for each detector have been determined from a set of calibration points obtained by elastic diffusion of light ion beams on a heavy target¹¹, usually ^{197}Au .

¹¹The target is chosen in order to increase the grazing angle of the reaction and to hit more detectors with the elastically scattered ions.

However, no runs with calibration beams are available for the present experiment. Therefore, another calibration strategy is exploited.

For the two stage telescopes (INDRA rings 6 to 9) a calibration procedure similar to that of the FAZIA telescopes has been adopted. In fact, the calibration with the triple alpha source is available also for the Si detectors of INDRA. Moreover, their thickness is known from previous experimental campaigns. With respect to FAZIA telescopes, more ion species have been used for the CsI calibration (up to $Z = 6$)¹². The adopted calibration formula is eq. (3.1): however, since the parameters a_2 , a_3 , a_4 only depend on the characteristics of the crystals, which have not been replaced since the previous INDRA campaigns, only the a_1 gain parameter has been extracted from the fit procedure, since it is the only one related to the response of the read-out chain. The a_2 , a_3 , a_4 parameters of the 5th INDRA experimental campaign have been adopted [18].

The CsI detectors of INDRA rings 10 to 17 have not been calibrated in this experiment, since the calibration procedure adopted for INDRA rings 6 to 9, that relies on the calibration of the first stage Si detectors, cannot be used for the remaining rings, not featuring a Si stage.

3.3.3 Energy assignment

The initial energy of each identified fragment is calculated as the sum of the energies released in each detector that it impinged on. First, the deposited energy is calculated from the available calibration parameters for all the detectors involved, starting from the one where the fragment stopped, and the total energy is evaluated as their sum. Then, two possible cases are treated:

- if all the detectors crossed by the fragment are calibrated, the consistency among the fractions of the total energy released in each layer is checked, according to the predictions of energy loss calculations based on the (Z, A) and the total energy of the identified fragment and on the thicknesses of the involved detectors.
- if the calibration parameters of one of the crossed detectors are missing, the “unknown” ΔE can be inferred from the energy deposited in the other stages. As an example, if the calibration is missing for just the Si1 stage of a FAZIA telescope, the $\Delta E(\text{Si1})$ can be obtained from the residual energy $\Delta E(\text{Si2}) + E_{res}(\text{CsI})$. Conversely, if the detector immediately in front of the uncalibrated one is calibrated, the residual energy can be calculated from the ΔE released in the calibrated detector. Knowing a precise value for the detector thicknesses is mandatory also in this second case.

¹²A different set of elements has been used for the calibration procedure in rings 6,7 and in rings 8,9, depending on the isotopic resolution of the corresponding Si-CsI telescopes. For rings 8 and 9, where a good mass discrimination is achieved thanks to the 300 μm thick Si detector used as first stage, one isotope for each element from $Z = 3$ to $Z = 6$ has been used. Rings 6 and 7 feature a worse isotopic resolution: the lithium isotopes cannot be easily discriminated, and therefore the Si-CsI correlation for ${}^4\text{He}$ has been used instead of that of ${}^6\text{Li}$.

Table 3.5: List of the possible calibration codes (ECodes) that can be assigned to a fragment. The fragments whose ECodes are those reported in green are marked as “good particles”.

ECode	Code meaning
-1	Calibration not attempted
0	No calibration
1	All detectors calibrated
2	Energy partially calculated
3	Not stopped within the telescope
4	Incoherency

After the whole procedure, a calibration quality code (ECode) is assigned to each particle, as reported in Tab. 3.5. These codes differ from those adopted in previous FAZIA experiments: the codes used in previous INDRA campaigns have been adopted.

To summarise the whole multistep procedure, performed within the KaliVeda framework:

- for each acquired event (i.e. for each accepted trigger), from the *raw data* (e.g. signal amplitudes, current waveforms) associated to a single telescope, the information associated to a detected particle is formed;
- a set of particles is thus assigned to an event;
- identification matrices are produced from particle data, identification grids are drawn manually, so that the (Z, A) information can be added to each identified particle in a subsequent step;
- the identified particles are exploited in order to calibrate the single detectors, so that the calibrated energy information can be added to each particle in a subsequent step;
- the last step is the production of the so called *recon data*, or reconstructed events: at this point, each particle holds the information on its (Z, A) , energy, direction in the laboratory reference frame, together with the identification and calibration quality codes previously introduced.

After the event reconstruction procedure is completed, the physics events are ready to be analysed. A first overview of the reconstructed physics events will be presented in the next section, to illustrate the reliability of the identification and calibration procedure and the conditions adopted to reject spurious events.

3.4 Event selection

A reconstructed physics event contains information on all the fragments marked as “good particles” after the identification and calibration procedures in KaliVeda: to summarise, the fragments with

$\begin{aligned} \text{IDQuality} &< 4 \\ \text{IDCode} &= 2, 3, 11, 12, 23, 33 \\ \text{ECode} &= 1, 2 \end{aligned}$
--

are accepted. As explained in Sec. 2.3, the particles are already grouped in the event by the acquisition system, according to a user-defined coincidence window. However, various time markers are attached both to the particles and to the event: this information can be used to perform further selections and discard some spurious events from the analysis. In particular, the time markers associated with the particles are:

- **GtTag**: time marker of the first particle detected by FAZIA.
- **DetTag**: time marker of a particle detected by FAZIA. The difference $\text{DetTag} - \text{GtTag}$ corresponds to the delay between the particle and the beginning of the FAZIA event.
- **MT**: time marker of a particle detected by INDRA, i.e. the delay between the particle and the beginning of the INDRA event.

Moreover, for each global event, also the time stamps generated by CENTRUM for the FAZIA event and the INDRA event (**FTS** and **ITS**, respectively) are stored. The difference between these two values corresponds to the delay between the INDRA and the FAZIA events that have been grouped together in the same global event. These time markers can be used to spot and discard anomalous events. In our case, some “safety cuts” have been imposed, determined by studying the distributions of the time markers and their delays. After these cuts, less than $\sim 1\%$ of the events for each system has been discarded.

After the first gross event selection based on the time markers, some other conditions are imposed on the global characteristics of each event. A set of global variables, such as:

- $(Z_{\text{tot}}, A_{\text{tot}})$: total detected charge and mass;
- $\sum p_z/p_{\text{beam}}$: ratio between the sum of the momenta along the z-axis of all the detected particles and the original momentum of the projectile (which is directed along the z-axis by definition of the reference axes);

is calculated for each event. As an example, the correlation between the Z_{tot} and the $\sum p_z/p_{\text{beam}}$ obtained for the system $^{64}\text{Ni} + ^{64}\text{Ni}$ at 32 A MeV is shown in Fig. 3.15 (similar plots are obtained for the other reactions); the dotted red line indicates

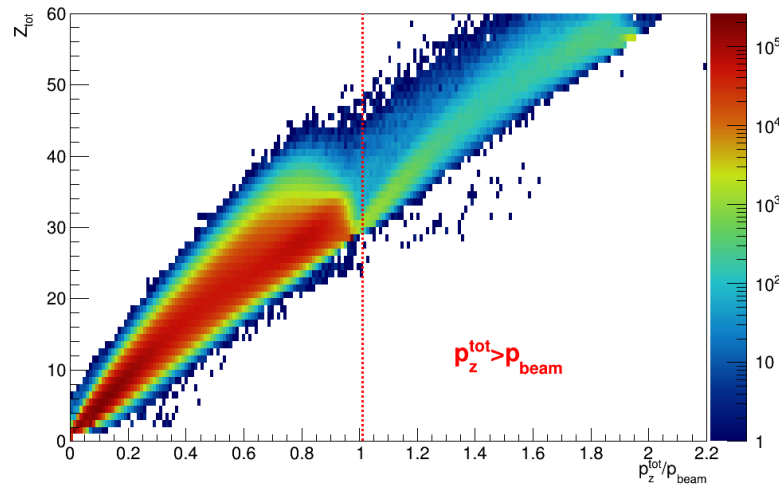


Figure 3.15: Z_{tot} vs $\sum p_z/p_{beam}$ correlation obtained for the system $^{64}\text{Ni}+^{64}\text{Ni}$ at 32 A MeV. The correlations obtained for the other reactions do not show substantial differences.

the condition $\sum p_z = p_{beam}$, i.e. the condition of momentum conservation along z . Therefore, the events located on the right side of the red line, for which $\sum p_z > p_{beam}$, do not satisfy the momentum conservation law; these events are probably spurious coincidences in which the products of two (or more) almost simultaneous collisions have been detected within the same acquisition time window and grouped together as they were produced in the same physics event. Most of these spurious events can be discarded by requiring the products in the exit channel to be compatible with the characteristics of the entrance channel, i.e. by keeping only those events that satisfy the following conditions on the aforementioned global variables¹³:

$$\begin{aligned} \sum p_z/p_{beam} &\leq 1.01 \\ Z_{tot} &\leq Z_p + Z_t = 56 \\ A_{tot} &\leq A_p + A_t \end{aligned}$$

where $Z_{p,t}$ ($A_{p,t}$) are the charge (mass) numbers of the projectile and target. In the events on the left side of the red line, for which $\sum p_z < p_{beam}$, part of the momentum along z has been lost, due to the fact that some reaction products have not been detected. However, many strongly incomplete events populate the bottom-left region of the plot in Fig. 3.15. Since we are interested in the analysis of more complete events, in which a higher fraction of the reaction products has been detected, the following conditions have been added:

$$\begin{aligned} \sum p_z/p_{beam} &\geq 0.4 \\ Z_{tot} &\geq 12 \end{aligned}$$

¹³The exact condition for momentum conservation would be $\sum p_z/p_{beam} \leq 1$: the limit set in the present analysis is 1% higher in order to take into account the possible calibration uncertainties.

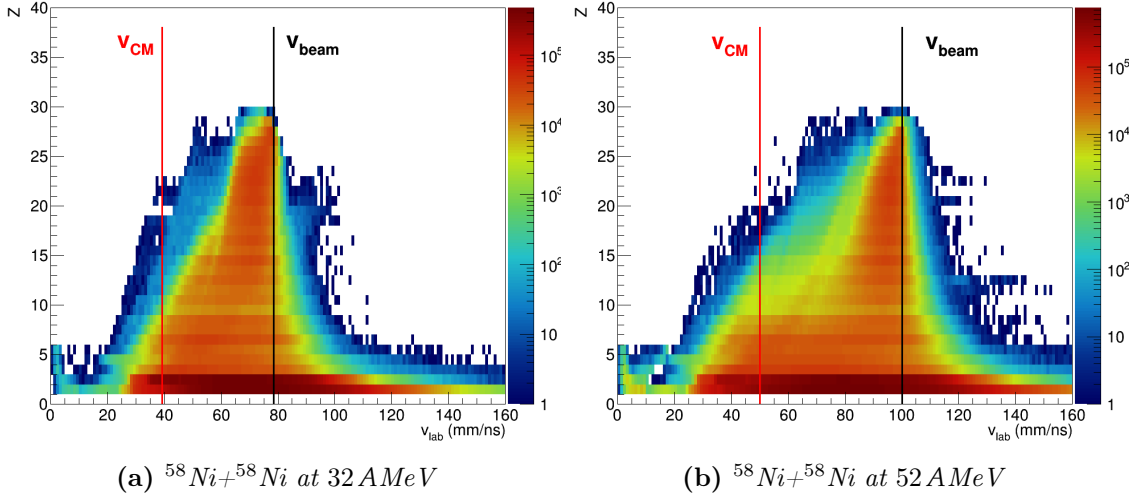


Figure 3.16: Z vs v_{lab} correlations for all the fragments detected in the reaction $^{58}\text{Ni}+^{58}\text{Ni}$ at 32 AMeV (panel (a)) and 52 AMeV (panel (b)). The plots obtained for the other systems do not show substantial differences, since at this level the main features are determined by the beam energy. The isotopic identification of the fragments has not been required. Due to the lack of statistics, the identification procedure cannot be applied to fragments with $Z \gtrsim 28 - 29$.

In summary, only the events satisfying the following global conditions have been considered for the analysis:

$$\begin{aligned}
 0.4 &\leq \sum p_z/p_{beam} \leq 1.01 \\
 12 &\leq Z_{tot} \leq Z_p + Z_t = 56 \\
 A_{tot} &\leq A_p + A_t
 \end{aligned}$$

By rejecting all the events that do not satisfy these conditions, the statistics for each system has been reduced to $\sim 46\%$ (57%) of the total statistics for the reactions at 32 AMeV (52 AMeV).

3.4.1 Charge and velocity distributions

We now consider only the events that satisfy the conditions just introduced. In Fig. 3.16 two correlation plots between the charge Z and the velocity in the laboratory frame v_{lab} of all the detected particles are shown. This kind of correlation is often exploited in experimental studies of heavy ion collisions at Fermi energies [42, 44, 57, 67, 69], because it offers a good overview of the global characteristics of the acquired events. The plots in Fig. 3.16 have been obtained from the data of the system $^{58}\text{Ni}+^{58}\text{Ni}$ at 32 AMeV (panel (a)) and 52 AMeV (panel (b)), requiring only charge identification and energy calibration. Similar correlations are obtained

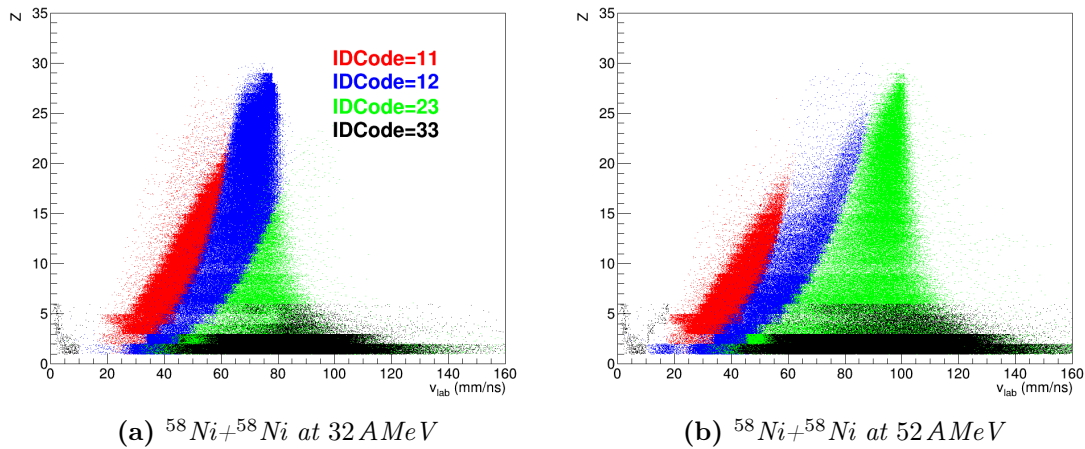


Figure 3.17: Z vs v_{lab} correlations for all the fragments detected in FAZIA in the reaction $^{58}\text{Ni}+^{58}\text{Ni}$ at 32 A MeV (panel (a)) and 52 A MeV (panel (b)). The different colours represent the techniques that have been exploited for the identification of each fragment. The colour code is the same in both panels.

for all the studied systems. In both panels one can spot an increase in statistics towards the QP region, i.e. the area where $Z \sim Z_p$ and $v \sim v_{beam}$. Two vertical lines have been drawn to guide the eye: the black one indicates the velocity of the projectile and the red one the velocity of the CM, both in the laboratory reference frame (see Tab. 3.2). For increasing atomic number Z (up to $Z \sim 28$, which can be associated to QP residues for $v > v_{CM}$) the velocities of the fragments tend to converge towards the v_{beam} value, as expected: this can be interpreted as an indication that the calibration procedure produces reasonable results. The QT-like fragments would be located in correspondence of the larger Z values, on the left side of the red line, i.e. at $v < v_{CM}$, but they are not detected due to the energy thresholds for identification.

The same Z vs v_{lab} correlations, including only the fragments detected by FAZIA, are plotted in Fig. 3.17 with a different colour depending on the technique that has been exploited for the identification of each fragment (refer to Tab. 3.4 for the association of the IDCode to the various techniques). The identification methods that have been employed allow to populate different regions of the Z vs v_{lab} plot, according to the respective identification threshold. The Si1-PSA technique (ID-Code=11, in red) features the lowest energy threshold, and its use allows to identify a large quantity of fragments with low v_{lab} , around and below that of the CM. Another possible observation regards the different fractions of reaction products that are identified with each technique at the two beam energies, as shown by the different extension of the coloured areas in Fig. 3.17; this is a direct consequence of the penetration power of fragments with different energies. In fact, in the reaction at the higher beam energy, also the energy and velocity distributions of the ejectiles will

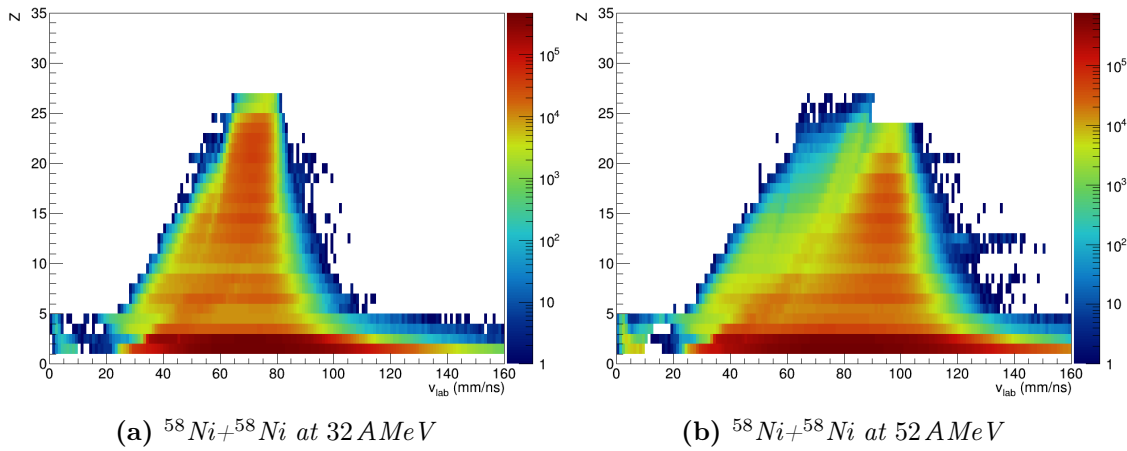


Figure 3.18: Z vs v_{lab} correlations for all the fragments detected in the reaction $^{58}\text{Ni}+^{58}\text{Ni}$ at 32 A MeV (panel (a)) and 52 A MeV (panel (b)), requiring both charge and mass identification.

be shifted towards higher values. More particles will thus be stopped, e.g., in the CsI, and therefore identified via Si2-CsI or CsI-PSA technique, instead of Si1-PSA or Si1-Si2. However, the different techniques do not feature the same identification capability, and this reflects into a different performance of the apparatus at the two energies. This is particularly true when the mass identification is required: as an example, in Fig. 3.18 the Z vs v_{lab} correlations including all the fragments identified both in charge and mass for the same two reactions are shown. The worse identification capability at 52 A MeV can be noticed from the loss of statistics in the plot in Fig. 3.18b for the heavier products, in the area of the QP remnant, by comparing the plots in Fig. 3.18 with the respective plots in Fig. 3.16.

Theoretical models and simulations

In order to understand the physics processes that govern the observed phenomena, a comparison between the experimental results and the predictions of a model is mandatory. For the simulation of the reaction mechanism employed in this work, the evolution of a heavy ion collision is subdivided into two phases, and two different theoretical models have been used in order to properly describe each step.

The first step, referred to as **dynamical phase**, is the one in which the actual interaction between projectile and target takes place. The products of this phase are called *primary fragments*. The mechanisms coming into play in this primary interaction are usually simulated by means of *dynamical transport models*, that consider the interactions among the particles and follow the resulting time evolution of the system. Several simulation codes of the initial dynamical evolution, exploiting different kinds of approaches, are available. In this work the AMD (Antisymmetrized Molecular Dynamics) model [14, 118–120] has been employed (see Sec. 4.1).

After that, in the **statistical phase**, the hot primary fragments undergo statistical de-excitation, and the so-called *secondary fragments* are produced. In this step, each dynamical product is considered as an excited system in equilibrium that dissipates energy by decaying according to the branching ratios of all the open de-excitation channels (e.g., particle and gamma emission and fission), eventually reaching its ground state. An example of such *statistical code* (also called *afterburner*) is GEMINI [15, 121], used in this work and described in Sec. 4.2. The secondary products produced in the simulation after the evaporation phase correspond to the fragments which are actually detected in the experiment. In fact, the time span of the primary interaction ($\sim 10^{-5}$ ns) is much shorter than the time of flight of the fragments towards the detectors (~ 10 ns).

For a meaningful comparison of the model predictions with the experimental data, the secondary fragments produced in the statistical phase of the simulation must be filtered through a software replica of the experimental apparatus, also taking into account the working status and the identification thresholds of each detector (see Sec. 4.3). In Sec. 4.4, some characteristics of the filtered simulated data will be shown and compared with the general features of the experimental data.

4.1 Dynamical model: the AMD code

The dynamical transport models aim at the description of the time evolution of the colliding nuclear system, a typical quantum many-body problem. Since no viable analytical solution exists, several approaches based on different approximations have been developed. As already mentioned, for a proper description of the interaction mechanism in heavy ion collisions at Fermi energies both mean field contributions and nucleon-nucleon (N-N) collisions must be considered. This must be taken into account when choosing the dynamical code to employ.

The available dynamical codes can be grouped into two big classes of transport models [122]:

- BUU type, based on the Boltzmann-Uehling-Uhlenbeck equation, in which the one-body density matrix is propagated in a mean field that considers the contribution from all the nucleons of the system. In the low energy regime, where the mean field description is reliable, the Vlasov equation offers a good approximation of the problem. At higher energies, N-N collisions must be taken into account, and this can be done by introducing a collision term: the effect of the collisions can be either considered on average (Boltzmann-Vlasov equation) or by including also the stochastic fluctuations from the average (Boltzmann-Langevin equation). BLOB [123] and SMF [124] are two examples belonging to this class of dynamical codes.
- QMD (Quantum Molecular Dynamics) type [125, 126], based on a molecular dynamics treatment. Here, the nucleons are described as gaussian wave packets, and the evolution of their coordinates and momenta, rather than the evolution of the phase space density like in the previous class, is studied under the effect of a multi-body Hamiltonian. Two examples of QMD-type codes are CoMD [127, 128] and AMD [14, 118, 119].

The AMD (Antisymmetrized Molecular Dynamics) model has been used in the present work, since it has already been adopted for the description of heavy ion collisions at Fermi energies, with satisfactory results [60, 67, 129] also in the specific studies of our group. AMD was born as an evolution of the QMD code where the antisymmetrisation of the wave function of the many-nucleon system is introduced [14, 118, 119], also including the treatment of N-N collisions. This model has been further developed during the last thirty years, in order to refine the description of the interaction mechanisms. The formation of light clusters [120] and the mechanism of pion production [130] have been recently implemented.

In the basic formulation of AMD, the wave function of the many-nucleon system is expressed as the Slater determinant¹ for A nucleons [14]:

$$\Phi(\mathcal{Z}) = \frac{1}{\sqrt{A!}} \det[\phi_{\mathbf{z}_i} \chi_{\alpha_i}] \quad (4.1)$$

¹The antisymmetrisation introduced through the use of the Slater determinant intrinsically allows to take into account the Pauli exclusion principle, and thus the fermionic nature of the nucleons.

where χ_{α_i} are the spin-isospin states, with $\alpha_i = \uparrow p, \downarrow p, \uparrow n$ or $\downarrow n$, and $\phi_{\mathbf{z}_i}$ is the spatial component of the wave function of the i -th single particle state, described as a gaussian wave packet:

$$\phi_{\mathbf{z}_i} = \left(\frac{2\nu}{\pi}\right)^{\frac{3}{4}} \exp\left[-\nu\left(\mathbf{r} - \frac{\mathbf{z}_i}{\sqrt{\nu}}\right)^2 + \frac{1}{2}\mathbf{z}_i^2\right] \quad (4.2)$$

where $\mathcal{Z} \equiv \{\mathbf{z}_i\} = \{\mathbf{z}_1, \mathbf{z}_2, \dots, \mathbf{z}_A\}$ are the complex² variational parameters of the wave function corresponding to the centroids of the gaussian packets, and ν is a parameter representing their width (the value $\nu = 0.16 \text{ fm}^{-2}$ has been adopted [118]). The time evolution of the wave packets composing the many-nucleon system is determined by means of the time-dependent variational principle (see Refs. [14, 118, 119] for details):

$$\delta \int_{t_1}^{t_2} dt \frac{\langle \Phi(\mathcal{Z}) | (i\hbar \frac{d}{dt} - H) | \Phi(\mathcal{Z}) \rangle}{\langle \Phi(\mathcal{Z}) | \Phi(\mathcal{Z}) \rangle} = 0 \quad (4.3)$$

where H is the Hamiltonian of the system, including both the mean field contributions and the N-N collisions. In fact, since we are interested in the description of heavy ion collisions at Fermi energies, both the mean field contributions and the N-N collisions must be taken into account.

The **mean field** contributions can be included in the Hamiltonian by exploiting different expressions of the effective interaction [118, 119]. In the present work, the Skyrme SLy4 potential [131] has been exploited, with incompressibility modulus $K_0 = 230 \text{ MeV}$ and saturation density $\rho_0 = 0.16 \text{ fm}^{-3}$, which are widely accepted values (see Sec. 1.2). For each measured reaction, two separate simulations assuming the two parametrisations of the symmetry energy already introduced in Sec. 1.2 have been performed: for the *asy-stiff* one, the symmetry energy at ρ_0 and the slope parameter have been set to $S(\rho_0) = 32.0 \text{ MeV}$ and $L_{sym} = 108 \text{ MeV}$, while for the *asy-soft* one $S(\rho_0) = 32.0 \text{ MeV}$ and $L_{sym} = 46 \text{ MeV}$ have been adopted.

The **N-N collisions** are treated as stochastic transitions from an AMD state to another. The transition is inhibited if the final state is occupied, in order to take into account the Pauli blocking³. The transitions between AMD states are governed by the in-medium N-N cross section, treated as a free parameter in this model, and expressed through the parametrisation [132]:

$$\sigma = \sigma_0 \tanh\left(\frac{\sigma_{free}}{\sigma_0}\right), \quad \sigma_0 = y\rho^{-2/3} \quad (4.4)$$

where σ_{free} is the free-space cross section. The default value of the screening parameter $y = 0.85$ (see Ref. [132]) has been assumed in this work.

²The real component is related to the position, while the imaginary one to the momentum.

³The method adopted for the implementation of N-N collision is the one described in Ref. [129], based on randomly generated test particles for each step. A collision is attempted according to a geometrical condition. When two test particles $(\mathbf{r}_1, \mathbf{p}_1)$ and $(\mathbf{r}_2, \mathbf{p}_2)$ collide, the momenta of the two physical coordinates $(\mathbf{R}_{k_1}, \mathbf{P}_{k_1})$ and $(\mathbf{R}_{k_2}, \mathbf{P}_{k_2})$ are changed: if the condition $\nu|\mathbf{R}_k - \mathbf{R}_j| + |\mathbf{P}'_k - \mathbf{P}_j|/(4\hbar^2\nu) < 1.46^2$ is satisfied $\forall j (\neq k)$ with the same spin-isospin state as k , the final momenta \mathbf{P}'_k (with $k = k_1, k_2$) are allowed by the Pauli principle.

In the update of the original AMD code presented in Ref. [120] the clustering effects, a subject which is still strongly debated in the literature, have been introduced. This correction has been implemented in order to better reproduce the observed number of emitted free protons compared to those bound in light particles (d, t, ^3He , α) and heavier fragments. In fact, many different transport models tend to overestimate the proton multiplicity in the final state [120]. A proper treatment of cluster correlations is necessary to correctly simulate the global reaction dynamics. Moreover, some isospin observables used to study the symmetry energy are related to the isospin content of the light fragments produced in the reaction, which strongly depends on the cluster formation. In the AMD code, the cluster formation is considered by taking into account the possible correlations in the construction of the set of final states of a N-N collision. The transition probabilities to clusterised states are obtained as described in Ref. [120]. The clusterised final state is again expressed as a Slater determinant and propagated according to the AMD equation of motion. A cluster can be broken in the collision with other nucleons in the system. In order to obtain a better agreement with some experimental data, a semi-empirical correction, explained in Ref. [129] and also applied in the present work, has been later introduced in order to suppress cluster correlation in nuclear medium.

The primary fragments are produced by AMD in a highly excited state. The AMD calculations considered in this work have been stopped at 500 fm/c, which, in previous works, has been found to be a time long enough to be sure that the dynamical phase is concluded and the mutual Coulomb repulsion between the primary reaction products is negligible [129]. However, it must be noted that the actual interaction time approximately ends around 150-200 fm/c (considering the splitting time between the QP and the QT): therefore, some de-excitation ejectiles will be already produced in the following time steps of the AMD simulation [68], though such decays do not strictly follow a statistical model, as the one introduced in Sec. 4.2.

4.1.1 Characteristics of the primary fragments

About 20000 primary events have been simulated with the AMD code for each Ni+Ni system measured in the E789 experiment, for both energies⁴. For each reaction, two separate calculations have been run, one using the asy-stiff parametrisation, one using the asy-soft one. The simulations have been stopped at 500 fm/c. The impact parameter follows a triangular distribution, growing linearly up to $b = 11.6$ fm, slightly larger than the b_{gr} for all reactions (see Tab. 3.2). In the following, the reduced impact parameter $b_{red} = b/b_{gr}$ will often be used. This section presents the main features of the primary fragments simulated with AMD, with a focus on the behaviour of the isospin observables among the inspected semiperipheral and peripheral reactions.

⁴The production of a larger number of primary events would be impractical due to the relatively long CPU time required by the AMD calculations.

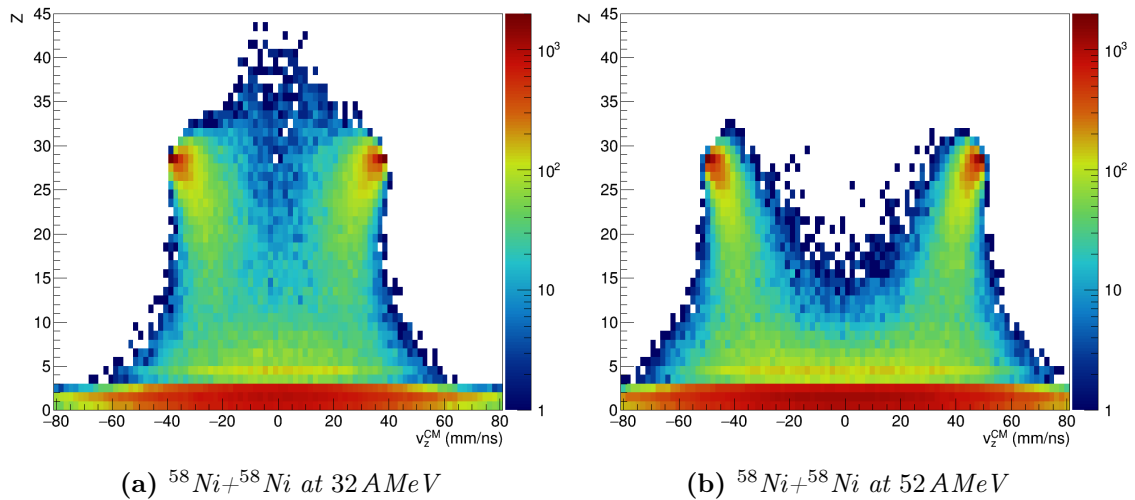


Figure 4.1: Z vs v_z^{CM} correlation of the simulated (asy-stiff) primary fragments for the reaction $^{58}\text{Ni}+^{58}\text{Ni}$ at the two energies 32 A MeV and 52 A MeV. Similar plots are obtained for the other systems.

General characteristics – In Fig. 4.1 an example of the Z vs v_z^{CM} correlation of the (asy-stiff) simulated primary fragments is shown: the data refer to the reaction $^{58}\text{Ni}+^{58}\text{Ni}$ at the two energies 32 A MeV (Fig. 4.1a) and 52 A MeV (Fig. 4.1b). In both plots, the regions associated to the QP-like and QT-like fragments can be readily identified, in correspondence of the two narrow spots placed at $Z \lesssim 28$: the one with $v_z^{\text{CM}} > 0$ (i.e. going forward in the CM reference frame) corresponds to the QP-like fragments, while the other, with $v_z^{\text{CM}} < 0$ (going backward) corresponds to the QT-like fragments. Besides the obvious difference of the absolute values of the v_z^{CM} components for the two beam energies, the distributions of the primary Z in the two plots are clearly not the same, with the reaction at 32 A MeV producing heavier fragments, especially at the CM velocity.

In order to better appreciate the difference between the two beam energies, the Z vs v_z^{CM} correlations are shown in Fig. 4.2 for five different centrality bins, selected by means of the b_{red} , from central (left) to peripheral (right) collisions. Correlations obtained at 32 A MeV (52 A MeV) are displayed in the top (bottom) panels. In both cases, the exit channel for the most peripheral collisions is clearly binary, as expected for a DIC at intermediate energy (see Sec. 1.1.1), characterised by two big fragments, the QP and the QT, and a few LCPs and IMFs, the latter mostly around $v_z^{\text{CM}} \sim 0$, especially at 32 A MeV. Moving towards more central collisions, in which more energy is dissipated, the QP and QT lose more nucleons and become gradually lighter, also due to the opening of other reaction channels, e.g. multifragmentation or breakup. For the most central collisions a clear difference emerges between the two energies. In fact, for the reaction at 32 A MeV some heavy fragments (with atomic numbers around and even above Z_{proj}) are produced in a sort of incomplete-fusion, while for the one at 52 A MeV there is an enhanced production of lighter fragments, consistent

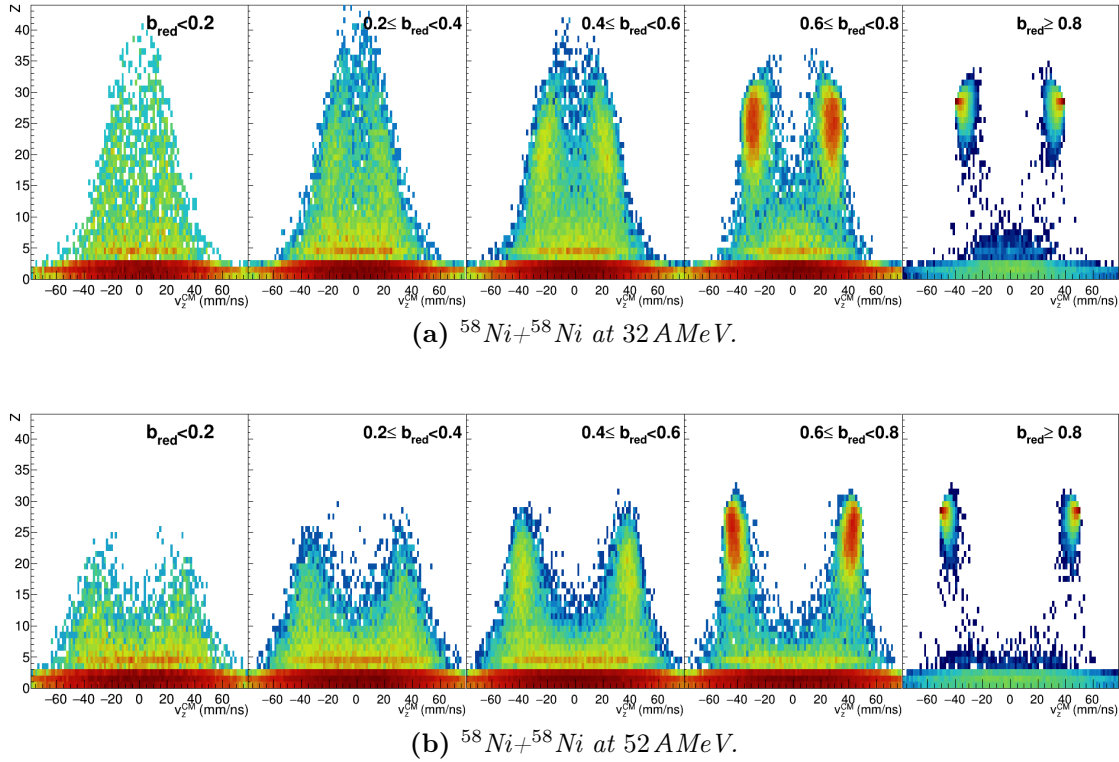


Figure 4.2: Z vs v_z^{CM} correlation of the simulated (asy-stiff) primary fragments for the reaction $^{58}\text{Ni}+^{58}\text{Ni}$ at the two energies 32 AMeV and 52 AMeV, for five centrality (b_{red}) bins, from central (left) to peripheral (right) collisions. Similar plots are obtained for the other systems.

with a multifragmentation process.

Since we are interested in the study of peripheral and semiperipheral DIC events, in which the binary exit channel can be easily recognised, we will concentrate, from now on, on the collisions with $b_{red} > 0.6$. The DIC events are then selected by requiring two big fragments, with $Z \geq 10$; in order to momentarily exclude the breakup events, we consider only those in which no fragment with $5 \leq Z \leq 9$ is produced. The two heaviest products are identified as the QP ($v_z^{CM} > 0$) and the QT ($v_z^{CM} < 0$).

Properties of the QP and QT fragments – In Fig. 4.3 the $\langle N/Z \rangle$ of the QP thus selected is reported as a function of the b_{red} of the simulated event, for all the inspected systems at the two bombarding energies 32 AMeV (panel (a)) and 52 AMeV (panel (b)): this observable, already introduced in Sec. 1.1.2, is widely used to study the isospin content of the products of a reaction. The errors on the y -axis are statistical; when not visible, they are smaller than the marker. The results of the simulations with both the asy-stiff and the asy-soft symmetry energy parametrisations are shown. In all cases, for the most peripheral reactions ($b_{red} \sim 1$) the QP retains the $\langle N/Z \rangle$ of the projectile, i.e. 1.07 for ^{58}Ni and 1.29 for ^{64}Ni . How-

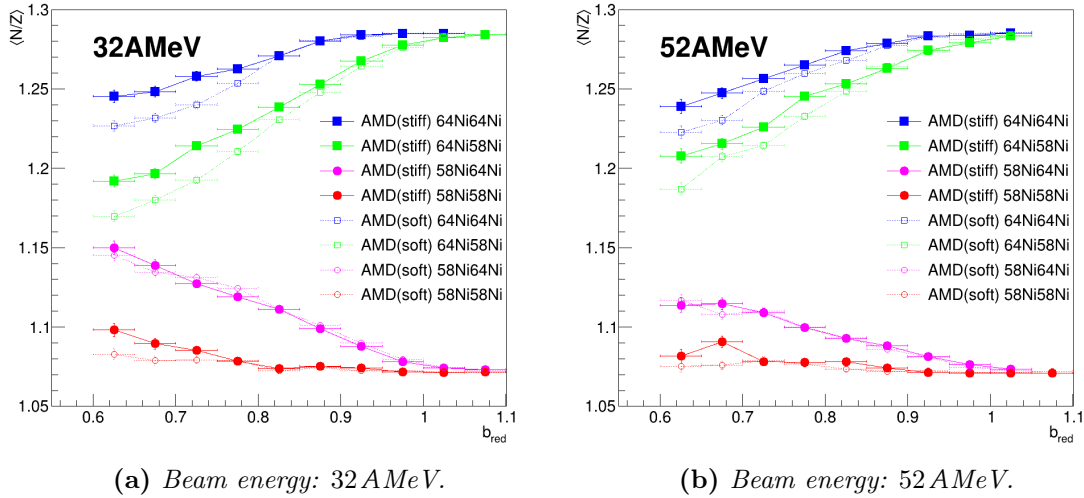


Figure 4.3: $\langle N/Z \rangle$ of the primary QP vs b_{red} of the reaction. All the systems $^{58,64}\text{Ni}+^{58,64}\text{Ni}$ are plotted in different colours for both the symmetry energy parametrisations tested with the AMD code: the solid line and the full symbols indicate the asy-stiff parametrisation, the dotted line and the open symbols the asy-soft one. Reactions induced by a neutron rich (deficient) projectile are represented by squares (circles). The two panels report data for the two beam energies. Please note that the b_{red} value starts at 0.6, thus excluding the most central collisions.

ever, the evolution of $\langle N/Z \rangle$ with increasing centrality (decreasing b_{red}) depends on the system. In particular, the $\langle N/Z \rangle$ of the QP produced in the reactions with the neutron rich (deficient) projectile tends to decrease (increase) with decreasing b_{red} , as one can recognise by looking at the different behaviour of the squares and circles in Fig. 4.3. A different behaviour is observed also between the systems with the same projectile and different targets, with a gap that becomes wider with increasing centrality: this fact can be interpreted as a consequence of the isospin diffusion mechanism. In fact, as the centrality increases, the contact time also increases and more nucleons are exchanged, and therefore, driven by the E_{sym} contribution, the QP and the QT originated in the two asymmetric reactions $^{58}\text{Ni}+^{64}\text{Ni}$ and $^{64}\text{Ni}+^{58}\text{Ni}$ emerge more equilibrated in terms of isospin, with $\langle N/Z \rangle$ that tends roughly to the average value of the system (1.18). This feature is more evident for the reactions at lower energy (32 AMeV, Fig. 4.3a), for which a longer interaction time is expected. A certain effect of the stiffness of the symmetry energy is observed on the $\langle N/Z \rangle$ of the QP emerging from the less peripheral reactions, more evident in the systems with a ^{64}Ni projectile. As expected, the asy-soft parametrisation induces a higher degree of isospin equilibration for $\rho < \rho_0$. However, the secondary decay can strongly modify the features of the primary fragments, in general substantially reducing the sensitivity to the symmetry energy stiffness in the final products, as

will be shown in Sec. 6.1.1.

In order to disentangle the role of protons and neutrons in the isospin transport we can study separately the behaviour of $\langle Z \rangle$ and $\langle N \rangle$ of the QP as a function of b_{red} , as shown in Fig. 4.4. The same properties for the QT are shown in Fig. 4.5. Only the results of the calculations with the asy-stiff parametrisation are plotted. As the centrality increases, the average proton and neutron contents of the QP tend to decrease for all the reactions, as expected due to the higher degree of dissipation. The loss of nucleons is even more evident at the higher beam energy (Fig. 4.4b). However, the evolution of $\langle Z \rangle_{QP}$ and $\langle N \rangle_{QP}$ as a function of b_{red} shows some differences among the studied systems. In particular, the behaviour of $\langle N \rangle_{QP}$ ($\langle N \rangle_{QT}$) is only dependent on the projectile (target), and not on the other partner of the collision, while the behaviour of $\langle Z \rangle_{QP}$ is different for each reaction. For the symmetric systems (red and blue squares) the gap between the two $\langle Z \rangle_{QP}$ graphs can be explained as a consequence of the different neutron richness of the projectile: in fact, the neutron deficient QP ^{58}Ni tends to lose more protons (and/or less neutrons). The behaviour of the asymmetric systems shows an additional feature, again associated to the isospin diffusion between projectile and target. For example, the $\langle Z \rangle_{QP}$ obtained for $^{58}\text{Ni}+^{64}\text{Ni}$ (at both energies) is always lower than that obtained for the symmetric reaction with the same projectile, and this observation can be explained with the hypothesis of a net proton transfer from the projectile to the neutron rich target: this interpretation is also supported by the average proton and neutron contents of the QT, shown in Fig. 4.5, where the $\langle Z \rangle_{QT}$ obtained for $^{58}\text{Ni}+^{64}\text{Ni}$ is greater than that obtained for $^{64}\text{Ni}+^{64}\text{Ni}$, although the target is the same. The opposite behaviour is found for the system $^{64}\text{Ni}+^{58}\text{Ni}$. From these observations we deduce that in AMD the isospin diffusion is mostly driven by the net proton transport rather than by the net neutron transport.

Properties of LCPs and IMFs – The isospin characteristics of the emitted LCPs and IMFs in the primary events can also be explored. In Fig. 4.6 the $\langle N \rangle / Z$ and the standard deviation σ_N of the isotopic distribution of the LCPs and IMFs emitted in coincidence with QP and QT in the selected DIC events are plotted as a function of Z . The plots of $\langle N \rangle / Z$ vs Z show a clear hierarchy: the isotopic ratio for the neutron rich $^{64}\text{Ni}+^{64}\text{Ni}$ is the highest, that for the neutron deficient $^{58}\text{Ni}+^{58}\text{Ni}$ is the lowest, and those for the mixed systems are located in between them. The neutron richness of the emitted particles thus reflects the neutron content of the total system. However, no clear dependence on the asy-stiffness of the symmetry energy is evidenced. Conversely, some sensitivity to the different parametrisation can be spotted in the σ_N vs Z plots, as expected from theoretical evaluations [133]: the isotopic distributions of the light products are in fact wider in the asy-stiff case [67]. The $\langle N \rangle / Z$ of the emitted LCPs and IMFs can also be studied as a function of the velocity component along the beam axis v_z^{CM} (similarly to the $\langle N \rangle / Z$ vs v^{lab} presented in Sec. 1.1.2). In fact, different v_z^{CM} regions can be associated to different sources of the emitted particles, and the neutron content of the emissions will reflect the neutron richness of the source. The particles emitted forward with respect to the

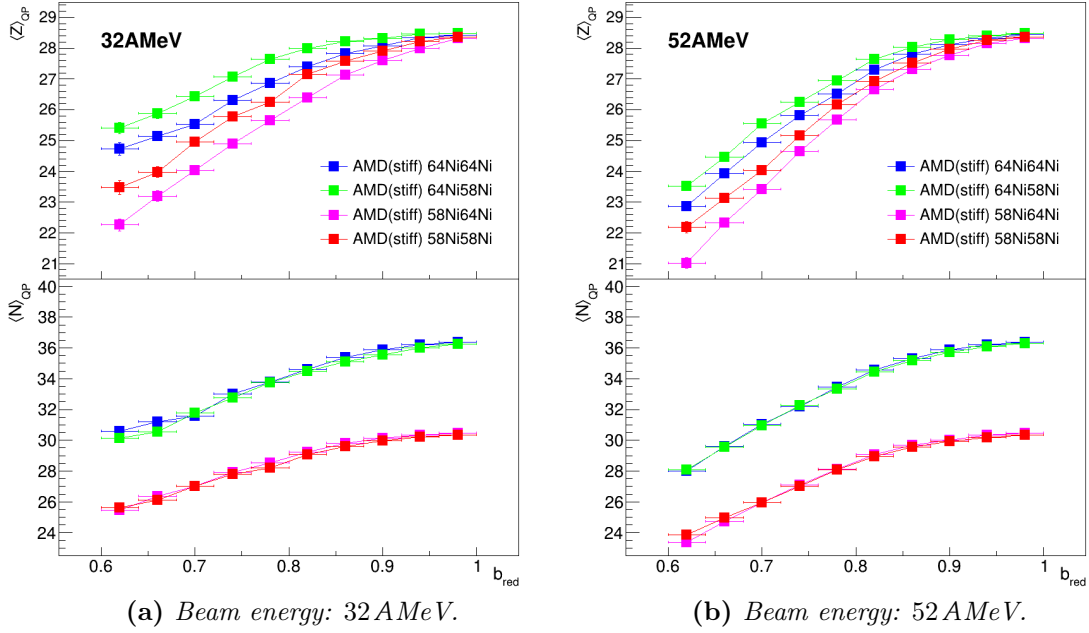


Figure 4.4: Average proton and neutron content of the primary QP vs b_{red} of the reaction for all the systems $^{58,64}\text{Ni}+^{58,64}\text{Ni}$ and for both energies, obtained assuming the asy-stiff parametrisation.

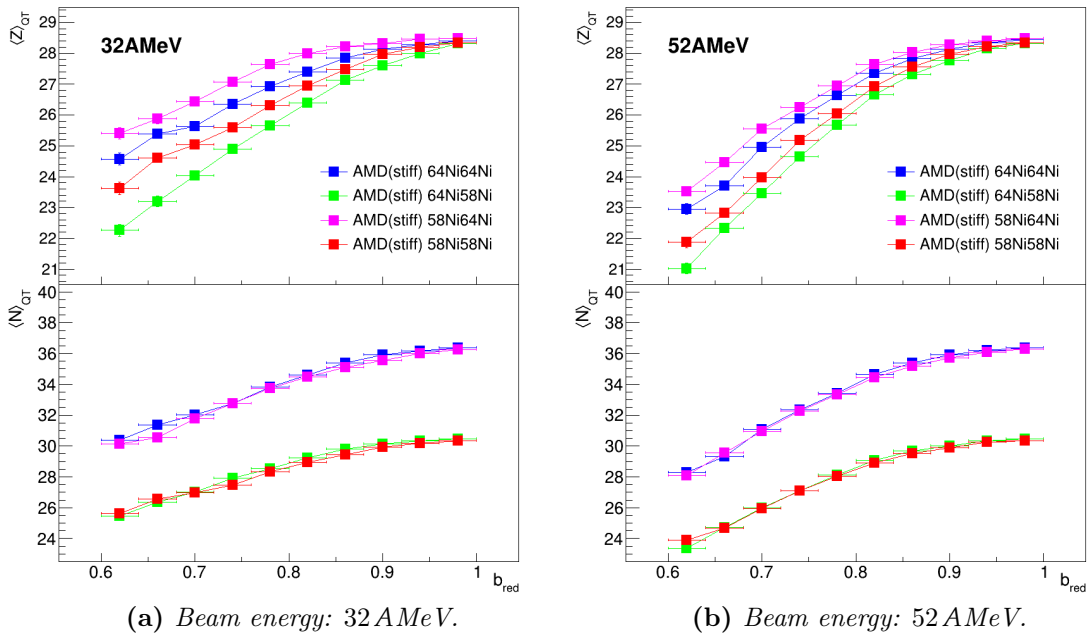


Figure 4.5: Average proton and neutron content of the primary QT vs b_{red} of the reaction for all the systems $^{58,64}\text{Ni}+^{58,64}\text{Ni}$ and for both energies, obtained assuming the asy-stiff parametrisation.

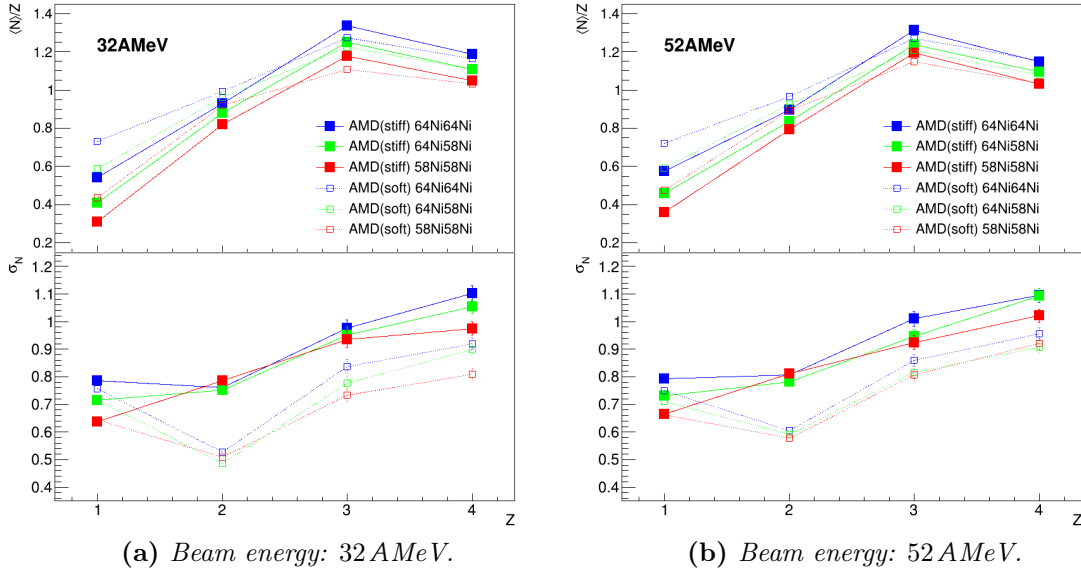


Figure 4.6: Isospin characteristics of the primary LCPs ($Z = 1, 2$) and IMFs ($Z = 3, 4$) produced by AMD in coincidence with QP and QT for DIC events for all the reactions and for both energies. The results for the system $^{58}\text{Ni}+^{64}\text{Ni}$ coincide with those for $^{64}\text{Ni}+^{58}\text{Ni}$.

QP (backward with respect to the QT) are mainly produced in the fast QP (QT) de-excitation, while in the region in between the velocities of the QP and the QT we can find particles from multiple origins, including the contributions from neck-like sources. The plots of the $\langle N \rangle / Z$ as a function of v_z^{CM} of the primary LCPs and IMFs in coincidence with QP and QT are shown in Fig. 4.7 (for the asy-stiff parametrisation). The results for the reactions at 32 A MeV are presented in panel (a): here, an indication of the neutron enrichment at midvelocity, possibly related to the isospin drift phenomenon, can be found in the fact that the $\langle N \rangle / Z$ is maximum for $v_z^{CM} \sim 0$. This feature is evident for $Z = 1$, and becomes less and less clear for the heavier fragments also due to the more limited variation of $\langle N \rangle / Z$ among their possible isotopes. At 52 A MeV (panel (b)) some difference is found, mostly for $Z = 1$. For example, for the system $^{64}\text{Ni}+^{64}\text{Ni}$ the maximum of the $\langle N \rangle / Z$ plot is wider than at 32 A MeV, extending towards the QP and QT regions: the shape of the plot can be modified by the fast emissions of the neutron rich QP and QT, which can be expected to be more important at 52 A MeV. In the mixed system $^{64}\text{Ni}+^{58}\text{Ni}$ ($^{58}\text{Ni}+^{64}\text{Ni}$), the maximum of the $\langle N \rangle / Z$ plot is instead shifted towards the region of the neutron rich QP (QT).

Breakup fragments – Since the QP breakup mentioned in Sec. 1.3 is mainly a dynamical process [21, 22, 60], we can expect to find some events of this type already among the AMD primary events. In order to select them, we consider the semiperipheral and peripheral collisions ($b_{red} > 0.6$) in which two forward-oriented

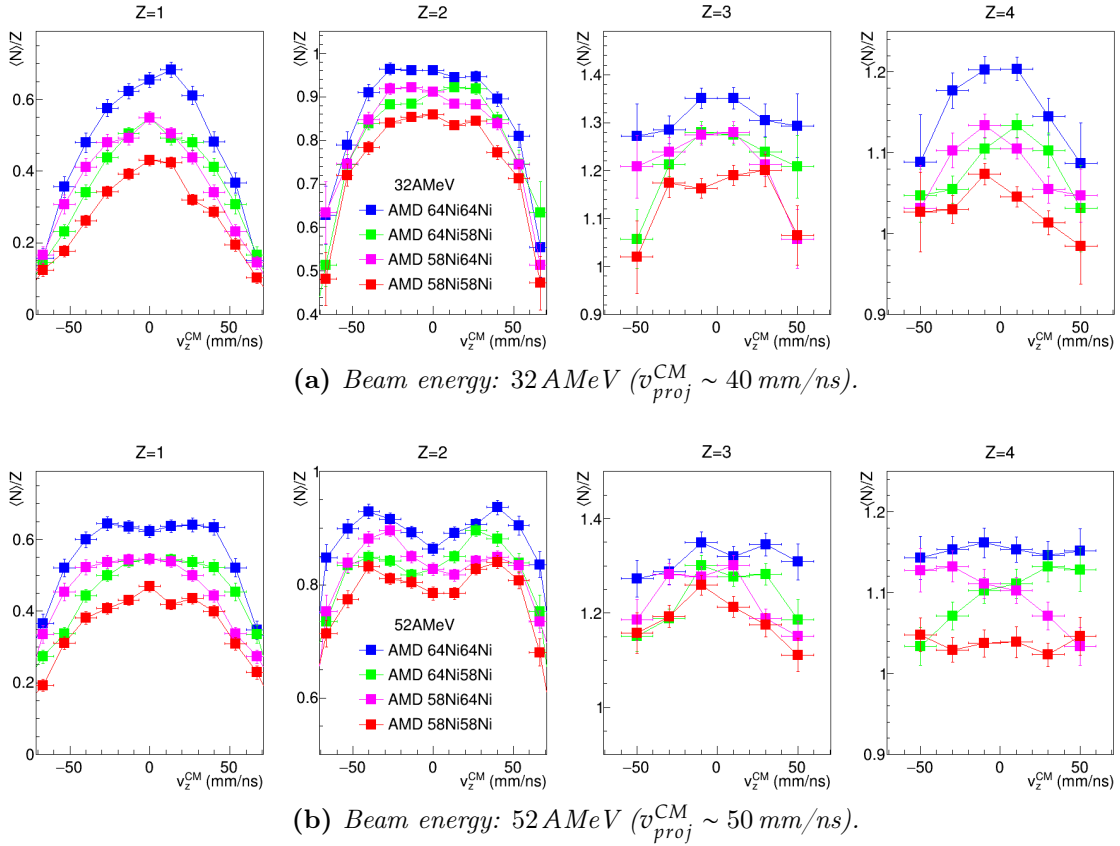


Figure 4.7: $\langle N \rangle / Z$ vs v_z^{CM} of the primary LCPs and IMFs produced by AMD in coincidence with QP and QT for DIC events in the reactions $^{58,64}\text{Ni} + ^{58,64}\text{Ni}$ and for both energies, obtained assuming the asy-stiff parametrisation.

fragments ($v_z^{CM} > 0$) with $Z \geq 5$ are produced. These two collision products are good candidates to be formed in the breakup of the QP, and they are labelled as heavy (Z_H) and light (Z_L) according to their charge number. Notice that this is not a strict selection, but it can be useful to give an idea of the incidence of the breakup events. In Fig. 4.8a the correlation between the Z and v_z^{CM} of the two breakup fragments obtained in the AMD asy-stiff simulation for the reaction $^{58}\text{Ni} + ^{58}\text{Ni}$ at 32 A MeV is shown. In the plot on the left, two populated regions are visible: one includes heavy fast fragments, with $Z \sim 20$, the other contains lighter fragments, with $Z \lesssim 10$, located at lower velocities. In the plot on the right, the same Z vs v_z^{CM} correlation is drawn in different colours for the heavy (in red) and light (in black) breakup fragments, in order to better highlight the two loci associated to them. Fig. 4.8b shows the Z vs v_z^{CM} correlation of the QP reconstructed from these two fragments, by summing their charge numbers and considering the velocity of their center of mass: the average velocity of the reconstructed QP is lower than that of the QP in the previous selection of binary DIC events, suggesting a larger average dissipation in the observed breakup channel. As evident from the plots in

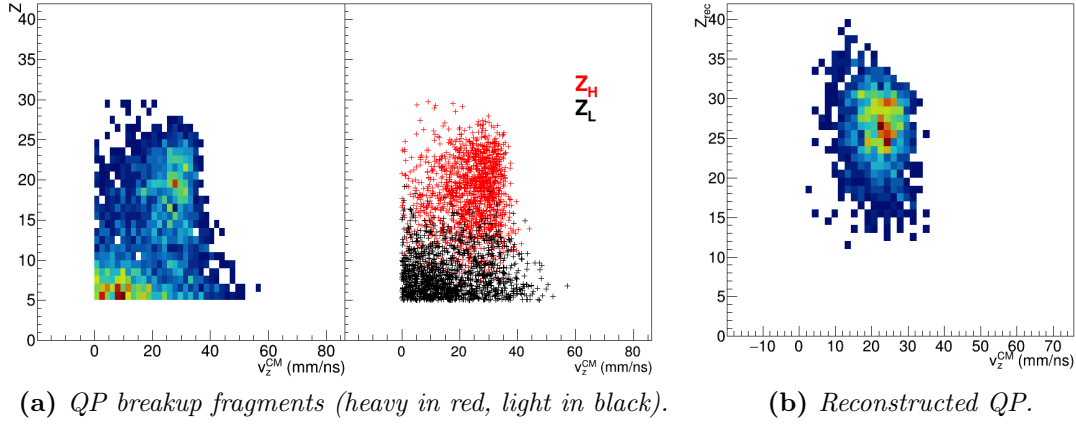


Figure 4.8: Z vs v_z^{CM} correlations for the QP breakup primary events for the reaction $^{58}\text{Ni}+^{58}\text{Ni}$ at 32 A MeV. The correlations for the two breakup fragments and for the reconstructed QP are shown. The asy-stiff parametrisation is assumed for this AMD calculation.

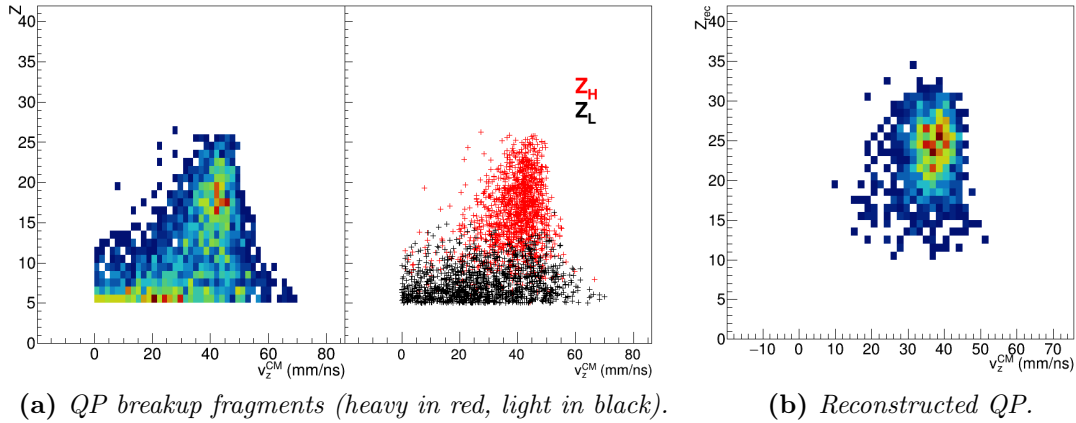


Figure 4.9: Z vs v_z^{CM} correlations for the QP breakup primary events for the reaction $^{58}\text{Ni}+^{58}\text{Ni}$ at 52 A MeV. The correlations for the two breakup fragments and for the reconstructed QP are shown. The asy-stiff parametrisation is assumed for this AMD calculation.

panel (a), the split is preferentially asymmetric in Z , as expected for a dynamical breakup (see Sec. 1.3). Moreover, the light fragment is mostly emitted backwards with respect to the heavy one, as can be noticed from their average velocities along the beam direction. This last feature can be visualised also by means of the α angle, defined in eq. (1.7). In Fig. 4.10a the correlation between the α angle and the charge asymmetry parameter η , defined as:

$$\eta = \frac{Z_H - Z_L}{Z_H + Z_L} \quad (4.5)$$

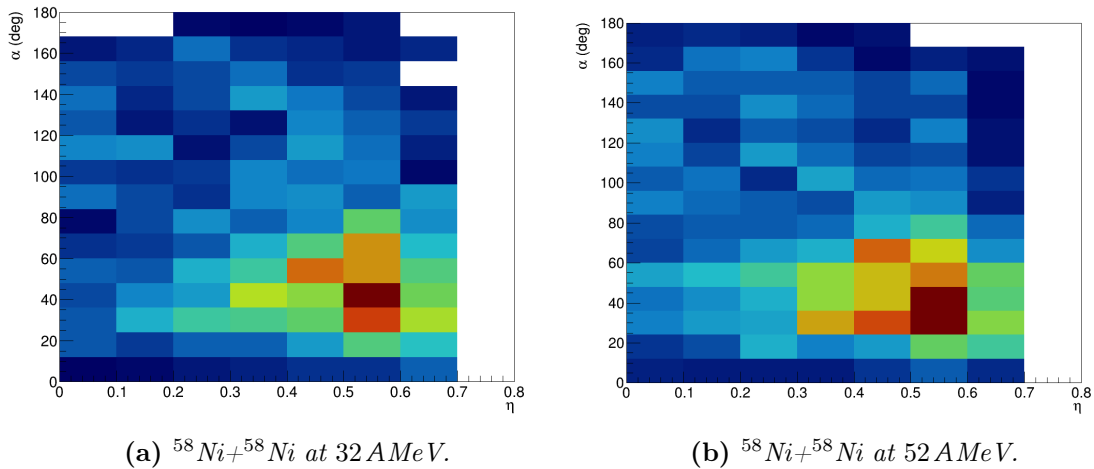


Figure 4.10: Correlation between the α angle and the charge asymmetry parameter η of the QP breakup primary fragments obtained with AMD asy-stiff calculations for the $^{58}\text{Ni}+^{58}\text{Ni}$ reaction at the two energies.

is shown. For a symmetric split $\eta = 0$, while a larger charge asymmetry between the two breakup fragments is related to an η value closer to one. In Fig. 4.10a one can notice that the most asymmetric splits, which are more populated, are associated to small α angles, corresponding to aligned configurations with the light fragment emitted backward. This behaviour is widely reported in the literature for the dynamical fission (see Sec. 1.3).

Similar remarks can be made about the plots in Fig. 4.9 and Fig. 4.10b, where the Z vs v_z^{CM} and α vs η correlations obtained for the breakup fragments produced in the reaction $^{58}\text{Ni}+^{58}\text{Ni}$ at the higher energy are shown. The other reactions feature an analogous behaviour.

4.2 Statistical model: the GEMINI code

For a complete description of the reaction, the hot nuclear fragments produced by the dynamical code must be processed by a statistical code, or afterburner, in order to simulate their decay towards the ground state. Many statistical codes (PACE [134], CASCADE [135], Simon [136], HF1 [137]...) are currently available. One of the most widely used in nuclear physics is GEMINI [15, 121]. GEMINI is a Monte Carlo code developed by R. J. Charity for the description of the de-excitation of hot nuclei, which is suitable for a large range of sizes, energies and angular momenta of the input nuclei. After a previous version developed in FORTRAN 90 [121], a second updated version called GEMINI++ [15] was implemented in C++. In this work the most recent version GEMINI++ has been employed.

The output file of the dynamical code (AMD in our case), namely the parameters defining the information on the charge Z , mass A , angular momentum J and exci-

tation energy E^* of all the primary fragments, is used as input for GEMINI, which treats each nucleus as an excited nuclear system in thermal equilibrium (just like in the CN model), i.e. each primary fragment is treated as an isolated excited source, decaying as a CN. The de-excitation is performed as a series of sequential binary decays, and the particle emission ends either when further emission is forbidden due to energy conservation laws, or when it becomes negligible due to the competition with other decay modes, such as γ -ray emissions.

Different formalisms have been implemented in GEMINI in order to properly treat the various de-excitation modes. In fact, the evaporation of light particles (implemented for n, p, d, t, ^3He , α , ^6He , ^{6-8}Li and ^{7-10}Be) is described by means of the Hauser-Feshbach formalism [26], while the total fission yield is calculated within the Bohr-Wheeler formalism [138], except for the fission of light systems or the asymmetric fission of the heavier ones, for which the Moretto binary decay formalism [139] is used. Note that not all the available statistical codes include fission among the possible decay channels.

The Hauser-Feshbach formalism for particle evaporation explicitly takes into account and conserves the angular momentum. This feature is extremely important since GEMINI is used also to simulate the decay of excited nuclei with high spin. According to this formalism, for the evaporation of a particle i from a nucleus with excitation energy E^* and angular momentum J_{CN} , the partial decay width can be expressed as [15]:

$$\Gamma_i(E^*, J_{CN}) = \frac{1}{2\pi\rho_{CN}(E^*, J_{CN})} \int d\varepsilon \sum_{J_d=0}^{\infty} \sum_{J=|J_{CN}-J_d|}^{J_{CN}+J_d} \sum_{l=|J-S_i|}^{J+S_i} T_\ell(\varepsilon) \rho_d(E^* - B_i - \varepsilon, J_d) \quad (4.6)$$

where J_d is the angular momentum of the daughter nucleus, S_i , J and ℓ are the spin, total and orbital angular momenta of the evaporated particle, ε and B_i are its kinetic and separation energies, T_ℓ is its transmission coefficient and ρ_{CN} and ρ_d are the level densities of the parent and daughter nuclei, respectively.

For the nuclear level density the Fermi gas approximation is assumed:

$$\rho_{Fg}(E^*, J) = \frac{(2J+1)}{24\sqrt{2}a^{1/4}U^{5/4}\sigma^3} \cdot e^S \quad \text{with} \quad S = 2\sqrt{aU} \quad (4.7)$$

where S is the nuclear entropy, a the level density parameter and U is the thermal energy obtained as the difference between the excitation energy and the rotational energy of a rigid rotor with the same density distribution of the nucleus, with a moment of inertia I_{rig} :

$$U = E^* - E_{rot}(J) = E^* - \frac{J(J+1)\hbar^2}{2I_{rig}} \quad (4.8)$$

In GEMINI the rotational energy $E_{rot}(J)$ is replaced by the yrast energy⁵ $E_{yrast}(J)$, in order to take into account the deformation of the nuclear shape due to the centrifugal

⁵The yrast energy $E_{yrast}(J)$ is defined as the minimum energy of a nuclear state with a given angular momentum J .

forces. The level density parameter $a(U)$, which undergoes strong fluctuations due to shell effects, is given by [140]:

$$a(U) = \tilde{a}_{\text{eff}}(U) \left[1 - \tanh\left(\frac{U}{\eta} + \frac{J}{J_\eta}\right) \frac{\delta W}{U} \right] \quad (4.9)$$

where δW is the shell correction to the liquid-drop mass, η and J_η are free parameters, and $\tilde{a}_{\text{eff}}(U)$ is an effective smoothed level density parameter; in practice, for the nuclei produced in our case $\tilde{a}_{\text{eff}} = A/k_0$, where $k_0 = 7.3$ MeV.

The transmission coefficient in eq. (4.6) is determined from the inverse reaction (particle absorption) by adopting the ingoing wave boundary condition (IWBC) model [141]: a distribution of Coulomb barriers is introduced, trying to describe the thermal fluctuations of the nuclear shape and/or the fluctuations of the diffuseness of its surface. This distribution is actually needed in order to fit the low-energy region of the experimental light particle energy spectra. The transmission coefficient $T_\ell(\varepsilon)$ is calculated as the average of three IWBC transmission coefficients:

$$T_\ell(\varepsilon) = \frac{T_\ell^{R_0-\delta r}(\varepsilon) + T_\ell^{R_0}(\varepsilon) + T_\ell^{R_0+\delta r}(\varepsilon)}{3} \quad (4.10)$$

associated to three different radii (R_0 , $R_0 \pm \delta r$) for the nuclear potential, where $\delta r \propto \sqrt{T}$ according to the hypothesis of thermal fluctuations, T being the nuclear temperature.

The kinetic energy spectra of the evaporated particles produced by GEMINI are sensitive to the parametrisation of the level density parameter, to the transmission coefficients and to the angular momentum dependence of the yrast energy. The required parameters have been tuned by R. J. Charity in order to reproduce experimental data from complete fusion reactions [15]. The provided standard set of parameters has been used in the present work.

4.2.1 The Evaporation Attractor Line (EAL)

As pointed out in Ref. [142], the nuclear residues obtained from the de-excitation of the hot primary fragments via particle evaporation tend to move in the chart of nuclides towards a locus called Evaporation Attractor Line (EAL), as shown in Fig. 4.11. In this plot, the evolution of the average N and Z of the evaporation residue with the excitation energy is represented by the solid curves, starting from different initial excited CNs. The lines clearly approach the EAL. The final position of the residue depends both on the initial position of the parent nucleus and on the initial available excitation energy. The EAL virtually divides the $N - Z$ plane in two parts. In fact, for high excitation, the primary fragments in the neutron rich side tend to emit more neutrons than protons, moving almost horizontally in the nuclide chart. On the other hand, the excited fragments on the neutron deficient side evaporate proton rich ejectiles, thus following a more vertical path. However, the $N - Z$ evaporation decay trajectory cannot cross the EAL. When a fragment

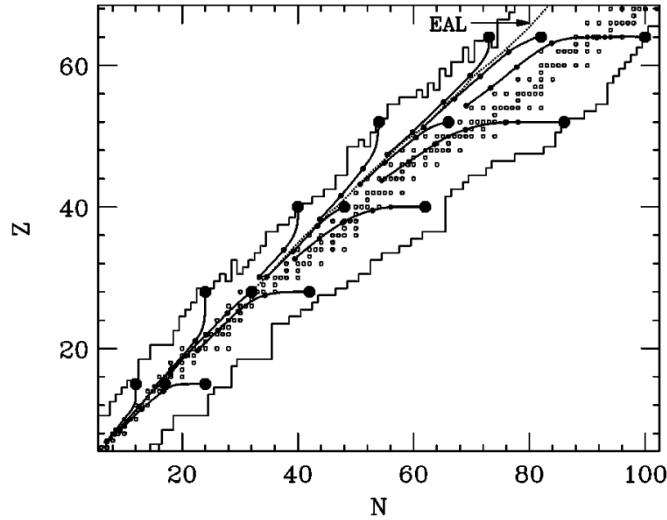


Figure 4.11: The EAL plotted on the chart of nuclides. The large solid circles indicate the original position of the parent nucleus. The curves follow the loci populated by the evaporation residues as the excitation energy increases, as predicted by the GEMINI code. From Ref. [142].

approaches the EAL, the proton and neutron emission probabilities are similar, and the subsequent evaporation products tend to fall along the line. The position of the EAL can be therefore obtained as the ratio between the partial decay widths for neutron (Γ_N) and proton (Γ_Z) evaporation. A parametrisation of the EAL evaluated from GEMINI calculations is [142]:

$$A = 2.072Z + 2.32 \times 10^{-3}Z^2 \quad (4.11)$$

The EAL coincides with the β -stability line for light nuclei, while for the heavier ones it deviates towards the neutron deficient region due to the larger Coulomb barrier for proton emission.

4.3 Software filter

As already mentioned in Sec. 4.2, the output file of the AMD code (primary events) is used as an input for the GEMINI code to produce secondary events. In order to increase the statistics, 100 secondary events have been produced for each primary event. The simulated data must then be filtered through a software replica of the experimental apparatus in order to compare them with the experiment. The software filter takes into account the geometrical features of the setup (e.g. the angular coverage of each detecting module), and the energy threshold, energy resolution and working status of each detector.

We have taken advantage of a software (`kaliveda-sim` [143]), which is part of the KaliVeda package. `Kaliveda-sim` accepts both primary and secondary events as input. For the primary events, it also includes a simulation of the decay of excited

fragments, based on GEMINI++. However, in our analysis, we have not exploited the GEMINI++ simulation included in `kaliveda-sim`. The primary events have been instead processed with a standalone version of GEMINI++. Only the filtering capabilities of `kaliveda-sim` have been exploited.

The simulated data can be filtered according to various experimental conditions: the user can choose among many datasets related to the experimental campaigns of both INDRA and FAZIA collaborations. The E789 experiment has been recently added to the list of available filters. Since the working status of each detector module can change during data taking, a specific run number can be specified when using a filter. Three different filter types are available in `kaliveda-sim`:

- *Geometric*: only the angular coverage of the setup is taken into account. The particles are considered detected if they hit at least one detector.
- *Geometry+Thresholds*: the particles must also have enough energy to escape the target and overcome the identification threshold of the apparatus. If two particles hit the same detector, they are both marked as unidentified and rejected.
- *Full*: this option works only for the datasets which are fully calibrated and implemented in KaliVeda. In this case, also the working status of each detector is taken into account to simulate the operability of each module.

The simulated distributions and plots that will be presented in the following have been obtained by applying the “Full” filter, unless otherwise specified. As an example, the effect of the application of the filter can be seen in Fig. 4.12, showing Z vs v_{lab} plots of the simulated secondary fragments produced in the reaction $^{58}\text{Ni}+^{58}\text{Ni}$ at 32 A MeV. The plot in panel (a) is the 4π distribution, i.e. the whole distribution with no filter applied, while the one in panel (b) is obtained after the application of `kaliveda-sim` “Full” filter. The lack of neutrons ($Z = 0$), which cannot be detected by the apparatus, and the depletion of the QT region due to the identification thresholds are evident.

The filtered events have been stored in a TTree object [112] having the same data structure as the one employed for the experimental data, with the only addition of some other useful information not available for the latter, e.g. the impact parameter of the collision, b , or the primary fragment from which each secondary particle originates. After that, both experimental and simulated data have been analysed with a code developed in Florence and used for physics analysis of heavy ion collisions since many years⁶ (`garf_analisi`). The final spectra and observations can be therefore considered as directly comparable.

⁶In principle, `kaliveda-sim` also includes a code for such an analysis. However it has not been used in this work.

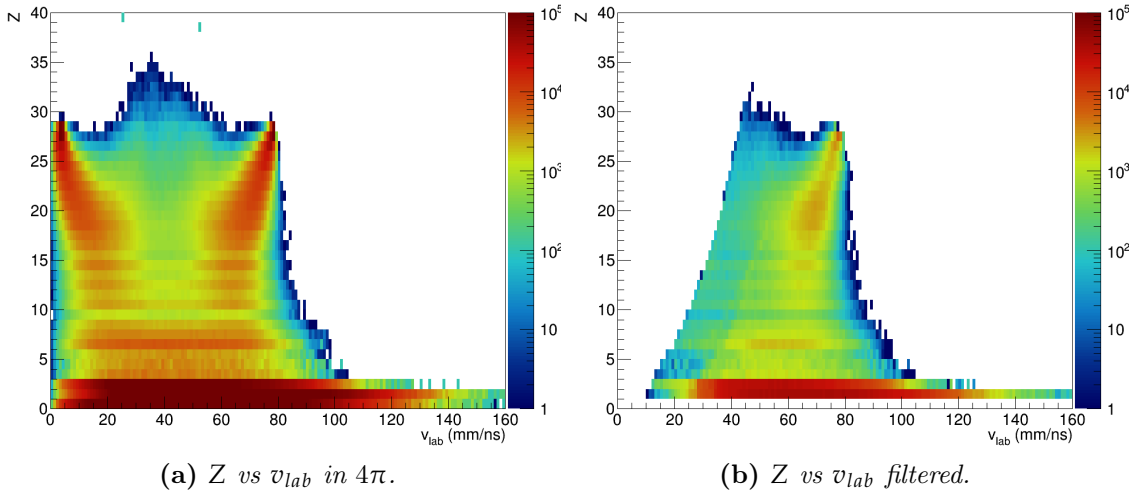


Figure 4.12: Z vs v_{lab} correlations of the simulated secondary fragments for the reaction $^{58}\text{Ni}+^{58}\text{Ni}$ at 32 AMeV. In panel (a) the 4π distribution is shown. In panel (b) the same event set is shown after being processed by the `kaliveda-sim` “Full” filter. The QT region has been cut out by the filter, due to the identification thresholds.

4.4 First comparisons with experimental data

Fig. 4.13 shows a first comparison between the results obtained with the experimental data and those obtained with the AMD+GEMINI simulation, filtered with `kaliveda-sim`: the Z vs v_{lab} correlations for all the fragments produced in the reactions $^{64}\text{Ni}+^{64}\text{Ni}$ at 32 AMeV (panel (a)) and 52 AMeV (panel (b)) are reported as an example. The experimental results are shown on the left, the simulated ones (for the asy-stiff parametrisation) on the right. The simulations with AMD+GEMINI well reproduce the main features of the experimental correlations. In all panels, the locus associated to the QP-like fragments is readily recognisable. Some difference is present between the two plots in panel (a), for the reaction at 32 AMeV. Firstly, the simulation slightly underestimates the statistics in the intermediate Z region ($9 \lesssim Z \lesssim 15$). Secondly, a region with $Z \gtrsim Z_{proj}$ and $v \sim v_{CM}$ (indicated by the blue arrow) is populated, at variance with the experimental data. The latter discrepancy, however, regards only a very small contribution in the overall statistics. More details can be appreciated in the distributions of the atomic number and velocity of the fragments, shown in Fig. 4.14a. The first two plots are the y -axis and x -axis projections of the plots in Fig. 4.13, respectively, while the rightmost plot is the velocity spectrum including only the fragments with $Z > 4$, thus excluding the LCPs and IMFs, which constitute most of the statistics (please note the linear scale on the y -axis of the rightmost panel). From the velocity distributions, it seems that the simulation slightly overestimates the energy dissipation in the collision, especially at 32 AMeV beam energy. In fact, in the rightmost plot, the velocity peak related to the QP-like fragments obtained with the AMD+GEMINI calculations is

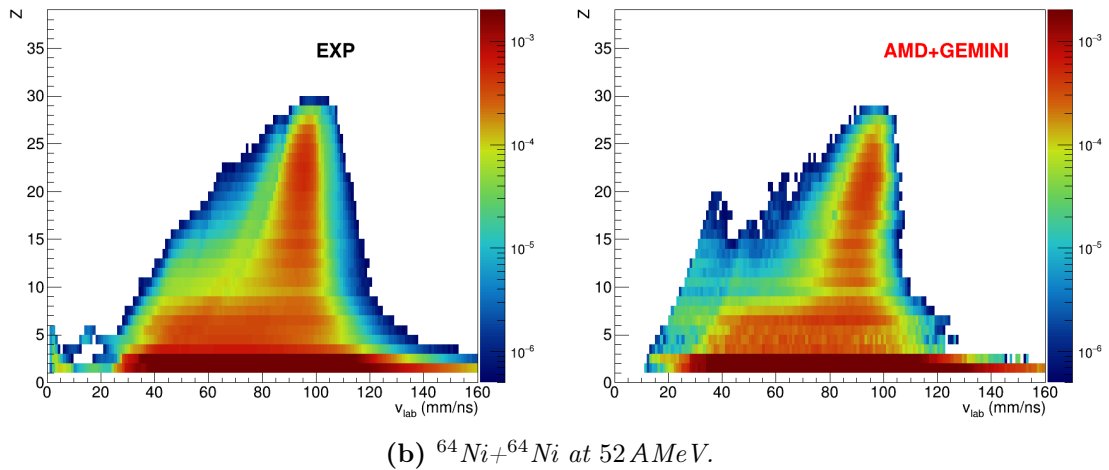
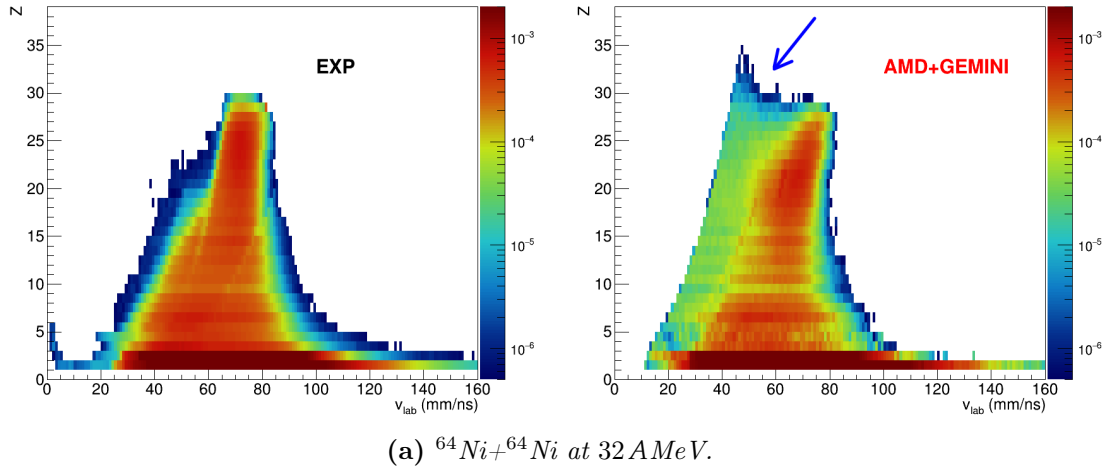


Figure 4.13: Comparison between the experimental (left) and simulated (right) Z vs v_{lab} correlations (filtered AMD+GEMINI, asy-stiff) for all the fragments produced in the reaction $^{64}\text{Ni}+^{64}\text{Ni}$ at the two beam energies. The plots are normalised to their integral.

shifted to the left with respect to the one experimentally obtained. This discrepancy has already been highlighted in the literature for other systems [60, 69]. In the central plot we observe a good agreement between AMD+GEMINI and the experimental data, perhaps with a slightly greater abundance of high energy LCPs in the simulations. In summary, however, the overall agreement between experiment and simulations is satisfying. In the other plots of Fig. 4.14 ((b)-(d)) the comparisons between simulated and experimental data for all the other reactions are shown. The reactions induced by beams of the same energy have similar characteristics in terms of charge and velocity distributions. Interesting differences arise when isospin related observables are investigated, as it will be shown in Chapter 6.

In the next chapter, a more detailed comparison between experimental and simulated data will be presented for the two reaction channels which have been studied in detail in this work: the QP evaporation and the QP breakup channels.

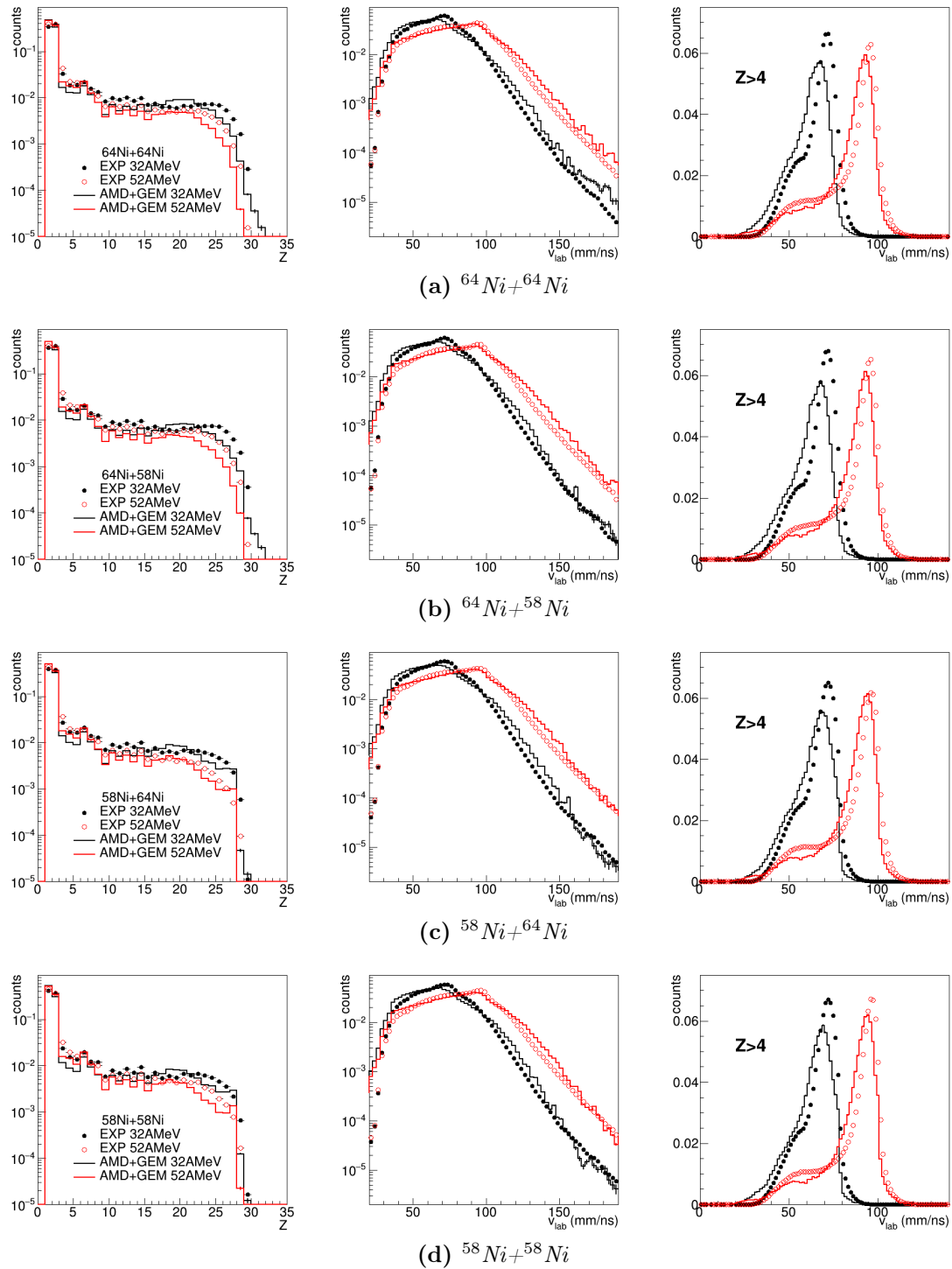


Figure 4.14: Distributions of Z and v_{lab} of the experimental and simulated (asy-stiff AMD+GEMINI, filtered) fragments produced in the $^{58,64}\text{Ni}+^{58,64}\text{Ni}$ reactions. All histograms are normalised to their integral.

Selection of the reaction channels

In Sec. 3.4, a preliminary selection of the experimental events has been presented. Since we aim at characterising different reaction mechanisms, the events satisfying the global conditions have to be further classified and analysed. In this work, two particular reaction channels have been studied in detail: the **QP evaporation** (or QP remnant) channel, in which a single heavy fragment is accompanied just by light particles ($Z \leq 4$), mostly produced by its de-excitation, and the **QP breakup** channel, characterised by the presence of two big fragments whose characteristics are comparable to those described in Sec. 1.3.

In the present chapter, the selection criteria for the QP evaporation and QP breakup channels will be presented. The same conditions will be applied both on experimental and simulated data, and a comparison between the results obtained with the experimental dataset and the AMD+GEMINI predictions will be shown. Since the simulated events include the information on the impact parameter b , they can also be exploited to study experimentally accessible order variables correlated to the reaction centrality. The last section is therefore devoted to a discussion on some reaction centrality estimators, that will be then used in the analysis presented in Chapter 6.

5.1 QP evaporation channel selection

In order to select the two reaction channels, some global characteristics of each event must be evaluated, such as the multiplicities M of different kinds of particles. The different fragments are classified according to their Z value, as shown in Tab. 5.1. Apart from the well known definitions of LCPs and IMFs, in this work we will use the label BF (Big Fragment) for $Z > 4$ and QPF (QP-like Fragment) for $Z > 14$.

The **QP evaporation** channel is characterised by the presence of just one big fragment, namely the **QP remnant**, accompanied by LCPs and, at most, IMFs. In the following, this channel will be briefly referred to as **QPr**. In order to be recognised as QP remnant, the big fragment must be forward emitted in the CM reference frame. Moreover, a lower limit for its charge range is imposed: as reported in Tab. 5.1, a QP-like fragment is required to have $Z > 14$, corresponding to a maximum projectile charge loss $\Delta Z = 13$, i.e. about 46% of the original projectile

Table 5.1: List of the abbreviations adopted in the following. Notice that the QP-like fragments (QPF) constitute a subclass of big fragments (BF).

Abbr.	Meaning	Z interval
LCP	Light Charged Particle	$Z = 1, 2$
IMF	Intermediate Mass Fragment	$Z = 3, 4$
BF	Big Fragment	$Z > 4$
QPF	QP-like Fragment	$Z > 14$

charge. This choice of the Z limit for the QPF is somewhat arbitrary. It is slightly lower but nevertheless consistent with what can be found in the literature (see e.g. Refs. [67,69]). However, we specify that the main observations that will be presented in the following have been tested also imposing a different value for the minimum atomic number of the QPF. In summary, an event fulfilling the conditions:

$$\begin{aligned} M_{BF} &= 1 \\ Z_{BF} &> Z_{QPF}^{lim} = 14 \\ v_z^{CM}(BF) &> 0 \end{aligned}$$

is considered a QPr event. At this level, no further condition is imposed on the accompanying LCPs and IMFs.

We now present some general properties of the events sorted into the QPr channel selection, without going into their isospin-related properties, which will be treated in detail in the next chapter. We will show first the behaviour of the heavier fragments, then we will concentrate on the emitted LCPs. From now on, unless otherwise specified, we only show model predictions for an asy-stiff parametrisation of the symmetry energy. In fact, most of the differences between the asy-stiff and the asy-soft parametrisations are noticeable only when it comes to analysing the isospin observables. As an example, in Fig. 5.1 the correlations between the charge and the velocity of the QP remnants of the events in the QPr channel for the reaction $^{58}\text{Ni}+^{58}\text{Ni}$ are shown for the two beam energies. The component of the v^{CM} along the beam axis is used on the abscissa. Both the experimental (left panels) and the AMD+GEMINI (filtered, right panels) results are reported. The area associated to the QP remnant is evident in each correlation, and tends to the original projectile velocity v_{beam}^{CM} , which is also indicated in each plot. A general agreement between the characteristics of the QPr events selected in the experimental and simulated datasets can be noticed, with the exception of a few central events (showing features compatible with an incomplete fusion process, i.e. $Z \gtrsim Z_{proj}$ and $v_z^{CM} \sim 0$, see Sec. 4.4) in the simulation of the reaction at 32 A MeV, in Fig. 5.1a.

The properties of the selected QP remnants can be appreciated in more detail in the histograms shown in Fig. 5.2: the distributions of the charge Z , the component of the velocity along the beam axis v_z^{CM} and the scattering angle θ^{CM} of the biggest fragment detected in the QPr events are there reported for all the studied reactions. All the distributions are normalised to their integral. The histograms drawn with the

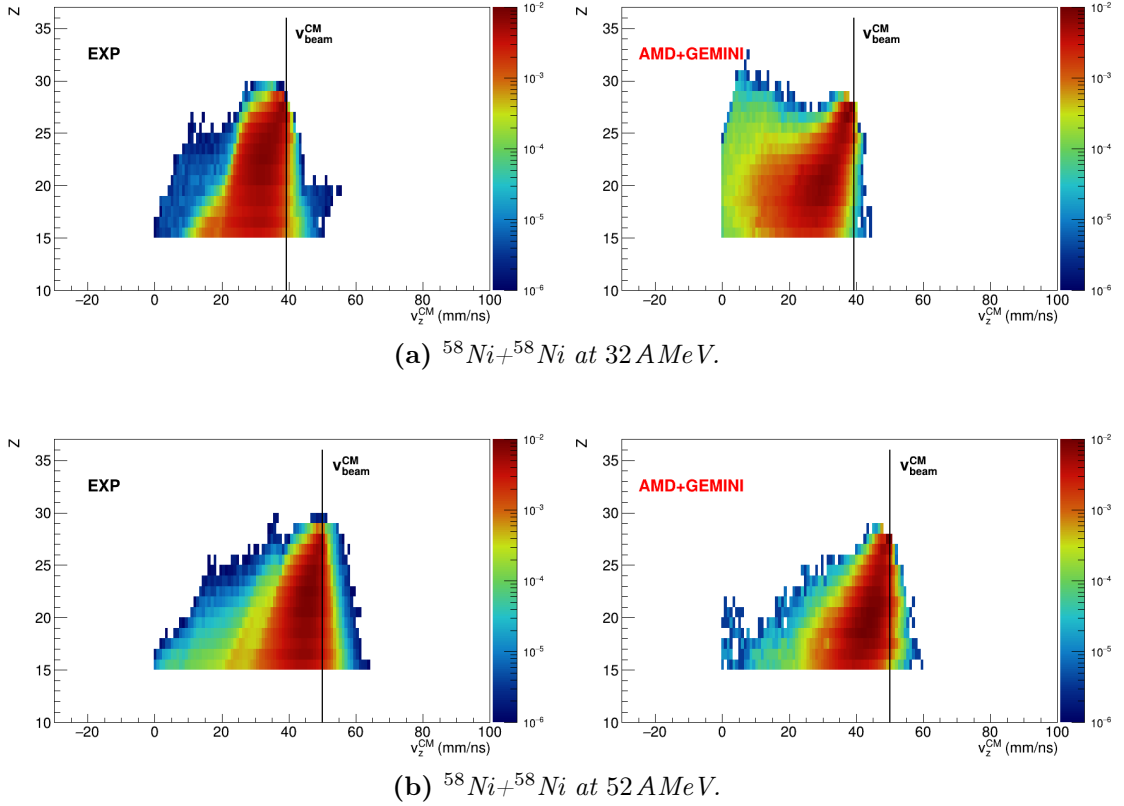


Figure 5.1: Comparison between the experimental (left) and simulated (right) Z vs v_z^{CM} correlations of the biggest fragment (QP remnant) of the events falling in the QPr channel selection. The plots are shown for the reaction $^{58}\text{Ni}+^{58}\text{Ni}$ at both energies: similar results are obtained for the other systems. The sharp cut at $v_z^{CM} < 0$ is due to the QPr selection condition $v_z^{CM}(BF) > 0$. The simulated plots are those obtained with AMD+GEMINI assuming an asy-stiff parametrisation of the N EoS. All the plots are normalised to their integral.

circular markers refer to the experimental data (full circles for 32 A MeV, open circles for 52 A MeV), while those drawn with a line are obtained with AMD+GEMINI (different colours are used for the two beam energies, see legend on each plot). Some differences between the model predictions and the experimental observations can be noticed in the Z distributions, shown in the leftmost plots: in fact, the QP remnants in the experimental events tend to be heavier than those in the simulated events, pointing in the direction of a higher degree of dissipation in the model, as anticipated in Sec. 4.4. In general, we find a better agreement for the reactions at 52 A MeV, for all the inspected systems. We also notice that the simulated distributions are smoother than the experimental ones: in the latter, a higher production yield is found for the even- Z QP remnants with respect to the neighbouring odd- Z ones. This odd-even *staggering* phenomenon can be better appreciated in Fig. 5.3, where the same experimental Z distributions already shown in the four leftmost plots of

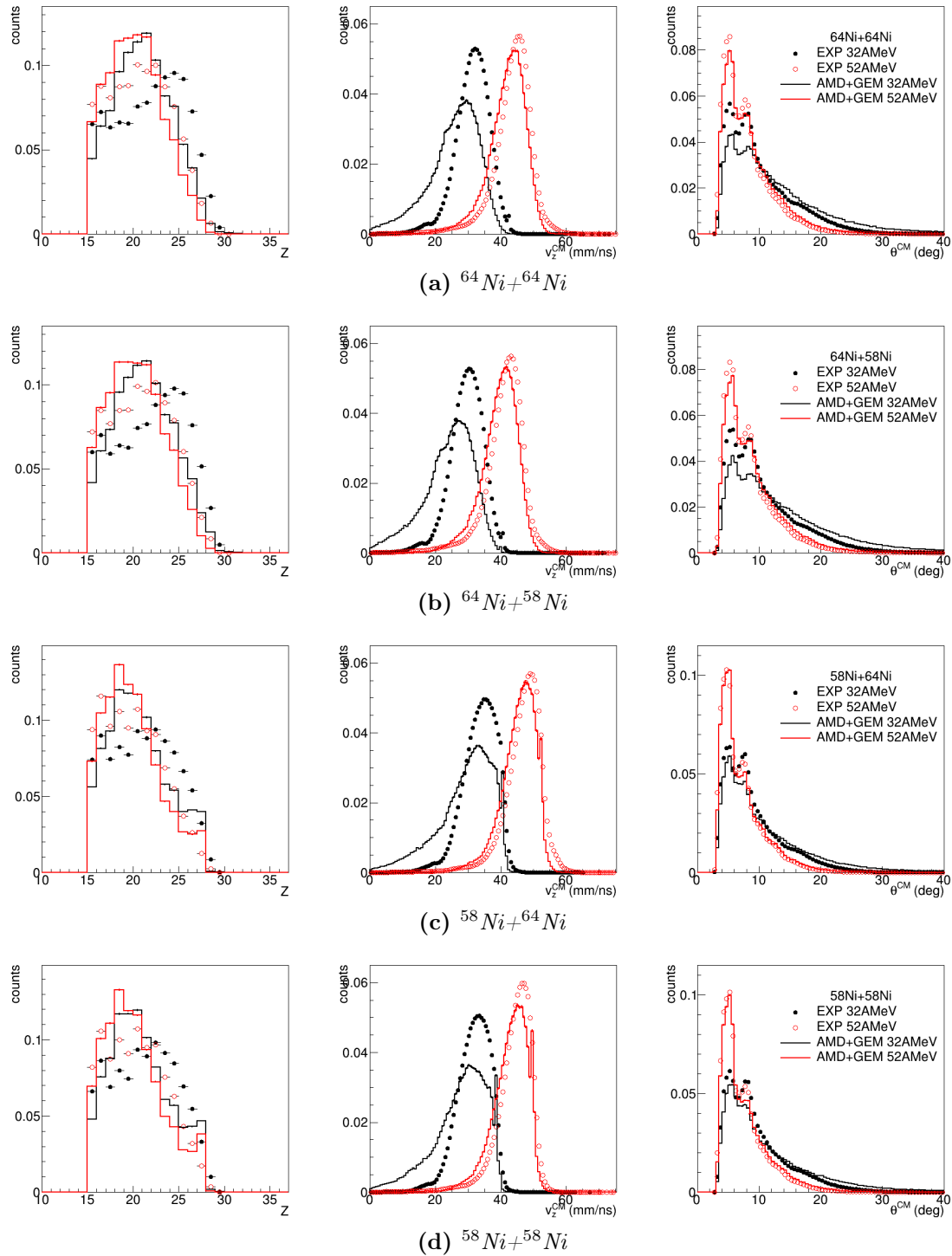


Figure 5.2: Comparison between the experimental and simulated (asy-stiff AMD+GEMINI, filtered) distributions of Z (left), v_z^{CM} (center) and θ^{CM} (right) of the biggest fragment (QP remnant) of the events falling in the QPr channel selection. All histograms are normalised to their integral. Each panel, from (a) to (d), refers to a different system.

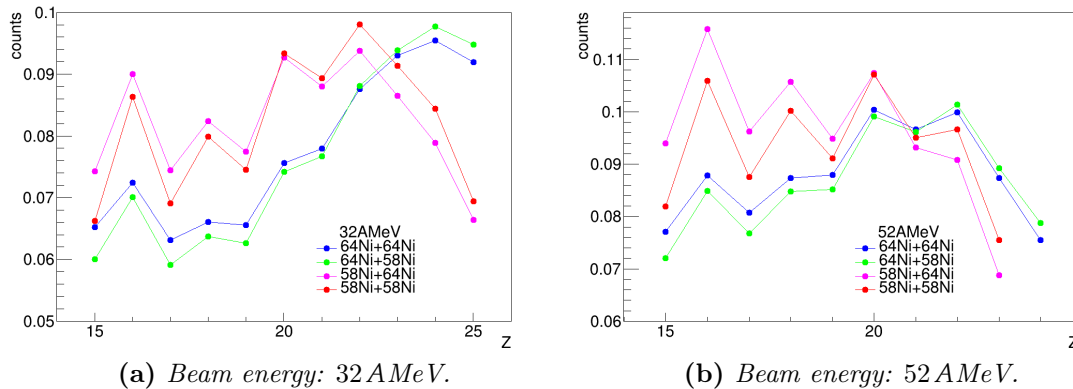


Figure 5.3: Experimental charge distributions for the QP remnants produced in the four reactions at 32 A MeV (panel (a)) and at 52 A MeV (panel (b)). The histograms are the same already shown in the left-most plots of Fig. 5.2 (experimental, drawn with circular markers). Here, lines are drawn to connect the markers, in order to guide the eye and to highlight the odd-even staggering phenomenon.

Fig. 5.2 are plotted with lines connecting the markers in order to guide the eye. The odd-even staggering is a very general observation in many contexts where nuclear species are produced, evidenced also at intermediate energies [144–146]. It is commonly interpreted as an effect of the nuclear pairing forces in the last steps of the de-excitation chain of the excited fragments produced in the interaction: in fact, in even-even nuclei the pairing interaction tends to increase the separation energies, thus suppressing the decay by evaporation at the end of the decay cascade, when the remaining excitation energy is low. As already recognised in Ref. [144], also in the present case the effect is more evident in the neutron deficient system. Moreover, by comparing the charge histograms associated to the different systems in Fig. 5.3, it can also be observed that the QP remnant produced in the reactions induced by the neutron rich ^{64}Ni projectile has generally a higher Z than that resulting from the ^{58}Ni -induced reactions. This can be interpreted as a result of the higher proton content of the emissions expected from the more neutron deficient QP produced in the second case.

By comparing the v_z^{CM} distributions for the QP remnants (central plots in Fig. 5.2) we notice that, in general, a better agreement between experimental and simulated data is obtained at 52 A MeV than at 32 A MeV. In the filtered AMD+GEMINI datasets, the average QP velocity is generally lower than in the experimental data, pointing towards a too large energy dissipation in the model: this behaviour is only slightly visible at 52 A MeV, while it is more pronounced at 32 A MeV, where a marked tail towards low v_z^{CM} can be seen in the simulated distribution. In some respects, this discrepancy at 32 A MeV can be ascribed to the above mentioned central events compatible with incomplete fusion events that we find in the AMD+GEMINI predictions. However, some refinements of the software filter are in progress in order to verify if these events can be due to incorrectly set identification thresholds.

A good agreement between experimental data and model predictions is found in the QP remnant θ^{CM} distributions (rightmost plots in Fig. 5.2). Also in this case, only a slight discrepancy can be noticed, mostly at 32 AMeV. However the main features of the distributions, related to the geometrical acceptance of the apparatus, are correctly reproduced by the software filter (see, e.g. the cut of the distributions at low θ^{CM} , corresponding to $\theta^{lab} \lesssim 1.4^\circ$, due to the small forward solid angle which is not covered by FAZIA).

Further characteristics of the selected QPr events can be seen through the emission pattern of the LCPs detected in coincidence with the evaporation residue of the QP. As an example, Fig. 5.4 shows the v_\perp vs $v_{//}$ correlations for α particles emitted in coincidence with a QP remnant. The reaction is $^{58}\text{Ni}+^{58}\text{Ni}$, both at 32 AMeV and at 52 AMeV. The velocity components are expressed in the CM reference frame, similarly to the plots shown in Fig. 1.2 of Sec. 1.1.1. Similar results are obtained for the other LCPs. The experimental plots, on the left, are quite well reproduced by the AMD+GEMINI filtered simulations. The forward semicircular Coulomb ring is clearly visible in each correlation, centered at the average velocity of the QP remnant for that reaction (see the velocity distributions in Fig. 5.2), thus pointing to the QP as the moving source of the emitted α particles¹. The corresponding backward Coulomb ring, related to the QT emission, is evidently absent, as expected; this is caused by the fact that most of the LCPs produced in the QT evaporation are collected by the uncalibrated INDRA rings, and cannot be included in these plots due to the lack of information on their velocity. Some QT forward emission contributions may be present in a region close to the CM ($v_{//} \sim 0$). Diagonal regions of lower statistics, associated to the presence of uncovered polar angle intervals (i.e. empty spaces between the INDRA rings) can also be recognised. This geometrical effect is nicely reproduced by the software filter. Since in FAZIA the dead areas are not associated to defined polar angle intervals, these artifacts are strongly reduced, as can be better appreciated in the bottom panel of each correlation (labelled as “FAZIA only”), where only the α particles hitting FAZIA are included.

The QPr channel can be further divided into two complementary subclasses. In the first one, the QP remnant is accompanied only by LCPs, mostly produced by its decay via evaporation (QPr+LCP). The second class is characterised by the presence of IMFs (only one IMF in most cases) in coincidence with the residue (QPr+IMF), generally together with other LCPs. The former subclass QPr+LCP is the most populated of the two. In Tab. 5.2 the percentages of the accepted events (i.e. those fulfilling the global conditions introduced in Sec. 3.4) that are selected by the QPr channel conditions are reported for each reaction, both in the experimental and the simulated dataset. The percentages relative to the QPr+LCP subclass are reported

¹In Sec. 1.1.1 it has been explained that the expected binary character of the exit channel emerges in the v_\perp vs $v_{//}$ plots for semiperipheral and peripheral reactions. Notice that by imposing a minimum limit for Z_{QP} we indirectly selected mostly semiperipheral and peripheral reactions, in which the degree of dissipation is lower and only a limited fraction of the original projectile charge is lost. The central incomplete fusion-like events in the simulations at 32 AMeV constitute an exception, but their contribution to the overall statistics is really small, and therefore the Coulomb rings remain clearly visible.

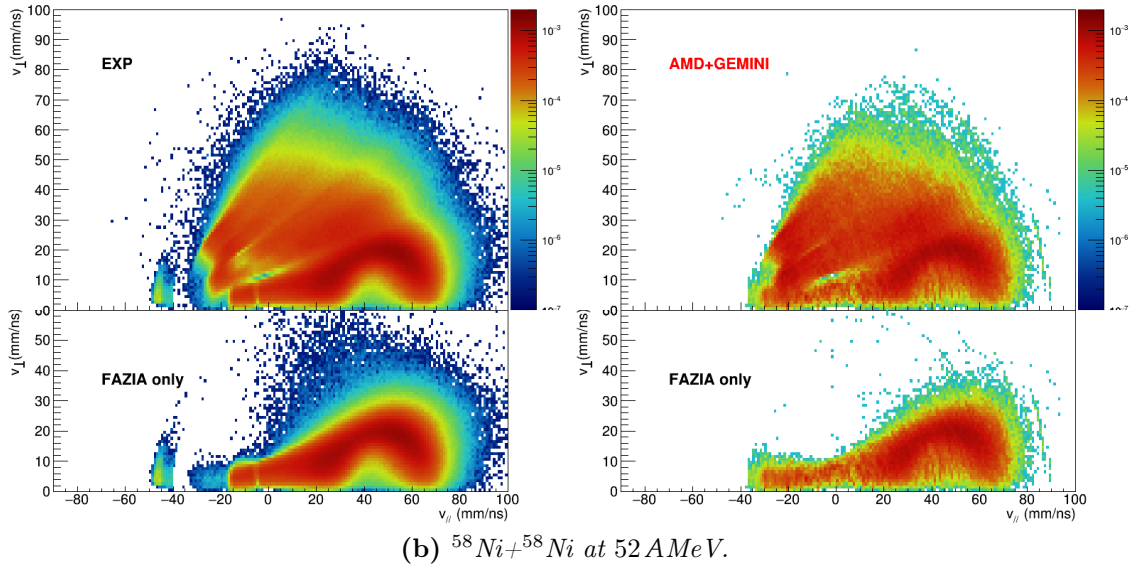
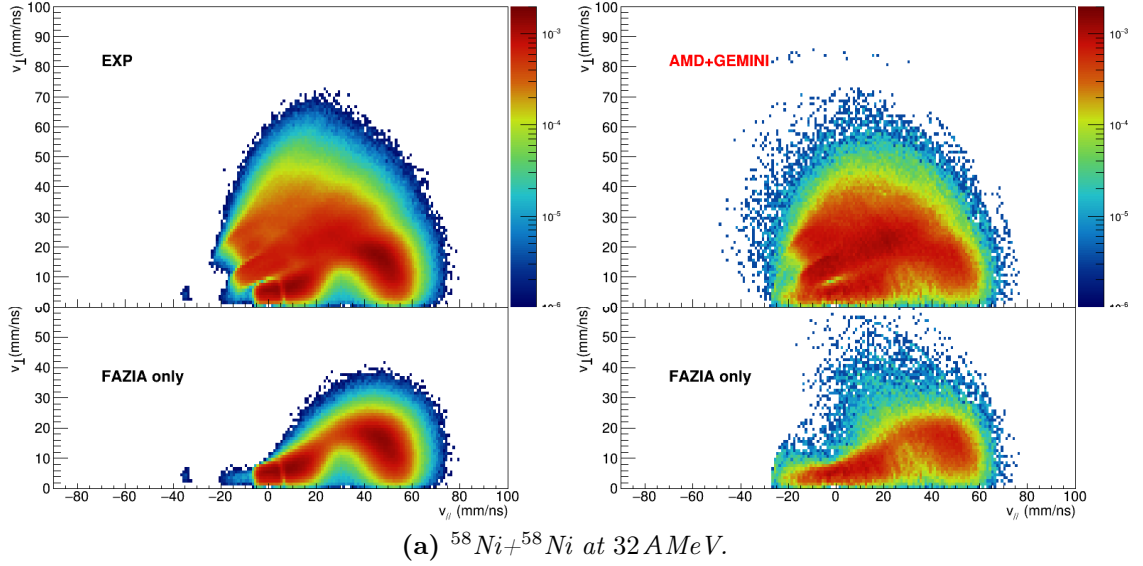


Figure 5.4: Correlations between the perpendicular v_{\perp} and parallel v_{\parallel} components of the velocities in the CM reference frame of the α particles in coincidence with the QP remnant for QPr events. The α particles are chosen for their high production yield, but similar results are obtained for the other LCPs. The system $^{58}\text{Ni}+^{58}\text{Ni}$ is shown as an example at both energies, 32 A MeV (a) and 52 A MeV (b). The experimental results are plotted on the left, while the AMD+GEMINI model predictions (asy-stiff) on the right. The bottom panel of each correlation (“FAZIA only”) is obtained considering only the particles detected by FAZIA. All the plots are normalised to the total number of QPr events in the specific reaction dataset.

Table 5.2: Experimental and simulated percentages of QPr events over the total number of events selected with the global conditions for each reaction. Only the results of the AMD+GEMINI simulations assuming an asy-stiff parametrisation are listed: the asy-soft parametrisation leads to similar results. The values reported in brackets refer to the fraction of QPr events in which the QP remnant is accompanied only by LCPs, without IMFs.

QPr channel	32 AMeV		52 AMeV	
	EXP	AMD+GEMINI asy-stiff	EXP	AMD+GEMINI asy-stiff
$^{64}\text{Ni}+^{64}\text{Ni}$	39%(33%)	47%(40%)	32%(27%)	33%(27%)
$^{64}\text{Ni}+^{58}\text{Ni}$	41%(35%)	48%(40%)	35%(30%)	33%(27%)
$^{58}\text{Ni}+^{64}\text{Ni}$	38%(34%)	47%(42%)	27%(24%)	31%(27%)
$^{58}\text{Ni}+^{58}\text{Ni}$	39%(35%)	48%(42%)	31%(27%)	32%(28%)

between brackets. As expected, both in the experimental and simulated results, the fraction of QPr events is lower for the reactions at 52 AMeV than for those at 32 AMeV. We can also notice that a better agreement between experimental results and model predictions is obtained for the reactions at 52 AMeV. This can be related to the incomplete fusion events in the simulations at 32 AMeV that in our analysis can be erroneously interpreted as QPr events with a slow QP remnant.

5.2 QP breakup channel selection

In a **QP breakup** event, **QPb** in the following, we expect the simultaneous presence of two big fragments (BF, see Tab. 5.1), with $Z > 4$. The two big fragments are marked as Heavy Fragment (HF) and Light Fragment (LF), depending on their charge Z . The original fissioning QP can be reconstructed from the two breakup fragment candidates, as a nucleus with charge number $Z_{rec} = Z_{HF} + Z_{LF}$, mass number $A_{rec} = A_{HF} + A_{LF}$, and velocity \vec{v}_{rec} equal to that of the CM of the HF and the LF. Moreover, the reconstructed parent nucleus is required to have a Z_{rec} meeting the same minimum charge condition imposed for the QP residue in the QPr channel, i.e. $Z_{rec} > 14$. It is also requested that $v_z^{CM}(rec) > 0$.

In events with two relatively large fragments, we must select the cases where they are compatible with a QP decay (that can be either a fast breakup or a fission with longer timescale). In fact, in the case $M_{BF} = 2$, three different scenarios can be assumed:

- QP fission event: the QP breaks up and both fragments with $Z \geq 5$ produced in the split are detected. This is the kind of event we are interested in.
- QT fission event: in principle, both the QP and the QT (or even both of them) can undergo fission, with similar probability. However, this kind of event can be excluded, because the detection of the products related to the QT phase

space is strongly suppressed by the apparatus acceptance, and therefore the simultaneous detection of both the QT fission fragments is very unlikely. This scenario will not be considered in the following.

- “mixed” event: an example of such event is a QP detected together with a fragment coming from a QT split which has been emitted forward, toward the CM². This class of events must be excluded. As already mentioned, the case in which both the QP and the QT (both unfissioning) are detected is extremely unlikely, due to the energy threshold for ion identification cutting out all the heavy fragments in the QT phase space, and therefore it has not been considered.

The two scenarios that we consider (QP fission and “mixed” event) differ greatly when it comes to the θ_{rel} vs v_{rel} correlation, where θ_{rel} is the relative angle in the CM reference frame and v_{rel} the relative velocity between the HF and the LF. In fact, we expect the θ_{rel} between the two QP daughter nuclei to be small, while bigger θ_{rel} values, closer to 180°, should be related to the “mixed” event scenario, in which the QP and a QT fragment have been detected. Moreover, we can expect the distribution of the v_{rel} between the QP and a QT fragment to cover a broad range of values, also including velocities quite higher than the values expected from the Viola systematics [147]. Fig. 5.5a and 5.5c show the θ_{rel} vs v_{rel} correlations obtained for the reactions $^{58}\text{Ni}+^{58}\text{Ni}$ at 32 AMeV and 52 AMeV respectively, as examples. Only the events in which both big fragments have been collected by FAZIA, for which we have mass identification and a more precise information on the emission angles, are included. Similar correlations are obtained for the other systems.

In the case of QP fission, we expect that in most cases both the HF and the LF generated from the QP are emitted forward in the CM reference frame, i.e. $v_z^{CM}(HF) > 0$ and $v_z^{CM}(LF) > 0$; the loci of the θ_{rel} vs v_{rel} plane associated to these events are evidenced in red in the plots shown in panels (b) and (d), on the right, where the regions in black include all the other events, in which at least one big fragment is backward emitted. We notice that the $M_{BF} = 2$ events with both the HF and the LF forward emitted populate the region located below $\theta_{rel} \sim 100^\circ$ at both energies, with v_{rel} compatible with a process basically driven by the Coulomb field. On the contrary, as expected, the distributions of the “spurious” events in which at least one big fragment is backward emitted are mostly located at larger values of θ_{rel} . The regions related to these events are evidently more populated at 52 AMeV. This can be ascribed to a kinematical effect, since for the higher beam energy the QT phase space is “boosted” forward in the laboratory frame, favouring the detection of QT fragments.

Among the events in which the reconstructed QP belongs to the QP phase space and the relative angle between the HF and the LF is below 100°, we select the QP breakup candidates by imposing a gate on the v_{rel} centered at the Viola systematics

²Other examples include the simultaneous detection of QP and QT (without a fission event), or of the QT together with a QP breakup fragment. However, the detection of a QT remnant is highly unlikely.

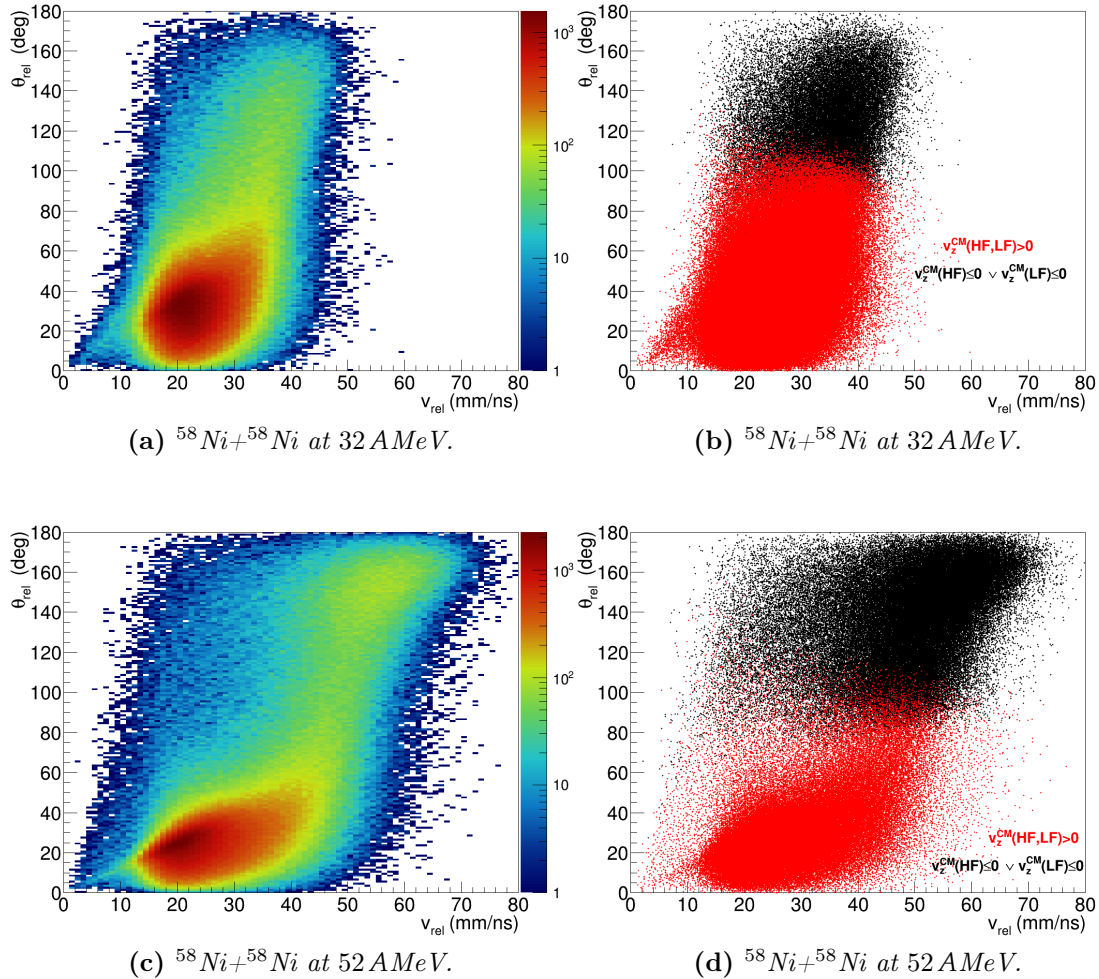


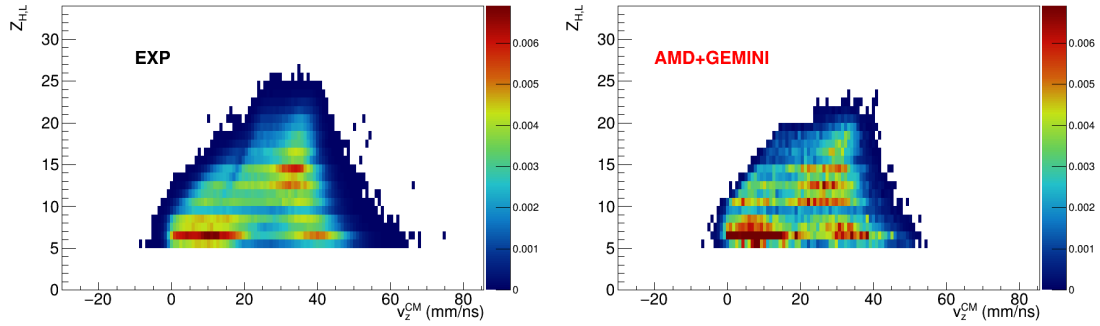
Figure 5.5: Experimental correlations between the relative angle in the CM reference frame, θ_{rel} , and the relative velocity, v_{rel} , between the HF and the LF in the $M_{BF} = 2$ case for the reaction $^{58}\text{Ni} + ^{58}\text{Ni}$ at 32 AMeV and 52 AMeV. Only the events in which both BF have been detected by FAZIA are included. The plots in panels (a) and (c), on the left, show the θ_{rel} vs v_{rel} correlations. In the plots in panels (b) and (d), on the right, the loci populated by events in which both BF are forward emitted in the CM reference frame are plotted in red; the black dots represent the events in which at least one big fragment is backward emitted.

[147]. The lower limit is set to $v_{rel} > 12$ mm/ns, in order to exclude the events where the v_{rel} between the two big fragments is too low to be compatible with their mutual Coulomb repulsion. The upper limit of the gate is chosen depending on the beam energy ($v_{rel}^{max} = 45$ mm/ns for the reactions at 32 AMeV and $v_{rel}^{max} = 60$ mm/ns for those at 52 AMeV). We have verified that the results presented henceforth are essentially stable against reasonable variations of these limits. In summary, we select the QPb event class through the conditions:

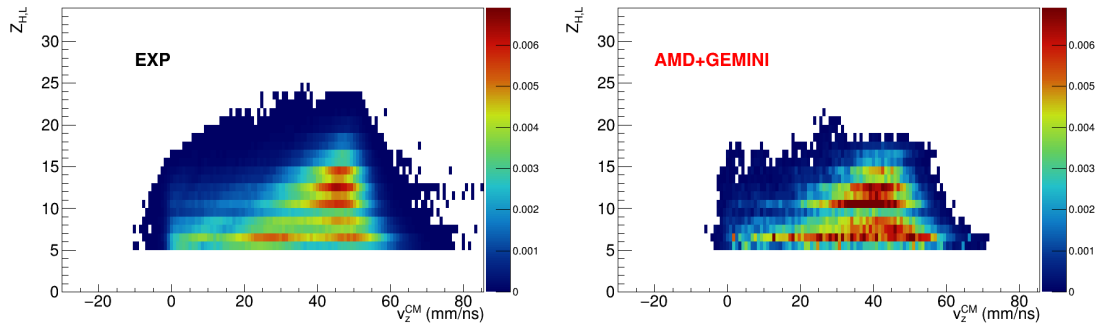
$$\begin{aligned}
 & M_{BF} = 2 \\
 & Z_{rec} = Z_{HF} + Z_{LF} > Z_{QP}^{lim} = 14 \\
 & v_z^{CM}(rec) > 0 \\
 & \theta_{rel} < 100^\circ \\
 & 12 \text{ mm/ns} < v_{rel} < v_{rel}^{max}
 \end{aligned}$$

We now move to investigate the general properties of these events. As an example, Fig. 5.6 shows for the $^{58}\text{Ni}+^{58}\text{Ni}$ reaction at both beam energies the Z vs v_z^{CM} correlations for both the HF and LF (panels (a) and (b)) and for the reconstructed QP candidate (panels (c) and (d)); on the left we show the experimental data, on the right the simulated data (for the AMD calculations an asy-stiff parametrisation of the NEMO3 has been used). By inspection of panels (a) and (b) one clearly sees that the QP split is mainly asymmetric with the LF mostly emitted at low v_z^{CM} , corresponding to backward emission in the decaying QP system. This evidence is very clear in the experimental data at 32 AMeV. At 52 AMeV there are larger velocity fluctuations of the LF and HF, which tend to mask the effect. The simulated data nicely follow the general behaviour of the experimental data, at both energies. We notice that these results confirm the phenomenology for the QP (and QT) breakup at Fermi energies introduced in Sec. 1.3.

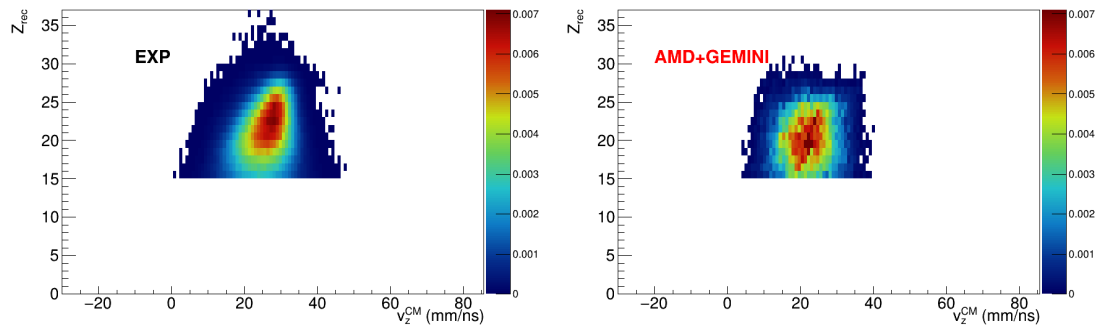
The Z vs v_z^{CM} correlations of the parent QP, reconstructed as the sum of the HF and the LF, are shown for the same reactions in panels (c) and (d) of Fig. 5.6: here, the sharp cut corresponding to the $Z_{rec} > Z_{QP}^{lim}$ condition is evident. The pattern resembles that of a forward emitted heavy QP fragment (see Fig. 5.1 for a comparison), but corresponding on average to a large dissipation (lower velocities and charges with respect to the QPr selection). A good qualitative agreement can be seen in the correlations produced from the experimental and simulated datasets, but, as already noticed in the QPr channel, also in the QPb case the reconstructed QP in the AMD+GEMINI simulations reveals a slightly more dissipative character of the model predictions. This can be better appreciated from the comparison of the charge Z_{rec} , velocity v^{CM} and diffusion angle θ^{CM} distributions of the reconstructed QP for all the reactions, obtained from the experimental (drawn as circular markers) and the simulated (drawn as a line) datasets, shown in Fig. 5.7 (that can be compared with Fig. 5.2). In fact, the QP reconstructed from the experimental QPb events tends to be heavier, faster, and to be emitted at smaller diffusion angles than the simulated one. This difference is more marked at 32 AMeV than at 52 AMeV. Moreover, in general, the model reproduces better the QPb distributions than the



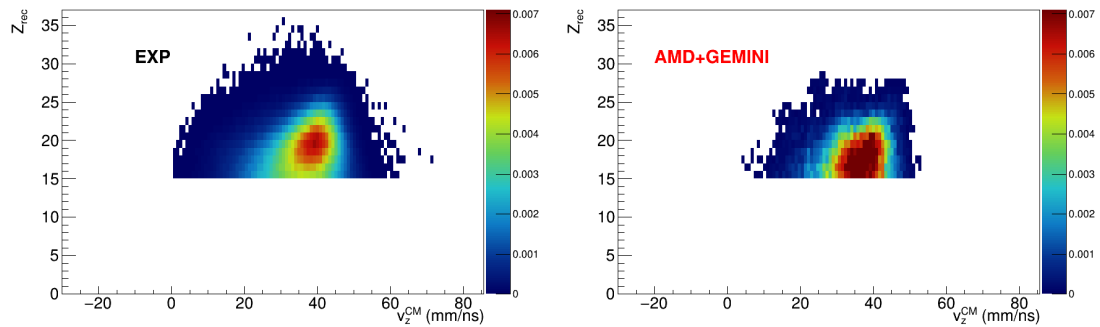
(a) Z vs v_z^{CM} of the HF and LF in $^{58}\text{Ni}+^{58}\text{Ni}$ at 32 A MeV.



(b) Z vs v_z^{CM} of the HF and LF in $^{58}\text{Ni}+^{58}\text{Ni}$ at 52 A MeV.



(c) Z vs v_z^{CM} of the reconstructed QP in $^{58}\text{Ni}+^{58}\text{Ni}$ at 32 A MeV.



(d) Z vs v_z^{CM} of the reconstructed QP in $^{58}\text{Ni}+^{58}\text{Ni}$ at 52 A MeV.

Figure 5.6: Experimental (left) and simulated (right) Z vs v_z^{CM} correlations of the HF and LF (panels (a) and (b)) and of the reconstructed QP (panels (c) and (d)) obtained for the events falling in the QPb channel selection in the reactions $^{58}\text{Ni}+^{58}\text{Ni}$ at 32 A MeV and 52 A MeV. The plots are normalised to the number of QPb events for that reaction.

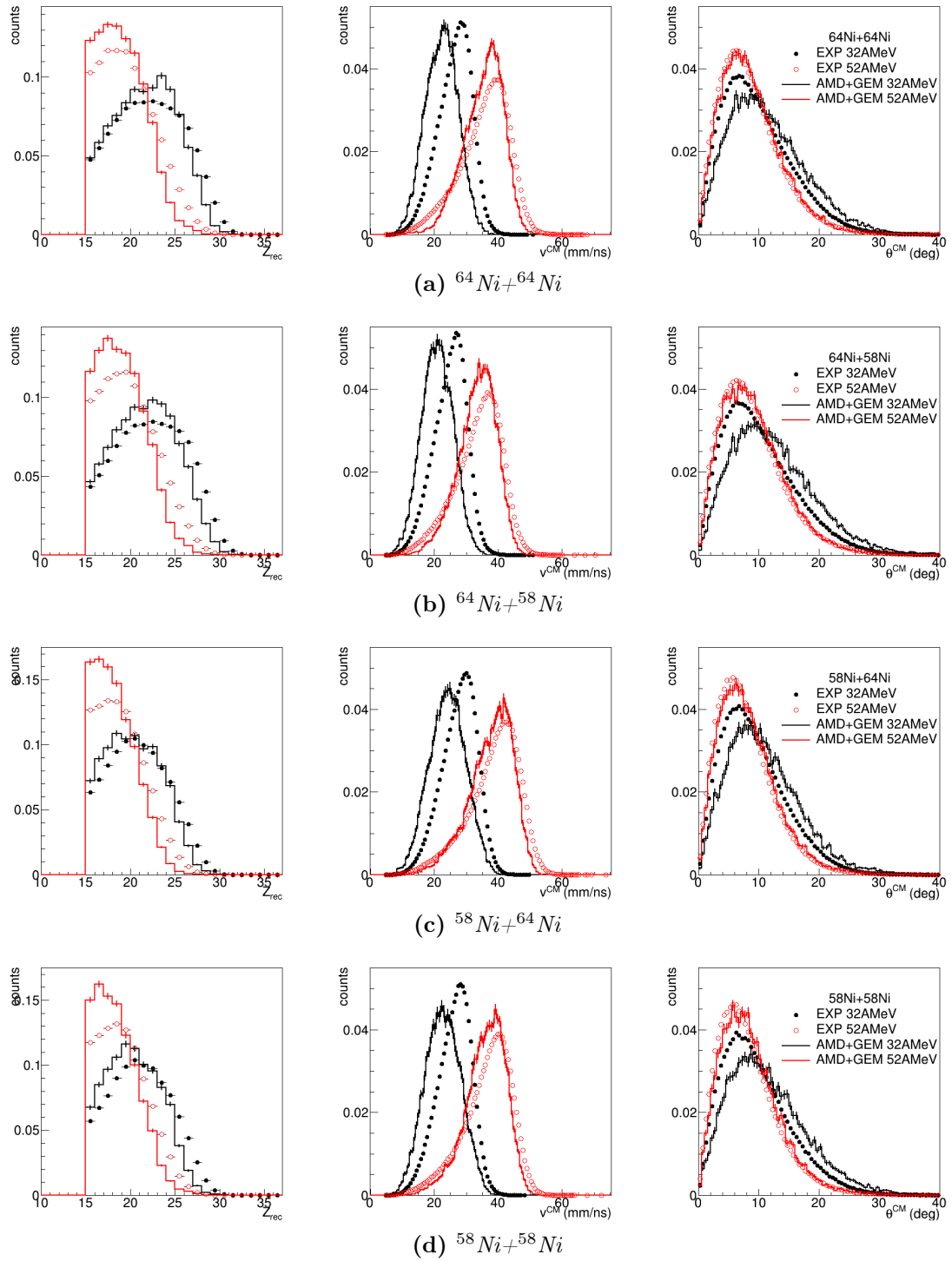


Figure 5.7: Comparison between the experimental and simulated (asy-stiff AMD+GEMINI, filtered) distributions of Z_{rec} (left), v^{CM} (center) and θ^{CM} (right) of the reconstructed QP for the events falling in the QPb channel selection. All histograms are normalised to their integral. Each panel, from (a) to (d), refers to a different system.

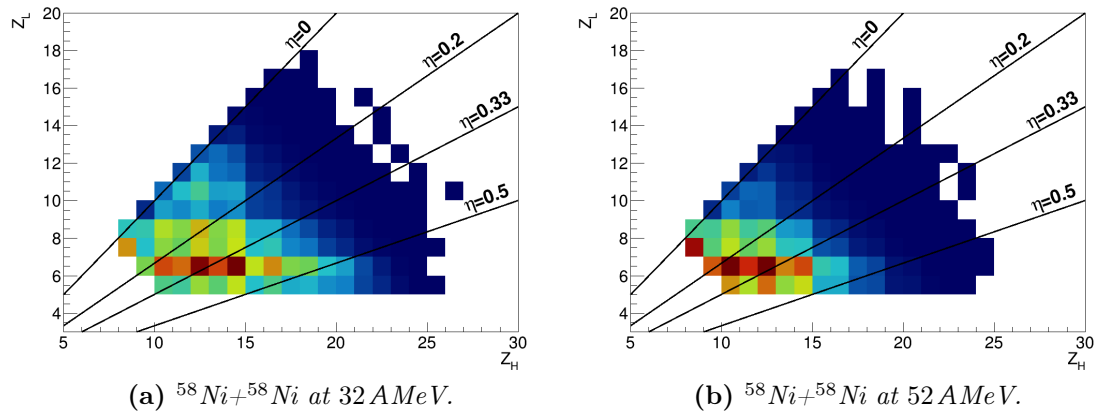


Figure 5.8: Experimental correlation between the charge of the LF and of the HF of the events in the QPb selection. The results for the reaction $^{58}\text{Ni}+^{58}\text{Ni}$ at the two beam energies are shown. Similar results are obtained for the other systems.

QPr ones (see Fig. 5.2). By comparing the distributions on the left side of Fig. 5.7 for the different Ni+Ni systems, we notice again that the average charge Z_{rec} of the reconstructed QP in the reactions induced by the neutron rich projectile ^{64}Ni is greater than that obtained in the reactions with the ^{58}Ni projectile, as observed in the QPr channel. In contrast, in this reaction channel we do not observe any effect such as the odd-even staggering observed in the experimental QP remnant Z histograms. Moving to the θ^{CM} distributions of the reconstructed QP (rightmost plots in Fig. 5.7), here the characteristics of the geometrical acceptance of the apparatus are not as evident as for the θ^{CM} histograms of the QP evaporation residue in the QPr channel (notice, e.g., that in Fig. 5.7 there is no sharp cut at low θ^{CM} , with respect to Fig. 5.2). In fact, for the QPb channel, this is expected since this information is obtained from the diffusion angles of the two breakup fragments.

So far, the events selected in this channel can be generally interpreted as QP fissions; no distinction has been made between the dynamical or statistical origin of the split. Therefore a careful analysis of their characteristics can be of interest. As we have already anticipated, the preferential asymmetry and the favoured emission of the LF towards the CM indicate a contribute of a dynamical fission process [20–22, 56, 57]. In Fig. 5.8 the experimental correlations between the charge of the LF and of the HF are shown for the reaction $^{58}\text{Ni}+^{58}\text{Ni}$ at the two beam energies. In the plots, the lines corresponding to some reference values of η are drawn to guide the eye, where η is the charge asymmetry parameter defined as in eq. (4.5). We remind that $\eta = 0$ corresponds to a symmetric split. We notice that, in both cases, in most of the QPb events the η parameter assumes values above 0.2, highlighting the asymmetry of the split. We want to stress that the choice of the threshold $Z > 4$ for the LF puts an upper limit in the accessible η , also considering the relatively

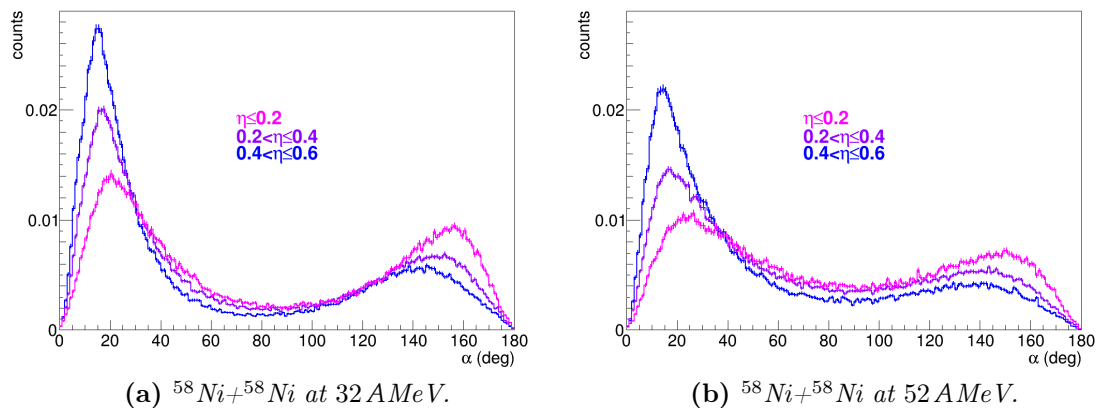


Figure 5.9: Experimental α angle distributions obtained for the reaction $^{58}\text{Ni}+^{58}\text{Ni}$ at 32 AMeV (panel (a)) and at 52 AMeV (panel (b)). Similar results are obtained for the other systems. The histograms are normalised to their integral.

small projectile charge³. In this respect, one could treat a selection of the QPr+IMF events (QP remnant with an IMF in coincidence) as a particular case of fission events with $Z_L = 3, 4$, in which higher charge asymmetry values can be obtained.

As anticipated in Sec. 1.3, the emission pattern of the two dynamical fission products is generally anisotropic, with the most strongly aligned configurations associated to the most asymmetric splits. We now consider the aspects related to the orientation of the HF-LF split with respect to the QP-QT separation axis, expressed by means of the α angle already defined in eq. (1.7) and widely used in the literature. In Fig. 5.9 the experimental distributions of the α angle for three η intervals are shown. The reaction is $^{58}\text{Ni}+^{58}\text{Ni}$ at 32 AMeV (panel (a)) and at 52 AMeV (panel (b)). For the most charge-symmetric splits, with $\eta \leq 0.2$, we find a rather symmetric α distribution: this is typical of a statistical fission, which has no preferential orientation in the reaction plane, since the memory of the entrance channel, including the information on the direction of the QP-QT separation axis, is forgotten. On the contrary, the asymmetric breakups occur in preferentially aligned HF-LF configurations, with the LF emitted backward. This characteristic is consistent with a dynamical fission event, as evidenced in multiple experimental observations in the literature [20–22, 56–58, 60]. It is possible to check these evaluations of the α angle distributions for different fission origins by exploiting the information provided by

³In order to better illustrate this point, let us consider a $Z = 28$ fissioning QP: the most asymmetric split entering the QPb selection would be that with $Z_L = 5$ and $Z_H = 23$, leading to an expected maximum η value around 0.64. Heavier reconstructed QP are less probable. Notice also that for the reaction at 52 AMeV, for which a lighter reconstructed QP is generally obtained (see Fig. 5.7), the fission asymmetry seems to be lower than at 32 AMeV.

Similar Z_L vs Z_H plots have been shown e.g. in Ref. [60] for the reaction $^{80}\text{Kr}+^{48}\text{Ca}$ at 35 AMeV, where the reconstructed fissioning QP was heavier, as expected; there, the obtained η distribution extended towards higher values.

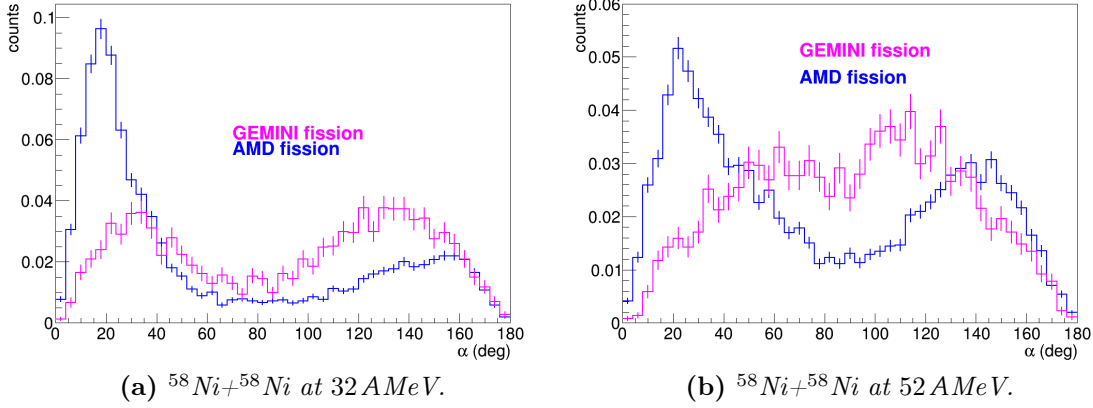


Figure 5.10: AMD+GEMINI simulated α angle distributions obtained for the reaction $^{58}\text{Ni}+^{58}\text{Ni}$ at 32 AMeV (panel (a)) and at 52 AMeV (panel (b)). The histograms are normalised to their integral. The distributions related to the QP fissions produced by AMD (dynamical fissions) and those produced by GEMINI (statistical) have been plotted in different colours.

the AMD+GEMINI simulations: here, we can easily distinguish between the fissions produced by AMD, whose origin is therefore dynamical, and those produced by GEMINI according to a statistical approach. In Fig. 5.10 the AMD+GEMINI α angle distributions for the same two reactions are shown: in each plot, the two different colours correspond to the different origins of the QP fission: the breakup events produced by AMD feature an anisotropic emission pattern peaked at small α values, while the fissions produced in GEMINI do not have the same behaviour, as expected. Both in the experimental distributions in Fig. 5.9 and in the simulated ones in Fig. 5.10 we notice a different behaviour between the reaction at 32 AMeV and that at 52 AMeV, with a less evident LF backward emission in the latter case. Similar observations can be done for the other systems.

Some other aspects of a QP breakup event can be related to the charge asymmetry η . In particular, we can study how the characteristics of the reconstructed QP vary in relation to η . Fig. 5.11 shows the average velocity of the reconstructed QP in the CM reference frame as a function of η , again for the reactions $^{58}\text{Ni}+^{58}\text{Ni}$ at the two energies. Both the experimental and simulated results are reported in the plots, together with two horizontal lines indicating the average velocity of the QP residue in the QPr channel selected in the same datasets. A clear evolution of the v_{rec}^{CM} with the η parameter can be noticed, with the most symmetric splits corresponding to the lower reconstructed velocities. Since the velocity of the original fissioning QP is related to the degree of dissipation, which in turn is related to the impact parameter, this is a possible hint that the most asymmetric (symmetric) splits are produced in the most peripheral (central) collisions. This behaviour is evident in both the experimental and the simulated data, with the reconstructed velocities in

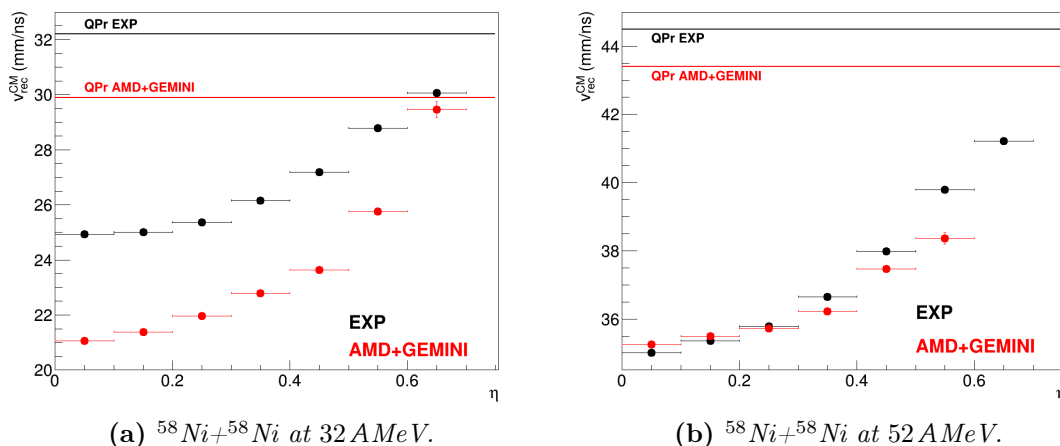


Figure 5.11: Average velocity v_{rec}^{CM} of the reconstructed QP in the CM reference frame vs charge asymmetry parameter η for the reaction $^{58}\text{Ni}+^{58}\text{Ni}$ at 32 A MeV (a) and 52 A MeV (b). Both experimental (black) and simulated (red) results are plotted. Statistical errors are plotted on the y -axis, horizontal error bars correspond to the bin width. The horizontal lines mark the average velocity of the QP residue in the QPr channel. Please note that the y -axis starts at 20 cm/ns (35 cm/ns) at 32 A MeV (52 A MeV).

the latter generally lower, due to the more damped character of the AMD+GEMINI predictions; we also notice a much better agreement at 52 A MeV. At 32 A MeV, the simulation produces a 10-15% lower velocity. Please note that in Fig. 5.11 the y -axis starts at 20 cm/ns (35 cm/ns) at 32 A MeV (52 A MeV). Moreover, we observe that the typical QP velocities obtained in the QPr channel are higher than the reconstructed ones obtained in the QPb case, a possible indication that the breakup events are generally produced in more dissipative collisions.

In principle, since no further specific condition has been imposed, the two breakup fragments can be accompanied both by LCPs and IMFs. However, the fraction of QPb events in which also an IMF is detected is negligible, therefore no subclass of the QPb channel has been defined and selected. In Tab. 5.3 the percentage of accepted events falling in the QPb selection for each reaction is reported. The QPb class is sensibly less populated than the QPr class, as evident from a comparison with the values reported in Tab. 5.2. The experimental results are also compared to the AMD+GEMINI model predictions; some discrepancies can be found, which are larger for the reactions at 32 A MeV.

5.3 Centrality estimation

Since the impact parameter b of the collision is not experimentally accessible, it is customary to identify some observable (hopefully) strongly correlated to b . Widely adopted centrality estimators rely on a good angular coverage of the experimental

Table 5.3: Percentages of QPb events among the total number of events selected with the global conditions for each reaction, including a comparison with the model predictions. Only the results of the AMD+GEMINI simulations assuming an asy-stiff parametrisation are listed: the asy-soft parametrisation leads to similar results in this respect.

QPb channel	32 AMeV		52 AMeV	
	EXP	AMD+GEMINI asy-stiff	EXP	AMD+GEMINI asy-stiff
$^{64}\text{Ni}+^{64}\text{Ni}$	7.5%	4.7%	5.1%	4.2%
$^{64}\text{Ni}+^{58}\text{Ni}$	6.9%	4.2%	5.1%	4.1%
$^{58}\text{Ni}+^{64}\text{Ni}$	5.7%	3.3%	4.0%	3.0%
$^{58}\text{Ni}+^{58}\text{Ni}$	5.3%	3.2%	3.8%	2.9%

apparatus. Examples of this kind of sorting parameters are the LCP multiplicity M_{LCP} [148] and transverse kinetic energy E_{trans}^{LCP} [11, 149]. Other estimators, like the flow angle θ_{flow} [150], are related to the shape and orientation of the event. The θ_{flow} angle has been usually exploited for the study of high multiplicity events (mostly central events) with 4π -apparatuses [45, 151], but it has been demonstrated to be useful also for the selection of the most central events in experiments with a limited angular coverage [67]. In this regard, when the geometrical coverage of the experimental apparatus is limited and the focus is on semiperipheral collisions, some other observables related to the characteristics of the detected QP are generally adopted: two examples are the Z_{max} of the heaviest fragment [152] and the reduced momentum p_{red} [69], i.e. the QP momentum along the beam axis divided by the momentum of the original projectile.

In this section an overview of the centrality estimators that have been studied in this work will be presented. The correlations of these order parameters with the reduced impact parameter b_{red} according to the AMD+GEMINI model predictions will be shown. When interesting, a distinction will be made between the correlations obtained considering separately the events in the two reaction channels QPr and QPb that we have just selected. The sorting parameters that are considered as the most suitable to the study of semiperipheral and peripheral collisions will be then exploited in Chapter 6.

Flow angle θ_{flow} – The evaluation of the θ_{flow} angle requires the evaluation of the momentum tensor in the CM reference frame T_{ij} :

$$T_{ij} = \sum_{n=1}^M \frac{p_i^n \cdot p_j^n}{p^n} \quad \text{with} \quad i, j = 1, 2, 3$$

where p_i^n and p_j^n represent the i -th and j -th components of the momentum \vec{p}^n of the n -th fragment in the event (p^n being its module), and M is the total multiplicity. According to the definition, all the fragments in the event are therefore considered.

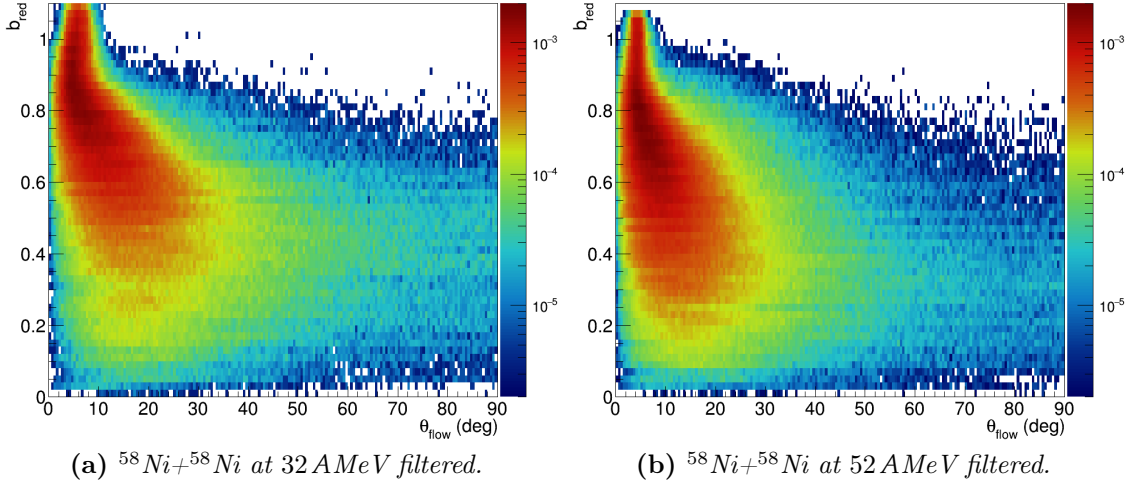


Figure 5.12: Simulated (AMD+GEMINI) correlations between b_{red} and θ_{flow} of all the events filtered according to the angular coverage of the apparatus, for the reactions $^{58}\text{Ni}+^{58}\text{Ni}$ at 32 AMeV (panel (a)) and at 52 AMeV (panel (b)). Both histograms are normalised to their integral.

This 3×3 tensor can be diagonalised: the three eigenvectors \vec{e}_i and the corresponding three eigenvalues λ_i can be associated to an ellipsoid in the momentum space⁴. Let \vec{e}_1 be the eigenvector corresponding to the largest eigenvalue λ_1 . The θ_{flow} is defined as the angle between the eigenvector \vec{e}_1 and the beam direction:

$$\theta_{flow} = \arccos(|\hat{e}_1 \cdot \hat{k}|) \quad (5.1)$$

where \hat{k} is the unit vector associated to the beam axis. The θ_{flow} indicates the predominant direction of the momenta of the ejectiles. In a collision with a binary output, it is strongly related to the diffusion angle of the QP (and QT), which is generally small, while for the most dissipative collisions a flatter θ_{flow} distribution is expected as the result of the emission from a central source.

The evaluation of the θ_{flow} angle clearly benefits from a full angular coverage⁵. In principle, the INDRA-FAZIA apparatus guarantees a good performance in this respect. However, the energy calibration has not yet been performed for modules with $\theta_{lab} > 45^\circ$. Therefore, the information about the momentum of particles emitted beyond 45° in the laboratory frame is missing. In Fig. 5.12 the correlation between the reduced impact parameter b_{red} and the θ_{flow} angle obtained with the AMD+GEMINI simulated data for the reactions $^{58}\text{Ni}+^{58}\text{Ni}$ at 32 AMeV (panel (a))

⁴In fact, the eigenvalues and eigenvectors of the momentum tensor are related to the shape of the whole event and its orientation with respect to the beam: various shape parameters, such as the sphericity, flatness, prolateness, eccentricity and jettiness [150], can be calculated from the λ_i values.

⁵This centrality estimator has already been used in experiments where a limited angular coverage could be exploited, as described in Ref. [67]; in that case, its strong correlation to the polar emission angle of the biggest fragment of the event has been demonstrated.

and 52 AMeV (panel (b)) is reported⁶. These plots refer to the simulated data filtered according to the actual angular coverage of the INDRA-FAZIA apparatus, including only the particles for which the momentum information is available. Even though part of the apparatus cannot be exploited for the evaluation of θ_{flow} , the observed behaviour is consistent with the expectations: in fact, semiperipheral and peripheral collisions are generally characterised by low values of θ_{flow} (close to the projectile grazing angles), while a less peaked, almost flat distribution is obtained for more central collisions (bottom part of the plots). Though some difference between the shape of the correlation obtained for the reactions at the two beam energies can be noticed, the general features are analogous. However, the correlation between θ_{flow} and b_{red} results to be rather weak, so that this observable is not the best choice as an order parameter.

Nevertheless, the θ_{flow} angle allows for a rough distinction between central and more peripheral events. In the present work the θ_{flow} angle has been exploited to exclude some of the most central collisions, corresponding to incomplete fusion or multifragmentation events: indeed, a condition $\theta_{flow} < 40^\circ$ has been adopted to exclude those events.

Transverse kinetic energy – The transverse kinetic energy E_{trans} associated to an event is the total kinetic energy related to the motion of all particles on a plane perpendicular to the beam axis. It is usually evaluated by considering either all the produced fragments, or uniquely the LCPs. In the following, we adopt the latter choice⁷, and we refer to the LCP transverse kinetic energy as E_{trans}^{LCP} .

In the most peripheral reactions most of the initial kinetic energy is kept by the QP and only a small fraction is transferred to the internal degrees of freedom, resulting in the production of a small number of LCPs, mostly forward focused. Therefore, the E_{trans}^{LCP} in peripheral reactions is expected to be small. On the other hand, for the more dissipative central reactions, a larger production of LCPs is expected, with a wider angular distribution, resulting in a higher E_{trans}^{LCP} . Within the AMD+GEMINI model predictions, the behaviour of the LCP transverse kinetic energy with respect to the reduced impact parameter b_{red} can be tested, e.g. by exploiting the unfiltered 4π simulation: in Fig. 5.13 the 4π b_{red} vs E_{trans}^{LCP} simulated correlations obtained for the reactions $^{58}\text{Ni}+^{58}\text{Ni}$ at 32 AMeV (panel (a)) and 52 AMeV (panel (b)) are shown. Similar behaviour is observed for the other systems. A strong and narrow correlation between the two variables can be readily noticed. The expected behaviour of E_{trans}^{LCP} as a function of the centrality is clearly confirmed by the model predictions at both beam energies. The E_{trans}^{LCP} distribution at 52 AMeV extends toward higher values than that obtained at 32 AMeV, as one might expect. Moreover, the distribution in panel (a) seems to be broader than the one in panel (b), more evidently for

⁶Some events with $b_{red} > 1$ are present in the plots in Fig. 5.12. These are related to the fact that the impact parameter distribution adopted for the simulations extends up to $b > b_{gr}$ (see Sec. 4.1.1).

⁷No substantial difference in the behaviour of this observable has been recognised by including all charged particles in the E_{trans} calculation.

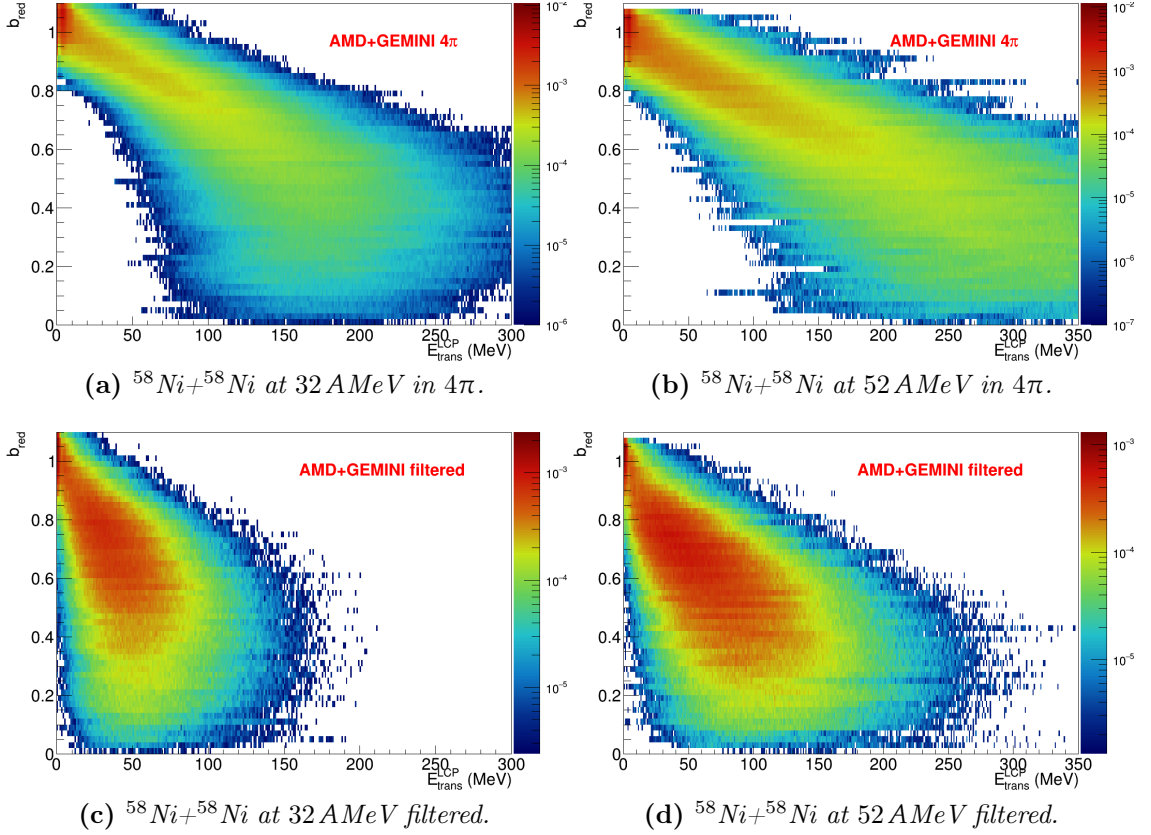


Figure 5.13: Correlations between b_{red} and E_{trans}^{LCP} for all the events in the AMD+GEMINI simulations for the reactions $^{58}\text{Ni}+^{58}\text{Ni}$ at 32 A MeV (panels (a) and (c)) and at 52 A MeV (panels (b) and (d)). The top panels refer to the unfiltered 4π model predictions, while the bottom panels show the filtered simulation (full filter), also requiring the energy calibration of the LCPs. The histograms are normalised to their integral.

$b_{red} < 0.5$.

This impact parameter estimator is widely used when the geometrical coverage of the experimental setup is good [11, 149]. In our case, as already seen for the θ_{flow} angle, also for the construction of this observable we can only consider the angular coverage given by the calibrated detecting modules. The effect on the E_{trans}^{LCP} variable of the actual angular coverage of the INDRA-FAZIA apparatus can be seen in Fig. 5.13, where the b_{red} vs E_{trans}^{LCP} correlations obtained from the AMD+GEMINI filtered simulations (requiring the energy calibration of the LCPs) of the same two reactions of $^{58}\text{Ni}+^{58}\text{Ni}$ are shown, in panel (c) (panel (d)) for 32 A MeV (52 A MeV). In both plots, the contraction of the distributions along the E_{trans}^{LCP} axis is evident: the total transverse kinetic energy of the LCPs after the application of the geometrical filter is strongly reduced. Moreover, large fluctuations are introduced and a broader E_{trans}^{LCP} distribution is obtained at both energies. The correlation to the centrality of

the collision is still present and visible, though severely spoiled by the loss of information due to the undetected or uncalibrated LCPs, particularly at 32 AMeV. Since a better sorting capability can be obtained with other centrality related observables, E_{trans}^{LCP} will not be exploited in the following analysis. Of course, it will be possible to refine this analysis, also including E_{trans}^{LCP} as an order parameter, when the energy calibration will be available for the full apparatus.

Particle multiplicity – The use of the particle multiplicity information for the evaluation of the reaction centrality relies on similar considerations as those illustrated for the transverse energy: a higher multiplicity is expected to be associated with a lower impact parameter. Also in this case, either the total particle multiplicity of the event or the multiplicity of a subclass of particles, usually the LCPs, can be adopted; in the following we present some considerations made on this latter observable, which we indicate as M_{LCP} from now on.

At variance with the E_{trans}^{LCP} variable, the M_{LCP} does not require a complete energy calibration of the apparatus. Just the identification of the detected fragments is needed. Unlike the calibration, the identification procedures have been completed for all the working INDRA-FAZIA modules; therefore, although we can still expect some differences between the M_{LCP} distributions obtained from the AMD+GEMINI simulations in 4π and those obtained after the application of the software filter, the correlation of this observable with the impact parameter should be less affected by the acceptance of the apparatus, with respect to E_{trans}^{LCP} . In Fig. 5.14 a comparison between the b_{red} vs M_{LCP} correlations obtained with the unfiltered (panels (a) and (b)) and the filtered (panels (c) and (d)) AMD+GEMINI simulated data is shown for the reactions $^{58}\text{Ni}+^{58}\text{Ni}$ at 32 AMeV and at 52 AMeV. A clear correlation is present in both the 4π model predictions, with a different extension on the M_{LCP} axis between the two reaction energies: a greater M_{LCP} production is found at 52 AMeV, as expected. A saturation of the LCP multiplicity at values between 15 and 20 is observed in panel (a) for the most central collisions at 32 AMeV, while at 52 AMeV, in panel (b), it increases more regularly with decreasing impact parameter. After the application of the filter, the correlation between the two variables is still visible, even if broadened by the loss of some LCPs due to incomplete angular coverage, malfunctioning detectors or energy thresholds. Moreover, the differences between the correlations at the two beam energies are less evident, see e.g. the maximum M_{LCP} values obtained for the most central collisions.

This can be noticed in Fig. 5.15a which shows the average b_{red} as a function of M_{LCP} for the neutron poor system at both beam energies. Some difference is found instead among the four reaction systems at the two energies, as evident from the plots in panels (b) and (c) of Fig. 5.15: here we notice that the same average b_{red} value corresponds to a greater LCP multiplicity for the most neutron deficient system. The lowest LCP production is related to the most neutron rich system, while the two mixed system show a similar behaviour, in between that of the two symmetric systems. As expected, the M_{LCP} depends on the proton to neutron content of

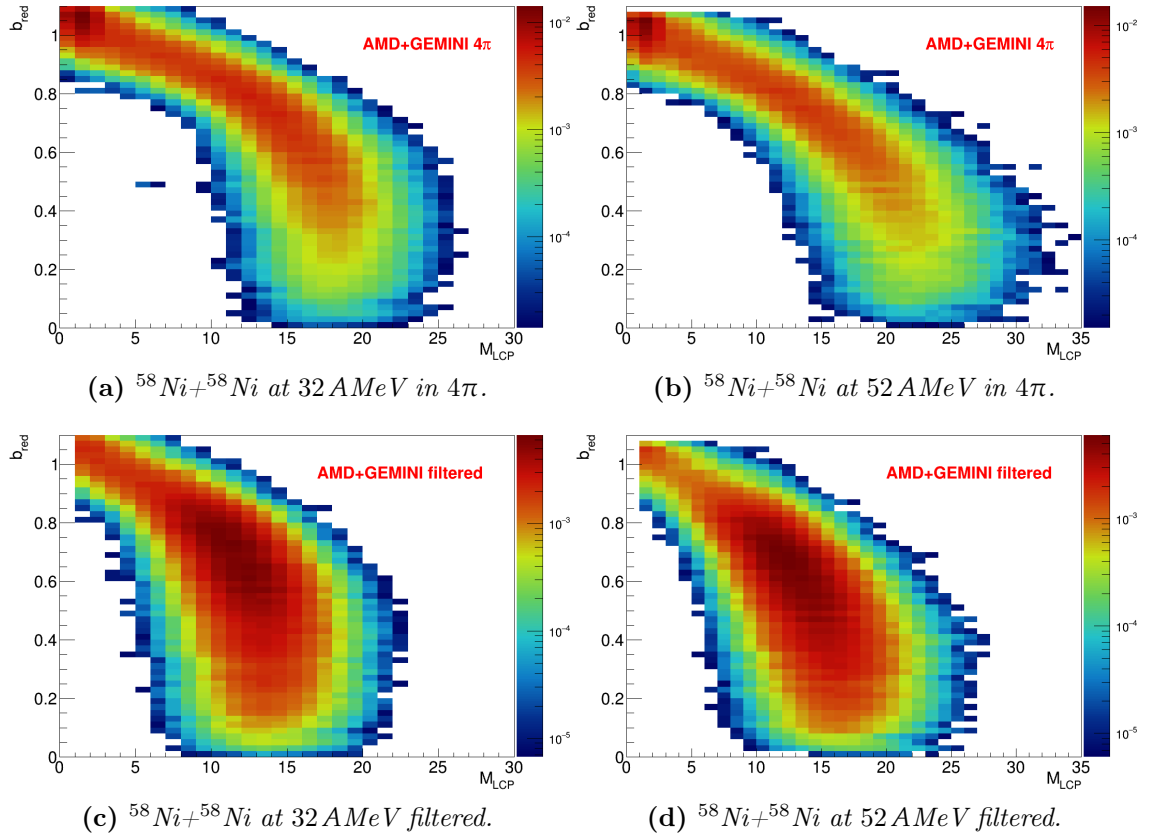


Figure 5.14: Correlations between b_{red} and M_{LCP} for all the events in the AMD+GEMINI simulations for the reactions $^{58}\text{Ni}+^{58}\text{Ni}$ at 32 AMeV (panels (a) and (c)) and at 52 AMeV (panels (b) and (d)). The top panels refer to the unfiltered 4π model predictions, while the bottom panels show the filtered simulation (full filter), though without requiring the energy calibration of the LCPs. The histograms are normalised to their integral.

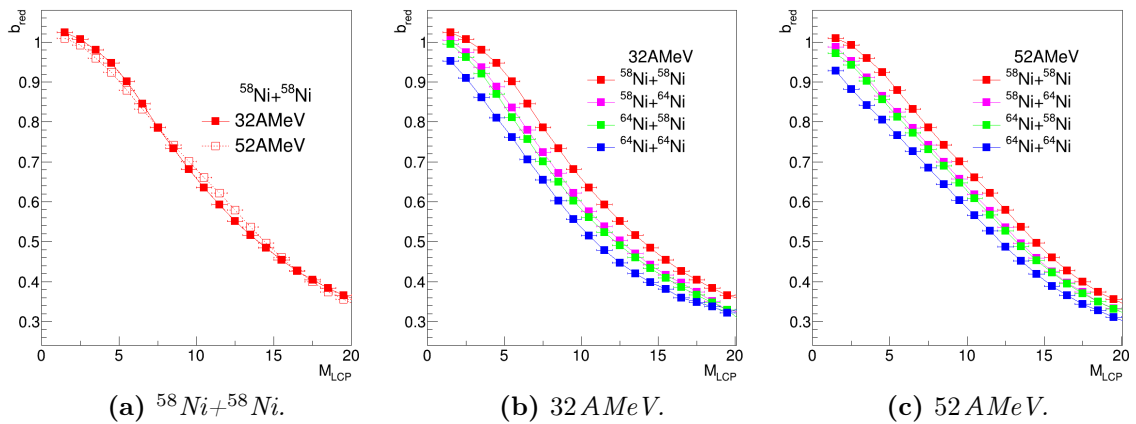


Figure 5.15: Comparison between the AMD+GEMINI predictions of the average b_{red} as a function of M_{LCP} for $^{58}\text{Ni}+^{58}\text{Ni}$ at the two energies (panel (a)) and for all systems at a given energy (panels (b) and (c)).

the studied system⁸; the characteristics here described make it an order parameter which can be suitable to study the evolution of the isospin content of the products of a single reaction as a function of the collision centrality, but which is not appropriate to make direct comparisons between the four different systems. The situation would probably improve if the experimental apparatus could also detect neutrons. However, the main results observed in this work, presented in Chapter 6, are not influenced by the missing neutron detection, since the M_{LCP} has not been used.

Reduced QP momentum p_{red} – The reduced momentum p_{red} of the QP, either detected or reconstructed, depending on the reaction channel, is defined as [69]:

$$p_{red} = \left(\frac{p_z^{QP}}{p_{beam}} \right)_{CM} \quad (5.2)$$

where p_z^{QP} is the QP momentum along the beam axis (z-axis) and p_{beam} is the projectile momentum, both evaluated in the CM reference frame. A more peripheral collision is in fact expected to be associated with a lower kinetic energy dissipation and smaller scattering angle of the QP, and therefore to a p_{red} value closer to 1. Since the p_{red} calculation relies only on the correct detection of the QP remnant (or of the two QP fragments in the breakup channel), it can also be exploited in case of limited acceptance of the setup. Even if the angular coverage of INDRA-FAZIA is good, we also consider this sorting parameter, which has already been proven to give a good performance as a centrality estimator [69].

The correlations of p_{red} with the reduced impact parameter obtained from the AMD+GEMINI filtered simulations are shown in Fig. 5.16 for the reactions $^{58}\text{Ni}+^{58}\text{Ni}$ at 32 A MeV (panel (a)) and at 52 A MeV (panel (b)). Similar correlations are obtained for the other systems. Since we need the QP information, these plots include only the events belonging either to the QPr or the QPb selection: in the latter case, the QP reconstructed from the two breakup fragments is considered. A clear and narrow correlation between the two variables is visible in both plots, particularly well defined for less central reactions, with $b_{red} \gtrsim 0.3$. The correlations for the two beam energies show a similar behaviour for semiperipheral and peripheral collisions, while for small impact parameters the histogram obtained for the reaction at 52 A MeV is less populated than the one at 32 A MeV. This is a consequence of the fact that only the p_{red} calculated for the events included in the QPr and QPb selections are plotted: for the most central collisions at 52 A MeV there is a higher probability of a multifragmentation-like outcome, with a consequent exclusion from both QPr and QPb gates. However, at both energies, this observable can be considered a reliable sorting parameter to study semiperipheral and peripheral reactions: therefore, in the following, we only present the results obtained for $p_{red} \gtrsim 0.3$ (indicated by the vertical line in Fig. 5.16).

⁸A similar comparison of the correlations between the reaction centrality and the E_{trans}^{LCP} for the four systems at the two beam energies has been done, both in 4π and after the application of the (actual) geometrical filter. In both cases, we find that the behaviour of the E_{trans}^{LCP} observable is less dependent on the isospin of the studied system with respect to that of the M_{LCP} .

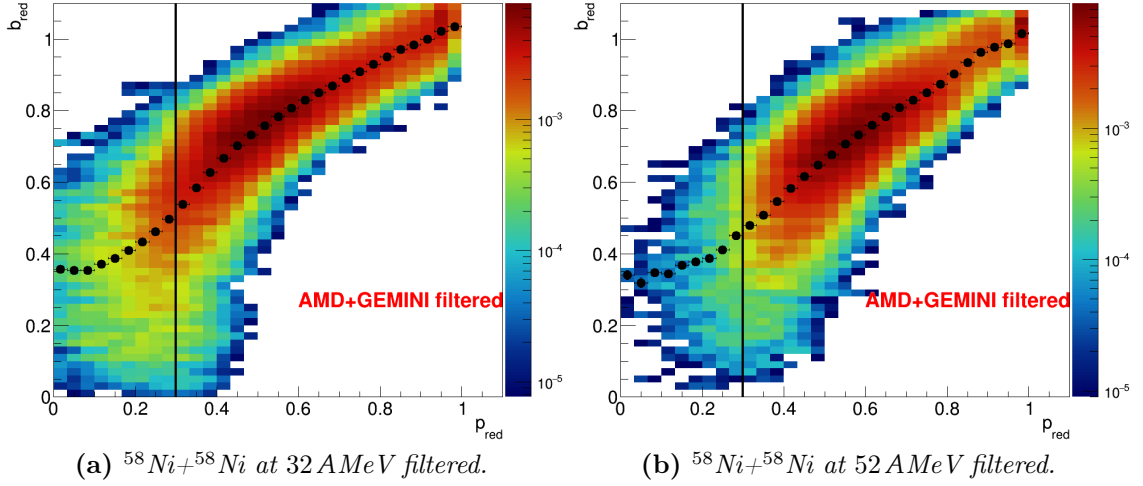


Figure 5.16: Correlations between b_{red} and p_{red} of the QP (or the reconstructed QP) for all the events included in the QPr or QPb channel selection in the AMD+GEMINI simulations for the reactions $^{58}\text{Ni}+^{58}\text{Ni}$ at 32 AMeV (panel (a)) and at 52 AMeV (panel (b)). The histograms are normalised to their integral. The black markers indicate the average b_{red} for each p_{red} bin (also shown in Fig. 5.17); the errors on the y -axis are statistical, often smaller than the marker size, while those on the x -axis are equal to the bin width. The vertical lines indicate the minimum p_{red} value (0.3) above which the correlations are considered reliable in the following analysis.

On the histograms in Fig. 5.16 the average b_{red} is also plotted (black markers). The average value is also reported in Fig. 5.17 as a function of p_{red} to compare the behaviour of p_{red} in the different reactions. Figure 5.17a shows the superposition of the average b_{red} vs p_{red} for the two reactions $^{58}\text{Ni}+^{58}\text{Ni}$ at 32 AMeV and at 52 AMeV: only a relatively small difference can be observed between the two beam energies. Figure 5.17 is the equivalent of Fig. 5.15 for the p_{red} parameter. At variance with Fig. 5.15 the behaviour for $^{58}\text{Ni}+^{58}\text{Ni}$ (panel (a)) is slightly dependent on the beam energy. However, in this case the behaviour at a given energy is almost independent of the reaction, as can be seen in panel (b) (panel (c)) for 32 AMeV (52 AMeV) beam energy. In fact, from its definition in eq. (5.2), it can be noted that the p_{red} variable is normalised to the initial momentum of the projectile: this kind of normalised scale can be expected to be more independent of the entrance channel, thus allowing for a more meaningful comparison of different reactions.

Having checked the similar behaviour of the b_{red} vs p_{red} correlation in the different systems of the E789 experiment, we now verify whether, according to the AMD+GEMINI model predictions, there are differences between the two reaction channels that we selected by means of the conditions presented in the previous sections. In Fig. 5.18 the comparison between the plots of the average b_{red} as a function of p_{red} for the QPr and QPb selections is shown for $^{58}\text{Ni}+^{58}\text{Ni}$ at 32 AMeV (panel (a)) and 52 AMeV (panel (b)). In the plots associated to the QPb channel,

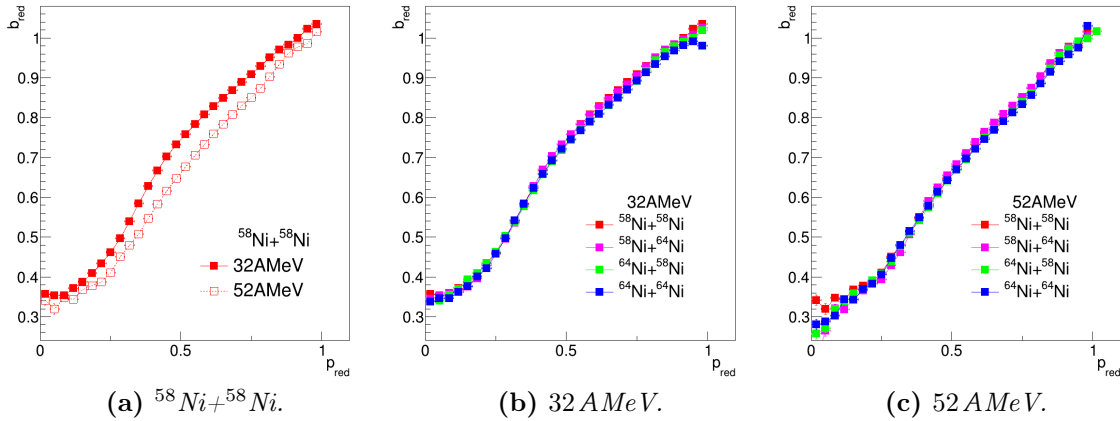


Figure 5.17: Comparison between the AMD+GEMINI predictions of the average b_{red} as a function of p_{red} for different energies (panel (a)) and for different systems at the two energies (panels (b) and (c)). In some regions of the latter, the plots associated to different systems are overlapped, and some points are hidden.

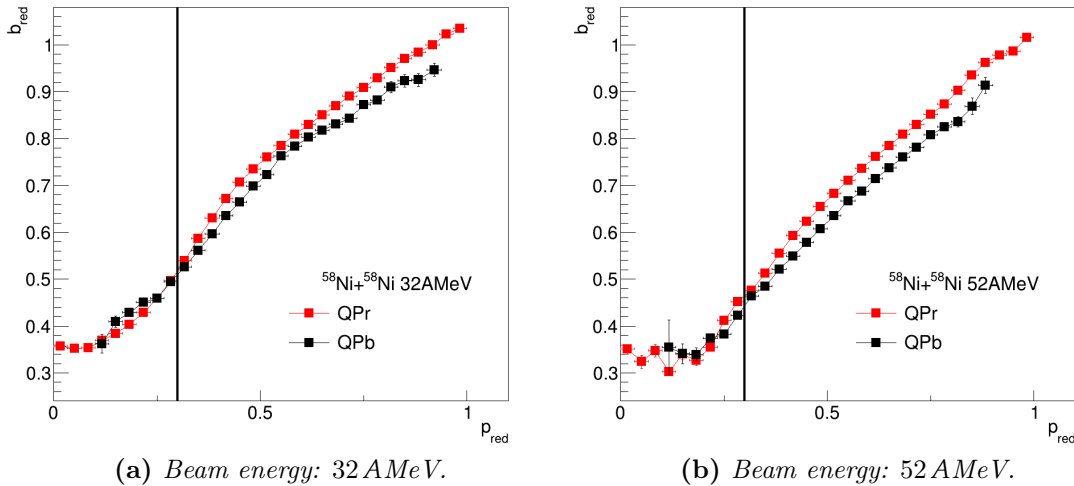


Figure 5.18: Comparison between the AMD+GEMINI predictions of the average b_{red} as a function of p_{red} for the two selected reaction channels QPr and QPb in the reactions $^{58}\text{Ni}+^{58}\text{Ni}$ at 32 A MeV and 52 A MeV. The plots obtained for the other systems show similar features. The vertical lines indicate the minimum p_{red} value (0.3) above which the correlations are considered reliable in the following analysis.

the minor oscillations that can be seen in the regions related to the most central ($p_{red} < 0.3$, which will be excluded) and to the most peripheral collisions are caused by the lack of statistics. In both panels, it can be noticed that the results for the two reaction channels are similar, particularly at 32 A MeV. Basing on this evaluation on simulated data, it seems safe to compare the results, reported as a function of p_{red} , between the QP evaporation channel and the QP breakup channel. In conclusion,

the reduced QP momentum along the beam axis p_{red} shows a clear correlation with the reaction centrality for $p_{red} \gtrsim 0.3$, which according to the model is independent of the neutron richness of the system. The behaviour is similar in the two output channels that we aim to study, and only minor variations can be found between the reactions induced by beams with different energies. The possible effect of these minor differences will be discussed in the next chapter when investigating the isospin equilibration. Due to its good sorting capability, together with its aforementioned good properties, p_{red} will be extensively used as centrality estimator in the following analysis.

5.4 Comparison between QPr and QPb channels

In this section we study, as a function of the centrality estimator p_{red} , two properties of the QP: the average charge $\langle Z \rangle$ and the average velocity $\langle v^{CM} \rangle$. Their behaviour is reported separately for the QPr and for the QPb reaction channels. In the latter case, the properties are evaluated for the reconstructed QP.

In Fig. 5.19 the average QP charge $\langle Z \rangle_{QP}$ is reported as a function of p_{red} , in red (black) for the evaporation (breakup) channel, for the reaction $^{58}\text{Ni}+^{58}\text{Ni}$ at 32 A MeV (panel (a)), and at 52 A MeV (panel (b)). A smooth correlation is found between the two observables, as expected, since the charge number of the QP is expected to decrease monotonously with increasing centrality, at least for semiperipheral and peripheral events. By comparing the plots for the two output channels we notice that for a given p_{red} , i.e. for a given centrality, the QP reconstructed from the breakup fragments is generally slightly heavier than the QP evaporation residue, with a wider gap at 32 A MeV. The difference between the two plots is about two charge units at 32 A MeV, and only one at 52 A MeV (varying slightly along the inspected p_{red} interval). A similar behaviour, including the amount of the difference between the two reaction channels, is observed for the other systems, though shifted towards their characteristic $\langle Z \rangle_{QP}$ (see the charge distributions in Fig. 5.2 and Fig. 5.7).

In Fig. 5.20 we show the average QP velocity in the CM reference frame $\langle v^{CM} \rangle_{QP}$ as a function of p_{red} for the two reaction channels, again for the reaction $^{58}\text{Ni}+^{58}\text{Ni}$ at the two beam energies. As expected on the basis of the definition of p_{red} , the two observables are clearly correlated. A slope change is clearly visible at about $p_{red} = 0.5$. The change is more marked for the QPr channel and for the greater beam energy (panel (b)). Again, by comparing the plots obtained for the two output channels, we find that the reconstructed QP is generally slower than the QP remnants in the QPr selection.

In summary, for a given reaction centrality, the QPb channel seems to select events where a heavier, slower QP is produced. A similar behaviour has been found in the AMD+GEMINI simulated data (both filtered and in 4π), also studying the $\langle Z \rangle_{QP}$ and $\langle v^{CM} \rangle_{QP}$ directly as a function of the reduced impact parameter.

Another interesting property of the QP is the diffusion angle in the CM $\langle \theta^{CM} \rangle_{QP}$.

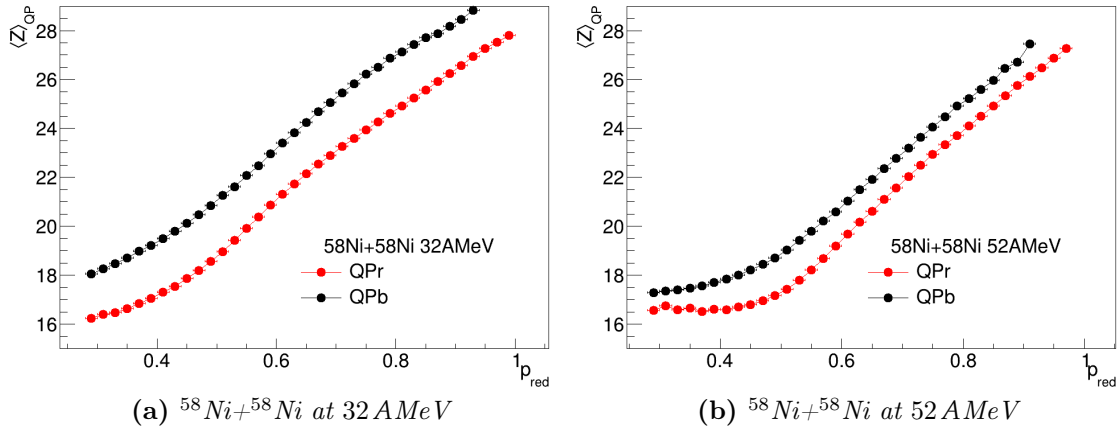


Figure 5.19: Comparison between the average charge of the QP residue in the evaporation channel and of the reconstructed QP in the breakup channel (experimental data). The results for the reaction $^{58}\text{Ni}+^{58}\text{Ni}$ are shown, at 32 A MeV in panel (a), 52 A MeV in panel (b). Similar results are obtained for the other systems.

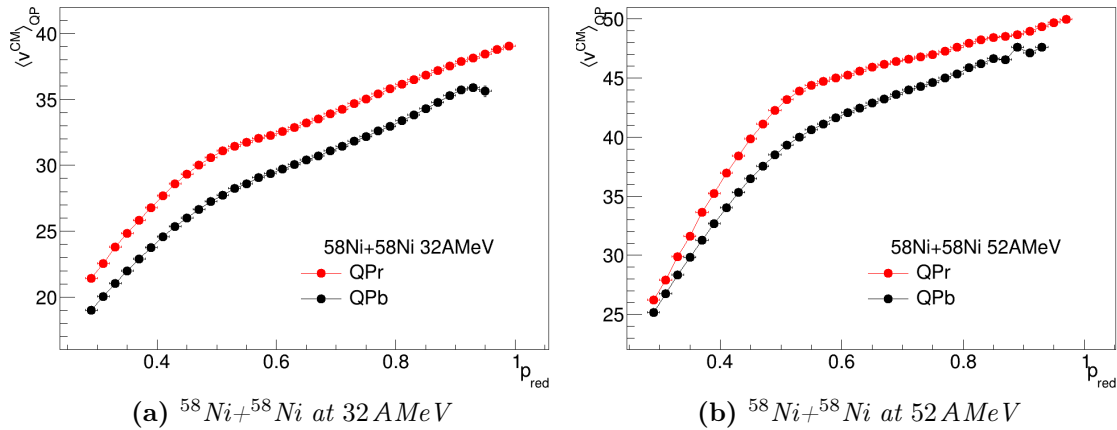


Figure 5.20: Comparison between the average velocity (in the CM reference frame) of the QP residue in the evaporation channel and of the reconstructed QP in the breakup channel (experimental data). The results for the reaction $^{58}\text{Ni}+^{58}\text{Ni}$ are shown, at 32 A MeV in panel (a), 52 A MeV in panel (b). Similar results are obtained for the other systems.

Unfortunately, when it comes to this variable, the geometrical acceptance of the apparatus differently affects the QPr channel and the QPb channel, making it difficult to compare them. Therefore, the diffusion angle $\langle \theta^{CM} \rangle_{QP}$ is not discussed in this work.

Isospin analysis

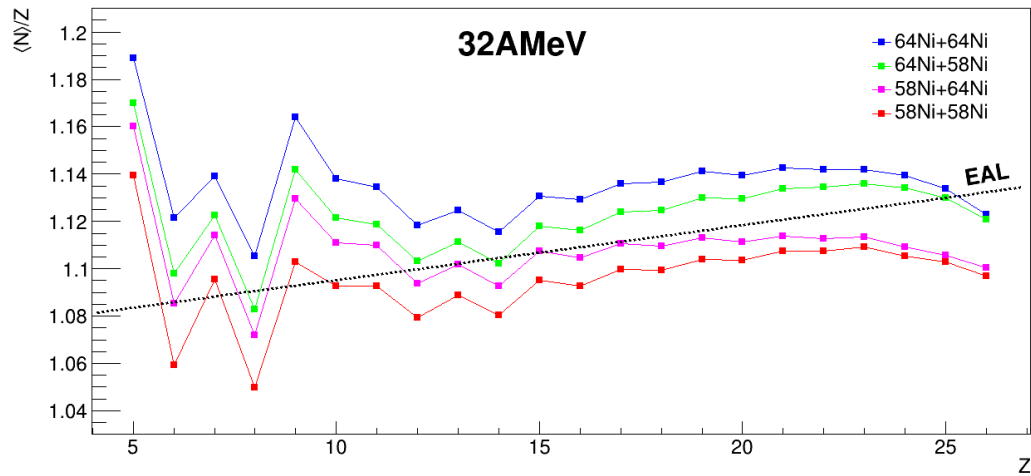
The main aim of the E789 experimental campaign is to study the isospin transport phenomena taking place between projectile and target during the contact phase of the collision, also comparing the results of four different reactions, $^{58,64}\text{Ni}+^{58,64}\text{Ni}$, at two different energies, 32 and 52 AMeV (see also Chapter 3). The long-term goal is to gather information on the symmetry energy term of the N EOS. In order to perform a study of this kind, the excellent identification capabilities (both in Z and A) of the INDRA-FAZIA apparatus have to be fully exploited. This part of the analysis will be illustrated in the present chapter. In fact, here we focus on the isospin characteristics of the detected fragments.

The results obtained for the different systems, beam energies, and selected reaction channels will be compared, in order to investigate the isospin dynamics, starting from the isospin diffusion between projectile and target in the asymmetric reactions. After a first general overview (Sec. 6.1), the isospin content of the different classes of fragments will be separately analysed. In Sec. 6.2 the neutron to proton ratio of the QP will be studied, in both the QPr and QPb event classes. The last sections are devoted to the analysis of the isospin characteristics of the emitted LCPs and IMFs in coincidence with the QP (Sec. 6.3) and those of the two breakup fragments HF and LF (Sec. 6.4). When relevant, some comparisons with the AMD+GEMINI model predictions will also be presented.

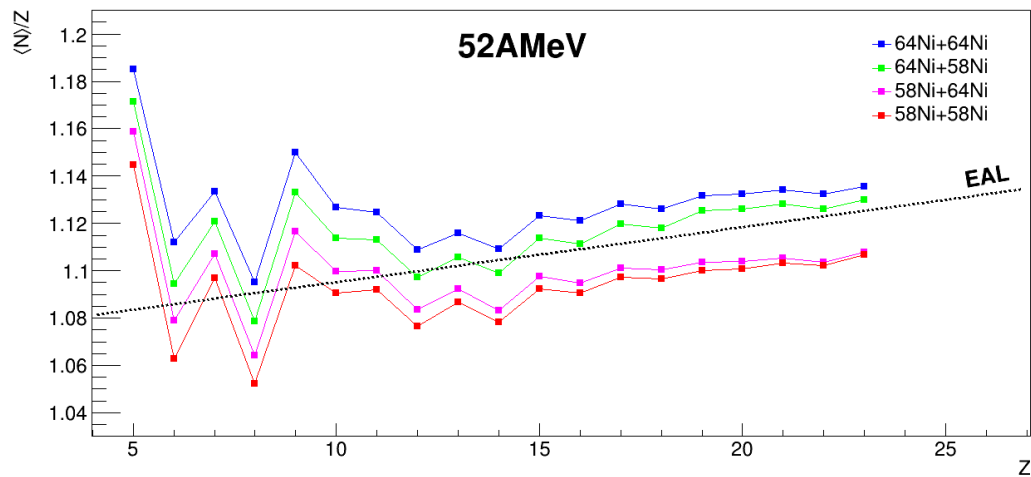
6.1 General isospin characteristics

As commonly done in the literature for this kind of studies, we use the average neutron to proton ratio $\langle N/Z \rangle$ as isospin observable (see Sec. 1.1.2). As an overview on the data, in Fig. 6.1 this quantity is reported as a function of Z for all the detected BFs with no selection on the exit channel. However, we remind that due to the acceptance of our apparatus, the great majority of the detected BFs belong to the QP phase space¹. The results for the four reactions at 32 AMeV (52 AMeV) are plotted in panel (a) (panel (b)). It can be easily noticed that the plots for the reactions

¹In fact, the observations that can be done on the plots in Fig. 6.1 for $Z > 14$ are generally valid also for the QP evaporation residue, since most of the events containing such a heavy fragment fall within the QPr selection.



(a) Beam energy: 32 A MeV.



(b) Beam energy: 32 A MeV.

Figure 6.1: Experimental plot of $\langle N \rangle / Z$ as a function of the charge Z for the BF ($Z > 4$) produced in the four reactions at 32 A MeV (panel (a)) and 52 A MeV (panel (b)), with no selection on the exit channel. The black dotted line represents the $\langle N \rangle / Z$ vs Z of the EAL (Evaporation Attractor Line, see Sec. 4.2.1), according to the parametrisation of eq.(4.11). We point out that there is still some uncertainty on the mass assignment for $Z = 26$, in panel (a).

at 52 A MeV extend only up to $Z = 23$, while those for the reactions at 32 A MeV extend up to heavier ejectiles. The explanation has been already given in Sec. 3.4.1 (see Fig. 3.18, in particular): at the higher energy, more fragments are identified by FAZIA² using the Si2-CsI ΔE -E correlation, featuring worse mass number identification with respect to the Si1-Si2 correlation. In the two plots of Fig. 6.1 it can be

²We remind that due to the reaction kinematics, the heavy QP-like ejectiles are generally emitted forward, and therefore collected by FAZIA.

noticed that the heavier ejectiles³ produced in the reactions induced by the neutron rich ^{64}Ni feature a $\langle N \rangle / Z$ sensibly lower than that of the original projectile (1.28), and, in the asymmetric reaction, also lower than the equilibrium value of the whole system (1.18). For the reactions induced by ^{58}Ni , the $\langle N \rangle / Z$ of the produced BFs is generally slightly higher than that of the projectile (1.07). This observation can be justified by taking into account both the role of the dynamical emission and the statistical emission from the excited source formed after the collision. As explained in Sec. 4.2.1, for the latter contribution we expect a general trend for the evaporation residue towards the EAL (black dotted line in Fig. 6.1). Indeed, we observe that the products of the four reactions, starting from the original $\langle N \rangle / Z$ value of the colliding system, clearly tend to approach the EAL; this is true for both beam energies, but the effect is slightly more pronounced for the reactions at 52 AMeV. Despite the strong role of statistical emission, the data clearly show the phenomenon of isospin diffusion. In fact, starting from the heavy products, almost exclusively belonging to the QP phase space (see e.g. Fig. 4.13), a different $\langle N \rangle / Z$ is observed for the reactions with same projectile and different targets (e.g. ^{64}Ni on ^{64}Ni , in blue, and on ^{58}Ni , in green), with an increasing $\langle N \rangle / Z$ gap with decreasing size of the ejectile. This different behaviour related to the neutron richness of the target, and therefore to the isospin asymmetry in the entrance channel, can be interpreted as the trend of the reaction partners toward isospin equilibrium, a trend whose effect survives the evaporation decay. The effect is slightly clearer at 32 AMeV than at 52 AMeV, as it can be expected due to the longer interaction time. In the following we further inspect this isospin transport phenomenon, also studying its evolution with centrality. Note that the most peripheral reactions, related to the production of the heaviest QP fragments, with $Z \sim Z_{proj}$, cannot be analysed in terms of isospin of the QP, due to the isotopic identification limits of the apparatus.

6.1.1 Comparison with AMD+GEMINI model predictions

The comparison of experimental isospin observables of the reaction products with theoretical predictions (see Chapter 4) allows to test the model reliability and to learn about the physics effects governing the isospin transport phenomena, also testing different recipes (asy-stiff and asy-soft) for the E_{sym} . In the previous chapter, we have shown that the AMD+GEMINI simulations satisfactorily predict many kinematical aspects of the produced ejectiles, both in the QPr and QPb channels; we now move to the isospin related aspects, widely studied for this combination of dynamical and statistical codes, also by the Florence group [60, 67–69, 129].

In Fig. 6.2a the average neutron to proton ratio $\langle N \rangle / Z$ of all the BF is plotted as

³The interpretation of the behaviour of the lighter BFs, with $Z \lesssim 10$ (which, we recall, in the present analysis are not considered QP-like fragments, see Tab. 5.1), is less straightforward, in some respects, also due to the larger $\langle N \rangle / Z$ variation related to a slight difference in the neutron content. The “oscillating” behaviour can be related to structure effects, such as pairing, that tend to bring down the $\langle N \rangle / Z$ of some even- Z nuclei, such as carbon and oxygen ($Z = 6, 8$, characterised by the preponderance of ^{12}C and ^{16}O , respectively, with $\langle N \rangle / Z = 1$). However, the clear hierarchy of the four systems is always respected.

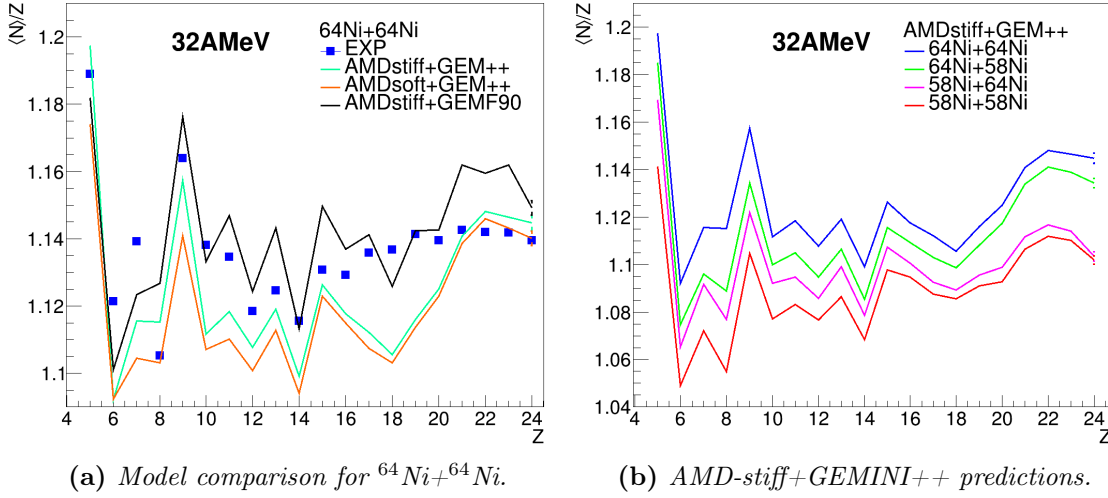


Figure 6.2: Model predictions for the $\langle N \rangle / Z$ vs Z of the BF produced in selected reactions studied in the E789 experiment (no selection on the exit channel). Panel (a): comparison of different model predictions (assuming different N_{EoS} parametrisations and/or employing different afterburners, see legend) for the reaction $^{64}\text{Ni}+^{64}\text{Ni}$ at 32 AMeV. Panel (b): AMD-stiff+GEMINI++ predictions for the four reactions at 32 AMeV. Please note the different y -axis range in the plots.

a function of Z for different inclusive datasets relative to the reaction $^{64}\text{Ni}+^{64}\text{Ni}$ at 32 AMeV. The blue markers refer to the experimental data (as in Fig. 6.1a), while the solid lines represent the results of three different model calculations on the same reaction. In particular, the green (orange) line refer to the AMD simulation assuming an asy-stiff (asy-soft) N_{EoS} parametrisation coupled to GEMINI++ as afterburner, while to obtain the data plotted with the black line the same AMD-stiff primary fragments have been de-excited with the FORTRAN 90 (F90 from now on) implementation of GEMINI⁴ (see Sec. 4.2). As expected from previous results in the literature, a very weak sensitivity to the stiffness of the symmetry energy is found at this level, as it can be noticed by comparing the two simulations exploiting GEMINI++ (green and orange lines); the definition of more sensitive observables on exclusive data is thus necessary [67]. Moreover, a larger difference is introduced by applying different afterburners to the same primary events, as it can be seen by comparing the green and black solid lines in Fig. 6.2a, both obtained from the same AMD-stiff calculation. No one of the three proposed calculations is found to well reproduce the experimental data, except for isolated fragment species.

The result represented in this plot indicates and confirms the heavy impact that the afterburner can have, larger than that of the symmetry energy parametrisation assumed for the transport model calculation. However, we can still look for hints

⁴As pointed out in Ref. [129], an important difference between the two GEMINI implementations lies in the adopted level density parametrisation. For further details on the different results that can be obtained with GEMINI F90 or GEMINI++ see Refs. [68, 129].

of some dynamical phenomena not destroyed by the statistical evaporation, e.g. by studying the relative behaviour of the four systems at the two energies, as done in the previous section. In the following, we will use the most recent version of GEMINI: the results for the filtered AMD+GEMINI++ simulations will be shown. A detailed study of the differences between the results obtained from the two versions of GEMINI as afterburner is foreseen. In Fig. 6.2b the AMD-stiff+GEMINI++ predictions for the $\langle N \rangle / Z$ vs Z of the BF produced in the four reactions at 32 AMeV are shown, using the same color code previously adopted in Fig. 6.1. Despite the different predicted values of $\langle N \rangle / Z$ with respect to the experimental ones, some features in common with those of Fig. 6.1a can be noticed: the clear hierarchy of the plots for the four systems is respected also in this case, and again the reactions induced by the same projectiles and different targets give systematically different $\langle N \rangle / Z$, indicating the action of the isospin diffusion mechanism. Given these considerations, in the following we will avoid showing direct comparisons of the neutron content (e.g. the $\langle N \rangle / Z$) of the ejectiles in the experimental and in the simulated datasets, but instead, we will present some selected features of the isospin observables (e.g. by exploiting the isospin transport ratio introduced in the following section) in order to highlight the effects of the dynamical phenomena.

6.2 Isospin characteristics of the QP fragment

We now move to a more exclusive isospin analysis of the different classes of ejectiles in the QPr and QPb reaction channels, starting with the properties of the QP. In this section, we aim to exploit the selection power of the experimental apparatus in order to study the isospin equilibration process between projectile and target by exploiting the properties of the QP residue in the evaporation channel (see Sec. 5.1) and of the reconstructed QP in the breakup channel (see Sec. 5.2). The evolution of the isospin equilibration with the reaction centrality will be studied by reporting the chosen isospin observables as a function of p_{red} (introduced in Sec. 5.3), which is correlated to the impact parameter almost independently of the studied system. Moreover, some comparisons will be done between the isospin equilibration observed in the two reaction channels.

6.2.1 Isospin equilibration in the QPr channel

We now consider the QPr channel, the most populated one. In the following, at first, we do not make any distinction based on the particles in coincidence with the QP residue, i.e. between the QPr+LCP and the QPr+IMF channels. The experimental $\langle N/Z \rangle$ of the QP evaporation residue as a function of p_{red} ⁵ is shown in Fig. 6.3: the four reactions at 32 AMeV are plotted in panel (a), those at 52 AMeV in panel (b). As a general observation, we notice a declining trend of the neutron content for de-

⁵For each p_{red} bin, the neutron to proton ratio is averaged over all the produced elements, according to their statistical weight.

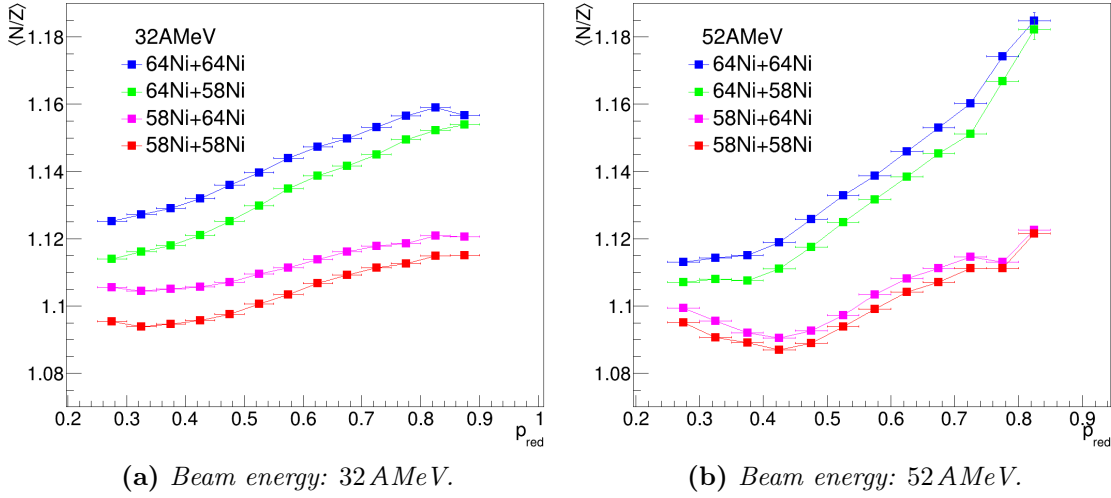


Figure 6.3: Experimental $\langle N/Z \rangle$ value as a function of p_{red} for the QP evaporation residue in the QPr channel selection for the four reactions at 32 A MeV (panel (a)) and at 52 A MeV (panel (b)). Statistical errors are plotted on the y -axis (generally smaller than the marker size), while the horizontal error bars are set equal to the p_{red} bin width.

creasing p_{red} , i.e. for increasing centrality, more evident for the reactions induced by the neutron rich projectile. This feature can be understood by considering that in more central collisions, more energy is dissipated in the internal degrees of freedom, resulting in the production of more excited fragments⁶. These hot fragments then evaporate, decreasing their atomic and mass number, and globally approaching the EAL: the decreasing behaviour of the $\langle N/Z \rangle$ of the QP remnant with increasing centrality reflects that of the EAL with decreasing atomic number Z (see Fig. 6.1). However, more deeply inspecting the results as for the isospin transport, we first observe that, at both energies, a clear ordering of the four systems is always respected: for each p_{red} value, the $\langle N/Z \rangle$ obtained for the asymmetric reactions are located between those of the two symmetric reactions. For the most peripheral collisions (located on the right in the plots in Fig. 6.3) we see that the isospin content of the QP residues produced in the reactions with the same projectile and different targets is quite similar, almost the same in some cases. Moving towards more central collisions (i.e. leftwards in the plots), we find an increasing gap between the $\langle N/Z \rangle$ of the QP remnant of the asymmetric reactions and that of the corresponding symmetric ones sharing the same projectile. Moreover, the $\langle N/Z \rangle$ values for the asymmetric systems (plotted in green and magenta) tend to approach each other. As anticipated, this evidence can be ascribed to the trend toward isospin equilibrium between projectile and target in the asymmetric reactions, producing a higher degree of equilibration for more central collisions (larger $\langle N/Z \rangle$ gap), as expected. Moreover, we observe that the equilibration effect is greater in the reactions at 32 A MeV with respect to

⁶This is a very general consideration, where the role of pre-equilibrium emission, which can modify the isospin content of the primary fragments, is not taken into account.

52 AMeV, as expected from the longer projectile-target interaction time at lower beam energy.

The isospin equilibration between projectile and target in the asymmetric reactions can be further highlighted by exploiting the **isospin transport ratio**, or *imbalance ratio* [19], a variable which evidences the effect of the equilibration in an asymmetric system by exploiting the information on the corresponding neutron rich and neutron deficient symmetric reactions. This method has already been used in various works [41, 132, 153, 154], also in the FAZIA group [69], and it is expected to help to constrain the density dependence of the symmetry energy of the N EOS by enhancing the differences resulting from the assumption of different parametrizations [10].

Let X be an isospin sensitive observable, such as the average neutron to proton ratio $\langle N/Z \rangle$, and let A and B be the two nuclear species employed in the reactions, having different N/Z values (greater for A with respect to B). The isospin transport ratio R calculated exploiting the observable X is defined as:

$$R_i(X) = \frac{2X_i - X_{AA} - X_{BB}}{X_{AA} - X_{BB}} \quad (6.1)$$

where $i = AB, BA$ indicates one of the two asymmetric projectile-target combinations, while AA and BB indicate the neutron rich and the neutron deficient symmetric systems, respectively. Since we have measured both the $^{64}\text{Ni}+^{58}\text{Ni}$ and $^{58}\text{Ni}+^{64}\text{Ni}$ asymmetric reactions, two different “branches” of the isospin transport ratio can be evaluated, using the symmetric reactions as a reference. If the isospin transport ratio $R(X)$ was calculated for the symmetric reactions, it would be constant and equal to 1 (−1) for $^{64}\text{Ni}+^{64}\text{Ni}$ ($^{58}\text{Ni}+^{58}\text{Ni}$), by definition. For the asymmetric reactions, the limit of the non-equilibrated condition corresponds to $R_i(X) = \pm 1$, while, in case of a linear dependence of X from the system isospin [19], a value $R_i(X) = 0$ is obtained for a fully equilibrated outcome. If the experimental conditions are the same for the four reactions, we can assume that by looking at the differences between them, exploiting eq. (6.1), the systematic uncertainties related to the apparatus are eliminated and the ratio is only affected by statistical errors [19]. Moreover, assuming a similar action in all the systems, also the effects of statistical de-excitation are largely bypassed by employing the ratio [68, 154]. Similarly, the isospin transport ratio allows to reduce the sensitivity to the effects of pre-equilibrium emission⁷, further highlighting the isospin diffusion between projectile and target [41]. In general, the isospin transport ratio technique allows to bypass any perturbing effect introducing a linear transformation on the considered isospin observable X [68].

In Fig. 6.4 the two branches of the isospin transport ratio $R_i(\langle N/Z \rangle)$ for the two asymmetric systems of the E789 experiment are reported as a function of p_{red} ; the same colour code of the previous plots has been adopted for the two asymmetric

⁷As explained in Ref. [41], without the isospin diffusion phenomenon, the pre-equilibrium emission of the projectile should be mostly target independent, and approximately the same for the asymmetric and symmetric reactions with the same projectile. By exploiting the difference between the inspected systems, its contribution is largely suppressed.

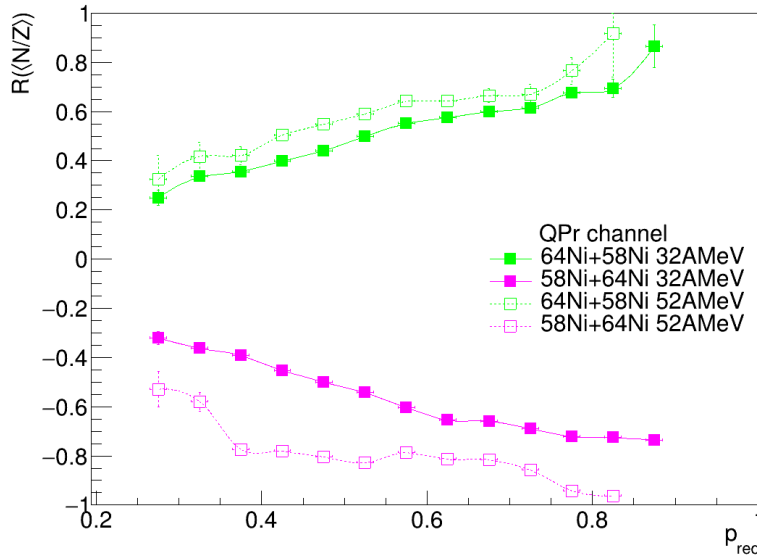


Figure 6.4: Isospin transport ratio calculated with the $\langle N/Z \rangle$ for the QP evaporation residue in the QPr channel selection, as a function of p_{red} (experimental data). The results for the asymmetric reactions $^{64}\text{Ni}+^{58}\text{Ni}$ and $^{58}\text{Ni}+^{64}\text{Ni}$ are plotted for both energies. The vertical error bars, often smaller than the marker size, correspond to statistical errors.

reactions. Both the results at 32 AMeV (full squares, solid line) and at 52 AMeV (open squares, dotted line) are plotted in the same panel, in order to facilitate their comparison. For the most peripheral reactions we obtain values of $R_i(\langle N/Z \rangle)$ close to ± 1 , with an absolute value always smaller than unity⁸. For decreasing p_{red} , i.e. increasing centrality, the value of $R_i(\langle N/Z \rangle)$ is driven towards zero in both branches: this evidence can be related to the action of isospin diffusion. The full equilibration $R_i(\langle N/Z \rangle) = 0$ is not achieved, probably because we are not investigating the most central collisions; indeed, the plots are only shown for $p_{red} \gtrsim 0.3$, since as pointed out in Sec. 5.3 the p_{red} variable cannot be considered a reliable centrality estimator below that value, for the most central collisions. The behaviour of the ratio as a function of p_{red} shows a very clear and regular trend, quite smoother at 32 AMeV. By comparing the results for the two beam energies, it can be noticed that a different degree of isospin equilibration seems to be achieved: indeed, the plots of $R_i(\langle N/Z \rangle)$ for the reactions at 32 AMeV are closer to zero than those at 52 AMeV⁹. Therefore, as already qualitatively observed in the $\langle N/Z \rangle$ vs p_{red} plots in Fig. 6.3,

⁸The mass number of the heaviest QP remnants, mainly produced in the most peripheral collisions, cannot be determined by FAZIA. In this analysis, only fully identified QP remnants are considered, so that $|R_i(\langle N/Z \rangle)|$ does not reach unity even for high p_{red} values.

⁹The difference is more evident between the lower branches of the isospin transport ratio (plotted in magenta), corresponding to the reaction $^{58}\text{Ni}+^{64}\text{Ni}$. This observation evidences an asymmetry of the two branches with respect to the full equilibration reference $R(\langle N/Z \rangle) = 0$, which is greater at 52 AMeV. This asymmetric behaviour of the ratio was not expected, in principle. Further investigations on this feature are underway. An hypothesis is related to a different role of statistical emission on the QP produced in the reactions induced by different projectiles.

the data indicate a larger degree of isospin equilibration reached at 32 A MeV than at 52 A MeV, for which a shorter projectile-target interaction time can be expected.

These results are not substantially modified by setting a different minimum limit Z_{QPF}^{lim} for the QP-like fragment (see Sec. 5.1), within a reasonable interval: in fact, due to the correlation between the size of the QP remnant and the p_{red} variable (i.e. the anticorrelation with the reaction centrality), choosing a higher (lower) Z_{QPF}^{lim} only slightly affects the leftmost points, at the lowest considered $p_{red} \sim 0.3$, that result slightly shifted towards less (more) isospin equilibrated configurations. However, the overall behaviour remains unchanged. This consideration stands also for the QPb reaction channel, analysed in the following.

QPr+LCP and QPr+IMF subclasses – We also checked whether a different behaviour is found between the two subclasses of the QPr channel, namely the QPr+LCP (QP remnant accompanied only by LCPs) and the QPr+IMF (with at least an IMF in coincidence with the QP) selections. The $\langle N/Z \rangle$ vs p_{red} plots obtained for the QPr+LCP subclass are essentially those presented in Fig. 6.3, since, as it can be seen from Tab. 5.2, these events constitute the large majority of the QPr channel selection. On the other hand, we observed that, for all the systems, the $\langle N/Z \rangle$ of the QP remnant in the events marked as QPr+IMF is lower than for the prevailing QPr+LCP events. A possible interpretation of this effect lies in the isospin drift phenomenon: in fact, the accompanying IMF, generally emitted at midvelocity, is likely to be generated from the neck region, showing its characteristic neutron richness and leaving behind a more neutron deficient QP remnant. However, by exploiting the isospin transport ratio technique, the same results are obtained for both the subclasses of the QPr selection. This confirms the capability of the method to isolate the equilibrating action of isospin diffusion between projectile and target, bypassing those effects, including the isospin drift, acting in a similar way in the four reactions.

6.2.2 Isospin equilibration in the QPb channel

We can analyse the events in the QPb channel selection in a similar way as seen in Sec. 6.2.1, by considering the isospin properties of the QP, reconstructed as the sum of the two breakup fragments. In Fig. 6.5 the experimental plots of the average neutron to proton ratio $\langle N/Z \rangle$ of the reconstructed QP as a function of p_{red} are shown for the reactions at 32 A MeV in panel (a), 52 A MeV in panel (b). The $\langle N/Z \rangle$ plots feature similar characteristics with respect to those shown in Fig. 6.3 for the QPr reaction channel. Also in this case, there is an evident declining trend of the $\langle N/Z \rangle$ towards more damped collisions, especially for the reactions induced by a ^{64}Ni projectile. However, under careful inspection, it can be noticed that the $\langle N/Z \rangle$ of the reconstructed QP in the breakup channel is generally lower with respect to that of the QP residue in the evaporation channel (note the different y -axis range in Fig. 6.3 and in Fig. 6.5). This can be interpreted as a consequence of the fact that in the QPb channel, the (Z, A) of the QP is obtained as the sum of the (Z, A) of

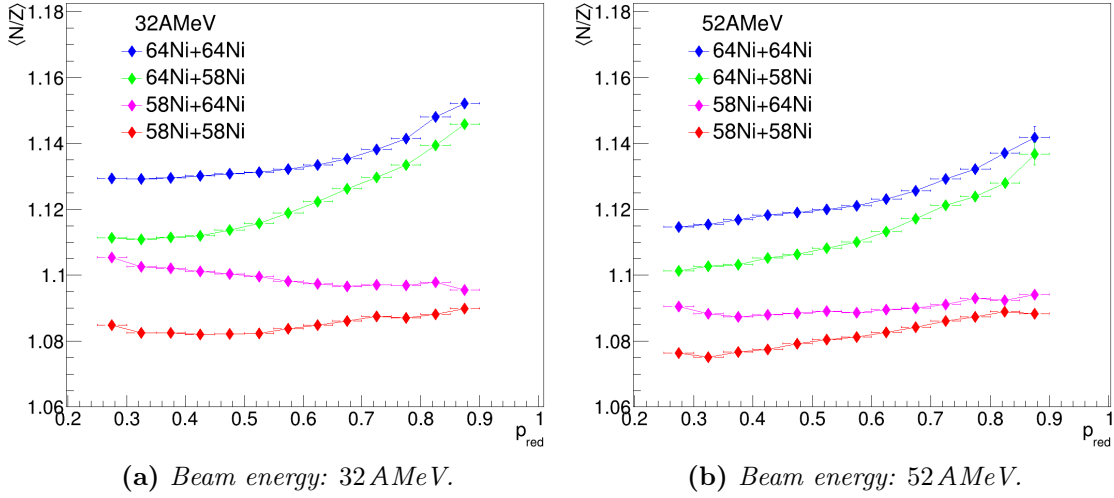


Figure 6.5: Experimental $\langle N/Z \rangle$ value as a function of p_{red} for the reconstructed QP in the QPb channel selection for the four reactions at 32 A MeV (panel (a)) and at 52 A MeV (panel (b)). Statistical errors are plotted on the y -axis (generally smaller than the marker size), while the horizontal error bars are set equal to the p_{red} bin width.

two lighter fission fragments, for which the EAL predicts lower $\langle N/Z \rangle$ with respect to heavier fragments (see Fig. 6.1); therefore, the $\langle N/Z \rangle$ of the reconstructed QP tends to assume lower values than those predicted for a QP residue with the same atomic number¹⁰.

However, also in the QPb reaction channel, we observe the clear hierarchy of the four systems, starting from the most neutron rich symmetric reaction, down to the most neutron deficient one. Concerning the two asymmetric systems, also in this case we notice that the distance from the data of the reference symmetric case increases with increasing centrality. Again, we highlight this evidence of isospin equilibration by exploiting the isospin transport ratio, calculated using the $\langle N/Z \rangle$ of the reconstructed QP. The experimental results for both asymmetric reactions (in green and magenta) and for both beam energies (32 A MeV in full diamonds, solid line, and 52 A MeV in open diamonds, dotted line) are shown in Fig. 6.6 as a function of p_{red} . Similarly to what observed in the QPr channel, we see a clear evolution towards isospin equilibrium with increasing centrality, starting from $R_i(\langle N/Z \rangle)$ values close to ± 1 for the most peripheral reactions¹¹, and tending to zero with decreasing p_{red} .

¹⁰As an example, exploiting eq. (4.11), for a $Z = 18$ residue, a value $\langle N/Z \rangle = 1.114$ is predicted for the EAL, while for the sum of two fragments with $Z = 11$ and $Z = 7$ we obtain $\langle N/Z \rangle = 1.094$. A difference of this entity would be visible in the $\langle N/Z \rangle$ scale shown in Fig. 6.5.

¹¹As in the QPr channel, also in this case we can expect a suppression of values of $|R_i(\langle N/Z \rangle)| \sim 1$ due to the lack of very peripheral reactions in the selection, but for a different reason. In fact, according to the model predictions, the QPb channel is well populated only for $b_{red} \lesssim 0.85$, and the statistics drops for the most peripheral collisions. Since this characteristics has been observed both in the filtered AMD+GEMINI simulations and in the 4π model predictions, it does not seem to be related to the apparatus acceptance, but to the properties of this output channel. On the other

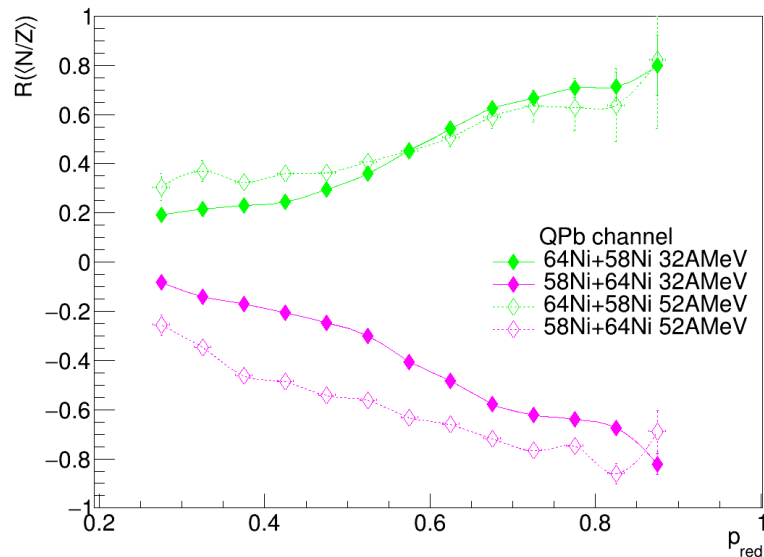


Figure 6.6: Isospin transport ratio calculated with the $\langle N/Z \rangle$ for the reconstructed QP in the QPb channel selection, as a function of p_{red} (experimental data). The results for the asymmetric reactions $^{64}\text{Ni}+^{58}\text{Ni}$ and $^{58}\text{Ni}+^{64}\text{Ni}$ are plotted for both energies. The vertical error bars, often smaller than the marker size, correspond to statistical errors.

Also for this channel, we find that even for the smaller p_{red} values ($p_{red} \sim 0.3$) the value $|R_i(\langle N/Z \rangle)| = 0$, i.e. the full equilibration, is not reached. By comparing this result with that for the QPr channel, we notice a steeper trend towards equilibration in a central p_{red} interval, mostly for the reactions at 32 AMeV. Concerning the differences between the results at the two energies, for the lower branch ($^{58}\text{Ni}+^{64}\text{Ni}$) we obtain a higher degree of equilibration at 32 AMeV than at 52 AMeV. The results for the upper branch ($^{64}\text{Ni}+^{58}\text{Ni}$) show a different behaviour: the plots are compatible within errors for the most peripheral p_{red} bins, while a gap develops only for increasing centrality, so that a larger equilibrium level seems to be reached at the lower bombarding energy for small p_{red} .

6.2.3 Comparison between QPr and QPb channels

In Sec. 5.3 it has been shown that the correlation between p_{red} and b_{red} is really similar between the QPr and QPb reaction channels. Basing on this result, we can rather confidently present the comparison between the isospin transport ratio obtained for the two selected output channels. In Fig. 6.7 the two branches of the isospin transport ratio obtained in the QPr channel (full squares, dark solid line) and the QPb channel (open diamonds, light dotted line) are compared for the reactions at 32 AMeV in panel (a) and at 52 AMeV in panel (b). In both plots, a quite general observation arises: the breakup channel generally shows a stronger trend toward

hand, it is quite feasible that the breakup channel may be associated to relatively large energy dissipated in the system.

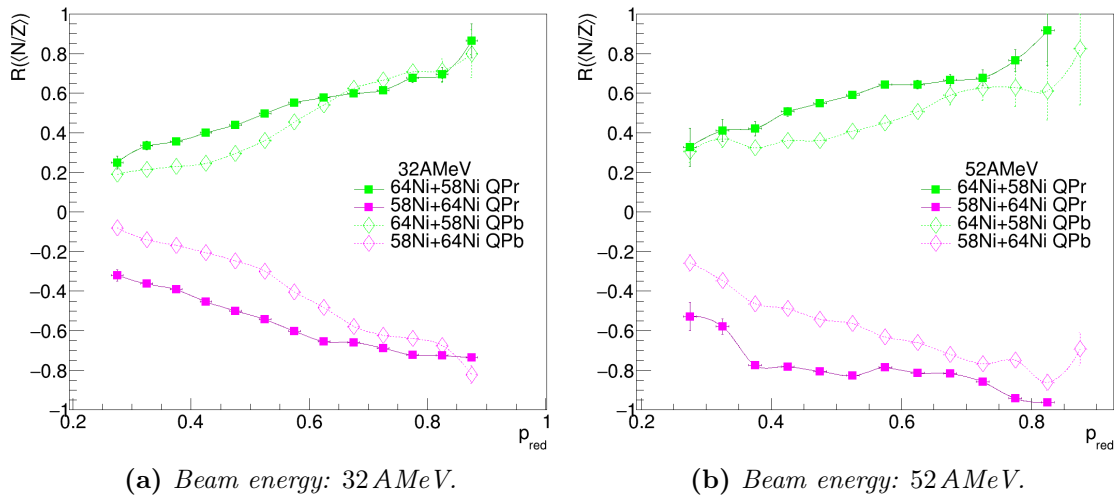


Figure 6.7: Comparison of the QP $\langle N/Z \rangle$ isospin transport ratio as a function of p_{red} between the QPr and the QPb channel selections (experimental data), at 32 A MeV (panel (a)) and at 52 A MeV (panel (b)). The vertical error bars, often smaller than the marker size, correspond to statistical errors.

isospin equilibration with respect to the evaporation channel for the same asymmetric reaction. At both energies, the difference is much stronger between the lower branches of the isospin transport ratio, i.e. for the reaction $^{58}\text{Ni}+^{64}\text{Ni}$ (in magenta). The difference is still evident also for the other asymmetric reaction, $^{64}\text{Ni}+^{58}\text{Ni}$ (in green), even if at 32 A MeV it is present only for less peripheral collisions.

However, though until now we have assumed the behaviour of p_{red} with centrality independent of the output channel, in Fig. 5.18 of Sec. 5.3 minor differences can be noticed between the b_{red} vs p_{red} correlations obtained for the two reaction channels in the simulated data. In order to investigate the possible role of these differences on the experimental data interpretation, in Fig. 6.8 we present the same plots of Fig. 6.7 after a rescaling of the x -axis from the p_{red} variable to b_{red} . The rescaling has been performed exploiting the AMD+GEMINI predictions on the b_{red} vs p_{red} correlations, selecting the one for the beam energy and output channel associated to each branch of the isospin transport ratio¹². Also in these plots we notice the different behaviour between the QPr and QPb channels, with the latter showing a higher degree of isospin equilibration, more evidently for the $^{58}\text{Ni}+^{64}\text{Ni}$ reaction.

This observation constitutes an open problem and deserves deeper investigation. The QP breakup channel seems to select a set of events where a more prominent role has been played by the isospin diffusion between projectile and target, resulting in a more isospin equilibrated QP. This may be due to the indirect selection of events in

¹²We recall that no variation of the b_{red} vs p_{red} correlation has been evidenced among the different systems inspected. However, we separately rescaled each branch of the isospin transport ratio exploiting the b_{red} vs p_{red} correlation obtained for the respective asymmetric system. Note that, unlike the plots in Fig. 6.7, those presented in Fig. 6.8 are model dependent.

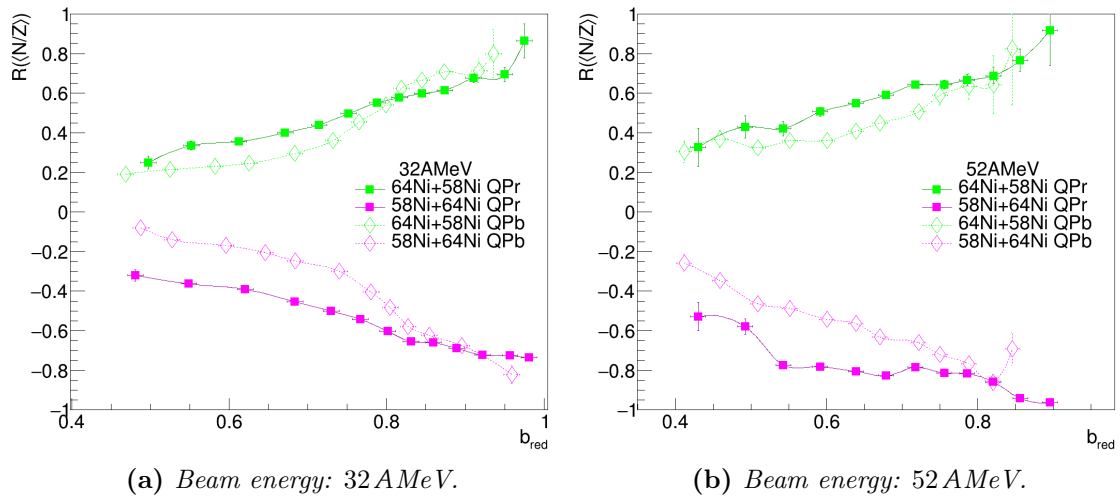


Figure 6.8: Comparison of the QP $\langle N/Z \rangle$ isospin transport ratio as a function of b_{red} between the QPr and the QPb channel selections, at 32 A MeV (panel (a)) and at 52 A MeV (panel (b)). The plots are obtained by converting the p_{red} axis of the plots in Fig. 6.7 into a b_{red} axis, by exploiting the b_{red} vs p_{red} correlations obtained with the AMD+GEMINI simulations. The vertical error bars, often smaller than the marker size, correspond to statistical errors. The horizontal error bars are related to the width of the b_{red} vs p_{red} correlations.

the tail of the distribution of some parameter related to the reaction dynamics (e.g. the density range explored in the neck region, through which the isospin diffusion takes place, or the contact time between projectile and target).

Comparison with FAZIA-SYM observations – It is worth mentioning, at this point, that a similar study has been carried out by the FAZIA collaboration also on the FAZIA-SYM data, in Ref. [69], where the asymmetric reaction $^{48}\text{Ca}+^{40}\text{Ca}$ at 35 A MeV has been compared to the two symmetric reactions at the same beam energy, an energy quite close to the 32 A MeV available in the E789 dataset. Also in that case, the isospin transport ratio calculated on the $\langle N/Z \rangle$ of the QP has been exploited to study the phenomenon of isospin diffusion as a function of the reduced QP momentum p_{red} . However, the comparison between the QP evaporation and QP breakup channels did not reveal any difference between them (see Fig. 6.9, taken from Ref. [69]). Moreover, in the FAZIA-SYM data, a globally smaller degree of isospin equilibration between projectile and target was found in the asymmetric system with respect to E789 data, reaching a minimum value $R_{AB}(\langle N/Z \rangle) \sim 0.6$ for $p_{red} \sim 0.3$.

A major difference between the two experiments lies in the geometrical coverage of the experimental apparatus: in the FAZIA-SYM experiment a 4 blocks FAZIA configuration has been employed, covering the forward angles up to $\theta_{lab} \sim 8^\circ$. In order to study the possible role of the apparatus acceptance on the different results,

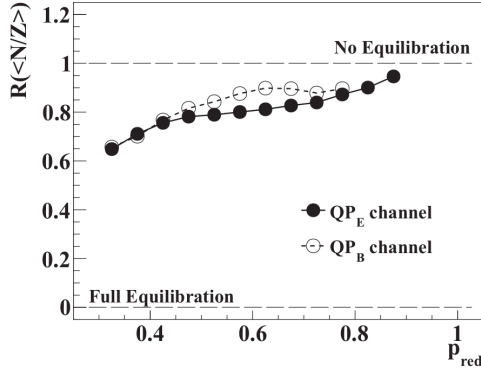


FIG. 6. Isospin transport ratio for the QP_E and QP_B channels as a function of p_{red} . Statistical errors are smaller than the symbol size. Symbols according to the legend. Lines are guides for the eye.

Figure 6.9: Isospin transport ratio calculated with the QP $\langle N/Z \rangle$ obtained according to the FAZIA-SYM experimental data on the reaction $^{48}\text{Ca}+^{40}\text{Ca}$ at 35 A MeV, for the evaporation (QP_E , in the legend) and the breakup (QP_B) channels. Figure and caption taken from Ref. [69].

we applied a filter simulating the FAZIA-SYM coverage on the E789 experimental data. However, this reduced geometry did not reproduce the differences on the isospin equilibration observed in the two selected reaction channels in the upper branches at 32 A MeV (i.e. those comparable to the asymmetric system measured in FAZIA-SYM). Moreover, the correlation of p_{red} with the reduced impact parameter behaves similarly in E789 and in FAZIA-SYM, according to the AMD+GEMINI model predictions.

Further investigations are foreseen in order to shed light on these different results, that, if we are able to exclude experimental effects (that, anyhow, should be bypassed by using the isospin transport ratio), could be related to the differences between the inspected systems, either in size, initial projectile-target isospin asymmetry, contact time or nuclear density intervals explored in the collision.

6.2.4 AMD+GEMINI model predictions

In Sec. 6.1.1 it has been pointed out that in the AMD+GEMINI++ simulations some hints indicate the action of isospin diffusion, although the experimental neutron content of the secondary fragments is not well reproduced. Moreover, the models have shown the strong effect of the evaporation decay on the $\langle N/Z \rangle$ of the final products; such an effect is larger than the effect of different choices of the symmetry energy term of the N EoS. It is therefore interesting to apply the isospin transport ratio technique to the model data, calculating it as done for the experimental events. This should help to enhance the isospin equilibration effect, also reducing the sensitivity to secondary decays. The AMD+GEMINI++ results for the isospin transport ratios calculated from the $\langle N/Z \rangle$ of the QP are plotted as a function of p_{red} in Fig. 6.10 for the four reactions at 32 A MeV (the reactions at 52 A MeV are not shown since the main features are qualitatively similar). The plot in panel (a) refers to the QP remnant in the evaporation channel, the one in

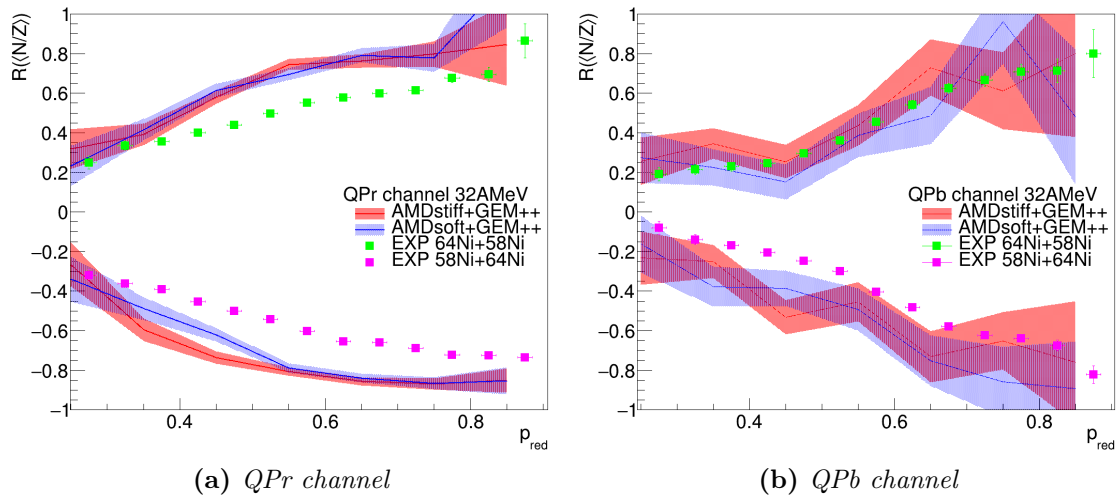


Figure 6.10: Isospin transport ratio calculated with the $\langle N/Z \rangle$ of the QP (remnant in the QPr channel, panel (a), reconstructed in the QPb channel, panel (b)), reported as a function of p_{red} , for the reactions at 32 A MeV. The full squares refer to the experimental results, with the vertical error bars, often smaller than the marker size, corresponding to statistical errors. The AMD+GEMINI++ predictions are plotted with solid lines; the width of the statistical errors is represented by the shaded bands.

panel (b) refers to the reconstructed QP in the breakup channel. The results of the simulations assuming an asy-stiff (asy-soft) parametrisation of the N EoS are plotted with the red (blue) solid line (the same color has been used for both branches of the ratio), with shaded bands representing the associated statistical errors. In each plot, the respective experimental result is also shown with full square markers for comparison (the same plots shown in Fig. 6.4 and Fig. 6.6).

For the QPr channel, the model clearly shows the evolution toward the isospin equilibration, as for the experimental data, with $R_i(\langle N/Z \rangle)$ moving towards zero for low p_{red} . However, no sensitivity to the asy-stiffness of the E_{sym} of the N EoS is obtained, since the plots associated with the two different AMD simulations are almost coincident within the errors. Moving to the comparison with the experimental results, the simulated data generally show a lower degree of equilibration, with a more marked discrepancy in a central interval of the inspected p_{red} range.

The simulated values of the isospin transport ratio in the QPb channel are evidently affected by larger errors, as a consequence of the lower statistics available for this less populated channel (see Tab. 5.3). A larger number of simulated events may help to narrow down these uncertainties. A fortiori, due to the larger fluctuations, within errors we can exclude any sensitivity of the result on the E_{sym} hypothesis. Concerning the comparison with the experimental plots, the agreement is rather good, though somewhat worse for the simulated lower branch with respect to the experimental points. Indeed, the two simulated branches seem to be more symmet-

ric with respect to the $R_i(\langle N/Z \rangle) = 0$ level than the experimental plots, as already previously noticed.

However, also in the simulated data we find the tendency to a larger degree of isospin equilibration in the breakup channel with respect to the evaporative channel, as it can be seen by comparing the two panels of Fig. 6.10. The difference between the two channels is even bigger than in the experimental data. This leads us to think that the AMD simulations can be exploited to track the differences between the dynamical scenarios in the primary events¹³, indirectly selected by the QPr and QPb conditions in the secondary events.

6.3 Isospin characteristics of LCPs and IMFs

As the BFs, also the lighter emissions, both LCPs and IMFs, enclose rich information on the isospin dynamics related to the collision event. As anticipated in Sec. 1.1.2, the isotopic composition of the LCPs and IMFs is generally studied in relation to their emission pattern (e.g. as a function of their velocity component along the beam axis, or along the QP direction), in order to link them to their original sources. For instance, since the decay products of the QP reflect its isotopic composition, they can be used as tracers for the isospin diffusion between the two reaction partners [42, 43, 67, 155]. A similar study is based on the same principle that we exploited in the previous section, analysing the isospin content of the QP (but in that case, from its direct identification). On the other hand, by analysing the characteristics of the LCPs and IMFs emitted at midvelocity, it is possible to highlight the isospin drift phenomenon in the neck region [43–46, 67], which can occur at Fermi energies and somehow overlap with the isospin diffusion for asymmetric systems.

In this section we analyse the isospin characteristics of the emitted LCPs and IMFs in order to isolate some effects of the isospin transport phenomena. The evidence for supporting the already observed isospin diffusion and the hints for isospin drift have been treated separately.

6.3.1 Ejectiles of the QP: isospin diffusion

In this section, we study the effect of isospin diffusion on the neutron content of the light particles produced in the QP de-excitation, considering the QP evaporation channel, QPr. In the statistical phase, the excited QP decays mostly through particle evaporation, with the production of LCPs. In the literature, the QP decay emissions are generally studied by considering the particles forward emitted with respect to the QP remnant, in order to exclude the backward emission, which could be a mix of statistical evaporation (from both the QP and the QT) and other emissions more linked to the dynamical phase of the collision.

¹³It is in fact possible to go back in time within each AMD simulated event, applying the fragment recognition algorithm described in Ref. [60], in order to extract interesting information on the reaction dynamics, e.g. the contact time between projectile and target, or the nuclear density distributions.

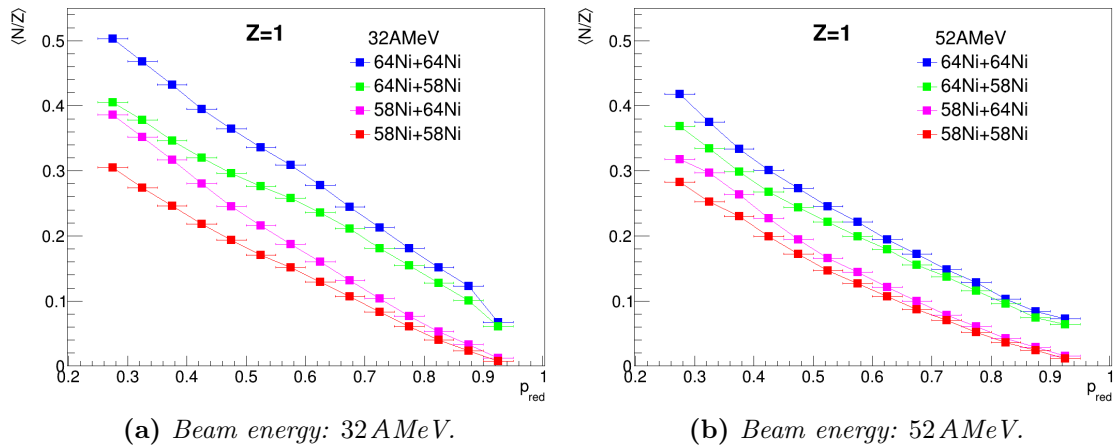


Figure 6.11: Experimental $\langle N/Z \rangle$ value as a function of p_{red} for the $Z = 1$ particles emitted forward with respect to the QP (QP channel) for the four reactions at 32 A MeV (panel (a)) and at 52 A MeV (panel (b)). Statistical errors are plotted on the y -axis (generally smaller than the marker size), while the horizontal error bars are set equal to the p_{red} bin width.

As done in the previous section, we employ the $\langle N/Z \rangle$ as isospin related observable, in this case, for the QP-forward emitted fragments. The characteristics of $Z = 1$ and $Z = 2$ particles have been studied separately. We only show the results for Hydrogen isotopes, since for Helium the α particles constitute almost the entire sample, thus reducing the sensitivity to small variations of the yield of the other isotopes¹⁴. In Fig. 6.11 the $\langle N/Z \rangle$ of the Hydrogen isotopes forward emitted with respect to the QP is reported as a function of p_{red} for the four reactions at 32 A MeV in panel (a) and at 52 A MeV in panel (b). In a way, we are looking at a complementary picture with respect to what presented in Fig. 6.3, where we observed a general loss of the QP neutron content with increasing centrality. Here, on the other hand, for all the reactions we find more neutron rich $Z = 1$ emissions for low p_{red} values, which is consistent with the idea that the decreasing trend of the $\langle N/Z \rangle$ of the QP remnant with decreasing p_{red} is at least partly due to the role of statistical emissions. However, a priori, the role of pre-equilibrium emission cannot be excluded [31]. In the plots in Fig. 6.11 we can identify some features similar to those observed in the $\langle N/Z \rangle$ vs p_{red} plots presented above, like e.g. the clear hierarchy of the four systems, respected at both energies. Also in this case, we observe a different behaviour between the reactions induced by the same projectile on different targets, and a clear trend of the two asymmetric systems towards isospin equilibration for the most damped collisions, at low p_{red} . Since, as mentioned, the chemical composition of the forward emitted Hydrogen particles is an observable sensitive to the isospin content

¹⁴To evidence the small variations of the population of ${}^3\text{He}$ and ${}^6\text{He}$, the isotopic and/or the isobaric yield ratios could be exploited [43,67]. For brevity, since no further information is brought, we decided not to report the results of such an analysis in this work.

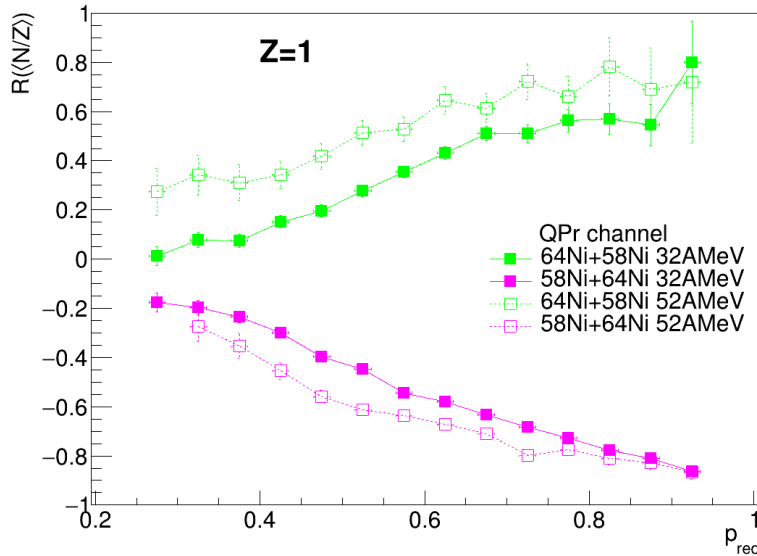


Figure 6.12: Isospin transport ratio calculated with the $\langle N/Z \rangle$ of the $Z = 1$ particles emitted forward with respect to the QP (QPr channel), reported as a function of p_{red} (experimental data). The results for the asymmetric reactions $^{64}\text{Ni}+^{58}\text{Ni}$ and $^{58}\text{Ni}+^{64}\text{Ni}$ are plotted for both energies. The vertical error bars correspond to statistical errors.

of the QP, we can exploit it to build the isospin transport ratio according to eq. (6.1), that also in this case can be plotted as a function of p_{red} . The resulting plot is shown in Fig. 6.12 for both asymmetric reactions (in different colours) at both energies (full squares, solid line for 32 AMeV and open squares, dotted line for 52 AMeV). The effect of isospin diffusion, driving the two systems towards equilibration for more central collisions is evident, and it is confirmed to be stronger for the reactions at 32 AMeV with respect to those at 52 AMeV¹⁵. Such a clean evidence of isospin diffusion also suggests that the role of pre-equilibrium emission within this selection of forward emitted $Z = 1$ particles is small, if one assumes that a strong contribution of promptly emitted particles could wash out the effect of the isospin equilibration process. By careful comparison of Fig. 6.12 with the result obtained exploiting the $\langle N/Z \rangle$ of the QP remnant shown in Fig. 6.4, we notice, common features aside, a slightly different trend of the isospin transport ratio as a function p_{red} . In fact, by using different isospin probes, different evolutions of the ratio can be obtained, even as a function of the same centrality estimator, as shown in Ref. [156] by comparing the results for three different isospin observables.

However, we notice a quite regular behaviour of all these plots, referring to $Z = 1$ particles reasonably selected as coming from the QP evaporation. To our knowledge, such rich and regular complementary results for the isospin transport ratio based

¹⁵Note that, at variance with what observed in Fig. 6.4, in this case the difference between the results for the two energies is more evident between the upper branches of the isospin transport ratio.

on both the $\langle N/Z \rangle$ of the QP (in both the evaporative and the breakup channels) and of the evaporated particles have never been presented in the literature.

6.3.2 Isotopic composition and emission pattern of LCPs and IMFs: isospin drift

In order to look for hints of isospin drift, we analyse the isospin content of LCPs and IMFs according to their emission pattern, i.e. to their orientation with respect to the QP. The isospin drift, i.e. the isospin transport phenomenon driven by barion density gradients in the interacting system, is expected to be responsible of the neutron enrichment of the so called neck region, which, during the QP-QT separation phase, expands reaching a local sub-saturation density (see Sec. 1.1.1). This can produce an unbalanced flux of more neutrons than protons towards the neck; the degree of imbalance, reflecting the final neutron enrichment of the fragments coming from that region, depends on the slope of the E_{sym} at $\rho < \rho_0$. In order to investigate on this point, we exploit a widely adopted method based on the comparison between the characteristics of the particles emitted forward with respect to the QP remnant and those of the particles emitted backward. In fact, while the former can be considered mostly related to the evaporative emissions of the excited QP, the origin of the latter is manifold, related both to the midvelocity emission and to the QP decay, also with possible contributions from the QT decay. In particular, in the following we label “backward” emissions those backward emitted with respect to the QP, but forward emitted with respect to the CM of the whole system, in order to reduce the contribution of the emissions belonging to the QT phase space [67].

In Fig. 6.13 the experimental $\langle N \rangle / Z$ value as a function of Z of the LCPs and IMFs in coincidence with a QP (QPr channel) are shown, comparing the results for forward (full circles, solid line) and backward (open circles, dotted line) emission. The results for the four reactions at 32 A MeV are shown in separate plots in panel (a), those for the higher beam energy in panel (b). The neutron enrichment in the backward emission is clearly observed: the respective $\langle N \rangle / Z$ is higher than the one obtained for the forward emitted particles. This observation stands for each fragment species, and for all the measured reactions at both bombarding energies¹⁶. For the two symmetric systems, where the isospin diffusion between projectile and target is suppressed since no isospin gradient is present between the two reaction partners, this neutron enrichment in the QP-backward emission can be quite safely interpreted as an evidence of isospin drift. On the other hand, in the asymmetric reactions, we must consider that both the effects of isospin drift and diffusion are present: the effect of the latter on the isospin composition of the QP is reflected both on forward (as evidenced in the previous section) and backward emission, due to the de-excitation contribution. Moreover, any interplay between the two phenomena, both taking place mostly in the contact region between projectile and target, may complicate the interpretation of the experimental observations. Additionally,

¹⁶The difference is less evident for $Z = 2$ due to the preponderance of α emission, that nails the respective $\langle N \rangle / Z$ to 1, with only minor variations.

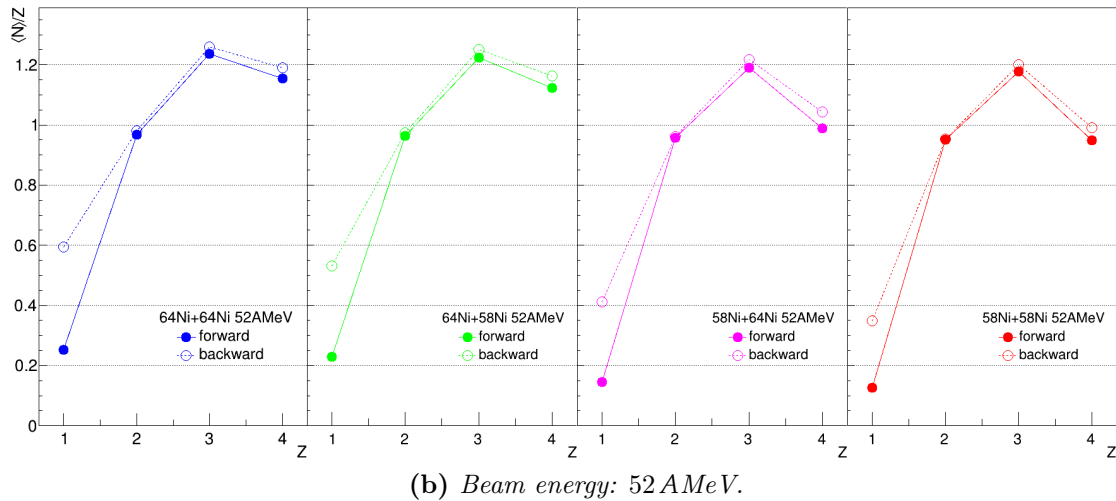
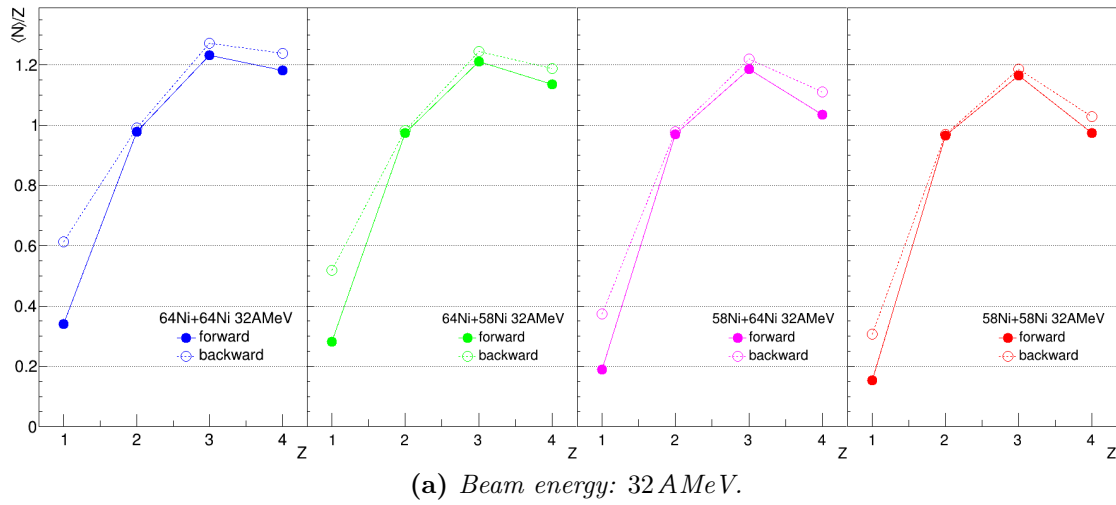


Figure 6.13: Experimental $\langle N \rangle / Z$ value as a function of Z for LCPs and IMFs in coincidence with a QP evaporation residue (QP channel). The results for the reactions at 32 A MeV are shown in panel (a), those at 52 A MeV, qualitatively similar, in panel (b). The different system are plotted separately. Both the results for forward and backward emissions (see text for details) are plotted. Statistical errors on the y -axis are smaller than the marker size.

a potential contamination of the QP-backward emission from the QT de-excitation would play differently in the two asymmetric reactions: in $^{58}\text{Ni}+^{64}\text{Ni}$ the emission from the neutron rich QT may contribute to the observed neutron enrichment in the QP-backward region, while in $^{64}\text{Ni}+^{58}\text{Ni}$ the scenario would be opposite, with the neutron deficient QT emission tending to wash out a possible effect of isospin drift. In summary, for the asymmetric reactions, the interpretation of the observed phenomenon is less straightforward. Therefore, when possible, the evaluations related to the isospin drift phenomenon are generally performed on isospin symmetric reactions [12], such as $^{64}\text{Ni}+^{64}\text{Ni}$ and $^{58}\text{Ni}+^{58}\text{Ni}$, in our case.

However, we want to stress that the observations on the light ejectiles here presented are, in a sense, not complete, due to the fact that we do not consider the free neutrons (whose emission mostly impacts the neutron rich system), which are not detected by our experimental apparatus. Moreover, additional and more stringent conclusions could be reached when the calibration of the LCPs detected by INDRA, covering a much broader phase space, will be available. The present study of the evidences related to the isospin drift phenomenon is therefore still preliminary. However, the observations done on Fig. 6.13 and discussed in this section are quite clear and promising, and indicate the possibility to highlight further characteristics of this dynamical process (by focusing on the symmetric systems).

6.4 Isospin characteristics of QP breakup fragments

As explained in Sec. 1.3, the isospin characteristics of the two QP breakup fragments are expected to carry information on the isospin transport phenomena, in a manner that depends on the time scales of the breakup itself compared with that of the reaction. Indeed, according to the picture presented before, we can assume a contact phase (reaction phase), after which a deformed and excited QP (and/or QT) emerges. This deformed QP can then fly apart featuring an initial internal isospin gradient, introduced, for example, by the action of the preceding isospin drift towards the neck and/or by the preceding isospin diffusion among imbalanced projectile and target (only for asymmetric reactions). Driven by this isospin gradient, the isospin equilibration within the QP starts, and ceases when the QP breaks up in two fragments, HF and LF. If this latter process is fast enough, the HF and the LF may retain some level of isospin imbalance, not fully equilibrated at the split time. Their isospin composition is thus related to the time Δt_{QPb} elapsed between the QP-QT split and the QP breakup, and to the details of the isospin transport during the preceding contact. Since the LF is generally produced in a region closer to the neck, it is expected to emerge more neutron rich, while, on the other hand, the HF is expected to be relatively more neutron deficient. This difference is gradually reduced as Δt_{QPb} increases. Such kind of arguments have been developed by some authors at *Texas A&M University* in various papers [58, 59], basing on data on reactions similar to those studied in this work. Indeed, by assuming a correlation between Δt_{QPb} and the α angle defined in eq. (1.7), in Refs. [58, 59] the isospin equilibration inside the QP prior to its breakup has been investigated by reporting the average isospin asymmetry $\langle \Delta \rangle = \langle \frac{N-Z}{A} \rangle$ of the HF and LF as a function of α , also obtaining a timescale of the equilibration process under a semiclassical hypothesis on the relationship between spin and rotation velocity.

In this section we aim at studying the characteristics of the fission fragments as emerging from our data, and then to check them in the light of the proposed interpretation. Since, within such an interpretation, the HF-LF isospin asymmetry is a consequence of isospin drift, following the observations of Sec. 6.3.2 the results for $^{64}\text{Ni}+^{64}\text{Ni}$ at 32 A MeV, the symmetric system with the strongest midvelocity neutron enrichment, will be presented. In order to compare our experimental results

with those of the already cited papers [58,59], we use the average isospin asymmetry $\langle\Delta\rangle$ instead of the $\langle N/Z\rangle$ exploited before as isospin observable. Following the observation of Ref. [60], where no correlation between Δt_{QPb} and the α angle has been evidenced within the AMD+GEMINI simulations, we avoid direct comparisons of the experimental data with the model predictions. We will limit our considerations to some selected HF-LF pairs, since a more comprehensive study of the phenomenon in relation to the charge asymmetry η of the split is made difficult by the limited η interval explored in our relatively small systems and by the low statistics available for each specific splitting configuration.

In Fig. 6.14 we show the $\langle\Delta\rangle$ of the HF, in red, and of the LF, in black, as a function of the α angle. Three specific HF-LF combinations¹⁷ have been plotted for two different sizes of the reconstructed QP ($Z_{rec} = 19$ in panel (a) and $Z_{rec} = 21$ in panel (b)). In the central plot of panel (a) we also plotted the result for the same $Z_H = 12$, $Z_L = 7$ pair of Ref. [59] for the reaction $^{64}\text{Ni}+^{64}\text{Ni}$ at 35 AMeV, which is similar to the reaction presented here; we stress that the results are quite comparable, even if in our case both the HF and the LF are slightly more neutron deficient. In our dataset, the limited statistics for each single HF-LF pair prevents us from extracting an accurate description of the evolution of the isospin content of the two breakup fragments with the α angle¹⁸. However, we satisfactorily observe very smooth data trends which are fully compatible to those obtained in Refs. [58,59]. In fact, the LF is always more neutron rich than the HF. Moreover, a larger asymmetry between the HF and LF is found for the most aligned configurations with the LF emitted backward (i.e. at low α angles), while a higher degree of equilibration is obtained for bigger α values (less evident for the pairs with $Z_L = 5$). We notice, however, that within the small charge asymmetries that we can probe (see Sec. 5.2), the value of $\langle\Delta\rangle_L$ (and its behaviour with α) depends mostly on the identity of the LF, and less on the partner HF: this can be seen by comparing the black dots for the same Z_L in the two panels of Fig. 6.14 (similar considerations can be done on Fig. 9 of Ref. [59] for the reaction $^{70}\text{Zn}+^{70}\text{Zn}$ at 35 AMeV). The same stands for $\langle\Delta\rangle_H$, whose behaviour with α however results flatter, due to the smaller possible variation of $\langle\Delta\rangle$ for heavier nuclei.

The good agreement between the experimental results and observations obtained in this work and in Refs. [58,59] makes us confident about further discussion and comparison. We consider the study shown in this thesis as preliminary, in view of further analyses to be carried out in the future.

In summary, our observations on the isospin content of the two breakup fragments are generally in good agreement with corresponding detailed results reported in the literature for similar reactions. Therefore, in the framework of the assumed interpretation of the microscopic mechanisms taking place in a QP breakup scenario,

¹⁷We consider the configurations with $Z_L = 5, 7, 9$ to select the most asymmetric splits for the chosen reconstructed QP: the cases with a LF with even Z (e.g. $Z_L = 6, 8$) are not shown, since, as already explained, these species see a preponderance of $N = Z$ configurations (i.e. $\langle\Delta\rangle = 0$) that can mask the searched effects.

¹⁸The most evident fluctuations are found around $\alpha \sim 90^\circ$: this region is in fact less densely populated due to the apparatus acceptance, that tends to cut out these “transverse” breakups.

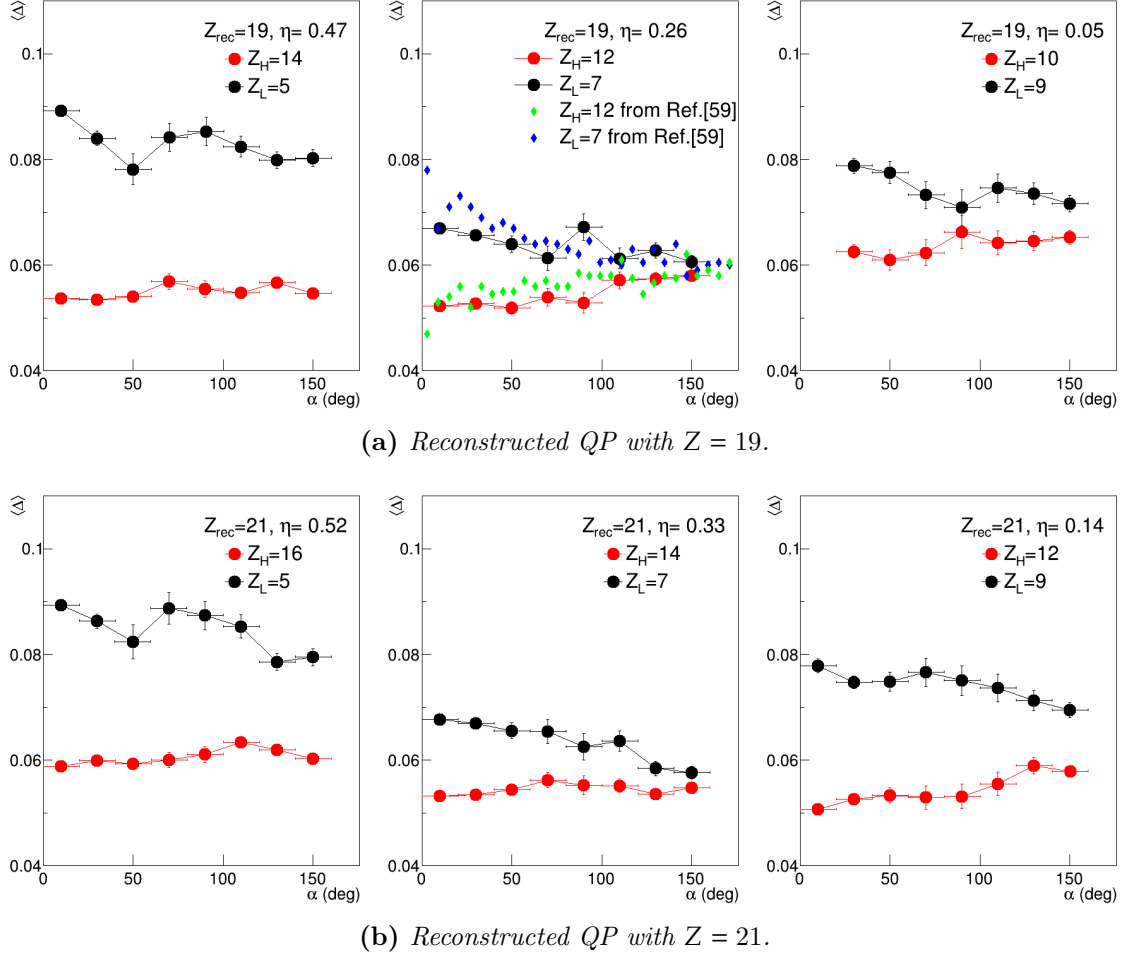


Figure 6.14: Plots of $\langle \Delta \rangle$ as a function of α for selected combinations of breakup fragments obtained from the experimental data of $^{64}\text{Ni}+^{64}\text{Ni}$ at 32 AMeV. The results for the HF (LF) are plotted in red (black). The plots for three configurations, with $Z_L = 5, 7, 9$, are shown, for a reconstructed QP with $Z_{rec} = 19$ in panel (a), and with $Z_{rec} = 21$ in panel (b). The blue and green points in the central plot of panel (a) are the $\langle \Delta \rangle$ vs α results for the LF and HF, respectively, for the same HF-LF combination, taken from Fig. 11 of Ref. [59], where the reaction $^{64}\text{Ni}+^{64}\text{Ni}$ at 35 AMeV has been studied.

our data lead to similar conclusions as those proposed in the literature. Specifically for the isospin variable, a possible explanation of the results is given in terms of the interplay between isospin diffusion and drift during the interaction and of the relevant decay times. For the breakup channel, assuming a fast sequential split, the action of isospin drift is found in the neutron enrichment of the LF with respect to the HF. The isospin diffusion within the deformed QP, taking place before its breakup, has been evidenced by showing the equilibration of the isospin content of the two fragments, evolving with an observable that is believed to be related to the Δt_{QPb} between the QP-QT separation and the QP breakup.

Summary and conclusions

The work presented in this thesis is part of the scientific program of the INDRA-FAZIA collaboration. The data collected in the E789 experiment, that was carried out at GANIL from April to May 2019, have been here analysed and discussed. The goal of the experiment was to probe the density dependence of the symmetry energy term of the NEdS [2, 3, 10] by studying the isospin transport phenomena in heavy ion reactions at intermediate energies, gathering information on both the isospin diffusion and isospin drift contributions [13]. The reactions $^{58,64}\text{Ni}+^{58,64}\text{Ni}$ have been investigated; the study of all the four possible combinations of ^{58}Ni and ^{64}Ni allows for the comparison of the two asymmetric systems with both the neutron rich and neutron deficient symmetric systems. By using appropriate techniques, such as the isospin transport ratio [19], this enables to inspect the two contributions to the isospin transport given by the mechanisms of drift and diffusion [13]. The four reactions have been measured at two beam energies, 32 A MeV and 52 A MeV, within the Fermi energies regime. The availability of data for two different beam energies allows to investigate possible differences in the isospin transport mechanisms associated with two different reaction dynamics with associated different interaction times. In order to perform this kind of study, related to the isospin content of the ejectiles produced in the reactions, the use of an apparatus capable of identifying the (Z, A) of the products is mandatory.

The E789 experiment has been the first campaign to exploit the coupled INDRA-FAZIA apparatus [16]. The 12 blocks of FAZIA [17], placed at forward polar angles (substituting the first five rings of INDRA), provide optimal identification of the charge and mass numbers of the detected ejectiles, with low energy thresholds. Isotopic discrimination can be achieved up to $Z \sim 20 - 25$ (depending on the employed identification technique), allowing for the study of the isospin characteristics of the fragments belonging to the QP phase space, without the use of a mass spectrometer. INDRA [18], on the other hand, provides an almost 4π angular coverage, which is generally useful for building global variables related to the reaction centrality. However, the energy calibration for the rings from 10 to 17 of INDRA is not yet available, thus preventing us from using a few, otherwise promising, global observables as centrality estimators. Instead, we have extensively used the reduced QP momentum along the beam axis p_{red} as centrality related observable [69], which can be calculated exploiting just the information on the QP, collected by FAZIA. A future improvement of the analysis presented in this thesis will include, when the full energy calibration of the apparatus will be available, the use of other centrality related parameters, such as the E_{trans}^{LCP} (see Sec. 5.3).

Two classes of events have been selected and studied. The first and most pop-

ulated one is the QP evaporation channel (labelled as QPr), characterised by the presence of a single big fragment compatible with a QP evaporation residue, accompanied only by LCPs and/or IMFs. The second event class is the QP breakup channel (labelled as QPb), with the presence of two big fragments, emitted mainly in the CM forward hemisphere. The characteristics of this selection of events have been investigated, showing the typical features of a QP *dynamical fission* (or *breakup*), namely the anisotropy of the emission pattern for the most asymmetric splits, with the light breakup fragment preferentially emitted backwards with respect to the heavy one, towards the CM [20–22].

The experimental data have been compared to the predictions of the dynamical transport model AMD [14], coupled to GEMINI++ [15] used as afterburner. The simulated data have been filtered with a software replica of the apparatus [143]. The general characteristics of the reaction products (e.g. the distributions of charge number, velocity, scattering angle) are nicely reproduced by the simulations, for both the selected reaction channels. The AMD+GEMINI++ simulated data have been also exploited for an investigation of some centrality estimators, which indicated the already mentioned p_{red} variable as the best choice for this purpose, for the present. In fact, within the model prediction, the clear and narrow correlation of p_{red} with the reduced impact parameter b_{red} results almost independent of the reaction, and only slightly dependent on the beam energy. Very similar correlations are also obtained between the two reaction channels.

Taking advantage of the optimal isotopic identification capability of the INDRA-FAZIA apparatus, we then focused on the isospin characteristics of the reaction products, in order to look for details of isospin transport, not destroyed by the statistical evaporation. Firstly, clear indications of *isospin diffusion* between projectile and target in the asymmetric reactions $^{64}\text{Ni}+^{58}\text{Ni}$ and $^{58}\text{Ni}+^{64}\text{Ni}$ have been shown. We investigated this process of isospin equilibration by exploiting the isospin transport ratio technique [19, 41, 69, 153, 154, 156], based on the comparison of the isospin characteristics of the ejectiles of an asymmetric reaction with those of the two corresponding symmetric reactions. This technique allows to bypass the systematic uncertainties introduced by the apparatus (assuming the same experimental conditions for the whole set of reactions), but also the effects of other processes whose action is similar in all the systems (e.g. the statistical de-excitation), thus allowing for a better estimate of the dynamical isospin equilibration effect. For the QPr event selection, we evaluated the isospin transport ratio as a function of p_{red} , exploiting the $\langle N/Z \rangle$ both of the QP remnant, from its direct identification, and of the $Z = 1$ LCPs emitted forward with respect to the QP, which are expected to be produced in its statistical decay and to reflect its isotopic composition [42, 43, 67]. In both cases, we obtained an evident and regular evolution towards isospin equilibration for increasing reaction centrality; to our knowledge such rich and complementary results on the isospin transport ratio based on the isospin composition of both the QP residue and of its evaporative emissions have never been presented in the literature. Both evaluations show a higher degree of isospin equilibration reached in the asymmetric reactions at 32 A MeV than at 52 A MeV, perhaps related to shorter

projectile-target contact times in the latter case. We have investigated the isospin diffusion also in the QPb event selection, by evaluating the isospin transport ratio on the $\langle N/Z \rangle$ of the QP reconstructed as the sum of the two breakup fragments (named HF and LF), again as a function of p_{red} . Also in this case, a clear trend towards isospin equilibration is found for increasing centrality, stronger at 32 A MeV than at 52 A MeV. Quite interestingly, by comparing the results for the isospin transport ratio in the two channels, we observed a stronger tendency to isospin equilibration on the QP in the breakup channel than in the evaporative channel. The interpretation of this result is not straightforward and deserves deeper investigation. The QP breakup channel seems to select, for a given centrality bin, a subset of events where a more effective isospin diffusion process took place, maybe due to a deeper and longer waveform overlap that the two reaction partners on average experience in the breakup case. Our results are at variance with those obtained by the FAZIA collaboration in the FAZIA-SYM experiment, in which the four projectile-target combinations of ^{48}Ca and ^{40}Ca were studied at 35 A MeV [69]. In FAZIA-SYM, no significant difference was found in the isospin transport ratio between the QP evaporative and the QP breakup channels. In this work we have been able to exclude the different geometrical acceptance of the employed apparatuses as a possible cause of the different results. Since, from the AMD+GEMINI++ simulations, we also obtain a similar p_{red} vs b_{red} correlation for the two systems, we can also probably exclude a different centrality selection as a cause for the discrepancy. Further investigations are thus foreseen in order to shed light on this comparison.

Similar evaluations on the isospin diffusion process have been carried out also within the AMD+GEMINI++ simulated data, assuming both the asy-stiff and the asy-soft recipes for the symmetry energy term of the N EoS. The isospin equilibration has been evidenced for both the selected reaction channels. Unfortunately, no sensitivity to the asy-stiffness of the E_{sym} has been obtained. Future analyses could be aimed at the selection of further observables more sensitive to the N EoS parametrisation (such as, e.g., the width of the isotopic distribution of LCPs and IMFs in coincidence with the QP, here presented in Sec. 4.1.1 only for primary fragments). However, the stronger trend towards isospin equilibration for the QPb channel is observed also within the model predictions. We therefore hope to exploit in the future the information provided by the AMD simulations to track the features of the dynamical processes [60] indirectly selected by the QPr and QPb conditions imposed on the secondary events.

Also the neutron enrichment of fragments at midvelocity has been clearly highlighted in the experimental data, possibly related to *isospin drift*. In particular, the clear neutron enrichment for all the light species (LCPs and IMFs) emitted backward with respect the QP is observed compared to those emitted forward, for all the investigated reactions in the QPr output channel and for both bombarding energies. For the symmetric reactions, in which the simultaneous action of isospin diffusion is absent, this can be quite straightforwardly interpreted as a promising sign of isospin drift. These results are quite preliminary, and we hope to further inspect the behaviour of the isospin composition of the midvelocity emission, e.g. by studying the

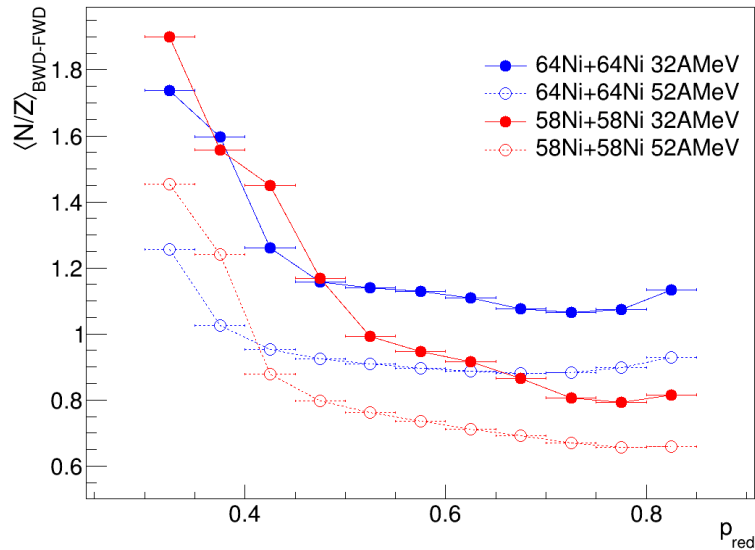


Figure C.1: Experimental plot of $\langle N/Z \rangle$ vs p_{red} , obtained from the difference between the backward and forward isotopic distributions of the LCPs and IMFs in coincidence with a QP (QPr channel). The results for the symmetric reactions at both energies are plotted. The errors on the y -axis are statistical, those on the x -axis correspond to the p_{red} bin width.

evolution of its neutron enrichment with the reaction centrality. As an example, for the two symmetric systems, in Fig. C.1 we show the plots of the $\langle N/Z \rangle$ evaluated on the difference between the isotopic distributions of the LCPs and IMFs emitted backward and those emitted forward with respect to the QP¹ in the QPr channel, reported as a function of p_{red} . The four plots show a common trend, with the midvelocity emission becoming more neutron rich for increasing centrality. This observation could suggest a more prominent action of the isospin drift mechanism for more central collisions, within the inspected p_{red} interval, with some differences emerging among the four reactions. However, this analysis is still preliminary, and further investigation is needed.

Lastly, we investigated the isospin characteristics of the two breakup fragments in the QPb channel. The interest in such kind of study stems from the fact that, assuming that the fission process is fast enough, the isospin composition of the two breakup fragments HF and LF (heavy and light fragment, respectively) is expected to retain some information on the isospin transport (both drift and diffusion) prior to the breakup, also depending on the time elapsed between the QP-QT split and the QP breakup itself, Δt_{QPb} . In particular, following the idea published in *Rodríguez Manso et al.* [59], we studied the evolution of the isospin content of the LF and the HF as a function of the α angle between the QP-QT separation axis and the QP fission axis, that according to a semi-classical picture can be considered

¹By exploiting this difference, we aim, on average, to cancel out from the backward emission the contribution of QP evaporation, assumed isotropic in the QP reference frame.

correlated to Δt_{QPb} . We observed a relaxation of the isospin imbalance between the LF and the HF for increasing α . The result is qualitatively, and in some respect also quantitatively, compatible with what reported in Ref. [58, 59]. The study on this topic presented in this work is still preliminary, and it will be developed in the future also thanks to the comparison with model predictions.

From an experimental point of view, anyhow, we underline that in this thesis we carried out several accurate analyses for the QP breakup channel that to our knowledge have been never attempted altogether on the same dataset. Together with those of the QP evaporative decay, our results, partly preliminary, offer a very comprehensive view of the isospin transport in heavy ion collisions at Fermi energies that, we believe, can help constrain fundamental ingredients contained in reaction models.

Bibliography

- [1] V. Baran et al., *Phys. Rep.* 410, 335 (2005)
- [2] J. Margueron et al., *Phys. Rev. C* 97, 025805 (2018)
- [3] B. A. Li et al., *Phys. Lett. B* 727, 276 (2013)
- [4] P. Danielewicz, *Nucl. Phys. A* 727, 233 (2003)
- [5] K. Iida et al., *Eur. Phys. J. A* 50, 42 (2014)
- [6] C. J. Horowitz, *Eur. Phys. J. A* 30, 303 (2006)
- [7] M. Di Toro et al., *J. Phys. G: Nucl. Part. Phys.* 37, 083101 (2010)
- [8] B.A. Li et al., *Int. J. Mod. Phys. E* Vol.7, N.2 , 147 (1998)
- [9] R. Płaneta, *Int. J. Mod. Phys. E* Vol.15, N.5 , 973 (2006)
- [10] P. Napolitani et al., *Phys. Rev. C* 81, 044619 (2010)
- [11] J. Łukasik et al., *Phys. Rev. C* 55, 1906 (1997)
- [12] R. Lioni et al., *Phys. Lett. B* 625, 33 (2005)
- [13] V. Baran et al., *Phys. Rev. C* 72, 064620 (2005)
- [14] A. Ono et al., *Prog. Theor. Phys.* 87, 1185 (1992)
- [15] R. J. Charity, *Phys. Rev. C* 82, 014610 (2010)
- [16] O. Lopez, *Nuovo Cim. C* 41, 165 (2018)
- [17] <http://fazia.in2p3.fr>
- [18] <http://indra.in2p3.fr/>
- [19] F. Rami et al., *Phys. Rev. Lett.* 84, 1120 (2000)
- [20] P. Glässel et al., *Z. Phys. A* 310, 189 (1983)
- [21] G. Casini et al., *Phys. Rev. Lett.* 71, 2567 (1993)
- [22] A. A. Stefanini et al., *Z. Phys. A* 351, 167 (1995)
- [23] D. Durand et al., *Nuclear Dynamics in the Nucleonic Regime* 1st ed., Taylor&Francis, Boca Raton (2000)
- [24] N. Bohr, *Nature* 137, 344 (1936)

- [25] V. Weisskopf, *Phys. Rev.* **52**, 295 (1937)
- [26] W. Hauser, H. Feshbach, *Phys. Rev.* **87**, 366 (1952)
- [27] J. Gosset et al. *Phys. Rev. C* **16**, 629 (1977)
- [28] I. Montvay, *Nuclear Fireballs in Heavy Ion Collisions*, in *Hadronic Matter at Extreme Energy Density*, Springer, Boston, 1980.
- [29] B. Borderie et al., *Ann. Phys. Fr.* **15**, 287 (1990)
- [30] W. Rösch et al., *Nucl. Phys. A* **496**, 141 (1989)
- [31] L. Lassen et al., *Phys. Rev. C* **55**, 1900 (1997)
- [32] M. Di Toro et al., *Eur. Phys. J. A* **30**, 65 (2006) *and references therein*
- [33] A. S. Botvina et al., *Phys. Rev. C* **59**, 3444 (1999)
- [34] F. Auger et al., *Phys. Rev. C* **35**, 190 (1987)
- [35] D. Durand, *Nucl. Phys. A* **630**, 52 (1998)
- [36] B. Borderie et al., *Prog. Part. Nucl. Phys.* **61**, 551 (2008)
- [37] Ch. O. Bacri et al. *Phys. Lett. B* **353**, 27 (1995)
- [38] R. Płaneta et al., *Phys. Rev. C* **38**, 195 (1988)
- [39] A. A. Marchetti et al., *Phys. Rev. C* **48**, 266 (1993)
- [40] H. Madani et al., *Phys. Rev. C* **51**, 2562 (1995)
- [41] M. B. Tsang et al., *Phys. Rev. Lett.* **92**, 062701 (2004)
- [42] E. Galichet et al., *Phys. Rev. C* **79**, 064614 (2009)
- [43] I. Lombardo et al., *Phys. Rev. C* **82**, 014608 (2010)
- [44] S. Barlini et al., *Phys. Rev. C* **87**, 054607 (2013)
- [45] Y. Laroche et al., *Phys. Rev. C* **62**, 051602 (2000)
- [46] D. Thériault et al., *Phys. Rev. C* **74**, 051602 (2006)
- [47] C. P. Montoya et al., *Phys. Rev. Lett.* **73**, 3070 (1994)
- [48] A. Kelić et al., *Eur. Phys. J. A* **30**, 203 (2006)
- [49] S. S. M. Wong, *Introductory Nuclear Physics* 2nd ed., Wiley, New York (1998)
- [50] B. T. Reed et al., *Phys. Rev. Lett.* **126**, 172503 (2021)
- [51] G. Ademard et al., *Eur. Phys. J. A* **50**, 33 (2014)
- [52] H. Müller et al., *Phys. Rev. C* **52**, 2072 (1995)

- [53] A. Ono et al., *Phys. Rev. C* 68, 051601 (2003)
- [54] L. Meitner, O. Frisch, *Nature* 143, 239 (1939) *and references therein*
- [55] C. Bertulani, P. Danielewicz, *Introduction to Nuclear Reactions* 1st ed., Taylor&Francis, Boca Raton (2004)
- [56] F. Bocage et al., *Nucl. Phys. A* 676, 391 (2000)
- [57] E. De Filippo et al., *Phys. Rev. C* 71, 064604 (2005)
- [58] A. Jedele et al., *Phys. Rev. Lett.* 118, 062501 (2017)
- [59] A. Rodriguez Manso et al., *Phys. Rev. C* 95, 044604 (2017)
- [60] S. Piantelli et al., *Phys. Rev. C* 101, 034613 (2020)
- [61] S. Carboni et al., *Nucl. Instr. Meth. A* 664, 251 (2012)
- [62] G. Pastore et al., *Nucl. Instr. Meth. A* 860, 42 (2017)
- [63] S. Barlini et al., *J. Phys.: Conf. Ser.* 1561, 012003 (2020)
- [64] S. Valdré et al., *Nucl. Instr. Meth. A* 930, 27 (2019)
- [65] G. Poggi, *Eur. Phys. J. Spec. Top.* 150, 369 (2007)
- [66] R. Bougault et al., *Eur. Phys. J. A* 50, 47 (2014)
- [67] S. Piantelli et al., *Phys. Rev. C* 103, 014603 (2021)
- [68] A. Camaiani et al., *Phys. Rev. C* 102, 044607 (2020)
- [69] A. Camaiani et al., *Phys. Rev. C* 103, 014605 (2021)
- [70] https://risp.ibs.re.kr/html/risp_en/
- [71] <https://www.fbk.eu/it/>
- [72] <https://www.cismst.de/>
- [73] L. Bardelli et al., *Nucl. Instr. Meth. A* 602, 501 (2009)
- [74] <http://www.topsil.com>
- [75] G. Poggi et al., *Nucl. Instr. Meth. B* 119, 375 (1996)
- [76] L. Bardelli et al., *Nucl. Instr. Meth. A* 605, 353 (2009)
- [77] S. Valdré, Bachelor Thesis, Università di Firenze (2009)
- [78] N. Le Neindre et al., *Nucl. Instr. Meth. A* 710, 145 (2013)
- [79] S. Valdré, *contribution at GDS topical meeting*, LNL, Italy (2017)
- [80] J. Pouthas et al., *Nucl. Instr. Meth. A* 357, 418 (1995)

-
- [81] J. Pouthas et al., *Nucl. Instr. Meth. A* 369, 222 (1996)
- [82] G. Wittwer et al., *contribution at 14th IEEE-NPSS Real Time Conference, Stockholm, Sweden (2005)*
- [83] N. Le Neindre et al., *contribution at FAZIA Days, Caen, France (2016)*
- [84] X. Grave et al., *contribution at 14th IEEE-NPSS Real Time Conference, Stockholm, Sweden (2005)*
- [85] S. Valdré et al., *Nuovo Cim. C* 41, 167 (2018)
- [86] S. Valdré et al., *Nuovo Cim. C* 43, A10 (2020)
- [87] G. F. Knoll, *Radiation Detection and Measurement* 4th ed., Wiley, New York, 2010
- [88] A. J. Kordyasz et al., *Eur. Phys. J. A* 51, 15 (2015)
- [89] N. Bohr, *Phil. Mag.* 25, 10-31 (1913)
- [90] C. A. Ammerlaan et al., *Nucl. Instr. Meth. A* 22, 189 (1963)
- [91] J. B. A. England et al., *Nucl. Instr. Meth. A* 280, 291 (1989)
- [92] G. Pausch et al., *Nucl. Instr. Meth. A* 322, 43 (1992)
- [93] G. Pausch et al., *Nucl. Instr. Meth. A* 337, 573 (1994)
- [94] M. Mutterer et al., *IEEE Trans. Nucl. Sci.* 47(3), 756 (2000)
- [95] S. Barlini et al., *Nucl. Instr. Meth. A* 600, 644 (2009)
- [96] L. Bardelli et al., *Nucl. Instr. Meth. A* 654, 272 (2011)
- [97] G. Pasquali et al., *Eur. Phys. J. A* 50, 86 (2014)
- [98] P. Ottanelli, PhD thesis, Università di Firenze (2019)
- [99] P.A. Tove et al., *Nucl. Instr. Meth.* 51, 261 (1967)
- [100] W. Seibt et al., *Nucl. Instr. Meth.* 113, 317 (1973)
- [101] W. Bohne et al., *Nucl. Instr. Meth. A* 240, 145 (1985)
- [102] T. Kurahashi et al., *Nucl. Instr. and Methods A* 422, 385 (1999)
- [103] F. Z. Henari et al., *Nucl. Instr. Meth. A* 288, 439 (1990)
- [104] H. A. Rijken et al., *IEEE Trans. Nucl. Sci.* 40(4), 349 (1993)
- [105] G. Pausch et al., *IEEE Trans. Nucl. Sci.* 44(3), 1040 (1997)
- [106] R. A. Winyard et al. *Nucl. Instr. Meth.* 95, 141 (1971)
- [107] F. Benrachi et al., *Nucl. Instr. Meth. A* 281, 137 (1989)

- [108] C. Frosin et al., *Nucl. Instr. Meth. A* 951, 163018 (2020)
- [109] O. Lopez, S. Piantelli et al., E789 proposal (2018)
- [110] P. Betti, Bachelor thesis, Università di Firenze (2019)
- [111] <https://cc.in2p3.fr/>
- [112] <https://root.cern.ch/>
- [113] <http://indra.in2p3.fr/kaliveda/>
- [114] <http://indra.in2p3.fr/kaliveda/KVedaLossDoc/KVedaLoss.html>
- [115] F. Hubert et al., *Atomic Data and Nuclear Data Tables* 46, 1 (1990)
- [116] M. Pârlog et al., *Nucl. Instr. Meth. A* 482, 674 (2002)
- [117] M. Pârlog et al., *Nucl. Instr. Meth. A* 482, 693 (2002)
- [118] A. Ono et al., *Phys. Rev. C* 53, 2958 (1996)
- [119] A. Ono, *Phys. Rev. C* 59, 853 (1999)
- [120] A. Ono, *J. Phys.: Conf. Ser.* 420, 012103 (2013)
- [121] R. J. Charity et al., *Nuclear Physics A* 483, 371 (1988)
- [122] J. Xu, *Prog. Part. Nucl. Phys.* 106, 312 (2019)
- [123] P. Napolitani et al., *Phys. Lett. B* 726, 382 (2013)
- [124] M. Colonna et al., *Nucl. Phys. A* 642, 449 (1998)
- [125] J. Aichelin et al., *Phys. Lett. B* 176, 14 (1986)
- [126] J. Aichelin, *Phys. Rep.* 202, 233 (1991)
- [127] M. Papa et al., *Phys. Rev. C* 64, 024612 (2001)
- [128] M. Papa et al., *J. Comput. Phys.* 208, 403 (2005)
- [129] S. Piantelli et al., *Phys. Rev. C* 99, 064616 (2019)
- [130] N. Ikeno et al., *Phys. Rev. C* 93, 044612 (2016)
- [131] E. Chabanat et al., *Nucl. Phys. A* 635, 231 (1998)
- [132] D. D. S. Coupland et al., *Phys. Rev. C* 84, 054603 (2011)
- [133] A. R. Raduta et al., *Phys. Rev. C* 75, 044605 (2007)
- [134] A. Gavron, *Phys. Rev. C* 21, 230 (1980)
- [135] F. Pühlhofer, *Nucl. Phys. A* 280, 267 (1977)

- [136] D. Durand, *Nucl. Phys. A* 541, 266 (1992)
- [137] G. Baiocco, *PhD thesis*, Università di Bologna (2012)
- [138] N. Bohr, J. A. Wheeler, *Phys. Rev.* 56, 426 (1939)
- [139] L. G. Moretto, *Nucl. Phys. A* 247, 211 (1975)
- [140] A. V. Ignatyuk et al., *Yad. Fiz.* 21, 485 (1975) [*Sov. J. Nucl. Phys.* 21, 255 (1975)]
- [141] G. H. Rawitscher, *Nucl. Phys.* 85, 337 (1966)
- [142] R. J. Charity, *Phys. Rev. C* 58, 1073 (1998)
- [143] <http://indra.in2p3.fr/kaliveda/KVSimDirGUIDoc/KVSimDirGUI.html>
- [144] I. Lombardo et al., *Phys. Rev. C* 84, 024613 (2011)
- [145] S. Piantelli et al., *Phys. Rev. C* 88, 064607 (2013)
- [146] M. D'Agostino et al., *Nucl. Phys. A* 875, 139 (2012)
- [147] V. E. Viola et al., *Phys. Rev. C* 31, 1550 (1985)
- [148] C. Cavata et al., *Phys. Rev. C* 42, 1760 (1990)
- [149] E. Plagnol et al., *Phys. Rev. C* 61, 014606 (1999)
- [150] C. Cugnon et al., *Nucl. Phys. A* 397, 519 (1983)
- [151] J. Frankland et al., *Nucl. Phys. A* 689, 905 (2001)
- [152] G. Casini et al., *Phys. Rev. C* 86, 011602(R) (2012)
- [153] L.-W. Chen et al., *Phys. Rev. Lett.* 94, 032701 (2005) *and references therein*
- [154] M. B. Tsang et al., *Phys. Rev. Lett.* 102, 122701 (2009) *and references therein*
- [155] S. Piantelli et al., *Phys. Rev. C* 96, 034622 (2017)
- [156] L. W. May et al., *Phys. Rev. C* 98, 044602 (2018)